HIGH TEMPERATURE NON-IDEAL COMPRESSIBLE FLOWS OF SILOXANE VAPORS

Thermal stability - Flow characterization using optical techniques

SIMONE GALLARINI

POLITECNICO
MILANO 1863

PhD in Energy and Nuclear Science and Technology
Politecnico di Milano

Cycle XXXII

Simone Gallarini
High temperature non-ideal compressible flows of siloxane vapors
Thermal stability - Flow characterization using optical techniques
PhD in Energy and Nuclear Science and Technology – Cycle XXXII

SUPERVISOR:
Prof. Andrea Spinelli
ASSISTANT SUPERVISORS:
Prof. Fabio Cozzi and Prof. Alberto Guardone
TUTOR:
Prof. Vincenzo Dossena

Politecnico di Milano
Energy Department
via Lambruschini 4
20156 Milano

ABSTRACT

Compressible flows of molecularly complex fluids operating at thermodynamic conditions close to the vapor saturation line and the critical point are of interest in various industrial applications. In the last two decades considerable advancements were made in the thermodynamic modeling and numerical simulation of highly non-ideal flows. However, experimental data are still scarce in the literature up to date, due to the hostile environment associated with such flows, that feature high temperature, high pressure, and possibility of fluid decomposition.

This thesis presents the first characterization by means pressure, temperature and direct velocity measurements of a flow of a molecularly complex fluid operating at non-ideal conditions. Tests were carried out on the Test Rig for Organic Vapors of Politecnico di Milano. A nozzle was selected as the simplest geometry of relevance for the study of fundamentals of the fluid-dynamics of such flows and for its representativeness of industrial applications, such as organic Rankine cycle turbines.

Siloxane fluids Hexamethyldisiloxane (siloxane MM - $C_6H_{18}OSi_2$) and octamethyltrisiloxane (siloxane MDM - $C_8H_{24}O_2Si_3$) were chosen for testing due to their relevance in high temperature ORC applications. In literature, data about their thermal stability are scarce or absent, thus their behavior and decomposition at temperatures comprised between 200 °C and 420 °C was studied with a dedicated experimental campaign.

First, a method based on the deviation of the vapor-liquid equilibrium curve of the fluid measured before and after thermal stress was employed, but it yielded contradictory results, due to the low volatility of the tested fluids. Thus, an improved method was adopted, based on chemical analysis of both vapor and liquid phases of the sample subjected to thermal stress. MM proved to be more stable than MDM. Moreover, due to the current interest in the use of mixtures in ORCs, an equimolar mixture of MM and MDM was also tested, showing a behavior that appears to be different from the simple superimposition of pure fluid ones.

With the information about the thermal stability of working fluids, their non-ideal fluid dynamics was then characterized. Experimental observations of non-ideal flows by means of pressure and temperature measurements, complemented with schlieren visualizations (from which the Mach number was measured), are first presented. The dependence of flow quantities on total conditions is proved. However, for a complete characterization of the flow, the independent measurement of velocity is necessary. To reach this goal, the Laser Doppler velocimetry (LDV) technique was chosen and a specifically designed seeding system was implemented. The adopted apparatus was conceived for seeding high temperature, high pressure and potentially condensible flows without contamination, and it is suitable to every application where at least some of these requirements are present.

The full characterization of a flow of a molecularly complex fluid operating at non-ideal conditions was carried out. Three different experimental cases are presented: a subsonic compressible nozzle flow with a large uniform region at Mach number equal to 0.7, a high velocity gradient supersonic flow at Mach number equal to 1.4 and a near zero velocity gradient flow at Mach number equal to 1.7. Temperature, pressure and direct velocity measurements are performed to characterize the flow at discrete points along the nozzle axis. Measured velocity is compared with both computational fluid dynamics (CFD) calculations and velocity computed from pressure and temperature measurements. In both cases the thermodynamic model applied was a state-of-the-art Helmholtz energy equation of state. Maximum observed deviations between measured velocity and those obtained from CFD or computed from pressure and temperature measurements are below 6.6% and reduce to $\approx 0 \div 4\%$ in most cases.

These are the very first direct measurements ever exploiting the LDV technique in a high velocity non-ideal flow and show the feasibility of laser Doppler velocimetry in this framework. This work poses the basis for a complete characterization of the flow with pressure, temperature and velocity measurements along the whole nozzle axis. Further, the LDV system presented in this thesis can provide reference values of velocity for the calibration of directional pressure probes in the non-ideal regime, that can be employed for the study of the fluid dynamics of linear blade cascades.

PUBLICATIONS

Some ideas and figures have appeared previously in the following publications:

- **Experimental observation and thermodynamic modeling of non-ideal expanding flows of siloxane MDM vapor for ORC applications,** *A. Spinelli, G. Cammi, C. C. Conti, S. Gallarini, M. Zocca, F. Cozzi, P. Gaetani, V. Dossena, A. Guardone,* Energy, Volume 168, 1 February 2019, Pages 285-294;
- **Thermal stability of hexamethyldisiloxane and octamethyltrisiloxane,** *L. Keulen, S. Gallarini, C. Landolina, A. Spinelli, P. Iora, C. Invernizzi, L. Lietti, A. Guardone,* Energy, Volume 165, Part B, 15 December 2018, Pages 868-876;
- **Experimental evidence of non-ideal compressible effects in expanding flow of a high molecular complexity vapor,** *A. Spinelli, G. Cammi, S. Gallarini, M. Zocca, F. Cozzi, P. Gaetani, V. Dossena, A. Guardone,* Experiments in fluids, 59:126, 2018;
- **Experimental observation of non-ideal expanding flows of Siloxane MDM vapor for ORC applications,** *A. Spinelli, G. Cammi, M. Zocca, S. Gallarini, F. Cozzi, P. Gaetani, V. Dossena, A. Guardone,* Energy Procedia, Volume 129, September 2017, Pages 1125-1132.

The following publications are in preparation:

- **Thermal stability of linear siloxanes and their mixtures** *S. Gallarini, A. Spinelli, L. Lietti, A. Guardone,* Applied thermal engineering;
- **Direct velocity measurements in high-temperature non-ideal vapor flows,** *S. Gallarini, A. Spinelli, F. Cozzi, A. Guardone,* Experiments in fluids;

CONTENTS

I THERMAL STABILITY OF PURE LINEAR SILOXANES AND MIXTURES

II CHARACTERIZATION OF HIGH TEMPERATURE NON-IDEAL NOZZLE VAPOR FLOWS

LIST OF FIGURES

LIST OF TABLES

1

INTRODUCTION

1.1 MOTIVATION AND OBJECTIVES

Compressible-fluid flows of molecularly complex substances at thermodynamic conditions close to the vapor saturation line and critical point are encountered in various applications in the oil and gas sector, in the chemical process industry, and in the energy field. The latter includes power systems as organic Rankine cycles (ORCs), supercritical carbon dioxide cycles (sCO2), steam Rankine cycles, and high temperature heat pumps. These kind of flows are typically vapor or supercritical fluid flows, occurring at moderate to high temperature, up to about 400 °C, in components which are typically unconventional turbomachines, valves, heat exchangers, and pipelines.

In last decades, ORCs gained a relevant role for power production from low to medium temperature energy sources, especially in the low/medium power range ($\approx 1\,kW$ to $\approx 100\,MW$) (Colonna et al. [26] and Macchi and Astolfi [57]). As working fluids, pure substances are the standard, but many recent studies discuss the possible improvement of efficiency achievable by employing mixtures (Weith et al. [94]). Organic compounds exhibit a thermal stability limit which is not far from typical ORC maximum operating temperature. Decomposition leads to a change in thermodynamic properties that is detrimental for cycle efficiency, while damaging or dangerous products can also form. Therefore, information about the thermal stability of the fluid is key for a good system design.

Another aspect with a significant impact on cycle efficiency is the fluid dynamic behavior of the turbine, which is the most convenient choice for the expander except for mini-ORC applications. The combination of the nature of the fluid and of the working conditions typically results in supersonic flows, where non-ideal effects are relevant (Colonna et al. [25]). This means that a departure of the behavior of the fluid from the well known ideal gas law $pv = RT$ is observed, where p is the pressure, v the specific volume, R the specific gas constant and T the temperature.

The simplest parameter able to describe the degree of non-ideality is the compressibility factor

$$Z = \frac{pv}{RT}, \tag{1.1}$$

which indicates the deviation of the volumetric behavior of the fluid from the ideal gas one. Due to the effect of inter-molecular forces, it can assume values either greater or lower than one. Approaching

$Z \neq 1$ *means non-ideal behavior of the fluid.*

the critical point or the saturation curve brings these effects into play. As a result of this behavior, the evolution of physical quantities in isentropic expansions of ideal or non-ideal gases is different. A second parameter, called fundamental derivative of gasdynamics Γ, represents the different behavior of the flow. Further details are given in Section 1.1.1 of this introduction.

In the last twenty years, considerable advancements in the thermodynamic modeling of fluids at highly non-ideal conditions were made (see for example Span and Wagner [74, 75]). Such high accuracy models were successfully implemented in computational fluid-dynamics (CFD) codes and are now widely used for the design and analysis of industrial components. An extensive theoretical literature about non-ideal compressible-fluid dynamics (NICFD) is available, but experimental data necessary to provide validation of CFD codes are still scarce. This is the consequence of the hostile environment in which measurements have to be performed, which requires dedicated facilities and specifically developed measurement techniques.

To fill this gap, the objective of this thesis is to experimentally investigate non-ideal compressible-fluid flows of organic compounds used as working fluids in organic Rankine cycles (ORCs). The focus is the expansion process occurring at high temperature in a thermodynamic region close to the vapor saturation curve and in proximity of the critical point, which is typical of ORC turbines. In the turbomachinery field the use of wind tunnels equipped with planar cascades for the detailed study of blade aerodynamics and related losses is common. However, applying measurement techniques and operating a wind tunnel for high temperature organic fluid flows poses some challenges. The problem can be simplified while retaining the fundamental aspects by choosing the converging-diverging nozzle as test geometry, being the simplest one representative of turbine passages.

For a complete flow characterization, independent pressure, temperature and velocity measurements are needed. In particular, regarding velocity, directional probes cannot be employed: differently from the ideal gas case, a fluid and operating conditions dependent calibration which is still under development is required. This brings the attention to optical techniques such as particle image velocimetry or laser Doppler velocimetry (LDV), which was selected for the present research.

Direct velocity measurements performed in this work are the first ever in a non-ideal compressible-fluid flow. To accomplish this task, it was necessary to implement a novel laser Doppler velocimetry system specifically conceived for high temperature, high pressure compressible flows with possibility of condensation, where no contamination of the fluid is permissible. Experiments were carried out with the Test Rig for Organic VApors (TROVA) at Crea Laboratory of Politecnico di Milano, an organic fluid wind tunnel designed for unconventional flow studies.

Fluids chosen for testing are hexamethyldisiloxane ($C_6H_{18}OSi_2$) and octamethyltrisiloxane ($C_8H_{24}O_2Si_3$), which are prominent working fluids employed in high temperature ORCs and feature a sufficiently wide thermodynamic region where non-ideal effects can be observed. Siloxanes are a class of organosilicon polymers in which silicon atoms are bound to each other through oxygen atoms. At least one organic group saturates the valences left free by oxygen. Being each oxygen atom sort of a link between silicon atoms, it can be considered as half belonging to each silicon atom. Therefore, the general formula of fundamental components of siloxanes is (Noll [65])

$$R_nSiO_{(4-n)/2}, \qquad n = 0, 1, 2, 3. \tag{1.2}$$

Depending on the value of n, each group takes a different name, based on the number of valences saturated by oxygen:

M $n = 3$

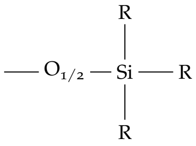

$$-O_{1/2}-\overset{\displaystyle R}{\underset{\displaystyle R}{Si}}-R$$

D $n = 2$

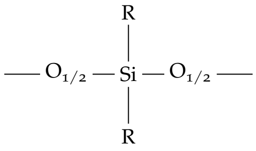

$$-O_{1/2}-\overset{\displaystyle R}{\underset{\displaystyle R}{Si}}-O_{1/2}-$$

T $n = 1$

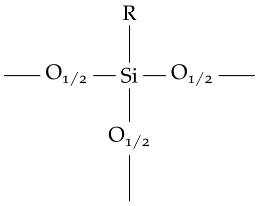

$$-O_{1/2}-\overset{\displaystyle R}{\underset{\displaystyle O_{1/2}}{Si}}-O_{1/2}-$$

Q $n = 0$

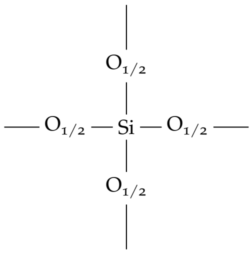

$$-O_{1/2}-\overset{\displaystyle O_{1/2}}{\underset{\displaystyle O_{1/2}}{Si}}-O_{1/2}- \quad .$$

The short nomenclature of this class of fluids follows this scheme. Both hexamethyldisiloxane and octamethyltrisiloxane are composed by methyl- (CH_3—) groups as R. The former features a combination of two M units, thus it is commonly called MM, while the latter features a central D unit closed on both sides by a M unit, making MDM. Figure 1.1 shows a 3D sketch of the molecules.

Data about the thermal stability limit of these fluids, both pure and in binary mixtures, are scarce or not available in literature. Thus, to

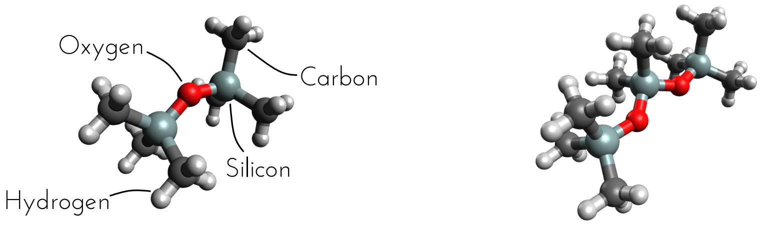

(a) Siloxane MM (b) Siloxane MDM

Figure 1.1: Molecular structure of siloxane MM and MDM.

correctly design the aforementioned experimental campaign for nozzle flow characterization (i.e. to set a maximum temperature threshold), it was mandatory to study the thermal decomposition of the fluids to be used. The degradation of these compounds occurring at high temperature was characterized and results are presented in dedicated chapters.

1.1.1 *Non-ideal compressible-fluid dynamics*

Some fundamental aspects of nozzle flows are recalled in this section.

The gasdynamics of a nozzle can be analyzed under the *quasi-one-dimensional* (quasi-1D) approach. If the radius of curvature of the nozzle curvilinear abscissa at any axial coordinate in the streamwise direction is large compared to the nozzle cross-sectional length, and the cross-sectional area profile is smooth and gradual, flow quantities can be assumed to be function of the axial coordinate only. Under the assumption of adiabatic flow and negligible body forces, the mass, momentum and energy balance equations take the form

$$\frac{1}{\rho}\frac{d\rho}{dx}+\frac{1}{V}\frac{dV}{dx}+\frac{1}{A}\frac{dA}{dx}=0 \tag{1.3a}$$

$$\rho V\frac{dV}{dx}+\frac{dp}{dx}=0 \tag{1.3b}$$

$$\frac{dh_T}{dx}=0, \tag{1.3c}$$

where x is the axial coordinate, ρ is the density, V is flow velocity, $A(x)$ is the cross sectional area, p is the pressure and

$$h_T=h+\frac{V^2}{2} \tag{1.4}$$

is the total enthalpy computed from the enthalpy h. For the solution of this problem, a volumetric equation of state $f(T,p,\rho)=0$ and a caloric equation of state (for example the specific heat at constant volume relation $c_v=c_v\,(T,\rho)$) defining the behavior of the evolving fluid must be specified. It appears clear, now, that once the geometry is known, for the complete characterization of the flow, pressure, temperature and velocity must be *independently* known, being density and enthalpy obtainable from the equations of state without further assumptions. Commonly, the flow in nozzles can be regarded as isentropic, if shockwaves are not present, yielding

$$\frac{dp}{dx} = \underbrace{\left(\frac{dp}{d\rho}\right)_s}_{c^2} \frac{d\rho}{dx}, \tag{1.5}$$

where c is the speed of sound in the medium. Indeed, in most applications viscous effects are limited to a thin boundary layer region and Reynolds numbers are sufficiently high to neglect the effect of viscosity.

For an isentropic flow and after some manipulation, expressions for gradients of flow quantities can be obtained from Equation 1.3:

$$\frac{1}{V}\frac{dV}{dx} = \frac{1}{M^2-1}\frac{1}{A}\frac{dA}{dx} \tag{1.6a}$$

$$\frac{1}{\rho}\frac{d\rho}{dx} = \frac{M^2}{1-M^2}\frac{1}{A}\frac{dA}{dx} \tag{1.6b}$$

$$\frac{1}{p}\frac{dp}{dx} = \frac{1}{1-M^2}\frac{\rho V^2}{p}\frac{1}{A}\frac{dA}{dx} \tag{1.6c}$$

$$\frac{1}{c}\frac{dc}{dx} = \frac{(\Gamma-1)\,M^2}{1-M^2}\frac{1}{A}\frac{dA}{dx} \tag{1.6d}$$

$$\frac{1}{M}\frac{dM}{dx} = \frac{1+(\Gamma-1)\,M^2}{M^2-1}\frac{1}{A}\frac{dA}{dx}, \tag{1.6e}$$

where

$$\Gamma = 1 + \frac{c}{v}\left(\frac{\partial c}{\partial p}\right)_s \tag{1.7}$$

is the fundamental derivative of gasdynamics, which is a non dimensional measure of the variation of speed of sound across an isentropic transformation (Thompson [84]) and $M = V/c$ is the Mach number. The first three equations state that for a subsonic case ($M < 1$), as a result of a cross-sectional area reduction in the streamwise direction ($dA/dx < 0$) velocity increases ($dV/dx > 0$), while pressure and density reduce ($dp/dx < 0$, $d\rho/dx < 0$). The opposite holds for the supersonic ($M > 1$) case. Last two equations highlight the effect of Γ on the behavior of the flow. Indeed, if $\Gamma > 1$ the speed of sound decreases along the nozzle axis ($dc/dx < 0$) as a result of an expansion and vice versa. For $\Gamma < 1$ an expansion produces an increasing speed of sound ($dc/dx > 0$) and a local decrease of the Mach becomes possible. For $\Gamma < 0$, peculiar behaviors such as negative shock waves are admissible (Thompson and Lambrakis [85]). Based on these behaviors, the value of Γ permits a distinction between *non-classical* flows, characterized by $\Gamma < 0$ and *classical* flows for $\Gamma > 0$.

The value of Γ discriminates between different gasdynamic regimes.

In the case of an ideal gas, $\Gamma = (\gamma + 1)/2 > 1$, thus leading to a monotonically increasing Mach number, decreasing speed of sound along an expansion and to the admissibility of compression shocks only. Further, if the assumption of constant specific heats and isentropic flow is made, Equation 1.3 can be integrated and manipulated to yield

$$\frac{T_T}{T} = \frac{h_T}{h} = \frac{c_T^2}{c^2} = 1 + \frac{\gamma - 1}{2} M^2 \tag{1.8a}$$

$$\frac{p_T}{p} = \left(1 + \frac{\gamma - 1}{2} M^2\right)^{\frac{\gamma}{\gamma - 1}} \tag{1.8b}$$

$$\frac{\rho_T}{\rho} = \left(1 + \frac{\gamma - 1}{2} M^2\right)^{\frac{1}{\gamma - 1}} \tag{1.8c}$$

$$\frac{A_t}{A} = \frac{M}{\sqrt{\left[\frac{2}{\gamma+1}\left(1 + \frac{\gamma-1}{2} M^2\right)\right]^{\frac{\gamma+1}{\gamma-1}}}}, \tag{1.8d}$$

where γ is the specific heats ratio, A_t is the throat cross sectional area and subscript T refers to total conditions. The last of these equations states that the Mach number is a function of the cross sectional area ratio and of the fluid (through γ). From Equation 1.8a to Equation 1.8c static-to-total ratios of p, T and ρ are function of Mach number only and, thus, of $A_t/A(x)$, for a given fluid.

The non-dimensional flow behavior of a PIG is independent on total conditions. The opposite holds for a non-ideal gas.

These equations describe the evolution of quantities along an isentropic transformation of a so-called polytropic ideal gas (PIG), which is characterized to be an ideal gas with constant specific heats (i.e. $\gamma = \mathrm{constant}$). Of course, due to non-ideality of the fluid ($Z \neq 1$) specific heats can depart from their ideal counterparts at thermodynamic regions near the the saturation curve or critical point, due to inter-molecular interactions. This leads to a dependence of the non-dimensional behavior of the flow on stagnation conditions.

Velocity is obtained from Equation 1.4, which for an ideal gas yields

$$V = \sqrt{2c_p\left(T_T - T\right)}, \tag{1.9}$$

where c_p is the specific heat at constant pressure. For a position along the nozzle axis, being the value of T_T/T determined by A_t/A, an increase of total temperature means an increase of velocity and vice versa. Total pressure has no effect being $h = h(T)$ for a PIG. In the non-ideal case enthalpy depends on both temperature and pressure, making the analysis not straightforward.

All nozzle flows analyzed in this work belong to the non-ideal ($Z < 1$) classical ($\Gamma > 0$) case and a dependence of flow parameters on total conditions is expected.

1.1.2 *Thermal stability of the working fluid*

Thermal stability is the ability of a fluid to preserve his main physical properties when heated at high temperature (see *ASTM D6743*

- 11(2015), Standard Test Method for Thermal Stability of Organic Heat Transfer Fluids [3]). Thus, it is a fundamental aspect to be considered every time a fluid has to be heated. Complex fluids (such as organic fluids molecules) generally suffer from degradation at relatively low temperature. Indeed, when heated, the molecule stores energy in its active degrees of freedom, that can be of translational, rotational, vibrational or electronic type. Translational and rotational degrees of freedom are active above $50\,\mathrm{K}$ and $250\,\mathrm{K}$ respectively. Vibrational degrees of freedom can be partially active at temperatures of interest for power engineering, while electronic ones activate above 10^4 K, thus they are never active in common energy engineering applications. If the molecule is particularly complex, this corresponds to a high number of vibrational degrees of freedom. Thus, when heated, such kind of molecule stores a great amount of energy in its vibrational degrees of freedom and this could lead to the cleavage of molecular bonds.

Complex organic fluids suffer from degradation at relatively low temperature.

Thermal stability is a property of the fluid itself and it is influenced by temperature, exposure time and, mildly, by pressure. The presence of contaminants within the fluid such as air, humidity, metallic catalysts, and lubricants dramatically influences degradation. If the thermal behavior of the fluid is considered in relation to the presence of such substances the term thermochemical stability is used (Macchi and Astolfi [57]).

In an industrial plant, thermal stability is to be considered in a wide variety of fields. In particular, in ORC systems, the maximum cycle temperature can be near the thermal stability limit of the working fluid. Furthermore, the working fluid is commonly in contact with the aforementioned contaminants, thus thermochemical stability is of essential importance. Erhart et al. [35] analyzed working fluids from operating ORCs after several tens of thousand working hours, finding up to 34% of decomposition, thus leading to major performance losses.

Decomposition products are commonly compounds that can be corrosive, toxic, flammable or can deposit on plant components inner surfaces. In ORC engines, their presence can damage essential parts, compromising the plant functionality. Some degree of decomposition is unavoidable, except for very low working temperature, thus the plant must be designed to prevent massive decomposition and can be operated to limit the penalization arising from the presence of degradation products. Chemically compatible materials must be employed, air and humidity leakages from external environment must be avoided, and actions should be taken to avoid the negative effect of decomposition products on the performance of the plant. As an example, the periodic evacuation of the condenser permits to avoid the reduction of efficiency resulting from a higher condensing pressure linked to the presence of low boiling products, while eliminating also air leaked inside the plant.

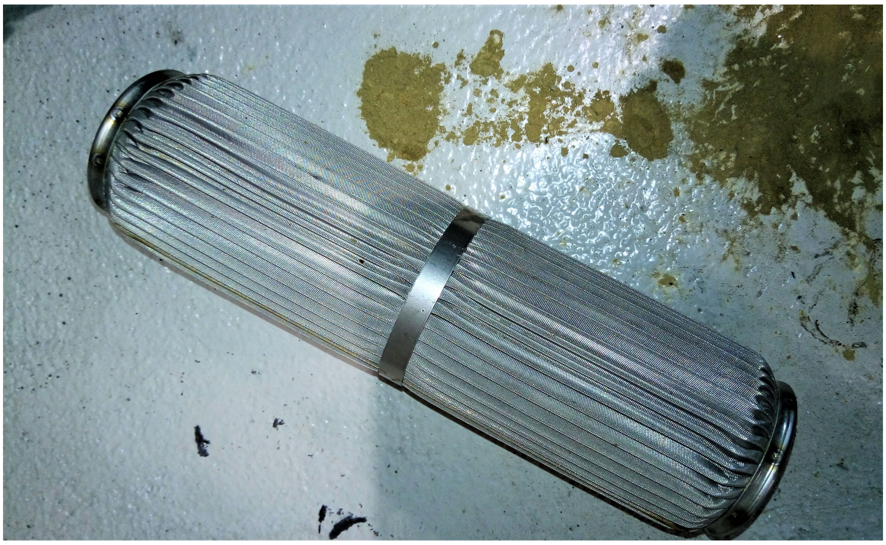

Figure 1.2: Cartridge of the main circuit filter of the TROVA, with the solid residue.

The wind tunnel employed in the present thesis (the TROVA), during its functioning with siloxane MDM faced some issues related to fluid decomposition. After tests where the maximum reached temperature was between 290 °C and 300 °C, major signs of fluid degradation were observed. Figure 1.2 shows the cartridge of the filter placed on the suction side of the circulating membrane pump. The sand-like residue visible in the top right corner of the picture was originated upon decomposition of the working fluid and was found in pipes and vessels as well, after inspection. The sediment was analyzed and the composition of the sample was mainly iron, silicon and oxygen, suggesting the presence of ferric oxide or silicon dioxide. The latter is the solid product of decomposition of siloxanes, while the former indicates the presence of humidity in the plant, which could have eased decomposition. Figure 1.3 reports a microscope image of the solid residue. The portion labeled as 3 was the one with the higher iron concentration, while a high quantity of silicon was found in the whole analyzed sample.

The analysis of thermal stability of the fluid can prevent expensive and time-consuming maintenance interventions.

After this event, the plant underwent a major maintenance. Indeed, solid particles were carried by the flow and fouled the test section at each test run. Further, the solid residue deposited on sealing surfaces of ball valves, leading to damage and loss of sealing performances of the valve due to scraping. The plant was entirely pickled and valves underwent maintenance. Further, procedures to avoid air and humidity leakages in the plant were subsequently adopted. To avoid unnecessary costs and losses of functionality, the analysis of thermal stability of the working fluid is of paramount importance.

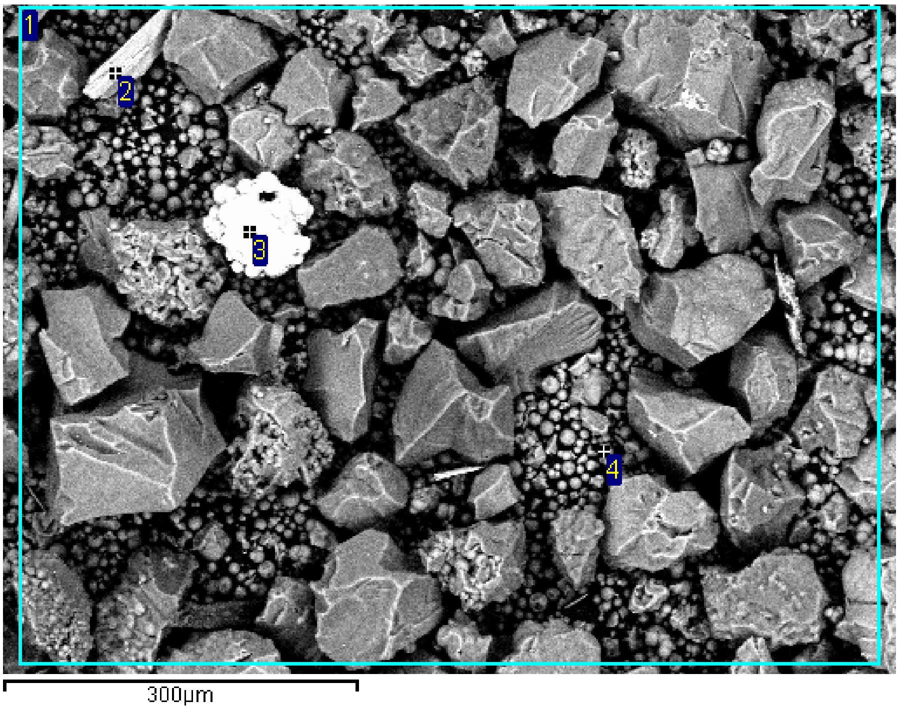

Figure 1.3: Microscope image of the solid residue found in the TROVA after decomposition.

1.2 WORK OUTLINE

This research project is composed by two complementary main research activities: the study of thermal stability of organic compounds on which fluid dynamics experiments have to be performed (Part i) and the experimental characterization of the non-ideal compressible fluid flow in nozzles (Part ii), with a particular focus on the performing of direct velocity measurements by means of LDV.

Regarding thermal stability, Chapter 2 presents a summary of the available methodologies for its study, with pros and cons. The first part of the research on thermal stability of linear siloxanes was carried out with a methodology found in literature which provided contradictory results, for the employed class of fluids (Chapter 3). For this reason, the methodology was improved, a new system was designed and tests on pure MM and MDM fluids as well as their equimolar mixture were carried out. Results and discussion are provided in Chapter 4.

Being aware of the thermal stability of the working fluid, the characterization of high temperature flows can be carried out. Chapter 5 discusses the current state of experimentation in the field of non-ideal gasdynamics, showing the inherent difficulties in carrying out measurements on such flows. Chapter 6 deals with the very first experimental tests of nozzle flows in the non-ideal vapor regime, employing pressure and temperature measurements and schlieren visualizations. However, to fully characterize the flow, the independent and direct measurement of velocity is needed. The last part of the work deals with the complete characterization of a point in a compressible flow of a molecularly complex fluid. The development of a seeding system specific for performing LDV in high temperature and pressure flows was necessary to perform the first direct velocity measurement ever in such flows (Chapter 7).

Finally, conclusions and a mention at future developments are provided in Chapter 8.

Part I

THERMAL STABILITY OF PURE LINEAR SILOXANES AND MIXTURES

Thermal stability is a key aspect for the selection of a working fluid and operation of an ORC plant. The TROVA makes no exception, thus the study of thermal stability of the fluid to be employed is fundamental.

This part of the work deals with the issue of thermal stability. In Chapter 2, methodologies for thermal stability assessment and results concerning organic fluids reported in literature are reviewed. Chapter 3 presents the experimental analysis carried out on siloxane fluid MM and MDM. Concluding, Chapter 4 reports an improved method for the analysis of thermal stability and the results of its application to siloxane fluids MM, MDM and equimolar MM/MDM mixture.

2

THERMAL STABILITY EVALUATION

The choice of the working fluid is a key aspect in the design of an ORC system, which affects the the thermodynamic cycle, the performance and cost of components (mainly the expander and heat exchangers), the plant layout, and safety requirements (see Macchi and Astolfi [57]). Among the requirements to be considered during working fluid selection, thermal stability plays a relevant role. Indeed, ORC power plants normally operate at a maximum temperature close to the the degradation point of the working fluid. The effect of decomposition can be loss of power and efficiency (see Macchi and Astolfi [57]), serious malfunctions of components (see Badr, Probert, and O'Callaghan [11], Ginosar, Petkovic, and Guillen [43] and Macchi and Astolfi [57]) or even the formation of toxic or highly flammable fluids, that can cause relevant safety problems during the operation of the plant.

Similar observations apply in the case of the TROVA. Indeed, to observe non-ideal behavior of fluids and thermo-fluid dynamics conditions typical of ORC turboexpanders, tests must be performed at a temperature close to or above the critical point of the fluid. In this thermodynamic region, the working fluid is typically near the temperature at which decomposition effects start to be non-negligible.

In the past, various methods for analyzing thermal stability were applied to different classes of fluids. Section 2.1 presents the main methodologies reported in literature up to date: theoretical methods (Section 2.1.1), the pressure deviation at constant temperature method (Section 2.1.2), the vapor pressure curve deviation method (Section 2.1.3), the chemical analysis method (Section 2.1.4), and, concluding, other less common methods (Section 2.1.5). Finally a review of thermal stability of organic fluids relevant for ORC applications is reported in Section 2.2.

2.1 METHODOLOGIES FOR THERMAL STABILITY ANALYSIS

The result of a thermal stability analysis is strongly dependent on the applied methodology, temperature range, test conditions and the research field for which the analysis is being carried out (Dai, Shi, and Qian [29]). Therefore, data reported in literature may be very scattered for the same fluid (for example see Badr, Probert, and O'Callaghan [11]).

The problem can be addressed from both a theoretical and experimental point of view, each being able to provide different information and insights. For this reason, results from experiments and theory are highly complementary in explaining a complex phenomenon such as thermal stability.

2.1.1 Theoretical methods

From a theoretical point of view, the decomposition of a single component working fluid can be considered as a first order reaction (see Andersen and Bruno [6]). This model states that the reaction rate is proportional to the reactant concentrations, thus

$$\frac{dC_A}{dt} = -kC_A, \tag{2.1}$$

where C_a is the working fluid concentration, t is the time and k is the first-order reaction rate constant. The reaction rate constant k is related to temperature through the so called Arrhenius equation

$$k = A \exp\left(-\frac{E_a}{RT}\right), \tag{2.2}$$

where A is the pre-exponential factor, E_a is the activation energy, T is the temperature and R is the universal gas constant. The first order model is useful, though it is approximated: indeed, decomposition products themselves may be species that can decompose, leading to a complication in the reaction model. However, to a first degree of approximation, the process can still be considered to be globally first order. The validity of such assumption can be checked experimentally. Indeed, the integration of Equation 2.1 leads to

$$-\ln\frac{C_A}{C_0} = kt, \tag{2.3}$$

where C_0 is the initial concentration of working fluid A, that after rearrangement gives

$$\ln C_A = \ln C_0 - kt. \tag{2.4}$$

Thus by measuring the concentration of compound A over time t it is possible to verify the linear relationship among them. An important parameter that is often reported in literature about decomposition kinetics is the so called *half-life* of the reaction $t_{1/2}$, that is obtainable from Equation 2.3 by imposing an halving of the concentration of A (i.e. $C_A/C_0 = 1/2$):

$$t_{1/2} = \frac{\ln 2}{k}. \tag{2.5}$$

The first order model allows the prediction of the lomg term decomposition of the fluid.

The advantage of the first order model is that it permits the prediction by extrapolation of the behavior of a fluid on the long term based on data measured along short periods of time.

More complex method for analyzing thermal stability like the density function theory (DFT) and molecular dynamics (MD) involve the detailed study of the reaction mechanism and path at a molecular level (see Dai, Shi, and Qian [29]). Simulation method may be used either to replicate the reaction mechanism or to calculate representative parameters of the molecule that are related to thermal stability, such as the dissociation energy of chemical bonds in the molecule.

2.1.2 *Pressure deviation at constant temperature method*

The most readily measurable property change related to decomposition phenomena is pressure variation. Indeed, the cleavage of molecules generally leads to the formation of a large amount of volatile products. The change in pressure is related to the rate of decomposition by an unknown proportionality constant. For this reason, this physical property change is more suitable than others (such as weight loss, viscosity change or heat of reaction) as an indicator of molecular cleavage [12].

Based on this line of thinking, Blake et al. [12] introduced a method for determining the thermal stability in which the fluid is stressed at constant temperature T, while pressure p is monitored. If a deviation of pressure at constant temperature is observed, this is attributable to the change in composition of the sample. The employed apparatus is shown in Figure 2.1. Pressure was measured by means of an isoteniscope, while the temperature was controlled by means of a thermostatic bath.

To establish a thermal stability limit is necessary to set a threshold on the pressure rise in time. When this threshold is passed, the temperature at which the stress is being carried out represents the thermal stability limit. In the study by Blake et al. [12] the decomposition point is defined as the temperature at which the compound shows an isothermal pressure rise of $67.2\,\mathrm{mbar/h}$. This method was applied to more than one hundred organic fluids from twelve different chemical families.

Later, Fisch and Verderame [38], Johns, McElhill, and Smith [50, 51], and Fabuss et al. [36] also used this method, whose indubitable strength is the simplicity. However, if the fluid is stressed at moderately high temperature, some precaution for pressure measurement (such as the adoption of high temperature pressure transducers or of pneumatic lines to distance the transducer from the sample vessel) are needed. This issues are discussed in more detail in Chapter 4.

The pressure deviation method is very simple, but it has limited sensitivity.

The pressure deviation at constant temperature method has a limited sensitivity and permits the detection of massive decomposition only. It is reported in the *ASTM D2879-10, Standard Test Method for Vapor Pressure-Temperature Relationship and Initial Decomposition Temperature of Liquids by Isoteniscope* [2].

This method, in combination with others, was employed in the present work to test the thermal stability of siloxane fluid MM and MDM, see Chapter 3.

2.1.3 *Vapor pressure curve deviation method*

To overcome the disadvantage of the low sensitivity of the isothermal pressure deviations method, Invernizzi [49] introduced an improved procedure specifically designed for testing ORC working fluids. Later, based on this methodology, Calderazzi and Colonna di Paliano [13] determined the decomposition of five fluorinated refrigerants. The adopted experimental procedure complements the method by Blake et al. [12] by analyzing the vapor pressure curve variation between the untreated and the stressed fluid and is referred here both as the vapor pressure curve deviation method or the VLE $p-T$ curve deviation method.

If the VLE curve is compared at low temperature, very small amounts of decomposition products can be detected.

This method is more sensitive than the one by Blake et al. [12] in detecting limited decomposition effects. Indeed, if the vapor pressure is measured at low temperature, even low amounts of decomposition products have a major impact on the measured saturated vapor pressure.

Later, Angelino and Invernizzi [9] applied this methodology to zero ODP refrigerants. Pasetti, Invernizzi, and Iora [67] improved the data analysis method introducing a procedure based on statistical hypothesis test to assess if the deviation in measured vapor pressure could be attributed to measurement uncertainties or not (hence to decomposition). They applied this method to several hydrocarbons employed in organic Rankine cycle systems. The experimental apparatus employed by Pasetti, Invernizzi, and Iora [67], an evolution of the one by Calderazzi and Colonna di Paliano [13], is reported in Figure 2.2. It is composed by a vessel filled with the fluid under test, which is positioned in an oven for the stress test or in a thermal bath for the VLE curve measurement.

This method remains fairly simple to apply. However, a thermostatic bath for vapor pressure measurement at a temperature lower than the ambient could be necessary to boost the sensitivity.

The vapor pressure comparison was employed in this work as main method to analyze the thermal stability of siloxane fluid MM and MDM (see Chapter 3) and as complementary information to chemical analysis to test the thermal stability of MM, MDM and a 50%/50% MM/MDM molar mixture (Chapter 4).

2.1.4 *Chemical analysis method*

The previously mentioned methods had the merit of a relative simplicity of application. However, they present some drawbacks:

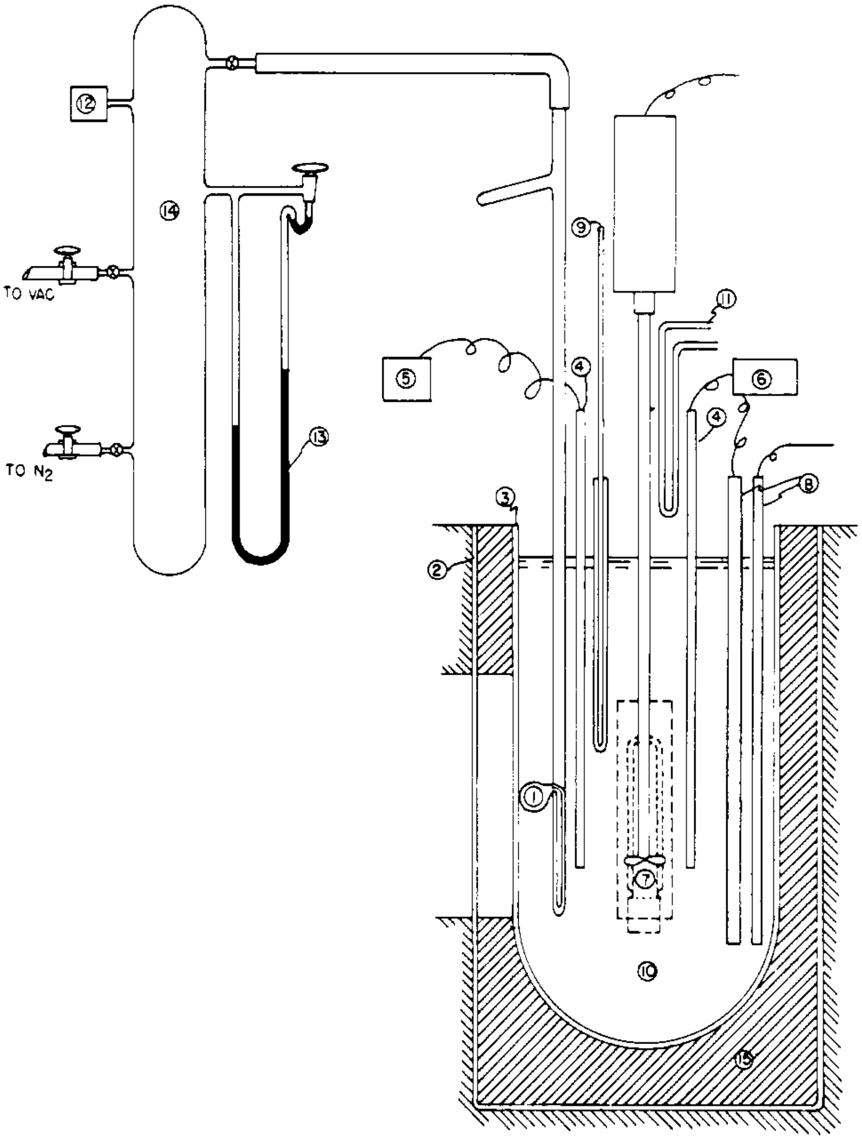

Figure 2.1: Experimental apparatus employed by Blake et al. [12]: (1) Isoteniscope, (2) Borosilicate glass jar, (3) Vycor jar, (4) Stainless steel resistance thermometer, (5) Wheatstone bridge, (6) Temperature controller, (7) Showcase bulb, (8) Firerod immersion heater, (9) Mercury thermometer, (10) Bath fluid, (11) Copper cooling coil, (12) Thermocouple vacuum gage, (13) Mercury manometer, (14) Expansion chamber, (15) Glass fiber insulation.

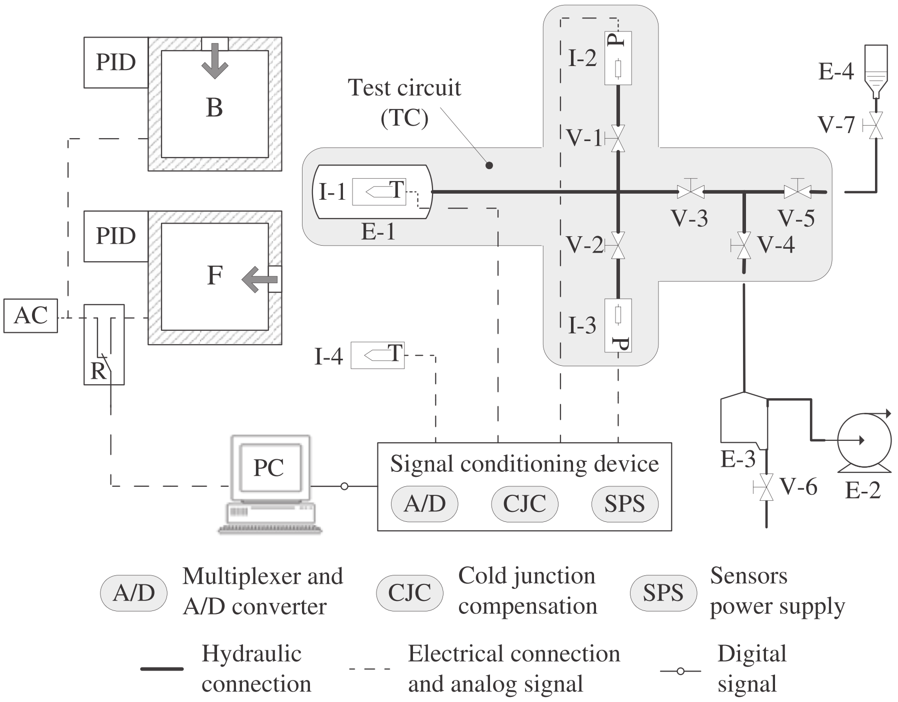

Figure 2.2: Schematic layout of the experimental apparatus by Pasetti, Invernizzi, and Iora [67]: (F) muffle furnace, (B) thermostatic bath, (AC) AC power, (R) security relay for the power supply of the furnace, (PID) temperature control panel, (PC) personal computer for the data acquisition and the system control, (E-1) sample cylinder, (E-2) vacuum pump, (E-3) vacuum trap, (E-4) graduated container, (V-1, V-2, V-3) high pressure valves, (V-4, V-5) low pressure valves, (V-6) Hoffman clamp, (V-7) pyrex tap, (I-1) thermocouple for the measurement of sample temperature, (I-2, I-3) pressure transmitters, (I-4) thermocouple for the measurement of ambient temperature.

- the nature of decomposition products is not known;
- the quantitative relation between decomposition extent and pressure (or vapor pressure) increase is not straightforward;
- the reaction path is normally quite complex and the cleavage of molecules can lead sometimes to the formation of high boiling compounds that can hinder the effect of volatile products on pressure.

A chemical analysis of the sample solves these issues, providing insights on the nature and amount of products formed upon decomposition (see Ginosar, Petkovic, and Guillen [43]). If the sample is in bi-phasic conditions, both the liquid and vapor phases must be analyzed, to have a complete picture of both low and high boiling compounds. Chemical analysis is the main tool that can provide complimentary information to the theoretical methods that were briefly discussed in Section 2.1.1 (see, for example, Andersen and Bruno [6]).

Chemical analysis provides more detailed information than the methods presented in Section 2.1.2 and Section 2.1.3, but its application is complex and the required instrumentation is expensive.

Chemical analysis were used in this work as main technique, complemented by vapor pressure comparison, for the thermal stability testing of MM, MDM and a 50%/50% MM/MDM molar mixture (Chapter 4). In Chapter 3 they were employed as complementary information to the VLE pressure deviation method.

2.1.5 *Other methods*

The methods presented so far could be applied to test both thermal and thermo-chemical stability, depending on the presence or not of contaminants in the sample to be tested. The *ASHRAE Standard 97-2007 (RA 2017) – Sealed Glass Tube Method to Test the Chemical Stability of Materials for Use within Refrigerant Systems (ANSI Approved)* [1] reports a consolidated method for testing the chemical stability of refrigerants. Glass tubes are used as containing material, are filled with the refrigerant, air, moisture, oil, and metal strips and are hermetically sealed. Finally they are heated at high temperature. The stressed tube is then compared with an untreated reference one and a chemical analysis is then carried out to gain full information about the mutual compatibility of the fluid and the contaminant.

The *ASTM D6743 - 11(2015), Standard Test Method for Thermal Stability of Organic Heat Transfer Fluids* [3] reports a static test method for organic heat transfer fluids to be carried out in absence of oxygen and water. The criterion for assessing stability is based on the comparison of the boiling range of the stressed and untreated fluid, measured by means of gas chromatography.

Besides using static test methods (i.e. those presented so far), thermal stability can be tested under cyclic stress conditions also. The aim is to assess the fluid behavior in conditions as similar as possible to those in a real ORC system. Thus, the more obvious way is to collect a sample of fluid from one or more different sections of a real functioning plant. For example, Erhart et al. [35] sampled and tested the working fluid from eight ORC power plant running with siloxane MDM. Curran [28] gathered data on the use of organic working fluids in operational ORC in the United States and other countries. The second option is to build a laboratory scale ORC system or a dedicated dynamic loop for thermal stability testing. They usually present multiple fluid collecting devices to allow the sampling of liquid or gas for chemical analysis.

Generally speaking, during a static test, the fluid is stressed to a greater extent than in a dynamic loop. Indeed, for the same test time, in a dynamic loop the time spent by a portion of fluid at high temperature is much lower than in the case of a static stress test.

2.2 OVERVIEW OF THERMAL STABILITY OF ORGANIC FLUIDS

Due to the chemical nature of the problem, thermal stability has an obvious correlation with molecular structure and properties of the fluid. Blake et al. [12] related thermal stability of over one hundred organic compounds belonging to twelve chemical classes to their structure. In a simple diatomic molecule, the activation energy of decompositon equals the bond strength [12]. In complex molecules, the weakest bond determines the thermal stability. Resonance appears to be essential, from a structural point of view, in increasing thermal stability. For example, benzene shows a high thermal stability, since resonance transforms its structure from one with alternating single and double bonds to one having six bonds with strength equal to about one and a half the one of a C–C bond.

However, frequently other low energy decomposition paths may exist and hybridization and bond strength are not the thermal stability limiting factor. As an example, for polydimethylsiloxanes the weakest bond is the C–Si bond ($78\,\mathrm{kcal/mol}$) but experimental observations suggest that the strongest Si–O bond is broken, according to Camino, Lomakin, and Lazzari [14], at 400 °C, while at 800 °C the scission of $Si-CH_3$ bonds prevails. Manders and Bellama [59] report no evidence of Si–O cleavage, while results are consistent with Si–C bond rupture to form methyl radicals, for experiments at $\approx 150\,°C \div 950\,°C$, thus the topic is quite complex.

The kinetically favored rupture of the Si–O bond appears to be promoted by the presence of silanols, ionic impurities, or apparatus surfaces. Thus it is evident how the presence of impurities can influence the thermal stability. Numerous studies analyze the influence of contaminants such as air, water, metals, lubricants. For example Ginosar, Petkovic, and Guillen [43] report a dramatic increase in decomposition of cyclopentane in presence of air. Erhart et al. [35] report a positive correlation between the amount of lubricant residues and degradation of MDM in a series of analyzed operating power plants.

Besides temperature, another factor that can play a role in decomposition is pressure. However, Andersen and Bruno [6] analyzed the effect of pressure in the range 32 bar to 850 bar reporting almost no influence on degradation.

About pure siloxanes, some thermal stability studies are available. A limit of 400 °C is reported by Colonna et al. [23] for siloxanes in general. Angelino and Invernizzi [7] provide a similar temperature range for cyclic siloxanes. Dvornic [33] studied extensively polysiloxanes but degradation temperatures are not mentioned. M. Preißinger [56] reports that the use of siloxane MM is possible as long as the fluid temperature does not exceed 300 °C. Dai, Shi, and Qian [30] studied the thermal stability of MM as a function of temperature, time and pressure, finding appreciable decomposition at temperatures as low as 240 °C. No literature can be found about the thermal stability of siloxane MDM.

As a general rule all organic fluids are mostly compromised above 350 °C to 400 °C.

3

LIMITS OF THE VLE $p-T$ CURVE DEVIATION METHOD

One of the key parameters when performing fluid dynamics tests in a wind tunnel (such as the TROVA) is the stagnation (or total) temperature T_T upstream of the test section. When dealing with non-ideal compressible-fluid dynamics, this temperature can lie in a range where the problem of thermal stability of the fluid can arise. Further, in a test rig such as the TROVA, this problem is enhanced by the presence of carbon steel as containing material, which can oxidize to form iron oxide. Other forms of contamination, such as humidity and oxygen, have been removed or reduced to a minimum amount thanks to the degassing of the fluid prior to heating and to the filling of the plant with nitrogen between tests (see Section 5.3). In order to set a maximum temperature threshold for stagnation temperature T_T in non-ideal compressible-fluid dynamics experiments to be carried out with the TROVA, an experimental survey about degradation properties of MM and MDM was carried out. Apart from the motivation related to the performing of tests with the Test Rig for Organic VApors, thermal stability remains a key topic in the ORC industry.

The experimental thermal stability analysis carried out using the vapor pressure curve deviation method (see Section 2.1.3) and the pressure deviation at constant temperature method is reported and discussed in this chapter. The adopted method is based on the methodology by Calderazzi and Colonna di Paliano [13] and uses statistical analysis to determine decomposition based on the deviation in vapor pressure introduced by Pasetti, Invernizzi, and Iora [67].

Section 3.1 illustrates the employed experimental apparatus, while Section 3.2 deals with the adopted test procedure. Analysis of retrieved data is explained in Section 3.3, while the results of the experimental campaign are reported and discussed in Section 3.4. Finally, conclusions are drawn in Section 3.5

3.1 EXPERIMENTAL APPARATUS

The experimental apparatus proposed by Calderazzi and Colonna di Paliano [13] and Pasetti, Invernizzi, and Iora [67] was taken as the basis for the design of the THESTA (THERmal STAbility test rig). The set-up was improved to carry out measurements on siloxane fluids and to permit the sampling of both liquid and vapor phase for chemical analysis. Indeed, this class of fluids shows a very low saturated vapor pressure (e.g. $p \approx 43\,\mathrm{mbar}$ at $T = 20\,°\mathrm{C}$ for MM and $p \approx 3.6\,\mathrm{mbar}$

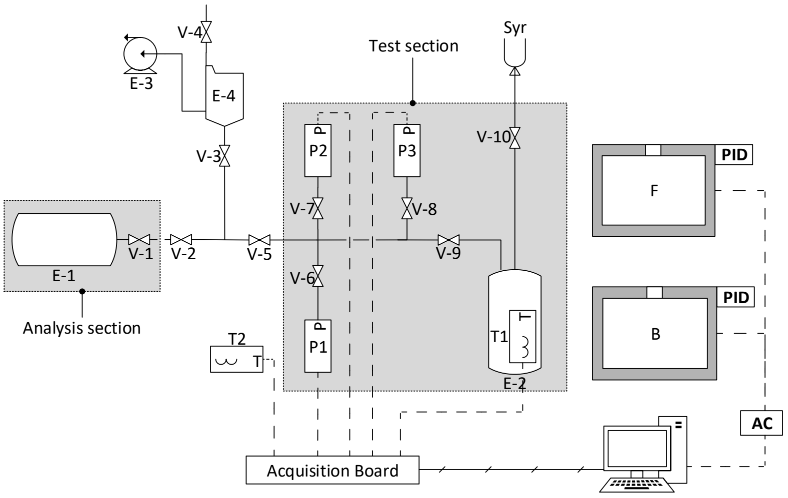

Figure 3.1: Schematic diagram of the experimental apparatus, the THESTA: temperature controlled oven (F), thermal bath (B), $150\,\mathrm{cm}^3$ vessels (E-1,2), pressure transducers (P-1,2,3), thermocouples (T-1,2), valves (V), vacuum pump (E-3), vacuum trap (E-4), loading syringe (Syr).

at $T = 20\,^{\circ}\mathrm{C}$ for MDM, from RefProp [55]), thus the apparatus is designed to measure pressures down to $2\,\mathrm{mbar}$.

Figure 3.1 shows the schematic of the setup. The THESTA is composed mainly by a a test section and an analysis section. The test vessel (E-2), three different pressure transducers (P1, P2 and P3), and the thermocouple (T1) are part of the test section. The analysis section is composed by the analysis vessel (E-1). A vacuum pump, a thermal bath, a furnace, and valves that permit the insulation of part of the setup when needed complete the system.

Figure 3.2 shows the a 3D view of the apparatus. The test vessel (E-2) has a volume of approximately $150\,\mathrm{cm}^3$ and is made of 316L satinless steel. The lower side of the cylinder is closed, while on the top a thermocouple housing and a pipe for the connection with the rest of the system are TIG welded. Stainless steel was chosen as material for the tubing and valves, due to its high chemical compatibility.

In order to measure the wide range of pressures resulting from the difference between stress temperatures and vapor pressure measurement temperatures while preserving a good accuracy, the system is equipped with three pressure transducers of different full scale: $1\,\mathrm{bar}$, $10\,\mathrm{bar}$, and $35\,\mathrm{bar}$. All transducers are of the capacitive type, and have a nominal accuracy of 0.5% of the full scale, that combined with the measurement chain uncertainties (see Section 3.3.1) yields a 95% confidence level expanded uncertainty of respectively $0.6\,\mathrm{mbar}$, $6\,\mathrm{mbar}$,

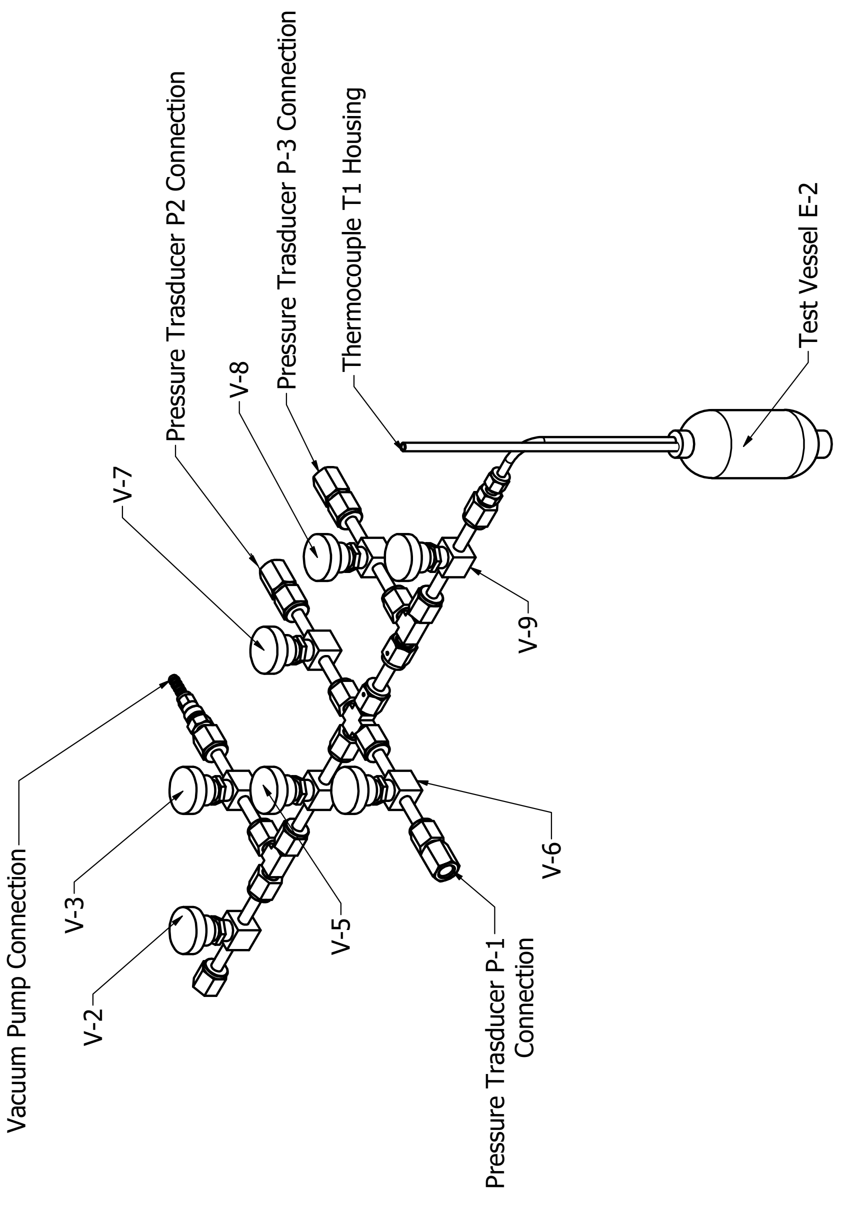

Figure 3.2: Three dimensional view of the THESTA.

Table 3.1: Pressure transducer specifications. $u_{ins,95}(p)$ is the 95% confidence level uncertainty.

Technology	Capacitance sensor
Measured quantity	Absolute pressure
Full scale	1 bar, 10 bar, 35 bar
Expanded uncertainty $u_{ins,95}(p)$	0.6 mbar, 6 mbar, 21 mbar

Table 3.2: Thermocouples specifications. $u_{ins,95}(T)$ is the 95% confidence level uncertainty.

Type	T	K
Range	−133 °C to 400 °C	−270 °C to 1370 °C
$u_{ins,95}(T)$	1 °C for $T = [-133; 133]$ °C	2.5 °C for $T = [-270; 333]$ °C
	0.0075T for other T	0.0075T for other T

and 21 mbar. All three can withstand a maximum temperature of 85 °C. In Table 3.1 are reported all useful pressure transducer data.

Two thermocouples of T and K type are employed for acquiring temperature during the vapor pressure measurement and the thermal stress phase respectively. Their 95% confidence level expanded uncertainty is 1 °C for T the thermocouple and 2.5 °C for the K one. Thermocouples specifications are reported in Table 3.2.

The thermal bath (B) is used to impose a stable temperature during vapor pressure measurements. The heat transfer oil can be employed from −20 °C to 200 °C. A PID controller controls the temperature with a stability of ±0.02 °C.

The thermal stress is carried out by the furnace (F). It has a temperature range of 25 °C to 1200 °C with a stability of ±2 °C. The PID controller can be programmed to heat up and cool down with a predetermined ramp and to maintain a constant temperature for a certain time. The non-condensible gas removal is achieved by means of a vacuum pump.

For chemical analysis, the liquid phase is sampled directly from the test vessel and is analyzed by means of gas chromatography (GC) with two capillary columns equipped with a flame ionization detector (FID) and mass spectrometer (MS). The analysis vessel, instead permits the collecting of a sample of the vapor phase for chemical analysis of light products formed upon degradation of the fluid. The instrumentation is similar, equipped with a capillary column specific for low boiling compounds and a thermal conductivity detector (TCD).

The total internal volume of the system is approximately 230 cm^3.

3.2 TEST PROCEDURE

Once the fluid to be tested is defined, the test procedure is composed by the following steps:

1. system preparation;
2. definition of the fluid mass to be loaded in the system;
3. chemical analysis of the virgin fluid (liquid phase only);
4. sample loading;
5. fluid degassing;
6. virgin fluid VLE pressure - temperature curve measurement;
7. high temperature fluid stress;
8. stressed fluid VLE pressure - temperature curve measurement;
9. chemical analysis of the stressed fluid (both vapor and liquid phases).

The same sample is stressed at increasing temperature.

Steps 7 and 8 are repeated at different stress temperature T_s on the same fluid sample. Step 9 is performed only after the last stress, the one at the highest temperature T_s, as shown by the flowchart reported in Figure 3.3. These steps are explained in detail in the following subsections.

3.2.1 *Preparation of the apparatus*

Before starting a new experimental campaign on the THESTA, any trace of impurities should be removed. Thus, the system is disassembled and traces of volatile compounds are removed by means of multiple cycles of heating and evacuation. Under the assumption that the virgin fluid is the heaviest compound present in the system, the temperature reached during the heating must be higher than its saturation temperature at ambient pressure. The system is finally assembled.

The calibration curve of each pressure transducer (P-i) is represented by a linear relationship

$$p_i = m_i V_i + q_i, \tag{3.1}$$

where p_i is the measured pressure, m_i is the slope, V_i is the measured transducer voltage and q_i is the intercept. In order to compensate for possible drift of the intercept, all transducers are subjected to the same pressure $p_0 \approx 0.8\,\mathrm{bar}$, that is measured by a high accuracy barometer, and the intercept q_i is calculated, before each sample is loaded, as

$$q_i = p_0 - m_i V_i. \tag{3.2}$$

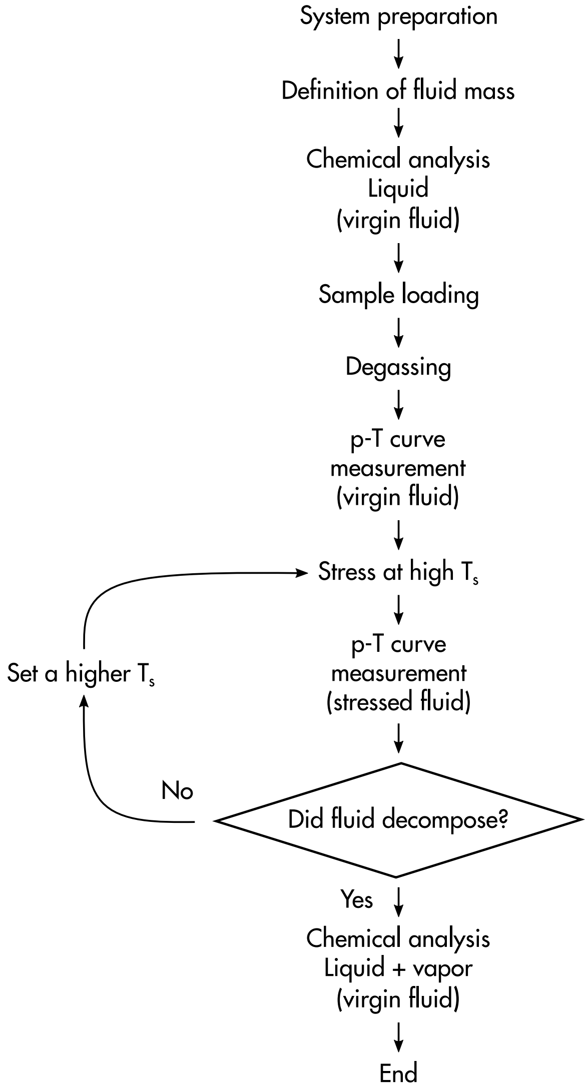

Figure 3.3: Flow chart of the experimental procedure.

3.2.2 *Leakage tests*

The sealing of the system is checked both in vacuum and pressure conditions with helium at 20 bar. Pressure readings are normalized to account for temperature variation.

3.2.3 *Sample loading and fluid degassing*

The THESTA test vessel is a closed system with a fixed volume, so, once fixed the contained mass, the pressure is a direct consequence of the reached temperature.

The fluid mass to be loaded in the system is determined based on the following constraints:

1. the fluid, during the VLE $p - T$ curve measurement, must be in two-phase condition;
2. the pressure at maximum test temperature must not exceed the full scale of the transducer used for pressure monitoring during the thermal stress.

The requirement that leads to a lower allowable mass sets the maximum mass that can be loaded.

Once the desired mass of fluid is defined, the desired quantity is withdrawn from the fluid tank with a syringe. The system is then evacuated, the syringe is connected and the contained fluid is sucked in the test vessel. As a result of this procedure, some liquid may remain trapped in the tubes between the valve and the syringe, leading to a lower than expected injected mass. Note that it is not relevant that the loaded fluid mass is controlled with high precision, since its influence on test results is negligible once it is in the range determined by the conditions set above. Further, some air may be introduced in the system, due to the non-perfect syringe/system connection or to some air that is trapped between the syringe and valve V-10 during the connection. Thus, a degassing procedure is necessary. The fluid is cooled to the lowest temperature reachable by the thermal bath, given the oil being used (−20 °C). At this temperature, the vapor quality is the lowest possible. The vacuum pump is turned on until the pressure stabilizes, removing the non condensible gases and the lowest amount possible of vapor. The fluid is then heated up to 50 °C, to promote the fluid mixing and the release of air being trapped the liquid. It is then cooled down to −20 °C again. At this stage, the majority of contained non-condensible gases is usually removed. If pressure, after heating and the subsequent cooling, is the same as after the first evacuation, the degassing is complete. However, normally, a second stage of degassing is required. The procedure is completed when after two consecutive evacuating/heating/cooling cycles the pressure remains unchanged, indicating that no other non-condensible gases have been released.

3.2.4 *VLE curve measurement of virgin fluid*

The parameter used to reveal if decomposition occurred after a thermal stress at temperature T_s is the vapor pressure deviation at a fixed temperature T between the virgin fluid and the stressed one. In principle, the vapor pressure value at only one temperature could be sufficient. However, to have a bigger picture and to better evaluate the entity of the decomposition phenomena it is preferable to perform the measurement over a range of temperature.

The measurement procedure is the following:

- the pressure transducer is put in connection with the test vessel and the loading and vacuum sections are isolated;
- the thermal bath is set to the desired temperature, at which the vapor pressure must be evaluated. Vapor pressure p_v and temperature are monitored during this transient;
- when the monitored pressure and temperature reach a stable value (considering measurement errors and the thermal bath temperature stability), p_v and T values are recorded for $10\,\mathrm{min}$ every 5 s;
- acquired data are processed (see Section 3.3) to obtain the measurement value.

This setup and this procedure are not able to provide very accurate vapor-liquid equilibrium measurements. However, since measurement conditions are the same at each stress temperature T_s and for the virgin fluid, the THESTA is sufficient to make comparison between $p_v - T$ measurements to detect a change in composition.

3.2.5 *Thermal stress*

The fluid is thermally stressed by putting the test vessel in the oven set at the stress temperature T_s for a stress time $t_s = 80\,\mathrm{h}$. During this phase only the pressure transducer chosen for pressure monitoring is in connection with the stress vessel. The temperature is monitored with a type K thermocouple, positioned in a thermowell placed at the center of the test vessel. After $t = t_s$, the oven automatically switches off and the system is cooled down by natural convection.

3.2.6 *VLE curve measurement of stressed fluid*

After the thermal stress, the new $p - T$ curve must be measured, to assess if the fluid underwent thermal decomposition. The measurement procedure is the same outlined in Section 3.2.4.

3.2.7 *Chemical analysis*

Only after the thermal stress at the highest temperature T_s, the fluid is chemically analyzed. This is not done after each stress temperature step since it would be necessary to drain some liquid and vapor, thus reducing the mass contained in the vessel. Further, as it is explained in the following, the sampling procedure involves the introduction of different compounds in the THESTA (such as Nitrogen, Helium, Argon or air) that would require a degassing procedure before the following stress test.

The THESTA permits the sampling of both liquid and vapor phase, to fully characterize the fluid composition. Indeed, in the two phases compounds have unequal relative quantities, depending on the different volatility of compounds in the mixture.

The system is pressurized using a He/N_2 /Ar mixture with to dilute the possible decomposition products, to avoid saturation of the signal in the GC. The analysis vessel is first evacuated and then pressure is balanced opening all valves connecting the test vessel to the analysis vessel. As a result, the analysis vessel contains the same mixture formed due to possible decomposition, diluted with He/N_2/Ar and can be easily detached to perform chemical analysis.

to thermal conductivity detectors.

The liquid is collected by opening the test vessel to open air and detaching it from the rest of THESTA after the vapor sampling. A small sample is then taken and analyzed.

3.3 DATA ANALYSIS

To assess the thermal stability of the fluid, a combination of the following analysis is conducted, to compensate for weaknesses of each single method:

1. deviation of pressure during isothermal stress (see Section 2.1.2);
2. comparison of VLE $p - T$ curve (see Section 2.1.3);
3. chemical analysis of the fluid *after* the stress at the highest stress temperature.

This section deals with the procedure adopted to reduce recorded measurement data to assess if decomposition occurred during a thermal stress test.

3.3.1 *Experimental uncertainties*

In this subsection, an expression for the uncertainty of each of the acquired values of pressure and temperature (p_i, T_i) of the VLE curve will be derived.

3.3.1.1 *Uncertainty in pressure measurements*

The behavior of the pressure transducer can be expressed by a linear relationship between voltage V, which is the output signal of the instrument, and pressure p, which represents the physical input to be measured:

$$V = g\,p + q \tag{3.3}$$

where g, expressed in [V/bar], is the static sensitivity obtained by the interpolation of the calibration points and q, expressed in [V], is the zero offset.

The pressure measurement uncertainty can be calculated as

$$u_{ins}(p) = \sqrt{\left(\frac{a}{1.96}\,p_{FS}\right)^2 + \left[\frac{\partial p}{\partial V}u(V)\right]^2} \tag{3.4}$$

where a is the nominal accuracy of the transducer, p_{FS} is the transducer full scale and $u(V)$ is the voltage measurement uncertainty calculated as:

$$u(V) = \frac{G_{daq}V + O_{daq}R_{daq}}{1.96} \tag{3.5}$$

where G_{daq}, O_{daq} and R_{daq} are respectively the *gain error*, the *offset error* and the *range* of the A/D module. The computed uncertainties are visible in Table 3.1.

3.3.1.2 *Uncertainty in temperature measurement*

The uncertainty in temperature measurement, visible in Table 3.2, was calculated as

$$u_{ins}(T) = \frac{\tau(T)}{1.96}, \tag{3.6}$$

where $\tau(T)$ is the thermocouple tolerance: namely the uncertainty extended at 95% confidence level.

3.3.2 *Pressure deviation in isothermal stress tests*

Regarding the pressure deviations during isothermal stress tests method, the quantity to be monitored can be reduced to the ratio of pressure to temperature $p/T = nR/V$, where p is the pressure, T is the temperature, n is the amount of constituents, R is the universal gas constant and V is the system volume. Indeed, if no changes in composition of the sample are present, n remains constant over time and the ratio p/T does not change.

3.3.3 *Pressure deviation in VLE measurements*

3.3.3.1 $p - T$ *measurement*

The $[p, T]$ values for each set point temperature of the thermal bath are obtained by averaging the pressure $p_{i,k}$ and temperature $T_{i,k}$ data recorded every 5 s over 10 min of acquisition:

$$T_i = \frac{1}{n} \sum_{k=1}^{n} T_{i,k}, \tag{3.7a}$$

$$p_i = \frac{1}{n} \sum_{k=1}^{n} p_{i,k}, \tag{3.7b}$$

where the subscript $k = 1, 2, \ldots, n$ denotes the acquired samples for each of the $i = 1, 2, \ldots, m$ measurements at different set point temperature of the thermal bath. The variability of acquired data around the mean value can be expressed by evaluating the sample variances $s^2_{T_i}$ and $s^2_{p_i}$ of mean temperature T_i and mean pressure p_i respectively:

$$s^2_{T_i} = \frac{1}{n-1} \sum_{k=1}^{n} \left(T_{i,k} - T_i\right)^2, \tag{3.8a}$$

$$s^2_{p_i} = \frac{1}{n-1} \sum_{k=1}^{n} \left(p_{i,k} - p_i\right)^2, \tag{3.8b}$$

Uncertainties related to T_i and p_i are calculated taking into account the uncertainty coming from instrument calibration and the dispersion (namely the variances $s^2_{T_i}$ and $s^2_{p_i}$) of acquired samples. This procedure holds for each measured $p - T$ curve.

3.3.3.2 *Reference* $p - T$ *VLE curve*

The criterion used to detect decomposition is based on the comparison between vapor pressure curves before and after thermal stresses. A significant difference between these curves is representative of a change in composition of the tested fluid. However, when performing the test, it is difficult to properly control all the infinite variables influencing the vapor pressure measurement (for example ambient temperature and the regulation dynamics of the thermal bath), leading to the impossibility to replicate the measurement at the exact same temperature T_i, before and after the stress phase. This makes the comparison between two measured pressure p_i values not straightforward.

For this reason it is necessary to build, starting from measured data, a continuous reference curve representing the virgin fluid, to which stressed fluid $p - T$ measurements can be compared.

The functional relation between vapor pressure and temperature is provided by the Clausius-Clapeyron equation (Poling, Prausnitz, and O'Connell [68])

$$\frac{dp}{dT} = \frac{\Delta h_v}{T \Delta v_v}, \tag{3.9}$$

where p is the vapor pressure, T the temperature, Δh_v the specific enthalpy of vaporization, Δv_v the difference in specific volume between saturated liquid and saturated vapor. If ideal gas behavior is assumed, Equation 3.9 becomes

$$\frac{dp}{dT} = \frac{\Delta h_v}{(RT^2/p)\Delta Z_v}, \tag{3.10}$$

where ΔZ_v is the difference in compressibility factor between saturated liquid and saturated vapor, and R is the specific gas constant. After rearrangement, this yields

$$\frac{d \ln(p)}{d(1/T)} = -\frac{\Delta h_v}{R \Delta Z_v}. \tag{3.11}$$

As reported by Poling, Prausnitz, and O'Connell [68], the ratio $\Delta h_v / \Delta Z_v$ is nearly independent of temperature in a wide thermodynamic region, so Equation 3.11 can be integrated, obtaining

$$p = \exp\left(A - \frac{B}{T}\right), \tag{3.12}$$

where A is the integration constant and $B = \Delta h_v / (R \Delta Z_v)$.

Thus, the reference curve is obtained assuming the exponential relation

$$p = p_{ref} = \exp\left(A - \frac{B}{T}\right) \tag{3.13}$$

between pressure p and temperature T.

A continuous reference curve for the virgin fluid is obtained applying the least squares method.

This relation can be simplified by linearization, to perform a linear regression, using the transformation of variables

$$y = \ln p, \tag{3.14a}$$

$$x = -\frac{1}{T}, \tag{3.14b}$$

yielding

$$y = A + Bx. \tag{3.15}$$

Both $x_i = -1/T_i$ and $y_i = \ln p_i$ appear to be uncertain, as a result of measurement uncertainty affecting p_i and T_i. This would require a fitting technique able to take into account the presence of errors in both variables (Draper and Smith [31], Fuller [40], and Mandel [58]). Indeed, fitting techniques find the best fit curve by minimizing the error (i.e. some kind of distance) between the curve and data. The presence of errors affects the definition of such distance.

The widely used ordinary least square (OLS) method is based on the assumption that only the response variable y is affected by error. Errors between model and observed points are calculated in a direction parallel to the y axis. Details on OLS can be found in any basic statistics book (see for example Montgomery, Runger, and Hubele [64]). For the purpose of this work, the OLS method is applied to obtain A and B, as done in Pasetti [66].

3.3.3.3 *Confidence index*

Each thermal stress temperature T_s is related to m couples of values $(p_i, T_i)|_{T_s}$ (i.e. the measured vapor pressure curve). The procedure depicted in the present section is carried out for each thermal stress temperature T_s.

The criterion for assessing the thermal stability is based on the evaluation, at temperature $T = T_i$, of the deviation $\Delta p_i|_{T_s}$ between reference vapor pressure $p_{ref}(T_i)$ of the virgin fluid and the vapor pressure $p_i|_{T_s}$ of fluid after a stress at temperature T_s, which is defined as

$$\Delta p_i|_{T_s} = p_i|_{T_s} - p_{ref}(T_i), \tag{3.16}$$

where

$$p_{ref}(T_i) = \exp\left(A - \frac{B}{T_i}\right). \tag{3.17}$$

It is worth pointing out that T_i refers to the temperature of the couple $(p_i, T_i)|_{T_s}$ and must not be confused with the couple of $(p_i, T_i)|_{virgin}$ measured on the virgin fluid and used to carry out the regression. Coefficients A and B are obtained minimizing the sum of squared residuals

$$SSR = \sum_{i=1}^{m} (y_i - A - Bx_i)^2 \tag{3.18}$$

using the m pressure and temperature measured points related to the virgin fluid $(p_i, T_i)|_{virgin}$.

To assess if the difference in vapor pressure is attributable to decomposition and not to measurement uncertainties, $\Delta p_i|_{T_s}$ must be compared to the uncertainty in pressure difference $u\left(\Delta p_i|_{T_s}\right)$. This is equal to saying that $\Delta p_i|_{T_s}$ is statistically relevant. This comparison can be carried out considering the confidence index of the vapor pressure deviation $i_C\left(\Delta p_i|_{T_s}\right)$, defined as

$$i_C\left(\Delta p_i|_{T_s}\right) = \frac{\Delta p_i|_{T_s}}{u\left(\Delta p_i|_{T_s}\right)}, \tag{3.19}$$

as proposed by Pasetti, Invernizzi, and Iora [67]. The confidence index is equal to the coverage factor to be applied to justify the deviation from zero of $\Delta p_i|_{T_s}$ with measurement uncertainties. One first chooses the confidence level k associated with the test result $\Delta p_i|_{T_s} \neq 0$. This identifies distinctively a value of $i_C(k)$. The criterion to assess the thermal stability limit is therefore equal to

$$i_C\left(\Delta p_i|_{T_s}\right) > i_C(k)\,. \tag{3.20}$$

Three different cases, associated to two values of the confidence level k are considered in this work:

$i_C\left(\Delta p_i|_{T_s}\right) \gtrsim 2.6$ means that the deviation can be attributed to decomposition with more than 99% probability.

$i_C\left(\Delta p_i|_{T_s}\right) < i_C(k = 0.9) = 1.645$ – the deviation in pressure can be explained with high probability with measurement uncertainties;

$i_C(k = 0.9) = 1.645 < i_C\left(\Delta p_i|_{T_s}\right) < i_C(k = 0.99) = 2.576$ – the deviation in pressure can be explained with measurement uncertainties only if the confidence index is extended to high values, thus the pressure deviation is probably due to decomposition;

$i_C\left(\Delta p_i|_{T_s}\right) > i_C(k = 0.99) = 2.576$ – the probability that the pressure deviation could be explained by measurement uncertainties is below 1%, thus the deviation is assumed to be caused by decomposition.

The uncertainty of the pressure deviation $u^2\left(\Delta p_i|_{T_s}\right)$ is expressed taking in account the uncertainty contribution of the measuring instruments and of the reference vapor pressure curve as

$$u^2\left(\Delta p_i|_{T_s}\right) = u^2\left(p_i|_{T_s}\right) + u^2\left(p_{ref}(T_i)\right) \tag{3.21}$$

where the uncertainty of the stressed fluid vapor pressure measurement is defined as a combination of the measuring instrument uncertainties and the variance of the n measured pressure data points for a fixed thermal bath set-point temperature:

$$u^2\left(p_i|_{T_s}\right) = u^2_{ins}(p) + s^2_{p_i}. \tag{3.22}$$

The uncertainty of the reference equation p_{ref} is given by

$$\begin{aligned} u^2\left(p_{ref}(T_i)\right) &= \\ &= u^2_{mod}\left(p_{ref}(T_i)\right) + u^2_{ins}\left(p_{ref}(T_i)\right), \end{aligned} \tag{3.23}$$

which is the sum of the uncertainties related to the model $u^2_{mod}\left(p_{ref}\right)$ and the measurement instruments $u^2_{ins}\left(p_{ref}\right)$.

The uncertainty contributed by the instruments is obtained propagating measurement uncertainties through the reference vapor pressure equation, leading to

$$\begin{aligned} u_{ins}^2\left(p_{ref}\left(T_i\right)\right) = & \\ & = \left[\left.\frac{\partial p_{ref}}{\partial T}\right|_{T_i} u_{ins}\left(T\right)\right]^2 + \\ & + u_{ins}^2\left(p\right), \end{aligned} \tag{3.24}$$

where $u_{ins}(T)$ is the thermocouple uncertainty and $u_{ins}(p)$ the pressure transducer uncertainty (see Table 3.1 and Table 3.2).

The regression was carried out on x and y as variables, thus the uncertainty related to the model $u_{mod}^2(p_{ref})$ can be computed from

$$u_{mod}^2\left(p_{ref}\right) = \left(\frac{\partial p}{\partial y}\right)^2 u_{mod}^2\left(y\right) \tag{3.25}$$

propagating the model uncertainty computed on the y variable. The prediction interval for the linearized best fit curve

$$\begin{aligned} u_{mod}^2\left(y\right) = & \frac{\sum_{i=1}^{m}\left(y_i - A - Bx_i\right)^2}{m-2} \cdot \\ & \cdot \left[1 + \frac{1}{m} + \frac{\left(x_0 - \bar{x}\right)^2}{S_{xx}}\right] \end{aligned} \tag{3.26}$$

is taken, where $x_0 = 1/T_i|_{T_s}$ is the x value computed using the temperature at which the stressed fluid vapor pressure is measured and

$$\bar{x} = \frac{1}{m}\sum_{i=0}^{m} x_i, \tag{3.27a}$$

$$S_{xx} = \sum_{i=0}^{m}\left(x_i - \bar{x}\right)^2. \tag{3.27b}$$

The prediction interval is appropriate, instead of the confidence interval, since we are looking for an interval around a value of y related to a value of x different from those used for the regression.

The procedure depicted here permits the calculation of the standard uncertainty. For the 95% confidence level uncertainty, uncertainties must be multiplied by a factor 1.96.

3.4 EXPERIMENTAL RESULTS

In this work, the thermal stability of linear siloxane MM and MDM was tested using the experimental and data analysis procedure depicted in Section 3.2 and Section 3.3. The fluids were supplied by Clearco Products Co. and were used without further purification. The

Table 3.3: Impurities contained in siloxane MM and MDM, as declared by the supplier.

	MM	
Fluid name	Chemical formula	Amount
Pentamethyldisiloxane	$C_5H_{15}OSi_2$	$< 0.1\%$
MOH	$C_3H_{10}OSi$	$< 0.5\%$
	MDM	
Fluid name	Chemical formula	Amount
D_6	$C_{12}H_{36}O_6Si_6$	$< 0.1\%$
D_5	$C_{10}H_{30}O_5Si_5$	$< 0.1\%$
D_4	$C_8H_{24}O_4Si_4$	$< 0.1\%$

supplier states that the sample of siloxane MM contains $< 0.1\%$ of pentamethyldisiloxane ($C_5H_{15}OSi_2$) and $< 0.5\%$ of trimethylsilanol (MOH, $C_3H_{10}OSi$). Regarding siloxane MDM, the sample is declared to contain $< 0.1\%$ of dodecamethylcyclohexasiloxane (D_6, $C_{12}H_{36}O_6Si_6$), $< 0.1\%$ of decamethylcyclopentasiloxane (D_5, $C_{10}H_{30}O_5Si_5$) and $< 0.1\%$ of octamethylcyclotetrasiloxane (D_4, $C_8H_{24}O_4Si_4$). Table 3.3 reports a summary of impurities contained in the fluids.

3.4.1 *Siloxane MM*

A sample of approximately 18 g was stressed from a stress temperature $T_s = 200\,°C$ to $T_s = 340\,°C$ with temperature increments $\Delta T = 20\,°C$.

In the following subsections an analysis of experimental results is carried out.

3.4.1.1 *Pressure deviation in isothermal stress tests*

The first analysis is carried out on pressure and temperature measurements acquired during the thermal stress. As explained in Section 2.1.2, a pressure deviation at constant temperature is an index of a change of composition of the sample. However, during a test, temperature is not rigorously steady, due to the dynamics of the PID controller of the oven. Thus, the effect of temperature fluctuations on pressure must be accounted for. The quantity to be monitored can be reduced to the ratio of pressure to temperature

$$\frac{p}{T} = \frac{nR}{V}, \tag{3.28}$$

where p is the pressure, T is the temperature, n is the amount of constituents, R is the universal gas constant and V is the system

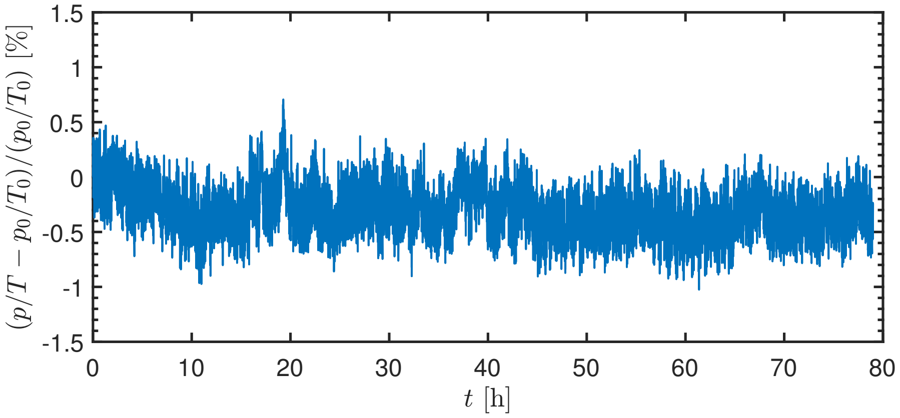

Figure 3.4: Percentage deviation of the p/T ratio during a stress test at $T_s = 340\,°C$ on siloxane MM, calculated as $\frac{(p/T - p_0/T_0)}{p_0/T_0}$. Reference pressure p_0 and temperature T_0 are calculated as the mean acquired pressure and temperature over the first hour of test time.

volume. Indeed, if no changes in composition of the sample are present, n remains constant and the ratio p/T does not change.

Figure Figure 3.4 reports the relative percentage change of p/T defined as

$$\frac{(p/T - p_0/T_0)}{p_0/T_0} \cdot 100 \tag{3.29}$$

as a function of test time during a stress test performed on siloxane MM at $T_s = 340\,°C$. Although data are relative to the highest stress temperature analyzed, no significant change in p/T is noticeable. The same consideration holds for all test performed at lower stress temperature. This indicates that, according to the pressure deviation during isothermal stress test method, no decomposition could be detected.

No pressure deviation at constant temperature was detected.

3.4.1.2 *Pressure deviation in VLE measurements*

Following the procedure depicted in Section 3.2, the VLE curve of the virgin fluid sample was measured in a temperature range from −20 °C to 90 °C. This range of temperature was chosen to evaluate the capability of an accurate measurement of the saturation pressure, by comparison with data reported in literature. Figure 3.5 reports VLE measurements performed in this work along with the curve predicted by RefProp [54] and compared with data published by Stull [81], Abbas et al. [4], and Flaningam [39]. The accordance is very good, except for very low temperatures, where the effect of small amounts of air still in the sample after the degassing procedure becomes appreciable.

For the purpose of comparing the virgin and stressed fluid VLE curves, only measurement in the range from −20 °C to 10 °C are considered.

The comparison of VLE measurements performed on the reference fluid and on the stressed sample is reported in Figure 3.6. Appreciable

Significant deviation of VLE curve for 240 °C and above.

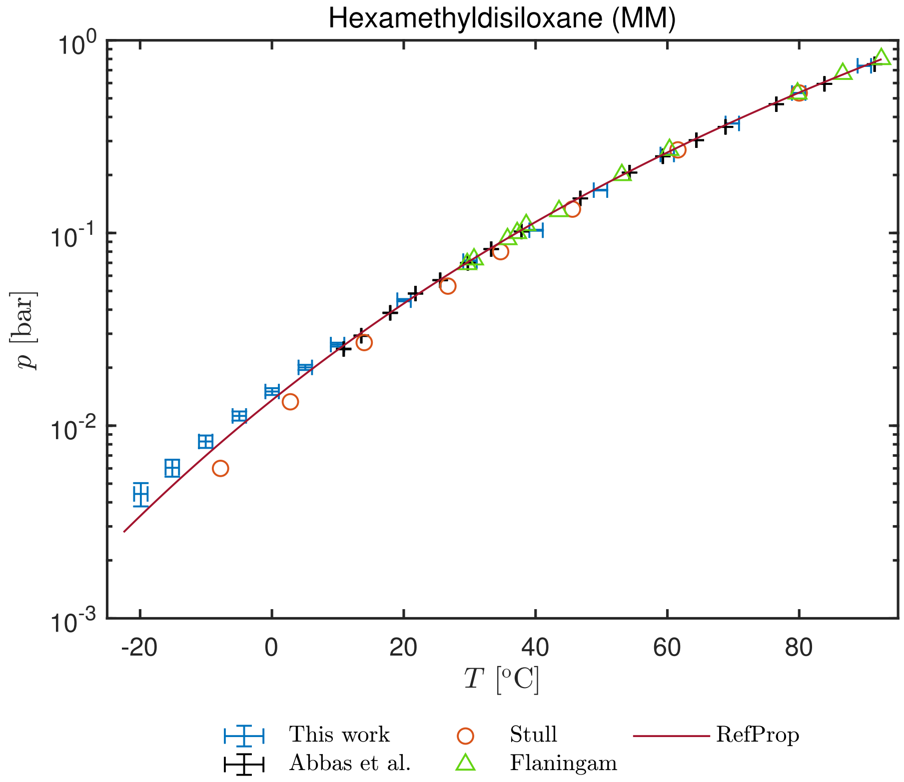

Figure 3.5: Experimental saturation curve of MM, in the range [−20 °C, 90 °C], compared with the curve predicted by the thermodynamic library RefProp and with data published by Stull [81], Abbas et al. [4] and Flaningam [39]. The pressure p axis is logarithmic.

deviation is observable, in particular between 220 °C and 240 °C.

Figure 3.7 reports the confidence index of the pressure deviation between the reference fluid and the stressed fluid for the same temperature interval in which the VLE curve was measured. Data relative to stress temperature $T_s = 240\,°C$ are clearly out of the 99% confidence level region, thus indicating that decomposition occurred with very high probability (see Section 3.3.3.3). For increasing stress temperatures, the confidence index further increases, indicating that the decomposition phenomena is getting stronger. As already seen from the trend of Figure 3.6, the increase of vapor pressure (and thus of the deviation), suggests that more and more light compounds are being formed as the stress temperature increases.

3.4.1.3 *Chemical analysis*

Results of chemical analysis carried out on stressed samples of siloxane MM are compared to those performed on the virgin fluid in Figure 3.8. Regarding the virgin fluid, only the liquid phase was analyzed, since the sample, prior to loading, is withdrawn from a tank at atmospheric pressure. Both liquid and vapor fractions were analyzed in the case of the stressed fluid. Data of the vapor phase are reported in Table 3.4.

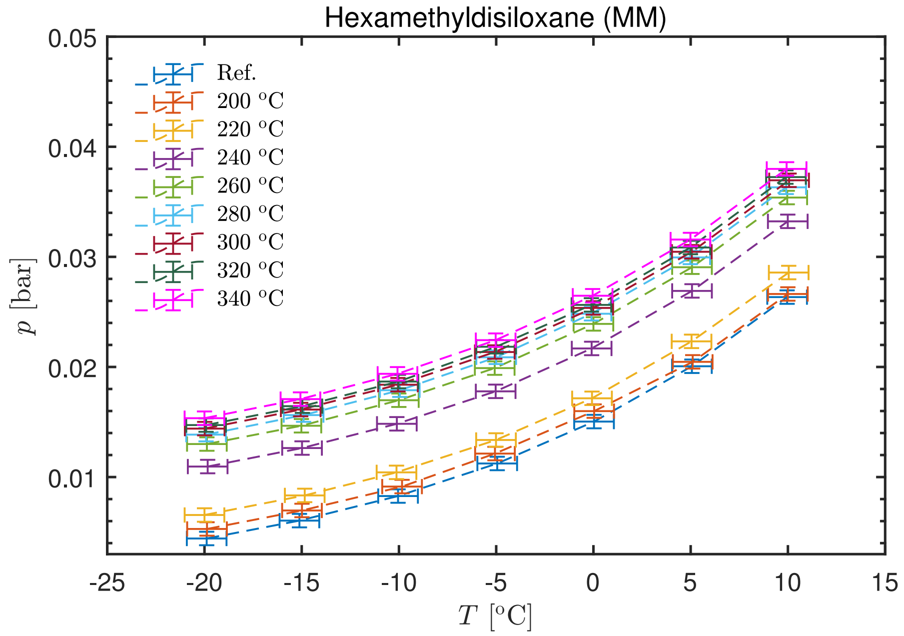

Figure 3.6: VLE measurements of the reference (virgin) fluid along with those performed after the the fluid underwent thermal stress in the range $T_s = 200\,°C \div 340\,°C$, with 95% confidence level uncertainties.

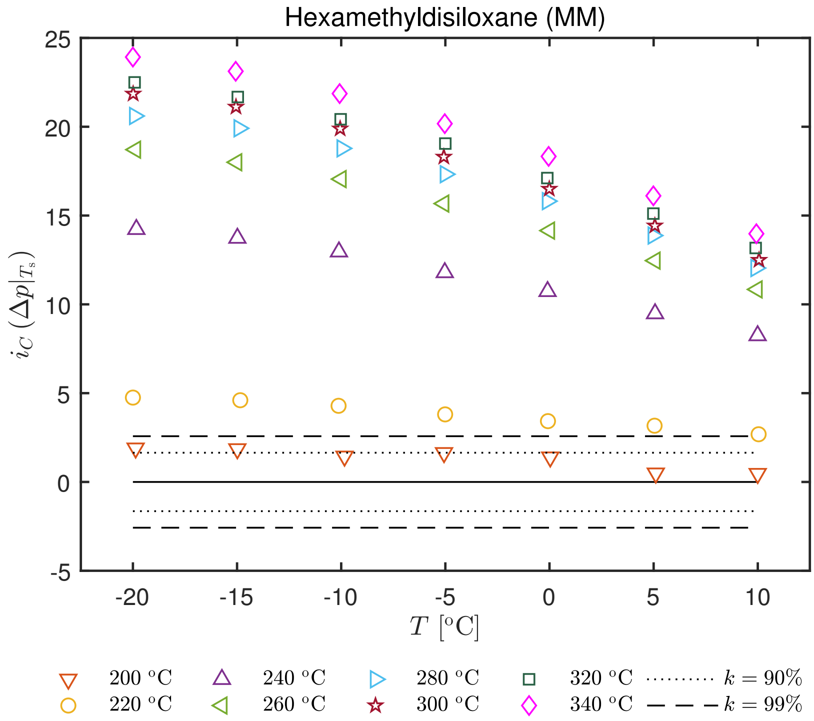

Figure 3.7: Confidence index of the deviation between the reference MM fluid and stressed fluid VLE pressure. The dashed and dotted lines represent the 99% and 90% confidence level respectively.

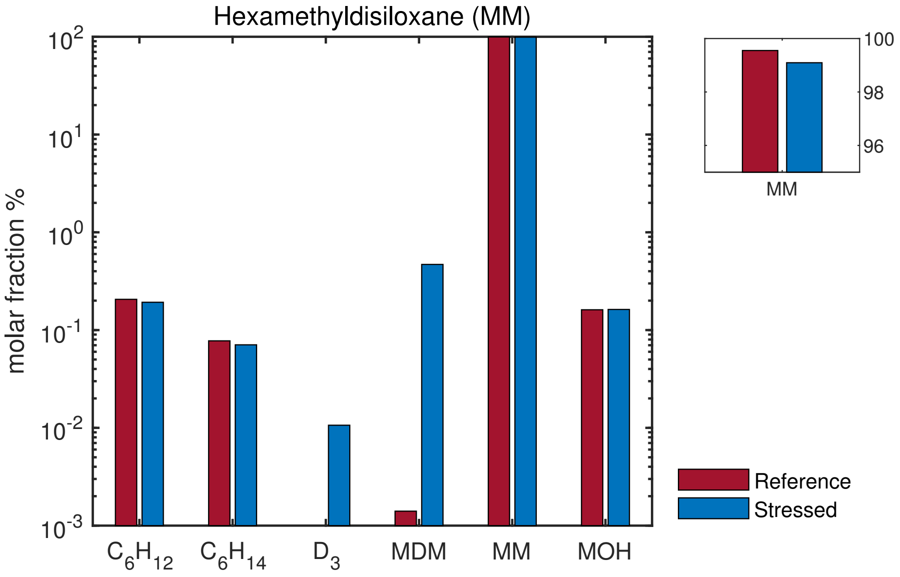

Figure 3.8: MM samples: chemical analysis of liquid phase. The virgin fluid and after stress at 340 °C are compared.

Table 3.4: Chemical analysis results of vapor phase of stressed MM after thermal treatment at 340 °C.

Component	Vapor [μmol]
Methane	1.19
Ethylene	0.057
Ethane	0.085
CO_2	0.256

Molar fractions are reported in a logarithmic scale. A detailed view of the top of bars of the main component MM is given in linear scale for the liquid phase. The virgin fluid features small amounts of C_6 hydrocarbons and trimethylsilanol (MOH[1]), which remain almost unaffected from the exposition at high temperature. The very small amount of MDM present in the virgin fluid rised by two orders of magnitude, suggesting that it is formed upon decomposition. The cyclic siloxane D_3 (hexamethylcyclotrisiloxane – $C_6H_{18}O_3Si_3$), that was not present before stress, formed. However, the reduction of molar fraction of MM is quite contained, from 99.6% to 99.1%. Regarding the vapor phase, detected decomposition products are carbon dioxide (CO_2) and the light hydrocarbons methane (CH_4), ethane (C_2H_6), and ethylene (C_2H_4). Methane results to be the main component. However only $1.19\,\mu\mathrm{mol}$ were detected with resect to a loaded amount of about $100\,\mathrm{mmol}$. The presence of CO_2 is an index of the presence of oxygen in the sample, and suggests that oxydation of carbon by the air that remained in the sample due to imperfect degassing took place.

Limited decomposition was observed with chemical analysis.

3.4.2 *Siloxane MDM*

Two different samples of siloxane MDM were tested. A first sample of 26 g was stressed at 200 °C and 250 °C. Unfortunately, during the test at 260 °C the oven encountered temperature control problems, that led to a sudden temperature overshoot to $\approx 310\,°C$ that compromised the sample. Thus, a second sample of 18 g was employed for stress tests from 260 °C to 350 °C.

In the following subsections experimental results of the MDM samples are reported.

3.4.2.1 *Pressure deviation in isothermal stress tests*

As done for the MM sample (see Section 3.4.1.2), pressure deviations during the stress were analyzed for the siloxane MDM sample in terms of p/T also. As in the previous case, no significant deviation was observed, indicating that according to the pressure deviation during isothermal stress tests method no appreciable decomposition effects were detected.

No pressure deviation detected at constant temperature.

3.4.2.2 *Pressure deviation in VLE measurements*

Following the procedure depicted in Section 3.2, the VLE curve of the virgin fluid sample was measured in a temperature range from 10 °C to 50 °C. Figure 3.9 reports experimental data of the measured VLE curve of the virgin MDM sample with 95% confidence index bars, along with the curve predicted by RefProp [54] and compared with data published by Stull [81] and Abbas et al. [4]. The accordance is

---

[1] Trimethylsilanol – $C_3H_{10}OSi$

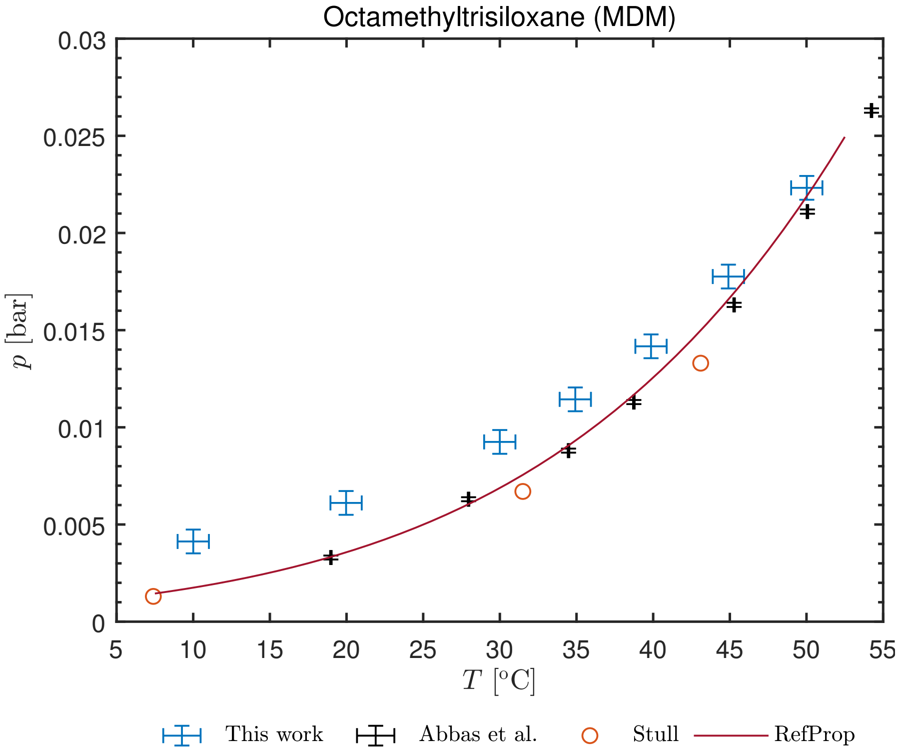

Figure 3.9: Experimental saturation curve of MDM, in the range [5 °C, 55 °C], compared with the curve predicted by the thermodynamic library RefProp and with data published by Stull [81] and Abbas et al. [4].

fairly good, except for very low temperature, were the presence of air remaining in the sample after the degassing procedure is appreciable. Due to the lower vapor pressure ($p \approx 43\,\mathrm{mbar}$ at $T = 20\,°\mathrm{C}$ for MM and $p \approx 3.6\,\mathrm{mbar}$ at $T = 20\,°\mathrm{C}$ for MDM), the degassing of the MDM sample is more difficult than of the MM one. Indeed, in the case of MDM, the saturation pressure to be achieved is similar to the lowest pressure achievable by the vacuum pump being employed. This leads to the greater impact of air impurities on VLE measurements of MDM than of MM.

Figure 3.10 reports the comparison of VLE measurements performed on the reference fluid and on the stressed sample. The deviation is appreciable but a clear trend for increasing stress temperature T_s is not present, as it was in the MM case: VLE curves first increase, then decrease and increase again, for increasing T_s.

Appreciable VLE curve deviation was detected at 260 °C and above.

The confidence index of the pressure deviation between the reference fluid and the stressed fluid is reported in Figure 3.11. Data concerning the stress at $T_s = 260\,°\mathrm{C}$ are well beyond the 99% confidence level limit, indicating that decomposition occurred. The absence of a clear trend is clear: for $T_s = 270\,°\mathrm{C}$ the deviation of stressed sample vapor pressure with respect to the virgin one is the greatest. For

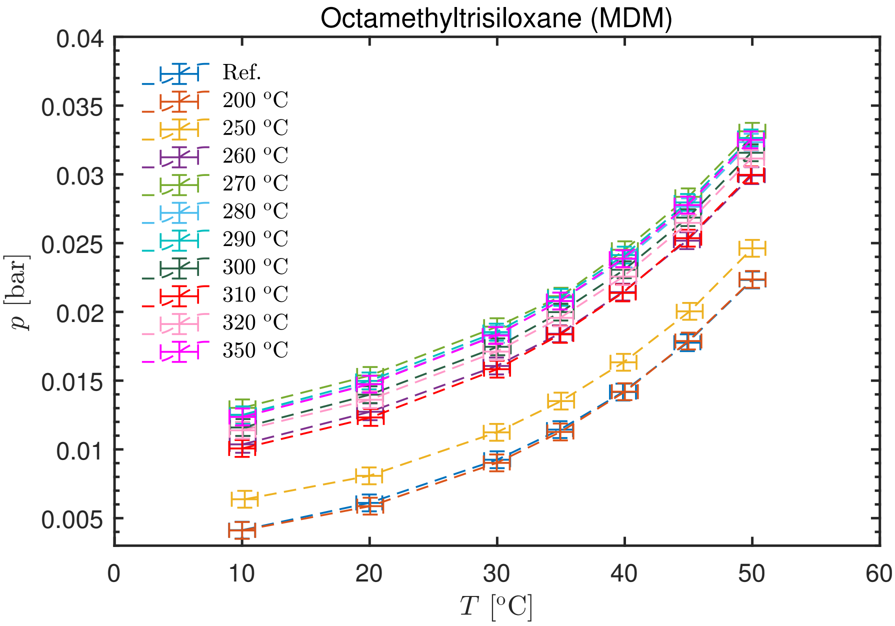

Figure 3.10: VLE measurements of the reference (virgin) sample along with those performed after the the fluid underwent thermal stress in the range $T_s = 200\,°C \div 340\,°C$, with 95% confidence level uncertainties.

$T_s = 310\,°C$ a local minimum is present, while for $T_s = 320\,°C,\ 350\,°C$ the confidence index increases again.

3.4.2.3 *Chemical analysis*

Figure 3.12 shows molar fractions of detected components in liquid samples of the virgin and stressed fluid. Detected impurities in the untreated fluid are silanols (MOH[2]) and siloxanes (D_3[3], D_4[4], MD_2M[5]). MM and D_3, which are the simplest linear and cyclic fluids of this category feature the greatest increase due to thermal treatment. A slight increase of MD_2M and trimethylsilanol is observed, beside the formation of MD_3M[6], which was not present in the virgin fluid. However, all this components are present in traces with respect to siloxane MDM, which does not undergo substantial decomposition.

Limited decomposition is observed from chemical analysis

Table 3.5 reports the detected amounts of volatile compounds in the vapor phase. As for the case of MM (Section 3.4.1), methane, ethylene, ethane, and CO_2 are found in negligible amounts, with methane being the most present species.

---

[2] Trimethylsilanol – $C_3H_{10}OSi$

[3] Hexamethylciclotrisiloxane – $C_6H_{18}O_3Si_3$

[4] Octamethylciclotetrasiloxane – $C_8H_{24}O_4Si_4$

[5] Decamethyltetrasiloxane – $C_{10}H_{30}O_3Si_4$

[6] Dodecamethylpentasiloxane – $C_{12}H_{36}O_4Si_5$

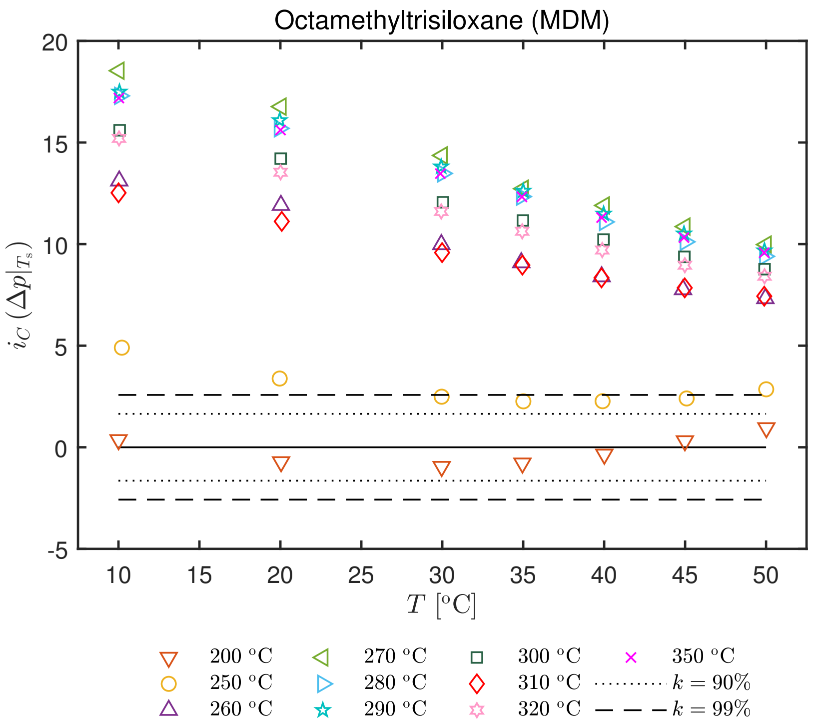

Figure 3.11: Confidence index of the deviation between the reference MM and stressed fluid VLE pressure. The dashed and dotted lines represent the 99% and 90% confidence level respectively.

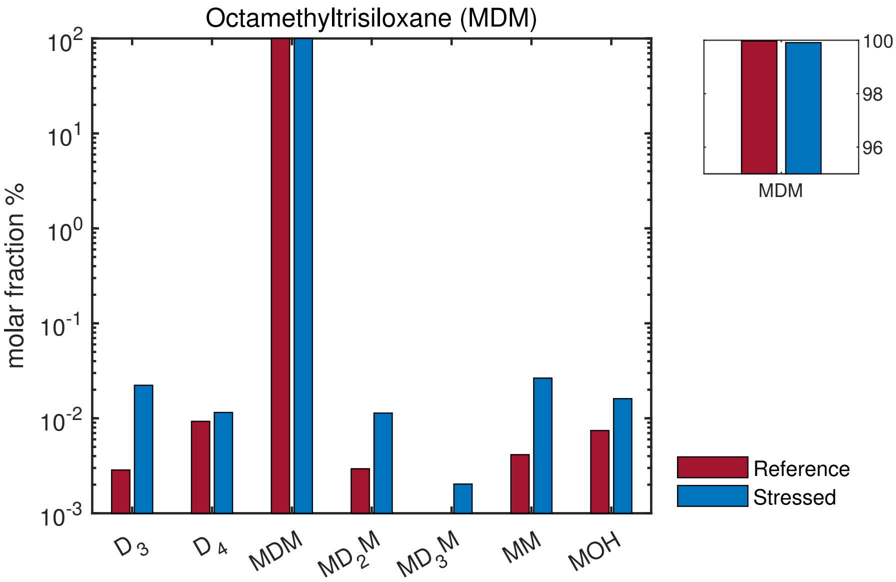

Figure 3.12: MDM sample: chemical analysis of the liquid phase. Virgin fluid and after stress at 350 °C are compared.

Table 3.5: Chemical analysis results of vapor phase of stressed MDM after thermal treatment at 350 °C.

Component	Vapor [μmol]
Methane	0.948
Ethylene	0.025
Ethane	0.05
CO_2	0.524

3.4.3 *Results discussion*

Based on the deviation of vapor pressure from the reference fluid, it can be concluded that appreciable decomposition of MM occurs from a stress temperature $T_s = 240\,°C$. For increasing T_s, the extent of decomposition increases, leading to an increasing deviation of vapor pressure, representative of the formation of light compounds. Indeed, chemical analysis evidence that methane, ethylene, ethane and carbon dioxide are formed upon degradation. Cyclic compound D_3 and linear MDM, which are heavier than MM, are formed.

Regarding MDM, a significant departure of the VLE curve is observed for $T_s = 260\,°C$. The pressure deviation increases until $T_s = 270\,°C$, followed by a decrease at $T_s = 310\,°C$ and a further increase for higher stress temperatures. This behavior could be representative of the formation of heavy compounds that balance the increase of vapor pressure due to light ones.

Results reported in Section 3.4.1 and Section 3.4.2 show higher sensitivity of the VLE curve comparison method with respect to the pressure deviation during isothermal stress tests one. Indeed, both in the MM and MDM case, the latter method did not evidence appreciable decomposition effects, while the former distinguished different amounts of decomposition extent after the performed stress tests. However, chemical analysis showed that, both for MM and MDM, after the highest temperature stress test the decomposition of the fluid was limited.

This inconsistent result pones a question on the capability of the applied method to provide reliable results, for siloxanes. Indeed, this class of fluids shows a very low saturated vapor pressure (e.g. $p \approx 43\,\mathrm{mbar}$ at $T = 20\,°C$ for MM and $p \approx 3.6\,\mathrm{mbar}$ at $T = 20\,°C$ for MDM) and a very low concentration of decomposition products (like methane, for example) has a major impact on the value of measured vapor pressure, leading to a pressure deviation that is certainly not attributable to measurement uncertainties. The comparison of vapor pressure curves alone can result in a thermal stability limit corresponding to negligible amounts of decomposition products, for fluids that have such low vapor pressures. Further, this method is not only based on physical considerations and the result depends on two different aspects:

- The temperature range at which the vapor pressure curve is measured impacts on the value of vapor pressure, thus, for low temperatures, small amounts of decomposition products lead to large variations in vapor pressure, whereas at high temperatures the impact is much more limited. If the vapor pressure is measured in a high temperature range, this behavior can lead to the conclusion that the thermal stability is higher than it would have been possible to conclude if the vapor pressure was measured in a low temperature range.
- The value of measurement uncertainty on both pressure and temperature impacts on the value of deviation between vapor pressure curves that can be attributed to measurement uncertainty and not to decomposition of the fluid sample, thus directly affecting the test result.

VLE pressure and chemical analysis results are contraddictory, there is the need for an improved method.

Rather obviously, by reducing both measurement uncertainty and the temperature range at which vapor pressure curves are compared, it is possible to detect smaller and smaller quantities of decomposition products. The impact of such limited fluid decomposition on industrial applications cannot be assessed and may depend on the particular application and on the nature of degradation products. For this reason, rather than looking for a thermal stability limit in terms of temperature, where the entity of decomposition is not fully meaningful, it appears more significant to look for a trend of decomposition products concentrations for varying temperature. This method removes the ambiguity introduced by the value of measurement uncertainty and by the range of saturation temperature investigated. Chapter 4 reports an extensive experimental campaign carried out on MM, MDM and 50%/50% MM/MDM molar mixture with an improved experimental procedure that aims at solving these issues.

It is worth noting that also the method proposed by Blake et al. [12] suffers from this kind of ambiguity, since the thermal stability limit depends on the limiting value chosen for the time rate of pressure rise during an isothermal stress test.

3.5 CONCLUSIONS

In this chapter, the test rig for the assessment of the thermal stability of organic fluids and experimental results regarding siloxane MM and MDM were presented. The presented design permits the investigation of the behavior of the fluid under thermal stress conditions by analysis of the deviation of pressure under constant temperature stress conditions and of the VLE curve from the virgin fluid one. Lastly it permits the analysis of both the liquid and vapor fraction of the sample.

The experimental apparatus and procedure were first presented, followed by the methodology adopted for the analysis of data. Finally, the thermal stability and decomposition products of MM and MDM were assessed.

MM was stressed from 260 °C to 340 °C. No decomposition was detected analyzing the pressure deviation during the stress. Comparing the vapor pressure curves, data suggest a thermal stability temperature of 240 °C. Chemical analysis show minor amounts of decomposition products.

MDM was stressed from 200 °C to 350 °C. No pressure deviation occurred during the thermal stress. By comparing the VLE curves, a thermal stability temperature of 260 °C can be assumed. Chemical analysis show minor amounts of decomposition products.

The results presented in this chapter evidence an inconsistency between chemical analysis and VLE curve comparison results. Indeed, the result of the analysis performed using the latter method is not dependent on physical reasons only. Further, the quantitative relation between the deviation in vapor pressure and the amount of decomposition is not easily retrievable. An improved method aimed at obtaining a composition trend of the degradation products after different thermal stress temperature i desirable. Such improved method is shown and employed in Chapter 4.

4

AN IMPROVED METHOD: APPLICATION TO MM, MDM AND MIXTURES

The results reported in Chapter 3 showed the inadequacy of the adopted method in determining the thermal stability of siloxanes. Indeed, while the pressure deviation at constant temperature method (see Section 2.1.2) did not evidence decomposition effects, the VLE curve comparison method (see Section 2.1.3) led to the conclusion of a rather low decomposition temperature. Finally, chemical analysis evidenced a limited amount of decomposition products only.

The relation between the deviation of vapor pressure (or the deviation of pressure during the thermal stress) and the entity of decomposition is not readily obtainable. Further, concerning the vapor pressure method, the test result is dependent on the temperature range chosen for the VLE curve measurement and on measurement uncertainty. These are certainly not physical quantities related to decomposition. Finally, these methods do not give an indication of the chemical species formed upon decomposition. From these considerations follows that it would be interesting to look for a trend of concentrations of decomposition products. Molar fractions are directly the physical quantity that represent the entity of decomposition. To reach this goal it is necessary to measure the composition of both liquid and vapor phases after each thermal stress, implying the use a new sample of fluid for each stress temperature T_s.

This chapter reports the experimental apparatus (Section 4.1), the test procedure (Section 4.2) and data analysis procedure (Section 4.3) necessary to obtain a trend of decomposition products for different stress temperature T_s. Section 4.4 reports test results for siloxane MM, MDM and 50%/50% MM/MDM molar mixture.

4.1 EXPERIMENTAL APPARATUS

The experimental apparatus is derived from the THESTA, that was presented in Section 3.1. Figure 4.1 reports a schematic of the improved design, called THESTA 2.0. The system is composed by:

- a test section (depicted in pink in Figure 4.1), used for vapor pressure measurements, thermal stress tests and loading of the selected sample;
- a connection section (depicted in green in Figure 4.1), used to connect the vacuum pump and the helium tank used for leakage tests to the system;

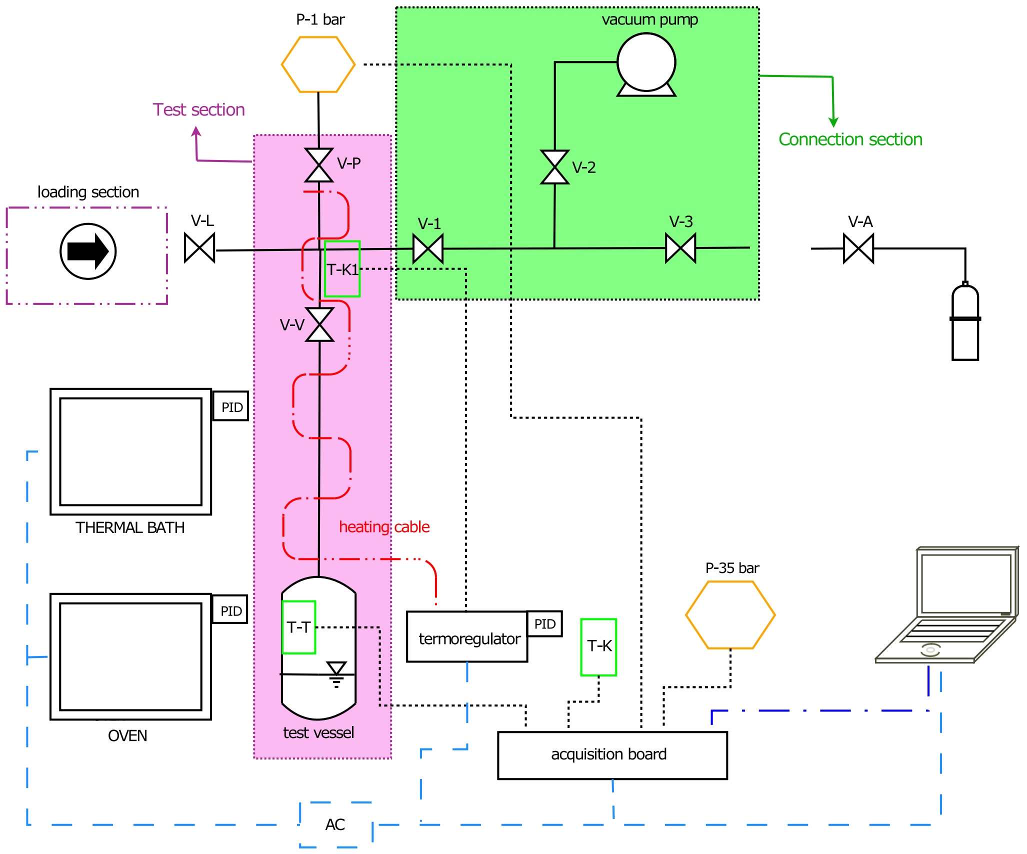

Figure 4.1: Schematic of the improved version, the THESTA 2.0: vertical oven, thermal bath, (AC) AC power supply, (PID) temperature control panel, (PC) personal computer for the data acquisition and the system control, (V-1...V-V) high pressure valves, (T-K and T-T) thermocouples for temperature measurement, (P-1, P-35) pressure transducers, (T-K1) thermocouple for temperature control of the heating cable.

- a loading section employed to load the fluid in the vessel.

Figure 4.2 reports a three dimensional view of the improved experimental apparatus. All components are made of 316L stainless steel to prevent possible damage being caused by acid decomposition products, to assure a proper mechanical resistance and a limited chemical interaction between inner surfaces and the fluid itself. The thermal bath, the oven, the vacuum pump, pressure transducers, thermocouples, and the acquisition system are the same presented for the THESTA in Section 3.1.

The overall design of the improved system results from the need to reduce as much as possible the portion of the setup containing the fluid and not subjected to high temperature during the stress phase. Indeed, in the works by Calderazzi and Colonna di Paliano [13], Pasetti, Invernizzi, and Iora [67] and in tests presented in Chapter 3 the pressure was monitored during the stress phase. Pressure measurements at high temperature pose the problem of sensor calibration curve drift due to thermal effects. To avoid such complication, all three studies opted for maintaining pressure transducers at ambient temperature by increasing the distance between the sensor and the test vessel. This causes vapor condensation in the pressure line. Liquid within the pressure line at ambient temperature is not stressed, thus, once the test is concluded, it dilutes the stressed sample. This results in lower relative percentage of decomposition products detected by chemical analysis and in lower vapor pressure curve deviation.

The whole amount of fluid is stressed in the THESTA 2.0.

In the improved system, the volume subjected to thermal stress is composed by the test vessel and the pipe connected to valve V-V. This volume is entirely contained in the oven during the stress phase, hence all the fluid being tested is stressed. To do so, it is necessary to accept the impossibility to monitor pressure during the stress phase. However, as shown in Chapter 3, the pressure deviation during isothermal stress tests method has low sensitivity, thus that criterion for thermal stability analysis was abandoned.

The maximization of the volume of fluid being stressed has one more positive consequence if the fluid to be tested is a mixture. Indeed, if zones of the test section are at very different temperatures, various zones of the volume may contain vapor or liquid with different concentration of compounds, depending on their density and volatility. This would lead to have a fluid in the test vessel with a composition that may differ from the expected one. The total volume of the system is now about $170\,\mathrm{ml}$.

During the vapor pressure measurement, only the test vessel is contained in the thermal bath. Stratification between the pressure transducer P-1 and the vessel should be avoided. If a temperature gradient is present in the system, it can affect the temperature measurement itself and also the vapor pressure measurement, since a variation in temperature corresponds to a variation of density. To avoid strat-

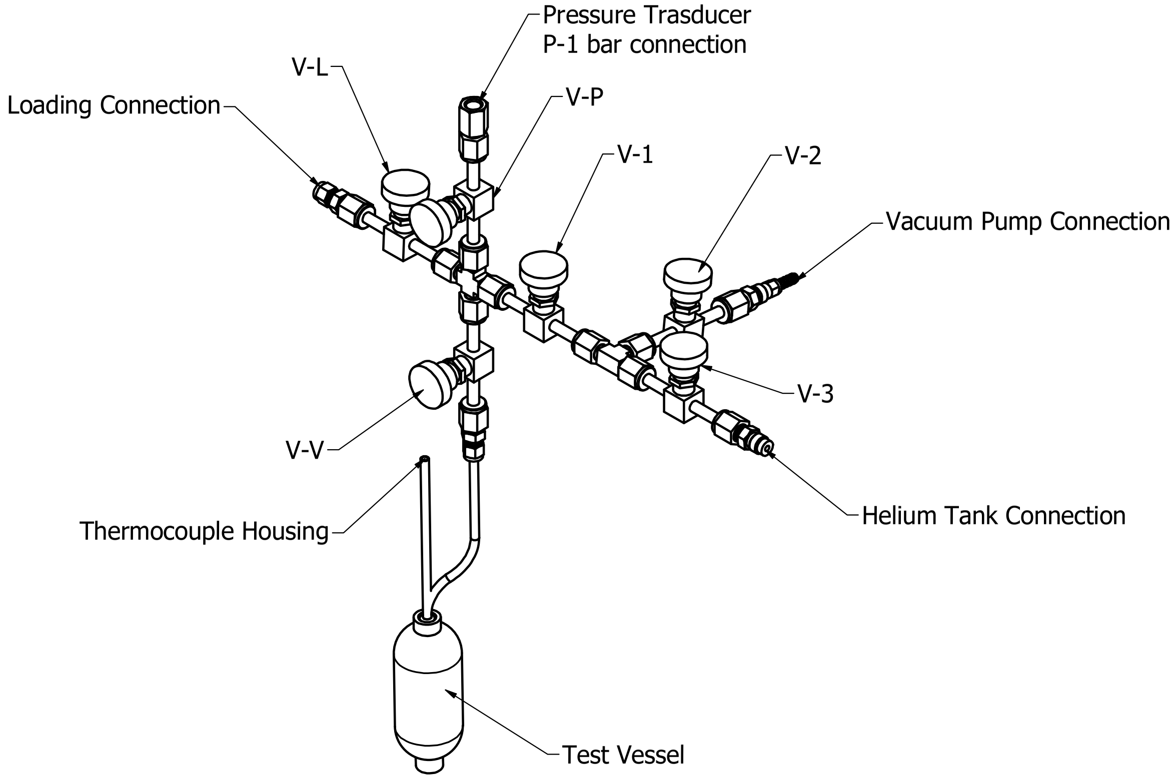

Figure 4.2: Three dimensional view of the THESTA 2.0 test and connection sections.

ification, a heating cable is placed next to the pipe connecting the test vessel to the pressure transducer P-1. This system is effective for temperature higher than the ambient one, while for temperature below ambient an error is still present, though limited.

4.2 TEST PROCEDURE

As previously discussed, using the methods by Blake et al. [12] and Calderazzi and Colonna di Paliano [13], Pasetti, Invernizzi, and Iora [67], used also in the work presented in Chapter 3, the interpretation of results is not straightforward. Thus, a novel method for determining thermal stability of organic fluids was developed.

The procedure is the following:

1. a sample of the fluid to be tested is analyzed by means of gas chromatography - mass spectrometry (GC-MS), to obtain a reference composition of the liquid phase of the fluid under scrutiny;
2. the fluid sample is loaded in a pressure vessel, where pressure and temperature can be measured, and it is then degassed;
3. the vapor-liquid equilibrium curve of the sample is measured by imposing constant temperature through vessel immersion in a thermal bath;
4. the fluid is stressed in an oven at constant temperature for 80 h;
5. the vapor-liquid equilibrium curve of the stressed sample is measured. This measurements are performed, compared to the virgin fluid ones and used to complement chemical analysis results (see the next point 6.);
6. samples of the liquid and vapor phase are collected and analyzed separately by means of GC-MS.

To perform chemical analysis, the test vessel is isolated and detached from the system, after having condensed as much fluid as possible by cooling the vessel to −20 °C. This is done to leave less fluid possible in the portion of the system between valve V-V and the pressure transducer P-1. The vessel is then pressurized to 5 bar with a mixture of known composition of helium, nitrogen, and argon to dilute vapor components and to provide a carrier gas for the analysis. Indeed, the vessel is in two-phase conditions and the pressure is well below ambient one. Thus, it is necessary to pressurize the vessel to inject the sample in the GC. Lastly, the vessel is connected to the gas chromatograph for the vapor phase analysis.

After that, the vessel is opened to ambient air and a sample of the liquid phase is collected for analysis in a gas chromatograph equipped

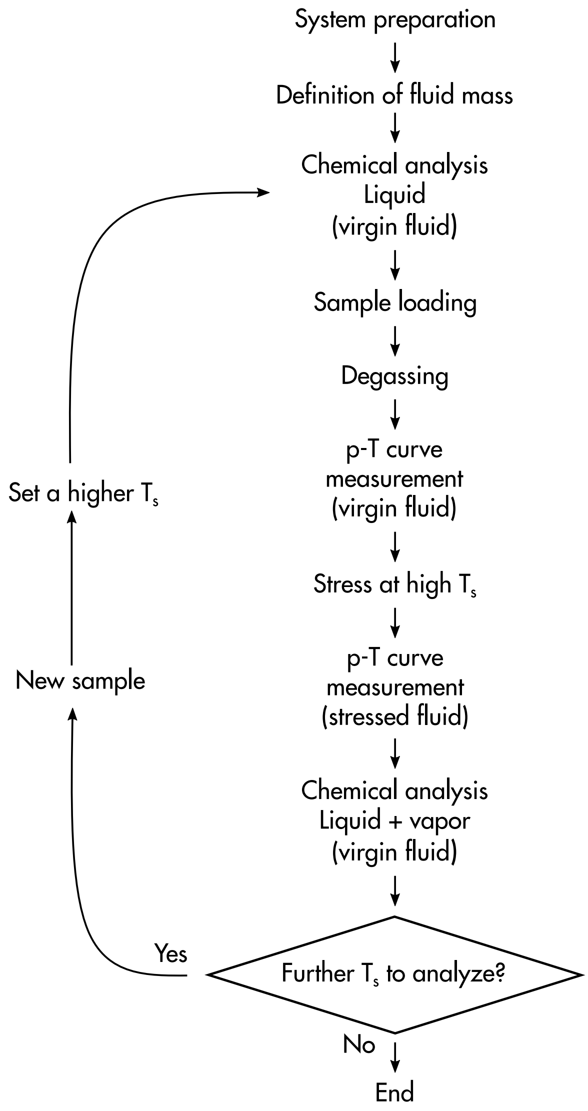

Figure 4.3: Flow chart of the improved experimental procedure.

with a flame ionization detector and a mass spectrometer coupled to two different capillary columns.

This procedure is entirely repeated for different stress temperatures, thus a different fluid sample is stressed and analyzed each time. This is in contrast to the procedure adopted by Calderazzi and Colonna di Paliano [13], Pasetti, Invernizzi, and Iora [67] and in Chapter 3, that stressed the same fluid sample repeatedly at different temperature. In the study by Calderazzi and Colonna di Paliano [13] and in Chapter 3 chemical analysis were performed after the stress at the highest temperature (the former study on liquid phase only, in the work presented in Chapter 3 on both liquid and vapor phases).

A different sample is stressed at each stress temperature, to carry out chemical analysis.

The presented method permits to obtain a trend of the concentrations of decomposition products in both vapor and liquid phases for different stress temperature. Therefore, this procedure allows to have a clear indication of the entity of decomposition at different temperatures; moreover, it provides results that are free from arbitrary assumptions on the criteria applied to define the decomposition point. This consideration is of fundamental importance.

The definition of a temperature limit not to be exceeded in the operation of plants may be useful in practical applications and in a design context. However, if this temperature is not clearly related to a definition of the extent of decomposition, it is of little engineering relevance. The reason for this statement comes from the physics of decomposition which is not an on/off process that activates once a certain temperature is reached. Decomposition occurs in a wide range of temperatures at a rate increasing with temperature; thus a single temperature as a marker of thermal stability limit is physically meaningless.

4.3 DATA ANALYSIS

VLE measurements are used to complement chemical analysis. The procedure used to analyze those experimental data is the same described in Section 3.3.

Regarding chemical analysis, the adopted procedure is slightly different for liquid and vapor. Regarding the vapor phase, the association between peaks and compounds is based on the comparison of the chromatogram with a standard one obtained with a mixture of known species. Indeed, the time at which a compound is eluted (called retention time, RT) depends on the compound only, if all other instrument parameters are kept constant. Thus, by comparing the retention time of each peak with the one on the reference chromatogram it is possible to identify the species present in the sample. On the quantitative side, the concentration of each compound is obtained through the application of a response factor, that relates the response of the detector (in terms of chromatogram peak area) to the concentration.

However, the obtained value is not the molar fraction of the components in the vessel after the stress, since it depends on the dilution applied to perform the measurement. The analysis is performed at ambient temperature T_{amb}, corresponding to a pressure in the vessel, prior to dilution, $p\left(T_{amb}\right)$. The vessel is then pressurized and the overall pressure can be expressed, with the hypothesis of ideal mixture, as

$$p = p_{DG} + p_{ND} = p x_{DG} + p_{ND}, \tag{4.1}$$

where p is the overall presure in the vessel after dilution, p_{DG} is the partial pressure of dilution gases, p_{ND} is the pressure in the vessel before the dilution, and x_{DG} is the molar fraction of dilution gases. By obtaining x_{DG} from Equation 4.1, it is possible to calculate the molar fraction of each compound x_i in the vessel before dilution as

$$x_i = \frac{x_{i,dil}}{1 - x_{DG}} = \frac{x_{i,dil} \cdot p}{p_{ND}}, \tag{4.2}$$

where $x_{i,dil}$ is the molar fraction of each compound after dilution (i.e. the concentration measured by the instrument).

Regarding the liquid fraction, the mass spectrometer provides a chromatogram with an a mass spectrum (in terms of abundance as a function of mass-to-charge m/z ratio) for each detected peak. The compound relative to each peak is obtained bay comparison of each mass spectrum with a large library. This permits the identification of the species present in the liquid sample.

A quasi-quantitative information on the relative amounts of each compound is provided by the chromatogram obtained with the FID (flame ionization detector). Each peak of the FID chromatogram is associated to a compound by comparison with the mass chromatogram provided by the MS, since compounds are eluted in the same order from the two columns and the shape of peaks is similar. The FID gives a response that is proportional to the mass fraction of each compound. The molar fraction is then easily obtained knowing the molar mass of each species.

4.4 RESULTS AND METHODS COMPARISON

The thermal stability of siloxane MM and MDM was tested using the methodology depicted in Section 4.2. Both fluids were supplied by Clearco Products Co. also in this case and have the same characteristics that are reported in Table 3.3. Since the result of chemical analysis of the experimental campaign reported in Chapter 3 was a negligible decomposition after stress at temperature $T_s = 340 \div 350$ °C, the experiments presented here were carried out mainly at higher temperature than the previous ones, namely at 270 °C, 350 °C, 390 °C, and 420 °C for both MM and MDM. For MDM only an extra test at 310 °C was

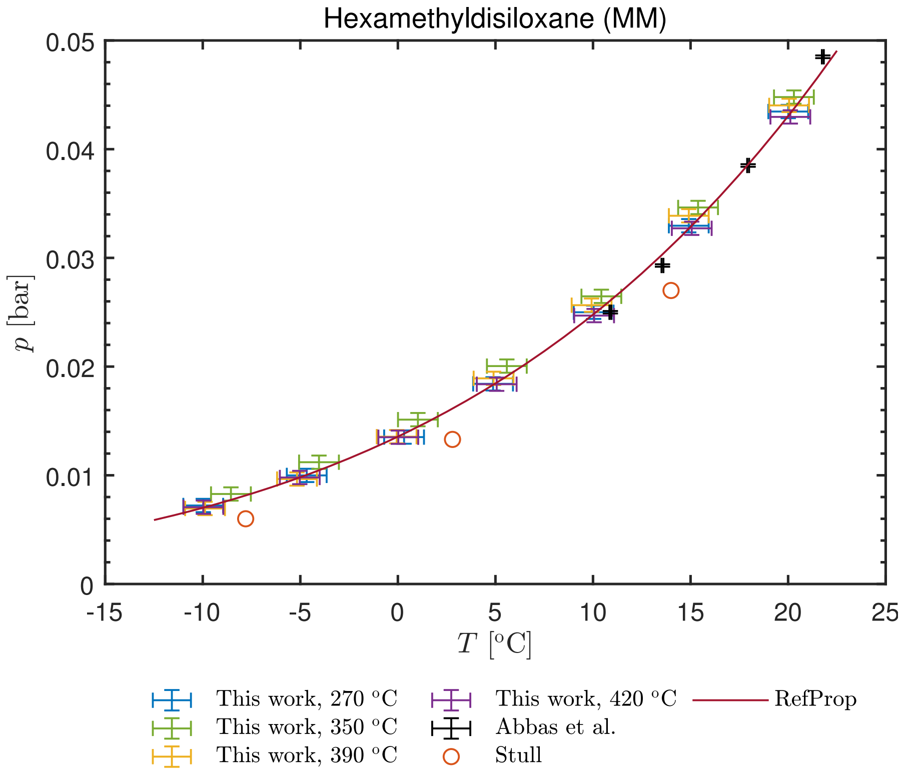

Figure 4.4: Experimental saturation curve of virgin MM employed for tetst at $T_s \in [270\,°C \div 420\,°C]$, in the range $[-10\,°C, 20\,°C]$, compared with the curve predicted by RefProp®and with data published by Stull [81] and Abbas et al. [4].

added, to verify the peculiar non-monotone pattern of VLE curves of MDM for increasing stress temperature.

VLE measurements are used both as complementary data to chemical analysis and to make a comparison between the method and experimental apparatus discussed in Chapter 3 and the present chapter.

4.4.1 *Siloxane MM*

Siloxane MM was tested at stress temperature T_s of 270 °C, 350 °C, 390 °C, and 420 °C. In the following, results of VLE measurements, confidence index analysis and chemical analysis are reported.

4.4.1.1 *Pressure deviation in VLE measurements*

Figure 4.4 reports the VLE curve measured on virgin fluid samples used for the stress test at 270 °C, 350 °C, 390 °C, and 420 °C, compared with values predicted by RefProp and with data reported by Stull [81] and Abbas et al. [4]. No data were reported by Flaningam [39] in this temperature range. A different sample was used for each stress temperature, thus the virgin fluid VLE curve was measured each time and four different sets of data are shown. The accordance between experimental points of this work and those predicted by RefProp and reported by Abbas et al. [4] is very good. Data reported by Stull [81] seem detached from the others. However, experimental uncertainty related to these measurements is not reported, thus a proper comparison cannot be made.

The comparison of VLE measurements performed on the reference fluid relative to each stress temperature T_s and on the stressed samples is reported in Figure 4.5a. The reference fluid data are, of course, the same of those presented in Figure 4.4 and are reported connected by a dashed line, as opposed to the stressed fluid VLE data, which are distinguishable by the dotted line. The deviation is contained for $T_s = 270\,°C$, where uncertainty bars are partially overlapped to the virgin fluid ones. For increasing stress temperature, however, the deviation becomes clear. For stress temperatures from 270 °C to 420 °C, a monotone trend of increasing mean level of VLE pressure is observed. The increasing deviation of data regarding different T_s clearly indicates decomposition of the fluid. The accordance is slightly better in this case than it was with measurements performed with the THESTA (first version) in Chapter 3.

Figure 4.5b reports the confidence indexes concerning the samples of siloxane MM, as a function of the temperature at which the VLE curve was measured. Confidence index corresponding to a confidence level of 99% and 90% are reported as dotted and dashed lines respectively. As discussed for the VLE curve comparison (Figure 4.5a), the sample stressed at 270 °C shows very limited deviation, and it does not lie completely out of the 99% confidence level region. Thus the deviation cannot be attributed to decomposition with high probability. Samples pertaining to $T_s = 350\,°C,\ 390\,°C,\ 420\,°C$ show greater decomposition effects, showing confidence indexes that span from 20 to above 100.

Between 270 °C and 350 °C the deviation becomes significant.

4.4.1.2 *Chemical analysis*

Chemical analysis were carried out on both liquid and vapor phase of the stressed sample, while, regarding the virgin fluid, only the liquid phase was tested. Results in terms of percentage molar fractions are reported in Figure 4.6. Regarding the liquid phase (Figure 4.6a), virgin and stressed fluid composition are compared. The reference fluid contains hydrocarbons C_6H_{12} and C_6H_{14}, and trimethylsilanol (MOH) as impurities. For increasing stress temperature very small quantities of both cyclic (D_3[1], D_4[2]) and linear (MD_2M[3], MD_3M[4]) siloxanes appear in traces. The notation $M^{C_2H_5}M$ means that an ethyl C_2H_5- radical substituted a methyl CH_3- one, thus making ethylpentamethyldis-

---

[1] Hexamethylciclotrisiloxane – $C_6H_{18}O_3Si_3$
[2] Octamethylciclotetrasiloxane – $C_8H_{24}O_4Si_4$
[3] Decamethyltetrasiloxane – $C_{10}H_{30}O_3Si_4$
[4] Dodecamethylpentasiloxane – $C_{12}H_{36}O_4Si_5$

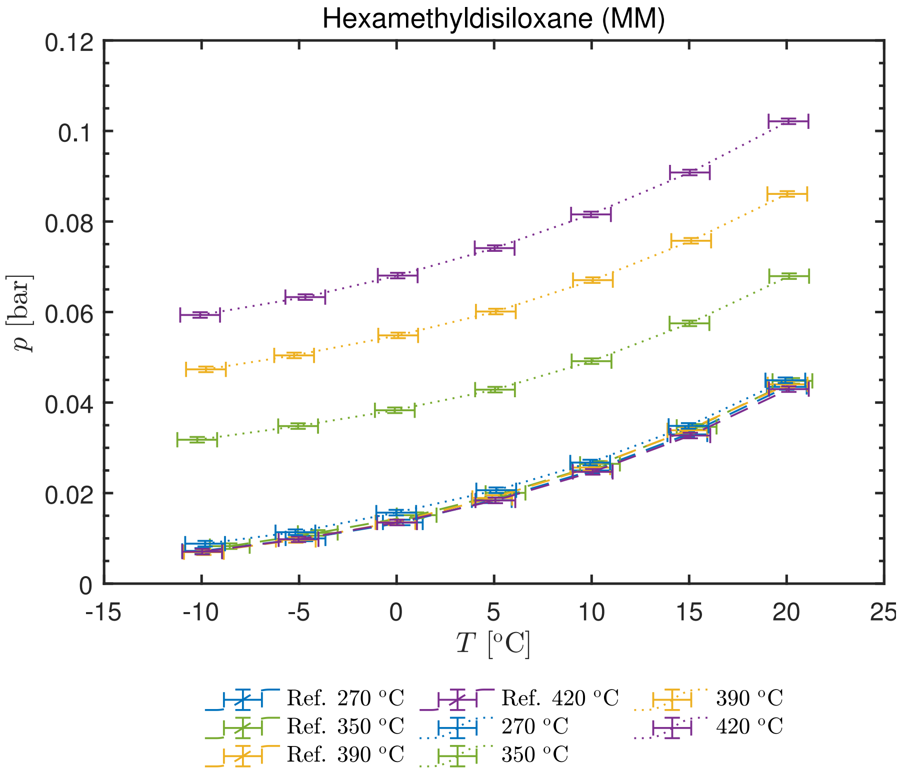

(a) VLE measurements of the reference (virgin) fluid (dashed lines) along with those performed after the the fluid underwent thermal stress (dotted lines), with 95% confidence level uncertainties.

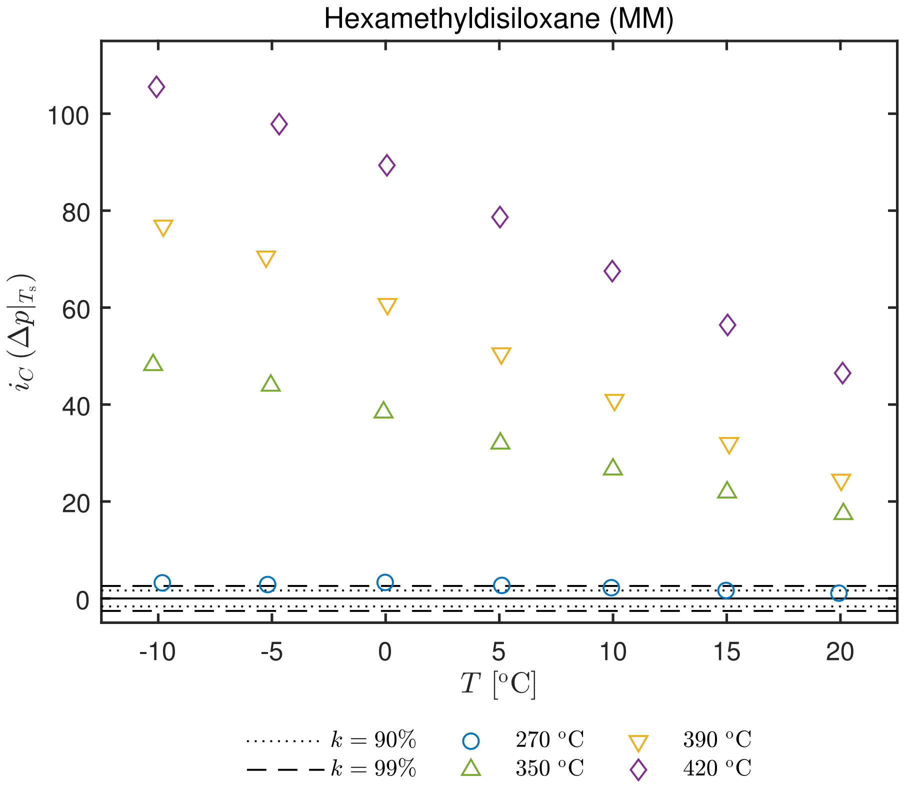

(b) Confidence index of the deviation between reference MM and stressed fluid VLE pressure. The dashed and dotted lines represent the 99% and 90% confidence level respectively.

Figure 4.5: Comparison of VLE curves of MM samples stressed at $T_s \in [270\,°\mathrm{C} \div 420\,°\mathrm{C}]$.

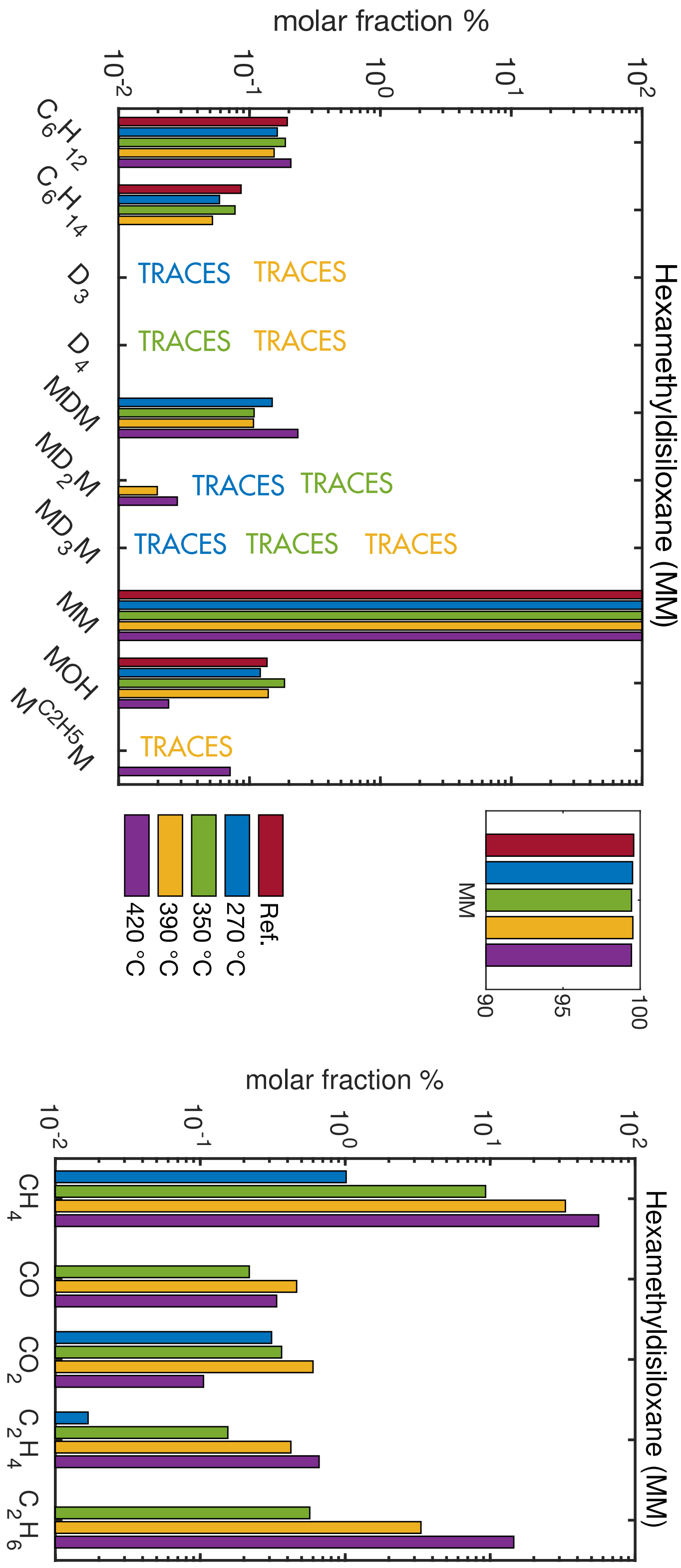

(a) *Liquid phase.*

(b) *Vapor phase.*

Figure 4.6: Chemical analysis of MM samples.

iloxane ($C_7H_{20}OSi_2$). The main decomposition product is MDM, that was not detected in the reference fluid. The impurity MOH seems to undergo decomposition. A detailed view of MM is reported, in linear scale: the quantity of components formed upon decomposition is negligible, since they cause a small variation of the molar fraction of the main component.

Figure 4.6b reports the results of the analysis carried out on the vapor phase. Main decomposition products are light hydrocarbons (CH_4, C_2H_4 and C_2H_6) and results of the oxidation of carbon (CO_2 and CO). Methane is the most present species and its dependence on stress temperature is clear, going from about 1% at 270 °C to about 56% at 420 °C. Increasing amounts of both ethane and ethylene are found, with the former reaching about 15% after the highest stress temperature. The presence of carbon monoxide and carbon dioxide is an index of imperfect degassing, which, however, is really difficult to be achieved with fluids showing such low vapor pressures. The decrease of both CO_2 and CO at 420 °C may be explained by the finite amount of oxygen in the sample, which limits the production of carbon oxides, with respect to the huge amount of organic fluid available for decomposition reactions, which make hydrocarbons fractions increase at the expense of the other ones. Last, but not least, it must be recalled that the presented molar fractions are referred to the whole vapor phase, thus accounting for the presence of high boiling compounds such as MM, that cannot be detected by the employed GC column.

4.4.2 *Siloxane MDM*

Siloxane MDM was tested at stress temperature T_s of 270 °C, 310 °C 350 °C, 390 °C, and 420 °C. In the following, results of VLE measurements, confidence index analysis and chemical analysis are reported.

4.4.2.1 *Pressure deviation in VLE measurements*

As for all other tests, the VLE curve of the reference virgin fluid was measured. Figure 4.7 reports the VLE curve of the virgin fluid sample used for the stress test at 270 °C, 350 °C, 390 °C, and 420 °C, compared with values predicted by RefProp and with data reported by Stull [81]. In this case also, a different sample is prepared for each stress test. The accordance between experimental data and those predicted by RefProp is fairly good. For low temperatures, the presence of residual air impurity is noticeable as an increase of measured pressure. However, compared to the experimental VLE curve reported in Figure 3.9, the deviation with respect to RefProp is lower. The degassing was carried out by repeating cycles of heating, cooling (thus condensing as much as possible the organic fluid) and degassing. It is worth noting that with fluids exhibiting a low saturation pressure such as siloxane MDM ($p \approx 0.1\ \mathrm{mbar}$ at $T = -20\,°C$, as predicted by

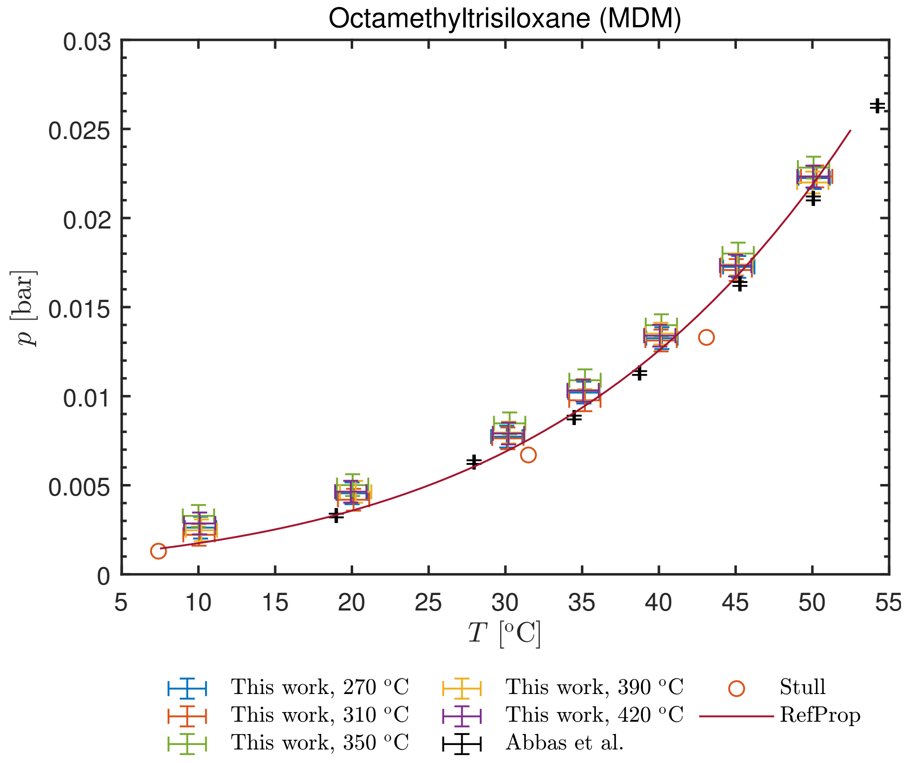

Figure 4.7: Experimental saturation curve of MDM, in the range [5 °C, 55 °C], compared with the curve predicted by the thermodynamic library RefProp®and with data published by Stull [81] and Abbas et al. [4].

RefProp) degassing at low temperature requires high performance vacuum pumps. Indeed, if the saturated vapor pressure of the fluid at the considered temperature is lower than the minimum achievable pressure by the pump, non-condensable gases remain inevitably in the vessel. Thus, to improve the degassing, starting from the campaign reported in this chapter the removal of non-condensable gases was carried out at 20 °C (corresponding to a saturation pressure of MDM slightly higher than the minimum one achievable by the vacuum pump) instead of −20 °C.

A comparison of VLE measurements carried out before and after siloxane MDM underwent thermal stress is reported in Figure 4.8a. Data of the reference (virgin) fluid are reported with the dashed line, while data pertaining to the stressed fluid are connected by dotted lines. Appreciable deviations are observed. The variation of the mean level of the VLE curve is non-monotone for increasing stress temperature, being pressure relative to $T_s = 270\,°C,\ 310\,°C$ the highest, and the one relative to $T_s = 350\,°C$ the lowest. However, the deviation is clear at any temperature.

Figure 4.8b reports the confidence index analysis relative to the measured VLE curves, in the range of temperature used for VLE $p - T$ measurements. All performed tests are beyond the 99% confidence

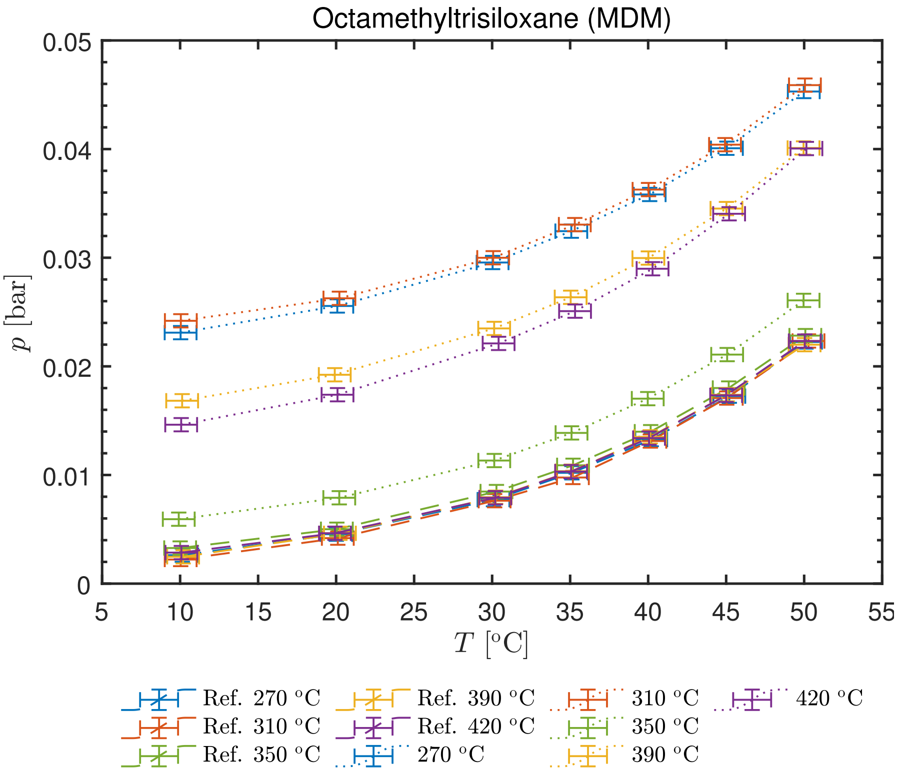

(a) VLE measurements of the reference (virgin) fluid (dashed lines) along with those performed after the the fluid underwent thermal stress (dotted lines), with 95% confidence level uncertainties.

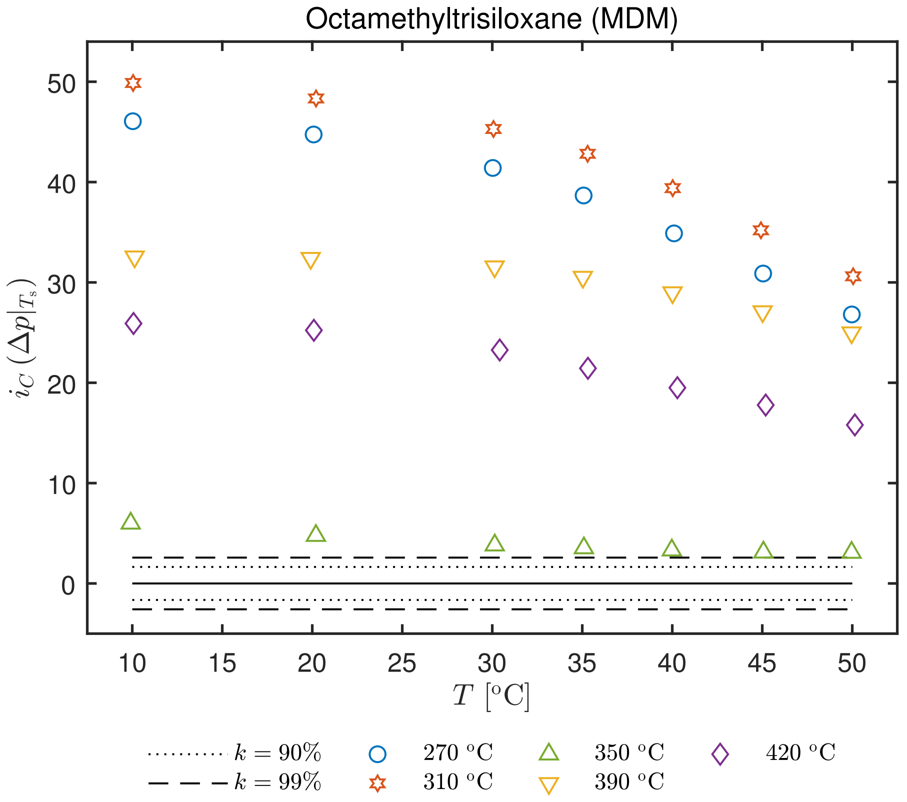

(b) Confidence index of the deviation between the reference MDM fluid and stressed fluid VLE pressure. The dashed and dotted lines represent the 99% and 90% confidence level respectively.

Figure 4.8: Comparison of VLE curves of MDM samples stressed at $T_s \in [270\,°C \div 420\,°C]$.

level limits, thus indicating that the deviation in vapor pressure curve, with high probability, cannot be imputed to measurement uncertainties.

4.4.2.2 *Chemical analysis*

The results of the chemical analysis that were performed on samples of virgin and stressed MDM are reported in Figure 4.9. The liquid fraction (Figure 4.9a) of the reference fluid contained impurities of siloxanes, namely D_4, MM, MD_2M, and MOH, probably coming from the production process. D_3, D_5[5], MD_3M, MD_4M[6], and MD_5M[7], which were not present in the reference fluid, formed as a result of decomposition. Traces of M^HM are detected after $T_s = 420\,°C$, where this notation means that an hydrogen atom substituted a methyl group, thus forming pentamethyldisiloxane. For increasing stress temperature, molar fractions of all decomposition products increase. Relative quantities of siloxane products decreases for increasing number of silicon atoms constituting the molecule. The fraction of MDM varies slightly up to $T_s = 310\,°C$, as can be seen from the detailed view of the top of MDM bars of Figure 4.9a. For increasing stress temperature up to 420 °C, the fraction of MDM undergoes a significant reduction until 94.5%.

Results of the chemical analysis of the vapor phase are reported in Figure 4.9b. Detected decomposition products are methane, ethane, ethylene. Both carbon dioxide and carbon monoxide are detected and indicate the presence of a small amount of air in the sample, which is even more difficult to avoid than for the case of MM, due to the lower vapor pressure of MDM, as discussed in Section 4.4.2.1. The molar fractions of CH_4 and C_2H_6 increase by almost two orders of magnitude, as a result of the increase of stress temperature. Methane is the most present product, reaching about 70%.

4.4.3 *Equimolar MM/MDM mixture*

After having characterized the thermal stability of pure linear siloxane fluids MM and MDM, an equimolar mixture of MM and MDM was characterized. The interest in mixtures of organic fluids derives from a possible increase of system efficiency (Angelino and Colonna [8] and Macchi and Astolfi [57]) due to a better matching between the cooling of the hot source and the heating and evaporation line of the working fluid. Indeed, in a zeotropic mixture, the phase change is not isothermal, resulting in a temperature profile that reduces the mean temperature difference on the hot heat exchanger, thus resulting in a decrease of dissipation. The use of mixtures in ORCs is still very

---

[5] Decamethylcyclopentasiloxane – $C_{10}H_{30}O_5Si_5$

[6] Tetradecamethylhexasiloxane – $C_{14}H_{42}O_5Si_6$

[7] Hexadecamethylheptasiloxane – $C_{16}H_{48}O_6Si_7$

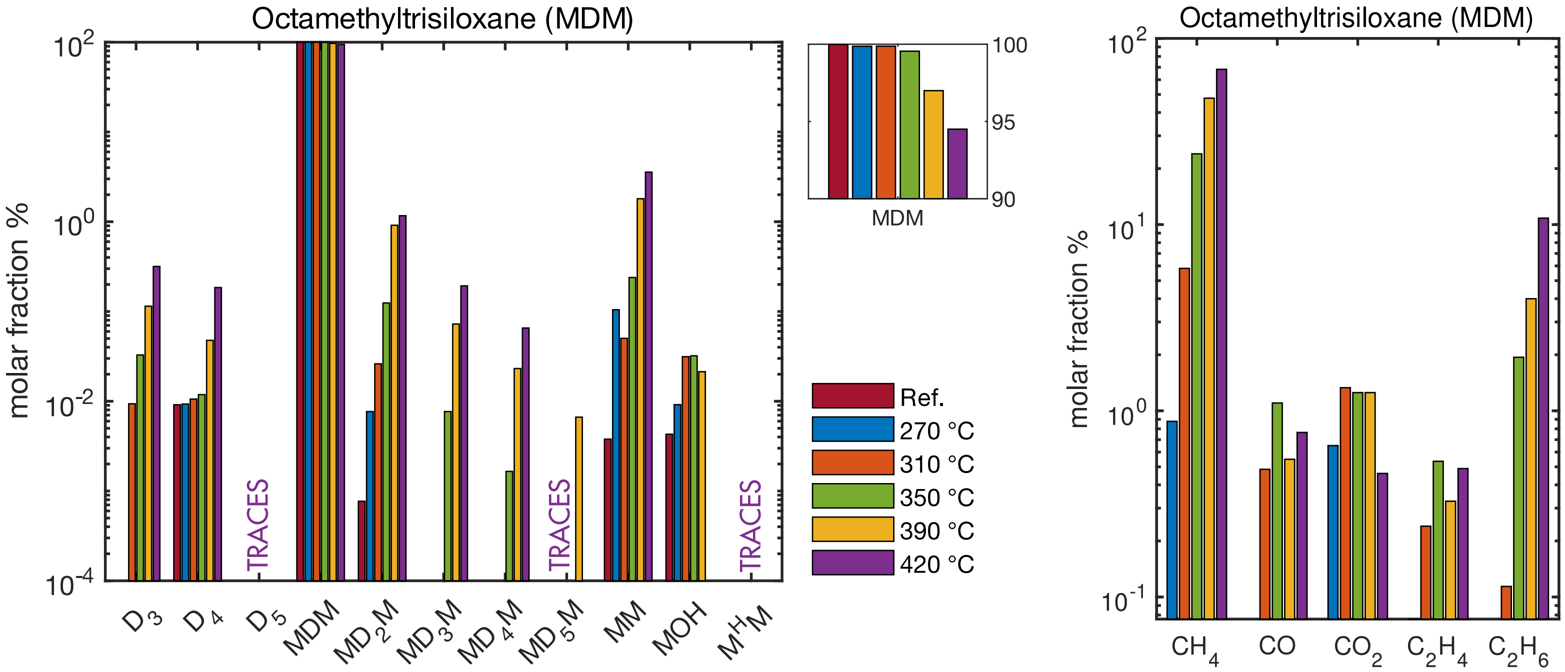

(a) *Liquid phase.*

(b) *Vapor phase.*

Figure 4.9: Chemical analysis of MDM samples.

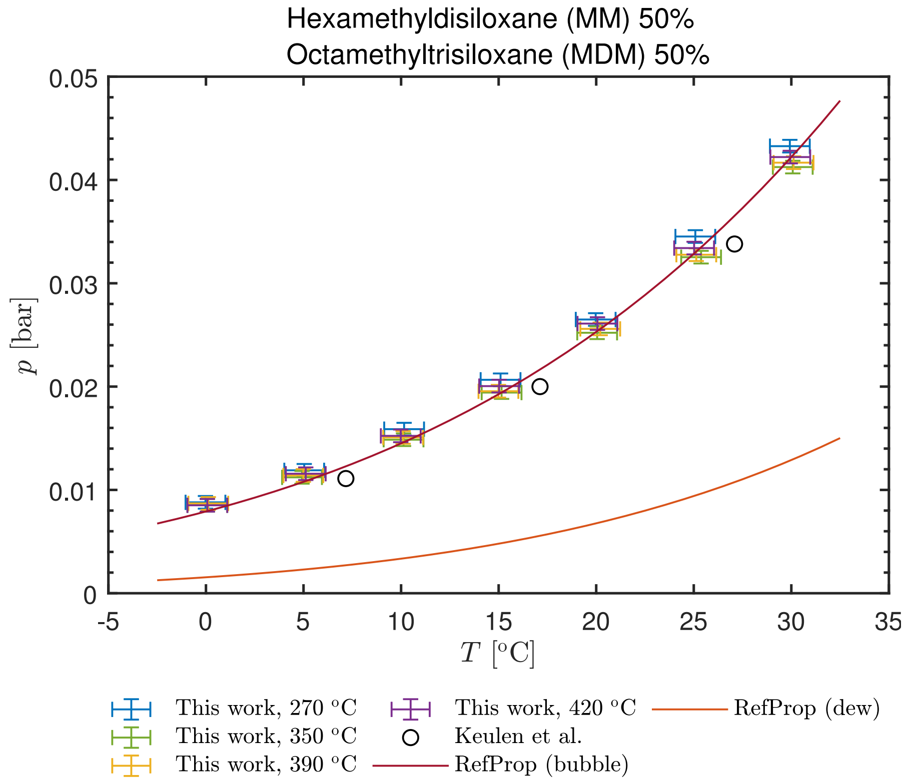

Figure 4.10: Experimental VLE curve of equimolar mixture of MM and MDM, in the range [0 °C, 30 °C], compared with the bubble and dew curve predicted by the thermodynamic library RefProp and with data published by Keulen et al. [52].

limited, mainly due to the increase of heat exchanger surface required by both the reduction of mean temperature differences and of phase transition heat transfer coefficients, which are lower for a mixture than for the pure fluid. Further, there may be problems in case of a leakage, in the sense that the fluid remaining in the plant may have a composition different from the design one, thus causing malfunctions or requiring expensive chemical analysis prior to replenishment.

Regarding the thermal stability, if main components of the mixture are molecularly similar, they may decompose to form the other component, hindering the effects of degradation. No literature about the thermal stability of mixtures of siloxanes exists yet, thus, even if not strictly required for the nozzle tests presented in this work, a study was carried out.

In this work, 25 g of equimolar mixture of MM and MDM were tested at 270 °C, 350 °C, 390 °C, and 420 °C.

4.4.3.1 *Pressure deviation in VLE measurements*

For the mixture also, the VLE curve of the virgin fluid was measured. Figure 4.10 reports the VLE curve of the mixture, compared to data measured by Keulen et al. [52] and the dew and bubble curve calculated with RefProp. Due to to the loaded mass and the temperature range, the VLE curve is practically indistinguishable from the bubble curve, even if an isochore is actually measured. The experimental VLE curve measured in this work is compatible with the bubble curve obtained from the model implemented RefProp, while it is slightly higher than data from Keulen et al. [52]. However, Keulen et al. [52] used an apparatus specifically conceived for the accurate measurements of bubble curves, while this system is not. They report that extreme care must be taken in fluid degassing of this class of fluids. Thus the higher value of pressure obtained in this work may be ascribed to the presence of small amounts of non-condensable gases, which are difficult to remove, as already discussed in previous sections. Nevertheless, the purpose of this work *is not* to accurately measure the bubble line of the mixture, but to have simply a reference curve representing the virgin fluid, thus the accordance of presented data is considered more than satisfactory.

Figure 4.11a reports the VLE curve measured on the virgin and on the stressed fluid, in terms of pressure p as a function of temperature T. Data relative to the virgin fluid are represented with the dashed line, while those pertaining to the stressed fluid are plotted with the dotted line. After $T_s = 270\,°C$, the deviation is very small. Increasing deviation is appreciable for increasing stress temperature T_s, which becomes relevant starting from $T_s = 350\,°C$.

Previous statements are further confirmed by the confidence index analysis reported in Figure 4.11b for the same temperature range. Confidence indexes relative to the stress at 270 °C lie within the 99% confidence index limit, thus making the deviation not significant. From stress temperature $T_s = 350\,°C$ and above, calculated confidence indexes are out of the 99% confidence level region, indicating that decomposition is present with very high probability, reaching values as high as about 110 for $T_s = 420\,°C$.

4.4.3.2 *Chemical analysis*

Chemical analysis were carried out on mixture samples as done for the pure fluids. Figure 4.12a reports the results of the analysis of the liquid fraction. The untreated sample contains the C_6 hydrocarbons coming from MM, D_4 coming from MDM, and MOH which was contained in both original samples. From the chemical analysis it results that the composition of the mixture is slightly shifted towards siloxane MM, being 51.6% and 48.3% the molar fraction of MM and MDM respectively.

Components that were not present in the virgin fluid and are formed due to decomposition are D_3, MD_2M, MD_3M, MD_4M and M^HM, even if the amounts of some of them are very limited. In the sample stressed at 420 °C, MD^HM was detected, where the notation indicates (as in previous sections) that hydrogen substituted a methyl group in MDM,

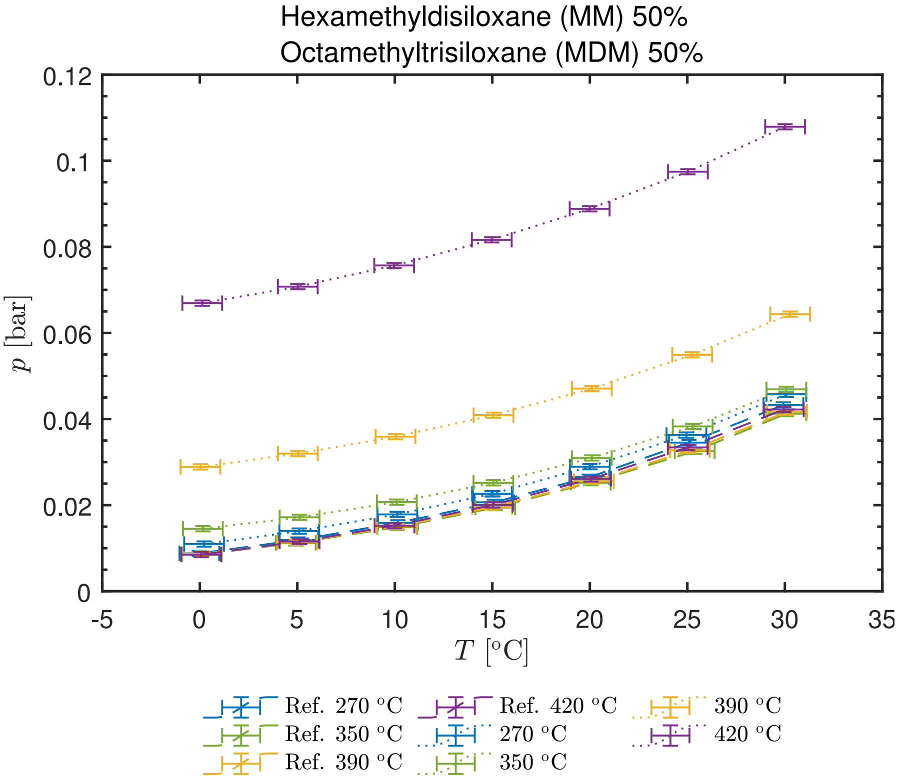

(a) VLE measurements of the reference (virgin) fluid (dashed lines) along with those performed after the the fluid underwent thermal stress (dotted lines), with 95% confidence level uncertainties.

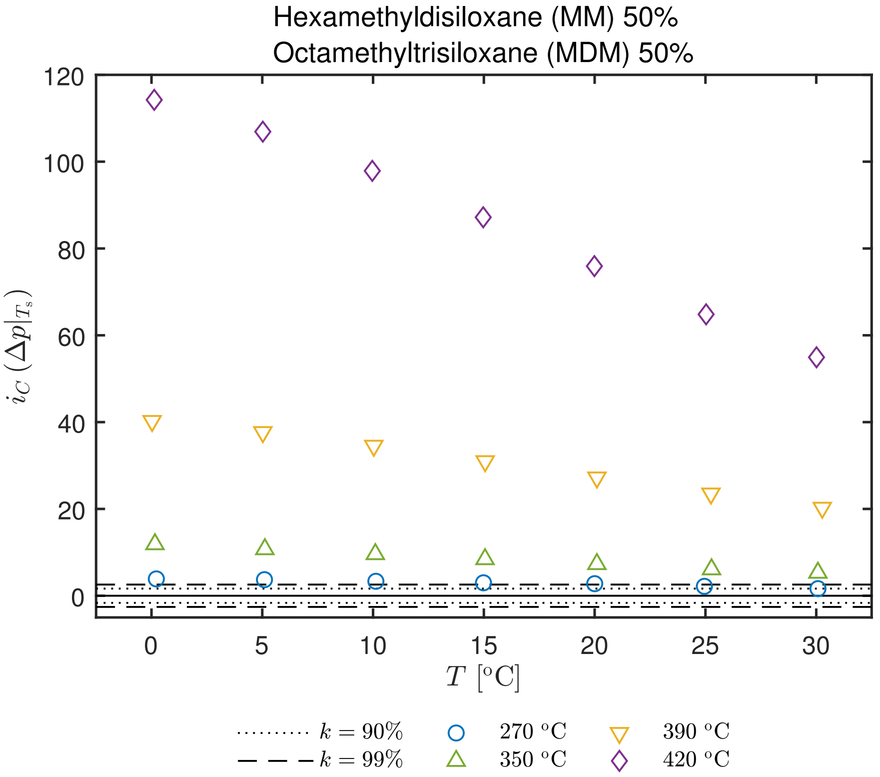

(b) Confidence index of the deviation between the reference MDM fluid and stressed fluid VLE pressure. The dashed and dotted lines represent the 99% and 90% confidence level respectively.

Figure 4.11: Comparison of VLE curves of equimolar MM/MDM mixture samples stressed at $T_s \in [270\,°C \div 420\,°C]$.

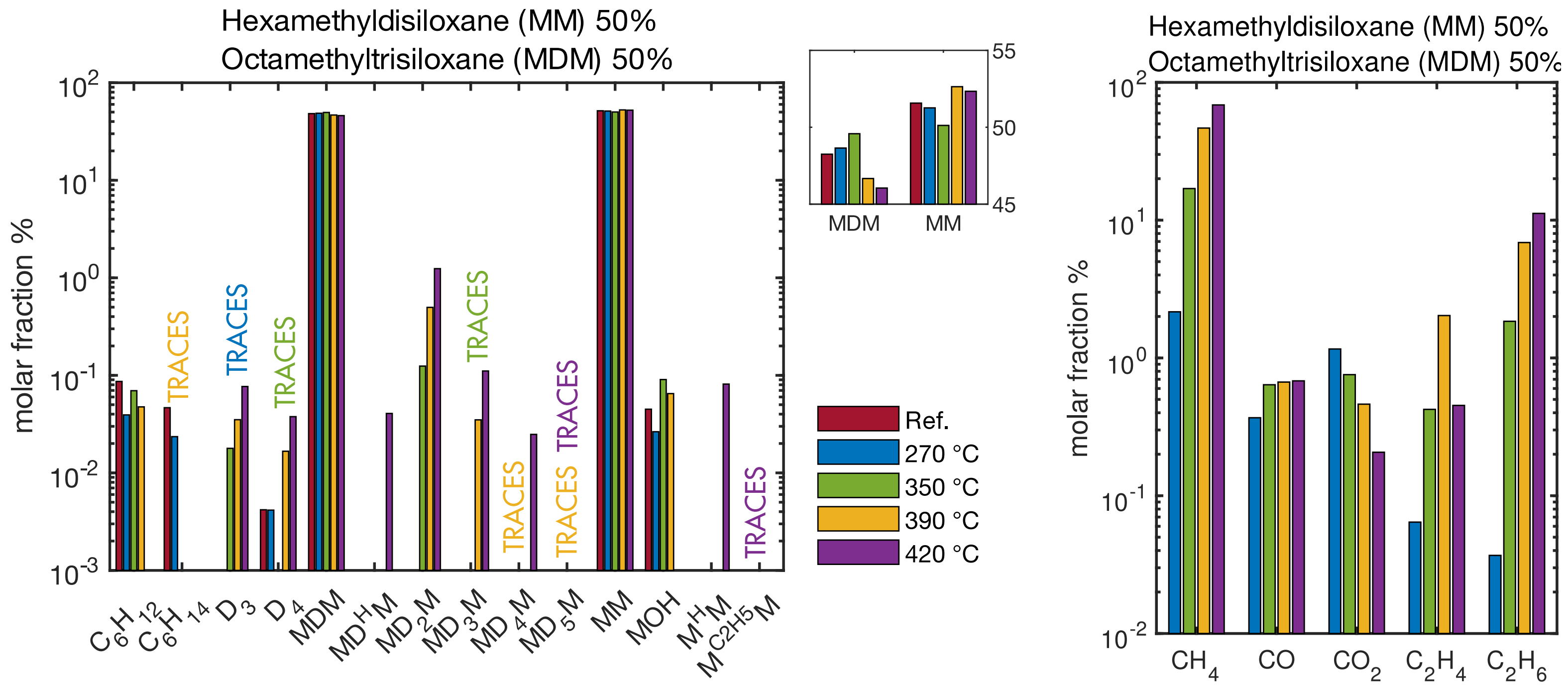

(a) *Liquid phase.*

(b) *Vapor phase.*

Figure 4.12: Chemical analysis of MM/MDM equimolar mixture samples.

thus forming heptamethyltrisiloxane ($C_7H_{22}O_2Si_3$). Traces of MD_5M and $M^{C_2H_5}M$ are also found. Molar fractions of siloxanes other than the two main components increase for increasing stress temperature, as a result of decomposition. Also here, for increasing molecular weight, relative amounts of siloxane products reduces.

Regarding the main components, the fraction of MDM slightly increases at the expense of MM from 270 °C to 350 °C, while considerably decreases between 350 °C and 390 °C with a corresponding increase in the MM fraction. At 420 °C the fraction of MDM has a further slight decrease, while MM remains stable.

Results of the analysis of the vapor phase are plotted in Figure 4.12b. As for the previously analyzed cases, detected products are methane, ethane, ethylene, carbon monoxide, and carbon dioxide. The presence of air is confirmed in this case also by the presence of CO_2 and CO. The fraction of carbon monoxide remains almost unvaried for increasing T_s, while CO_2 consistently decreases. As already seen for the pure compounds, the molar fractions of methane and ethane show a sharp increase for increasing temperature, confirming themselves the main decomposition products found in the vapor phase, reaching about 70% and 10% respectively.

4.4.4 *Results discussion*

Now that the data of the tests that were carried out on the three fluids were presented, a comparative discussion about the results and adopted methods is given.

Siloxane MM shows an increasing VLE pressure for increasing stress temperature, with deviations that become significant above 270 °C. Qualitatively, this is in accordance with the results shown in Figure 3.6 and Figure 3.7 of Section 3.4.1. On the other side, siloxane MDM does not show such monotone behavior, with deviations that are maximum at 270 °C. This behavior is also qualitatively similar to what was observed in Figure 3.10 and Figure 3.11 of Section 3.4.2. However, quantitative differences are present, both in MM and MDM cases between results shown in Chapter 3 and Chapter 4. The reason for that is to be attributed to the difference in both experimental procedure and apparatus employed. Indeed, in the former campaign, the *same* sample of fluid was stressed multiple times at increasing temperature T_s in the apparatus depicted in Figure 3.1 and Figure 3.2 of Chapter 3. For tests presented in the present chapter, the sample was stressed directly at the needed temperature T_s, employing the improved apparatus of Figure 4.1 and Figure 4.2. The THESTA 2.0 was designed to minimize the volume outside the oven. Indeed, the condensed fluid present in that portion of system undergoes no or only limited stress, possible only if some recirculation between hot and cold parts is present. Further, stressing the same sample at increasing temperatures may have an influence on the final result at the highest stress temperature, due to the history of the sample. For these reasons, the improved procedure and apparatus (THESTA 2.0) are considered to provide more accurate results.

Chemical analysis were performed after each stress at different temperature T_s, thus making possible to obtain a trend and an order of magnitude of fractions of the components of the mixture. Decomposition products found in the liquid phase are siloxanes, both linear and cyclic, present in decreasing amounts as the molecular weight increases. MDM is the only relevant decomposition product of MM in liquid phase. Only traces of other substances were detected. This result is in accordance with the result shown in Figure 3.8 of Section 3.4.1. MDM shows a relevant decomposition in liquid phase, with MM and MD_2M as main products, followed by many other heavier siloxanes in lower quantities. Of course, quantities of the single component being shown here are beyond the accuracy of the GC, but still yield a picture of the trend of each component fraction. Furthermore, the overall quantity of degradation products is for sure relevant and has an impact on the fraction of MDM, which reduces by about 5%. In the vapor phase, detected components are light alkanes and alkenes, with higher amounts of methane in case of MDM than MM.

MM seems to form mainly light compounds, whereas MDM seems to decompose to form high boiling compounds.

The measure of VLE curves together with liquid chemical analysis suggests that, in case of MDM, mainly high boiling compounds are formed. Indeed, the deviation of vapor pressure remains rather contained, while MDM in liquid phase decreases considerably. The high fraction of methane and ethane in vapor phase is compatible with the low volatility of MDM. The opposite is suggested for MM, where its molar fraction in liquid phase remains almost unchanged, while the deviation of VLE pressure is greater than for MDM. The presence of a lower percentage of CH_4 and C_2H_6 in the vapor phase of MM tests with respect to MDM ones is compatible with the higher volatility of MM.

Degradation products found in the vapor phase of siloxane MM tests are in accordance with those reported by Manders and Bellama [59] after laser induced degradation. Two papers by M. Preißinger [56] and Dai, Shi, and Qian [30] about the thermal stability of hexamethyldisiloxane in the range of temperature of interest for ORC applications were found in literature. The first one reported traces of high molecular weight siloxanes in liquid phase, with MM still exceeding 99%, after a test at $T_s = 420\,°C$ for 72 h. Decomposition products found in the vapor phase are light hydrocarbons, like methane, ethane, ethylene, propane, propylene. Dai, Shi, and Qian [30] confirmed the presence of the same compounds in vapor phase after stress at 360 °C. Regarding the liquid phase, linear siloxanes MDM, MD_2M and MD_3M were found beside MM, in decreasing amounts. They claim that a negligible mass of vapor products was detected and they observed non negligible decomposition in liquid phase, even at moderate temperatures up to 320 °C. Based on the results by M. Preißinger [56] and those presented in this chapter, the outcome of the study by Dai, Shi, and Qian [30] seems questionable.

The behavior of the mixture seems complex.

Regarding the mixture, from VLE measurements the trend is of a monotone increase of vapor pressure with stress temperature. The low deviation of curves until $T_s = 350\,°C$ is compatible with the result of the chemical analysis of the liquid phase, where a decrease in the fraction of MM and a corresponding increase of the fraction of MDM is observed, thus contributing to maintaining the measured vapor pressure low. The interaction between the two main components of the mixture seems to be complex and not a simple average of the behavior of the two components. For low stress temperatures, the decomposition of siloxane MM seems to be predominant, while if temperature is increased to 390 °C and above the decomposition of MDM seems to prevail. While, based on the results of pure fluids, the non negligible degradation of MDM at high temperature does not surprise, the considerable reduction of MM fraction at low temperature is somehow unexpected, since pure MM fluid showed limited decomposition.

4.5 CONCLUSIONS

The method adopted in Chapter 3 yielded contradictory results. After a careful analysis, the VLE pressure deviation method lacks in a clear connection between the result of the test in term of decomposition temperature and entity of decomposition: the thermal stability temperature is defined as the one at which a threshold set not only based on physical considerations is passed. For fluids having a vapor pressure as low as a few millibars, the deviation results significant even for very limited degradation. For this reasons, an improved method based on performing chemical analysis on both stressed and unstressed fluid was presented. If this procedure is repeated, it is possible to obtain a picture of decomposition products and their amount for different stress temperatures. Thus, the definition of an arbitrary criterion for defining a thermal stability temperature is avoided.

The thermal stability of siloxane MM, MDM and their equimolar mixture was analyzed adopting the improved methodology. Results show that in all cases decomposition products in liquid phase are siloxanes of growing molecular complexity, while the vapor phase features light hydrocarbons. MM showed to produce mainly vapor products, while the opposite holds for MDM.

In a plant, the elimination of non-condensable products is rather simple, by means of a vacuum pump. The relevant decomposition found at high temperature in the liquid phase of siloxane MDM samples suggests to pay attention to its thermal stability, since the removal of high boiling compounds is much more complex. These products may remain mixed in the working fluid, altering its properties and possibly causing performance degradation.

The behavior of the 50%/50% mixture is complex, with MM showing a slightly worse performance for low temperature than MDM.

To conclude, the tests presented here are carried out in an almost inert environment; in an actual plant the behavior may be worsened by the presence of carbon steel instead of stainless steel, lubricants, air or humidity. Most of these contaminants are reduced as much as possible in the TROVA, where the nozzle tests presented in Part ii were performed. However, the plant is made of carbon steel and a safe maximum temperature of about 310 °C and 280 °C for MM and MDM respectively are taken into consideration.

Part II

CHARACTERIZATION OF HIGH TEMPERATURE NON-IDEAL NOZZLE VAPOR FLOWS

Non-ideal compressible-fluid flows are encountered in many industrial cases. CFD codes coupled to state-of-the-art thermodynamic models are employed for design and analysis of system components or for research purposes. However, experimental data regarding such flows are scarce, due to the typical difficulty in performing measurements in such conditions. Part ii of this work deals with the experimental characterization of high temperature non-ideal flows of siloxane vapors. An introduction to the TROVA and the peculiarities of carrying out experiments in flows occurring in the dense gas region is presented in Chapter 5. Results of the first ever experimental campaign performed with siloxane MDM in the non-ideal regime, exploiting pressure and temperature measurements and schlieren imaging is presented in Chapter 6, while the first ever experimental campaign carried out on a non-ideal compressible flow performing pressure, temperature and direct velocity measrements by means of LDV is presented in Chapter 7.

5

EXPERIMENTAL NON-IDEAL COMPRESSIBLE-FLUID DYNAMICS

5.1 EXPERIMENTAL NON-IDEAL COMPRESSIBLE-FLUID FLOW CHARACTERIZATION

Many industrial applications involve non-ideal compressible-fluid flows. CFD codes implementing state-of-the-art thermodynamic models are currently employed for design and analysis of system components or for fundamental research purposes. However, experimental data regarding such flows are scarce, due to the inherent difficulty in performing measurements at high temperature, high pressure, near the thermal stability limit of the fluid and due to the possibility of fluid condensation. The use of standard measurement instruments is not straightforward and the design of specifically conceived systems is frequently required.

As an example, regarding static pressure measurement, in conventional air wind tunnels it is possible to attain a high spatial resolution by employing small wall pressure taps that are connected to transducers with pressure lines of a certain length. The high temperature of the flow and the proximity to the saturation curve line pose the issue of avoiding condensation, and the aforementioned classical solution can be adopted only if coupled to a purging system.

The measurement of fluid velocity is not currently attainable by using directional pressure probes, which would require a fluid dependent calibration which is now well established for air only. On the other side, the use of optical techniques such as laser Doppler velocimetry (LDV) or particle image velocimetry (PIV) requires flow seeding, which is not straightforward for the considered flow, due to the high pressure, high temperature, possibility of condensation and the need to avoid fluid contamination.

Apart from measurement technique aspects, a specifically conceived test rig able to provide a supersonic non-ideal compressible-fluid flow is required. The design of such a particular wind tunnel, entails difficulties related to the need of heating and pressurizing a considerable mass of fluid, of the order of 1×10^2 kg. The Test Rig for Organic Vapors (TROVA) was used in this work: it is an organic fluid wind tunnel built at Politecnico di Milano conceived for the characterization of non-ideal flows.

A summary of experimental studies in the field of NICFD is reported in Section 5.2. Section 5.3 presents details of the TROVA plant, while Section 5.4 deals with its instrumentation and measurement techniques.

5.2 EXPERIMENTAL STUDIES ON NICFD

Recently, the number of experimental facilities designed or built to provide data for the validation of CFD codes implementing state-of-the-art thermodynamic models for non-ideal flow simulation raised. Most of them are devoted to a characterization at system or component level. Papers by Cho, Cho, and Choi [17], Turunen-Saaresti, Uusitalo, and Honkatukia [87], Twomey et al. [88], and Uusitalo, Honkatukia, and Turunen-Saaresti [89] are an example of those studies. However, those experimental investigations do not give insights about the characteristics of the inner flow of the expander: indeed, measurements (by means of pressure probes and temperature sensors) can be carried out at component inlet, outlet or, in particular cases only, at inter-stage sections of machines. Thus, to obtain more detailed data, the design of test rig with dedicated test sections is required.

To overcome the difficulty in performing measurements on real rotating machines, dedicated wind tunnels with test sections accommodating linear cascades are commonly employed: great advancements in the understanding of turbine fluid-dynamics were obtained, see papers by Langston [53], Sieverding [73], and Wang et al. [92]. This eliminates the problem of having moving parts involved, the need of brakes and permits to scale up the size of the cascades, to ease the introduction of probes or the location of wall pressure taps. However, calibrated directional pressure probes are still under development for organic fluids.

For detailed studies of non-ideal compressible-fluid dynamics, specific wind tunnels are needed.

For these reason, a further simplification of the problem is necessary, employing a straight nozzle as fundamental geometry representative of ORC turbine cascades. This arrangement permits to obtain experimental data useful to understand the fundamentals of non-ideal fluid dynamics, for the calibration of loss correlations or the validation of CFD codes. Quantities that are commonly acquired are total and static pressure and total temperature at multiple locations inside the domain. Some of these facilities are equipped (or are designed to be equipped) with optical access for the implementation of techniques such as the particle image velocimetry, laser Doppler velocimetry or schlieren imaging (Head et al. [47], Spinelli et al. [77], and White and Sayma [95]).

Facilities aimed at this kind of studies are mainly of two types: some of them are basically an organic fluid wind tunnel implementing an organic Rankine cycle and that can be continuous or blow down operating; the other category features Ludwieg tube facilities. These are batch facilities where a volume filled with fluid at high pressure is seprated from a low pressure region by a fast operating valve. When this valve opens, a supersonic flow is established in the test section, for a time of the order of milliseconds. Of this type, the FAST (flexible asymmetric shock tube) was constructed at TU DELFT (Colonna et al. [24] and Mathijssen et al. [60]) for speed of sound measurements and for non-classical gasdynamics studies. A second one was constructed at Whittle Laboratory to study trailing-edge losses occurring in ORC turbines using sulfur hexafluoride (Durá Galiana, Wheeler, and Ong [32]). At university of Colorado at Boulder, a Ludwieg tube operating with PP10 was built to verify the existence of non-classical phenomena (Fergason, Guardone, and Argrow [37]).

Belonging to the organic wind tunnel category, the closed loop organic wind tunnel (CLOWT, see Reinker et al. [70]) built at Muenster university is now commissioned (Reinker, Kenig, and Wiesche [69]). This is a closed loop continuous running wind tunnel operating in the vapor phase only and featuring a transonic test section, designed for Novec 649 as working fluid.

A second continuously operating test facility is the ORCHID (organic Rankine cycle hybrid integrated device, Head et al. [47]), built at TU DELFT and currently under commissioning. This is a facility equipped with two different test sections, a first one consisting of an expander, with the aim of carrying out a component level characterization, and a second one designed to accommodate a converging-diverging nozzle, for fundamental gasdynamic studies. The test section is designed with optical access for the implementation of laser based techniques such as PIV.

Another facility featuring two test sections is under development at City, University of London (White and Sayma [95]). It is conceived for R1233zd and will feature a supersonic cascade test section and a twin-screw expander. The test section is equipped with an optical access on three sides, to carry out PIV.

Regarding batch operating facilities, a dense-gas blowdown facility was constructed at Imperial College London with the purpose of validating CFD codes for ORC working fluids. The test section features a converging-diverging nozzle designed to achieve Mach number $M = 2$ at the outlet. Robertson et al. [71] reported results of tests carried out with both Nitrogen and R1233zd(E) and comparison with CFD simulations.

The test rig for organic vapors (TROVA) belongs to the category of blowdown facilities implementing a nozzle test section (Spinelli et al. [77]). It is the first facility of this kind ever constructed and operated. Experimental results obtained with siloxane MDM were reported in [78, 79] and are part of this thesis. Further results at more non-ideal conditions close to the critical point of siloxane MM are reported in Cammi et al. [16], while Zocca et al. [98] reported the experimental characterization of oblique shockwaves in the non-ideal regime. During this thesis, the LDV technique was implemented in

The TROVA is the first wind tunnel for detailed fundamental NICFD studies.

the TROVA and the very first direct velocity measurements in non-ideal organic vapor flows were carried out. Next sections deal with a detailed description of the facility.

5.3 THE TEST RIG FOR ORGANIC VAPORS

The Test Rig for Organic VApors, TROVA, is a blow down wind tunnel designed to characterize non-ideal compressible-fluid flows of organic fluids (Spinelli et al. [77]). To achieve the complete characterization of a fluid flow the TROVA was conceived for the independent measurement of total pressure p_T, total temperature T_T, static pressure P and fluid velocity V_f.

5.3.1 *Working fluids and operating conditions*

The TROVA was originally designed to carry out experiments on siloxane MDM (representative of high temperature ORC working fluids) and on R245fa[1] (representative of low temperature ORC working fluids). The very first tests on organic fluids in the TROVA were carried out with siloxane MDM, but later siloxane MM was used instead, due to its better thermal stability and higher saturation pressure, which permits an easier management of the plant, while maintaining the peculiar non-ideal flow behavior.

However, the adoption of a batch configuration greatly simplifies the test rig control and operation and permits the adoption of a vast variety of working fluids with no or only marginal adjustments. Tests at a maximum pressure of $50\,\mathrm{bar}$ and $400\,^\circ\mathrm{C}$ can be performed, if the working fluid is able to withstand such a high temperature without undergoing substantial decomposition.

5.3.2 *Plant layout and thermodynamic cycle*

The fundamental idea behind the configuration of the TROVA is a batch organic Rankine cycle. With the aim of exploring a wide range of thermodynamic conditions while having a test section dimension sufficient for the insertion of pressure probes with negligible flow perturbation, the adoption of a discontinuous cycle type was mandatory. Indeed, the relatively large dimension of the test section results in flow rates that would require a heating capacity that was not affordable and practically feasible in the laboratory.

A temperature T - specific entropy s diagram of the thermodynamic cycle is depicted in Figure 5.1. The following transformations take place:

---

[1] 1.1.1.3.3-pentafluoropropane - $C_3H_3F_5$

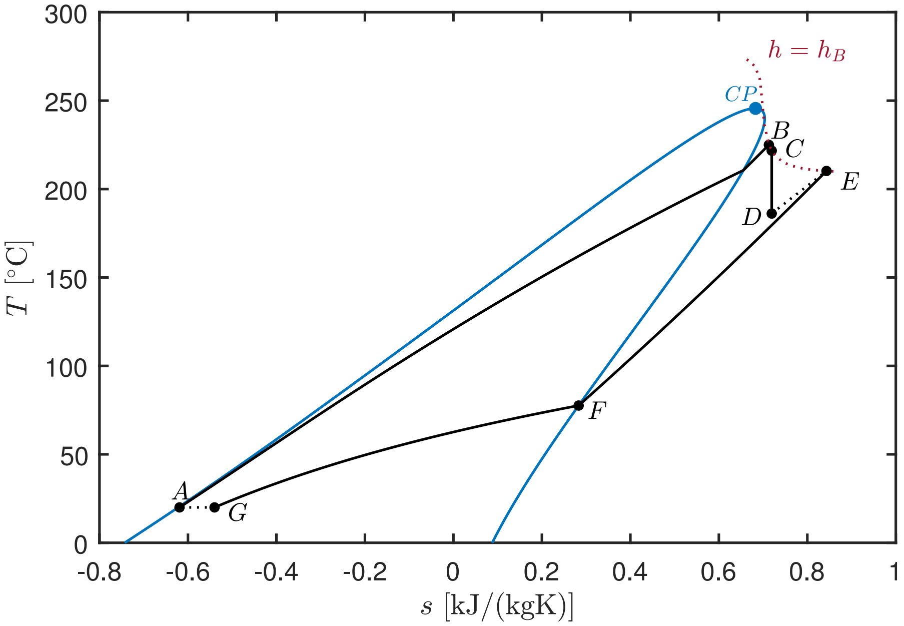

Figure 5.1: Temperature T - specific entropy s diagram of the thermodynamic cycle implemented in the TROVA. CP is the critical point. The blue line is the liquid and vapor saturation curve. Black lines represent the thermodynamic cycle, while the red dotted line represents the locus of points at $h = h_B$.

$A \rightarrow B$ the fluid is isochorically heated up (and, thus, pressurized) to saturated, superheated or supercritical conditions (depending on the test to be performed) in the high pressure vessel (HPV). Temperature and pressure conditions to be reached are chosen based on the maximum total temperature T_T and maximum total pressure p_T desired for the specific test. This transformation is controlled by increasing temperature at constant volume, for a predefined mass of fluid loaded in the vessel;

$B \rightarrow C$ pipes and valves ahead of the test section introduce a pressure drop, thus the fluid is expanded at constant total enthalpy;

$C \rightarrow D$ the organic fluid expands in the test section. This transformation can be regarded as isentropic, being the dissipation confined in the very thin boundary layer;

$D \rightarrow E$ the fluid slows down by means of complex shock/fan combinations and is eventually collected in the low pressure vessel (LPV) in superheated conditions;

$E \rightarrow F \rightarrow G$ the fluid is isochorically de-superheated ($E \rightarrow F$) and partially condensed ($F \rightarrow G$);

$G \rightarrow A$ to carry out a new test, the fluid is eventually transferred to the HPV, which has a different volume with respect to the LPV. Thus point A lies on a different isochoric line than G.

It is worth precising that once the test starts, point B is non longer fixed; enthalpy reduces due to the adiabatic emptying of HPV and points C and D change accordingly. Point E also changes in time due to LPV filling and transformation E → F → G is performed only after the test end.

Figure 5.2 reports a schematic of the TROVA. It consists of five main sections or circuits.

ORGANIC FLUID CIRCUIT It is the core of the TROVA, where the working fluid undergoes the aforementioned thermodynamic processes. Ocher lines and parts represent those normally interested by fluid in vapor state, while red ones represent those where the organic fluid is normally liquid.

This circuit is composed by the high pressure vessel (HPV), a $1\,\mathrm{m}^3$ tank which is filled with a predefined amount of fluid and where transformation A → B takes place by using $38.5\,\mathrm{kW}$ power electrical heaters. It is connected to the plenum and test section through pipes 4, 5, valve V3 and the main control valve (MCV), which are responsible for B → C transformation. Those pipes are heated as well, to avoid the possibility of fluid condensation during the test. Valve V3 is a ball valve that can be automatically operated and isolates the HPV from the test section. The MCV is a control valve equipped with a PID controller that can be used to regulate the total pressure p_T at which the test section is fed.

Downstream of the MCV, a plenum is present, where due to an increase in pipe diameter, the fluid slows to a velocity of about $1\,\mathrm{m/s}$. Here, due to the low velocity, total temperature and static pressure are measured and can be regraded as being the total conditions $T_T - p_T$ of the flow in the test section. The plenum is where the tracer particles are injected in the flow, to carry out laser Doppler velocimetry.

The test section is positioned downstream of the plenum. It is a flanged body where different planar nozzles can be mounted (i.e. to expand the fluid from C to D). An exploded view of the test section is reported in Figure 5.3. The rear part is closed by a plate where a series of $0.3\,\mathrm{mm}$ pressure taps is machined (Figure 5.4a). This plate is mirror polished, to implement a double passage schlieren technique. The nozzle passage area change is obtained by a pair of steel profiles, shaped depending on the test to be carried out. The front is closed by a quartz glass window (Figure 5.4b), to allow the application of optical techniques, such as the aforementioned schlieren imaging technique or laser Doppler velocimetry. The test section and the plenum, are electrically heated.

After the test section, the manual ball valve V4 and the low pressure vessel (LPV) are present. The LPV is a $5.6\,\mathrm{m}^3$ tank that

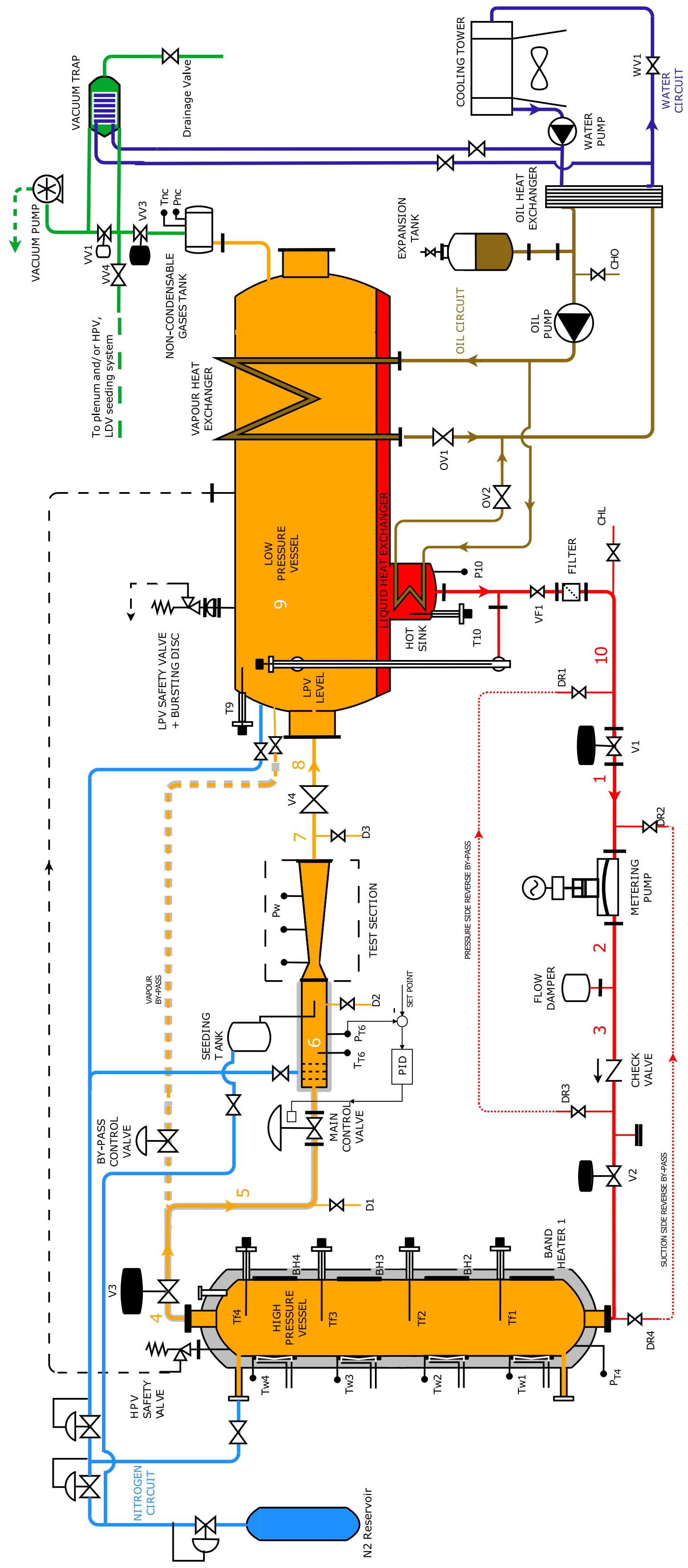

Figure 5.2: Schematic of the Test rig for organic vapors (TROVA).

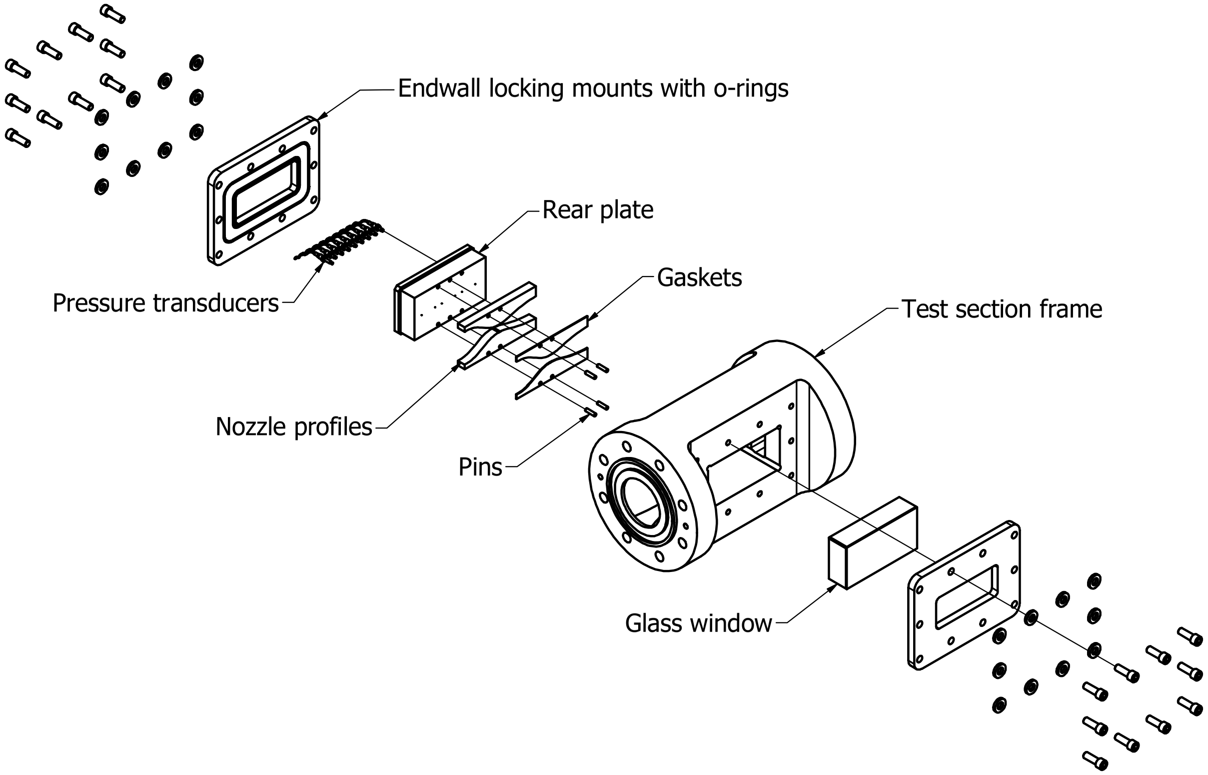

Figure 5.3: Exploded view of the test section.

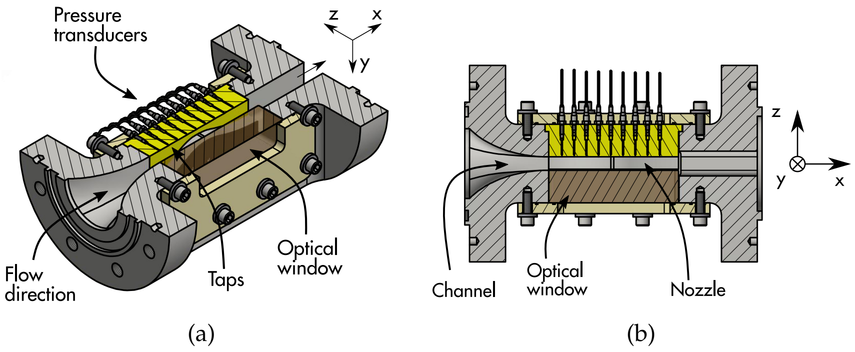

Figure 5.4: Cutted view of the test section.

acts as a collecting vessel for the fluid that is discharged by the HPV through the test section. The $E \rightarrow F \rightarrow G$ transformation takes place here, by means of a cooling system (described below). Lastly, the LPV is connected to the HPV through a membrane metering pump, for transferring back the fluid before carrying out another test.

The fluid can be discharged directly from HPV to LPV (without passing through the MCV, plenum ant test section) through the by-pass control valve (BPCV). This valve is of the same type of the MCV and is pneumatically actuated.

Figure 5.5 shows the HPV (the vertical vessel on the foreground) and LPV (the big horizontal vessel on the left in the background).

VACUUM SECTION This section (green in Figure 5.2) of the plant is responsible for non-condensible removal in the TROVA and can be selectively connected to different parts, to evacuate only a specific component (for example the LPV, the HPV, the seeding system or the plenum and test section). The evacuation is guaranteed by a rotary vane vacuum pump. A vacuum trap is installed to prevent from organic vapor removal, which acts by condensing the fluid present in the flow sucked by the vacuum pump.

OIL CIRCUIT This is an auxiliary circuit (depicted in brown in Figure 5.2) used to cool down the superheated vapor collected by the LPV at the end of a test. It consists of both a vapor and liquid heat exchanger, to effectively cool down the fluid to ambient conditions. The energy gained by the heat transfer fluid is rejected at the oil plate heat exchanger to the water circuit.

WATER CIRCUIT This circuit (dark blue in Figure 5.2) removes energy at the vacuum trap and the oil heat exchanger and finally rejects it to ambient air, by means of a cooling tower.

Figure 5.5: The high pressure vessel (on the right) and low pressure vessel (left) of the TROVA.

NITROGEN LINE The nitrogen line (light blue in Figure 5.2) consists of a N_2 cylinder pack of $0.8\,\mathrm{m}^3$ stored at $200\,\mathrm{bar}$ and a distribution line, equipped with multiple stages of pressure reduction. At ambient temperature, the pressure in the TROVA is near saturation, which is from a few mbar to tens of mbar. At these conditions, considering the plant dimensions, air intake through leakages is unavoidable. The presence of air (and, thus, humidity) is to be avoided, due to thermal stability problems (see Part i). Thus, nitrogen is used to pressurize the plant up to about $1\,\mathrm{bar}$ to avoid leakages. This line is used also to fill the HPV at a desired pressure in case of tests with nitrogen as working fluid.

5.3.3 *Plant operation*

When a test is to be carried out, thermodynamic conditions to be explored are chosen. The needed nozzle is designed, profiles are machined and mounted and the tightness of the test section is tested using pressurized nitrogen. Based on the setpoint pressure and temperature, the mass of fluid to be loaded in the HPV is calculated, from the volume of the vessel and temperature, to obtain the desired pressure. The required mass of fluid is then transferred. However, this operation entails some uncertainties, since the measurement of the amount of fluid present in the HPV is made by means of a visual level meter, thus implying the conversion from level to mass by using a 3D CAD model of the tank. The real vessel is, indeed, slightly different from the model, due to manufacturing reasons. The HPV is heated up and pressurized up to the desired condition using temperature as control variable. If the final pressure is above the setpoint the by-pass control valve could be used to reduce pressure without substantially varying temperature.

Another level of uncertainty is introduced by the fact that pressure and temperature in the HPV are not exactly the same as those in the plenum, due to the presence of pipes and valves in between (see transformation $\mathrm{B} \rightarrow \mathrm{C}$ in Figure 5.1). Due to these uncertainties, ensuring repeatability among different tests is not straightforward.

Due to the nature of the plant, test conditions are not easily exactly repeatable.

Once the correct amount of fluid is transferred to the HPV, the residual nitrogen (present to avoid air leakages) is removed using the vacuum pump and, once the saturation pressure of the working fluid at ambient temperature is reached, the heating procedure of the vessel starts. This phase takes approximately from $5\,\mathrm{h}$ to $10\,\mathrm{h}$, depending on the loaded mass and setpoint temperature. Electrical heaters on pipelines and test section are also turned on. During the last part of the heating-up, the LPV is vacuumized also.

The test is then carried out: when valve V3 and MCV are opened, the fluid flows through the plenum and test section. The HPV is emptied and the LPV is consequently filled. At the end of the test, the cooling system is turned on to condense the vapor collected by the LPV. Finally, the entire system is filled with nitrogen to avoid air leakages.

5.4 TROVA INSTRUMENTATION AND MEASUREMENT TECHNIQUES

5.4.1 *Temperature measurement*

Thermocouples are employed to measure total temperature in the plenum.

Total temperature T_T is measured in the plenum and together with total pressure p_T defines the condition of the nozzle flow being analyzed. Two different thermocouples of type K and type J (called TCK and TCJ respectively) are employed, both located at plenum axis.

Since the TROVA always operates in transient conditions, the problem of the dynamic response of thermocouples may arise. The time constants of two thermocouples whose hot junction diameter is $0.25\,\mathrm{mm}$ (TCK) and $0.7\,\mathrm{mm}$ (TCJ) were found to be $\tau_{TCK} = 0.33$ and $\tau_{TCJ} = 1.49$ using the two sensor method by Hung et al. [48] for a test carried out with the TROVA using siloxane MDM. Signal reconstruction is not required, since it would yield a signal that differs from the original one from much less than its uncertainty. Properties of siloxane MM and MDM are very close and the hot junction diameter of thermocouples employed in the TROVA is less or equal than those used for time constants estimation. Thus, reported values may be regarded as representative for all tests performed with the TROVA up to date. Details can be found in Cammi [15].

5.4.2 *Pressure measurement*

Total pressure is measured in the plenum and static pressure at the nozzle axis.

Pressure is measured both at the plenum wall, where due to low flow velocity takes the significance of total pressure p_T, and at the nozzle axis, where static pressure p is measured. Miniaturized piezoresistive transducers with a sensing element diameter of $3.8\,\mathrm{mm}$ and maximum working temperature of $454\,^{\circ}\mathrm{C}$ are employed. All pressure measurements are performed by means of wall taps, due to current unavailability of calibrated pressure probes for non-ideal flows.

Transducers are directly mounted on the rear plate, to make the line as short as possible. This solves two issues:

- the line-cavity system consisting of the pressure tap, the pneumatic line, and the transducer housing is kept as short as possible, thus increasing the frequency response. The resonance frequency of the system was assessed to be about $200\,\mathrm{Hz}$ using the method by Antonini, Persico, and Rowe [10]. This value was considered satisfactory, since the energy content of the transient in the TROVA is below $1\,\mathrm{Hz}$.

- condensation is avoided, since the line and the transducer are maintained at the same temperature of the whole test section. This avoids possible measurement bias arising from the presence of menisci. Further, condensation would have dramatic influence on the frequency response of the system. Indeed, at test start pressure is very low, of the order of tenth of mbar, since the test section is connected to the LPV, which is almost at liquid-vapor equilibrium. When V3 and MCV are opened and the fluid starts to flow, there is a sharp increase in pressure in the test section. Thus, the line cavity system fills. However, if the temperature of the line or of the transducer is sufficiently low, the fluid can condensate. Until condensation is occurring (i.e. until the cold part is filled with liquid), this continuously removes vapor from the line, thus reducing the pressure read by the transducer. This issue can be solved if pressure lines are filled with nitrogen before test start, thus avoiding the filling of the lines by organic vapor, removing the possibility of condensation.

On the other side, piezoresistive pressure transducers exhibit a shift in both intercept and sensitivity of the calibration curve if subjected to temperature change. To overcome this issue, transducers were calibrated at different operating temperatures.

The internal electric circuit features a Wheatstone bridge. An additional resistor was added on the power supply side. The voltage drop V_T on this resistor is dependent on transducer sensor temperature only. The relation between pressure p and voltage output of the transducer V_p is linear at constant temperature T; a second order polynomial relates both the slope m and intercept q of the linear $p = mV_p + q$ relation to the voltage drop on the additional resistance V_T, as experimentally verified. Thus, the behavior of the pressure transducer is represented by the surface

$$p = f\left(V_p, V_T\right) = \underbrace{\left(a + bV_T + cV_T^2\right)}_{m} V_p + \underbrace{\left(d + eV_T + fV_T^2\right)}_{q}, \qquad (5.1)$$

where a, b, c, d, e, and f are the coefficients of the polynomial defining the surface.

For each pressure transducer, 21 $p - V_p$ points were taken at 5 different temperatures spanning from 20 °C to 260 °C for a total of 105 $p - V_p - V_T$ points with both increasing and decreasing pressure ramps to account for possible hysteresis. These data were fitted with a least squares algorithm and, since all 3 input variables are affected by uncertainty, a Monte Carlo simulation is carried out to estimate the uncertainty $u_{p,new}$ related to a future pressure measurement p_{new} with $V_{p,new}$ and $V_{T,new}$ as inputs. Details about this procedure can be found in Cammi [15].

Pressure transducers are wall mounted and calibrated both in pressure and temperature.

The coefficient d may drift in time. The calibration surface shape remains the same, but it may vertically shift due to environmental conditions. To account for this effect, before each test run an online zero procedure is carried out. An auxiliary 1.75 bar full scale transducer (called O175) is used. It is connected to the plenum through a system of valves and it is sufficiently far away from it to be always at ambient temperature. Thus, this transducer is calibrated at ambient temperature only. Before each test run, the auxiliary 1.75 bar full scale transducer is put in communication with the ambient, whose pressure is measured using a high accuracy barometer, and the zero of O175 transducer calibration curve (also prone to change in time) is computed. Then, the auxiliary 1.75 bar full scale transducer is connected with the plenum and test section. Here, pressure normally ranges from 10 mbar to 200 mbar and O175 is now used as a reference to calculate the zero of all other transducers.

Summing up, since it is not possible to put all transducers at ambient pressure to calculate their zero from direct comparison with the barometer, the zero of transducer O175 is first computed using the barometer and it is then used as a reference for computing the zero of all other transducers. Of course, the use of the barometer and O175 auxiliary transducers introduce further uncertainty contributions, which are added to the final pressure uncertainty of each sensor.

Finally, the batch nature of the TROVA implies that pressure transducers work near their full scale at test start and well below it towards test conclusion. Therefore, transducers need to have very high accuracy, to maintain a low uncertainty also near their zero.

5.4.3 *Schlieren technique and Mach number measurement*

The schlieren technique is employed for identifying flow structures, to better understand pressure signals in time, and for local Mach number measurement. Indeed this technique exploits refractive index gradients induced by density variations in space to visualize the density gradient field. Image processing algorithms may be applied to detect flow structures related to sharp density variations and calculate flow quantities. These include Mach waves, compressing shocks or expansion fan edges. This technique was applied in the TROVA to analyze both Mach number in nozzle flows (results are briefly reported in Chapter 6 and are extensively discussed in Cammi [15] and Spinelli et al. [78]) and oblique shockwaves around a diamond shaped airfoil (Zocca et al. [98]).

5.4.3.1 *Schlieren imaging in non-ideal flows*

This subsection briefly introduces the schlieren technique and issues related to its application to non-ideal flows.

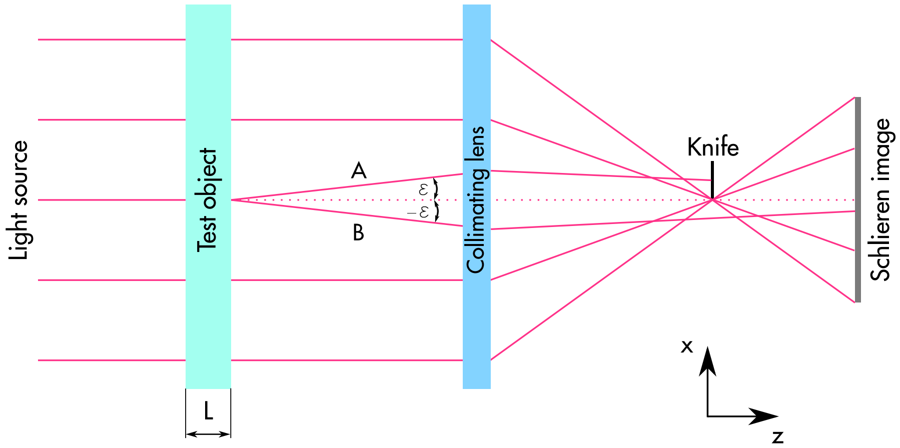

Figure 5.6: Schematic of the principle underlying schlieren imaging: the middle ray is deflected due to a density gradient. If the density gradient causes a positive deflection (A), the ray is blocked by the knife edge and the schlieren image shows a dark region. Instead, if the ray is deflected in the other direction (B), it is not blocked by the knife edge, and it reaches the image plane, making the image brighter.

The Gladstone-Dale relation (Gladstone and Dale [44])

$$n = 1 + k\rho \tag{5.2}$$

relates density ρ and refractive index n of a transparent media, through the Gladstone-Dale constant k. The schlieren technique exploits the behavior described by Equation 5.2: if the derivative along a direction x

$$\frac{\partial n}{\partial x} = k\frac{\partial \rho}{\partial x} \tag{5.3}$$

is taken, a space variation of density is related to a space variation of refractive index. It can be proven that a light ray crossing a region where a refractive index gradient in x direction is present experiences an angular deviation

$$\epsilon \approx \frac{L}{n_0}\frac{dn}{dx} \tag{5.4}$$

about its original path, where L is the depth of the perturbed region and n_0 is the refractive index at the location where the ray enters that region.

In the schlieren technique, a light source is used to illuminate the flow to be analyzed: light rays pass through the test object and a resulting image is formed on a recording plane (see Figure 5.6). Light rays deviated in one direction can be selectively blocked by the interposition of a so-called knife edge (ray A), while light rays deflected in the other direction are left undisturbed (B). Thus, the schlieren image shows dark regions in correspondence of density gradients that cause rays to be blocked by the knife and bright regions for opposite gradients.

In the TROVA, the schlieren technique is implemented in a double passage configuration: the light source and the image plane (i.e. the camera sensor) are placed on the same side of the test section. This is accomplished by mirror polishing the nozzle rear plate. This configuration was chosen to permit an easy arrangement of pressure taps and nozzle profiles. Further, all optical components can be placed on the same bench, simplifying alignment operations.

The application of schlieren to non-ideal compressible flows of organic vapor presents some issues. This topic is thoroughly treated in Cammi [15] and Conti et al. [27].

The main issue is related to flow structures exhibiting markedly high density gradient. Such structures may appear dark, even if they should be seen as bright. This was observed in several tests, where both shockwaves and expansion fans appeared dark. The system was set up for imaging compressions as dark regions and expansions as bright ones. Thus, a measurement range issue was clearly present.

If tests are carried out, on the same nozzle, with air (as opposed to an organic vapor), this issue is not observed. If an organic fluid is used, the intensity of this phenomenon decreases as ideal thermodynamic conditions are approached. It can be proven that

$$\frac{\partial n}{\partial x} = \frac{k \cdot p_T}{c^2} \cdot \frac{\partial \left(\frac{p}{p_T}\right)}{\partial x}, \tag{5.5}$$

where c is the speed of sound.

If two flows of MDM in the same nozzle at the same total conditions, one modeled with a real-gas model (such as the improved Peng Robinson Stryjek-Vera – iPRSV – by Stelt, Nannan, and Colonna [80]) and the second one with the polytropic ideal gas model (PIG), are compared, the influence of real-gas effects on the refractive index gradient can be outlined. Indeed, these two cases feature the same total pressure p_T and the same Gladstone-Dale coefficient k (the fluid is the same for both cases). The effect of the pressure ratio gradient turns out to be small, since pressure ratio changes due to non-idealities are contained. On the other side, real gas effects play a relevant role on the speed of sound, whose variation is responsible for appreciable deviations of refractive index gradient.

Instead, if several non-ideal vapor flows at different total conditions as those experienced in the TROVA are considered, the total pressure p_T becomes the main parameter governing $\partial n / \partial x$.

Finally, if flows of siloxane MDM, modeled as PIG, and air in the same nozzle at the same total pressure p_T are compared, the Gladstone-Dale constant and flow compressibility are the predominant parameters affecting the refractive index gradient. Indeed, pressure ratio derivative $\partial \left(p/p_T\right) / \partial x$ profiles result to be very similar between the two cases. The Gladstone-Dale constant k for MDM is almost double the air one, having a direct impact on the refractivity index gradient. The molar mass of MDM is about eight times higher than the air one leading to a consequently lower speed of sound, that contributes in yielding a higher $\partial n/\partial x$.

Summing up, the higher refractivity index gradients at same total pressure obtained with MDM than with air are mainly due to the higher Gladstone-Dale constant k and the higher molar mass (thus lower c). Comparing expansions of MDM happening in the TROVA and different total conditions, it turns out that higher values of $\partial n/\partial x$ are encountered in the non-ideal case, due to the higher total pressure p_T.

Measuring range issues arise due to the high Gladstone-Dale constant and low speed of sound of the organic fluid and worsen at high total pressure.

In conclusion, light rays that pass through regions of significant density gradients undergo higher deflection in the organic fluid case with respect to air, due to the higher refractivity index gradient. This causes the possibility of rays being lost by the optical system or being blocked by optical components frames. Thus, the schlieren image can show dark regions corresponding both to expansions or compressions. This issue makes performing schlieren imaging in non-ideal compressible flows not straightforward.

5.4.3.2 *Direct Mach number measurement*

Each time a small perturbation is induced in a supersonic flow, it propagates along the so-called Mach waves, whose angle α with respect to flow velocity is related to the local Mach number M by

$$M = \frac{1}{\sin\alpha}. \tag{5.6}$$

In a nozzle flow, those perturbations may be triggered by nozzle profile surface roughness. Indeed, peaks and valleys at the wall can be seen as infinitely small wall angle variations, triggering infinitely weak compression and expansion waves (Mach waves).

Mach number is measured by estimating the angle of mach lines visible in the schlieren image.

The schlieren technique can be exploited to visualize those lines. Images can then be processed by an automatic algorithm to associate a position and angle α with respect to the flow to each detectable Mach line. This procedure can be carried out at the nozzle axis, where the local flow velocity direction is known due to symmetry.

Cammi [15] presented a technique for identifying straight lines parameters, that was applied for Mach lines, shockwaves and expansion fan edges recognition. This algorithm simplifies line detection: indeed, Mach lines appear as gray scale lines with dull edges, where more than one line, with different position and angle, can be inscribed. The schlieren image is first cut into sub-portions and contrast is enhanced: as previously stated, lines are characterized by faded edges, that must be sharpened for a better processing. Then, the image is made black and white and the Hough transform is carried out to find set of probable lines lying in the black region corresponding to the Mach line.

Among these lines, the best one is chosen as the line lying in the middle of the black pixel band that crosses the maximum number of black pixels. Finally, the uncertainty on line angle α is computed, accounting for the discrete nature of the acquired image (the pixel of the image defines smallest resolvable dimension). Finally the uncertainty on Mach number is computed using the Taylor series method (Coleman and Steele [20])

5.4.4 *Direct velocity measurement*

Differently from perfect gas case, in non-ideal flows directional probes require a calibration procedure which is both fluid-specific and thermodynamic condition-specific. As an alternative, numerical calibration procedures can be adopted. Such techniques are under development, but not yet available if a high degree of accuracy is required.

In the field of non-ideal compressible flows the above considerations raised the interest towards measurement methods which do not require calibration, and specifically towards optical techniques laser Doppler velocimetry (LDV) and particle image velocimetry (PIV). Both PIV and LDV techniques guarantee the direct measurement of the flow velocity, providing that the flow is properly inseminated, namely that the velocity slip between the fluid and the tracking particles is considerably small. The flow seeding is particularly critical due to the need of introduce particles in a high temperature, high pressure and potentially condensing flow. Also, fluid contamination must be avoided. Solid particles chemically compatible and non-miscible in the working fluid are the only option to be considered, due to the high temperature they need to withstand to, without significant modification of their dimension and density.

No experimental studies about direct velocity measurements in high speed non-ideal flows were found in literature up to date. Head et al. [46] and Valori et al. [90] applied PIV to unconventional vapor flows; however, analyzed condition were either high temperature and low pressure or low temperature and high pressure. Further, both studies deal with natural convection, thus very low velocity. Flows to be studied in the TROVA feature, *at the same time*, high temperature, high pressure and high velocity, thus making LDV (or PIV) not straightforward.

LDV in non-ideal flows is not straightforward.

Though a punctual technique, LDV features, with respect to PIV, an easier implementation (the laser emitter and the receiver may be placed in the same device) and a higher attainable spatial and temporal resolution. For these reasons, LDV technique was selected for implementation in the TROVA.

A specifically conceived seeding system was designed. A liquid suspension of the tracer particle in the fluid to be tested is injected at high temperature and high pressure in the flow in a plenum ahead of the test section. Due to the high temperature, the liquid fraction evaporates and solid particles trace the flow.

The LDV technique, the seeding system designed for high temperature and pressure flows, its implementation in the TROVA, and the first direct velocity measurement in non-ideal flows are thoroughly discussed in Chapter 7.

6

LIMITS IN FIRST EXPERIMENTAL OBSERVATIONS OF NON-IDEAL FLOWS

The very first experimental campaign for the detailed study of non-ideal fluid-dynamics was carried out in the TROVA using siloxane MDM as working fluid (Spinelli et al. [78]). The purpose of this campaign was to observe for the first time ever the behavior of a nozzle flow in the dense gas region. For their relative simplicity of implementation, with respect to velocity measurement, only pressure and temperature measurements together with schlieren visualizations were carried out. However, though this does not permit a complete characterization of the flow field, these measurements are sufficient to observe some peculiar features different from the behavior of ideal gases. Indeed, both static-to-total pressure ratio p/p_T and Mach number M are expected to be dependent on total conditions $p_T - T_T$ for a given nozzle geometry, differently from the case of ideal gases, where total conditions do not have an impact (see Section 1.1.1).

This chapter presents and discusses the results of the aforementioned experimental activity. Section 6.1 reports the description of a typical test evolution and of the data extraction procedure. Test conditions and a description of the employed nozzles is reported in Section 6.2. Section 6.4 presents the experimental results and a detailed discussion. Finally, conclusions of the experimental campaign are drawn in Section 6.5.

6.1 TEST DESCRIPTION

As depicted in Section 5.3, the TROVA operates discontinuously, thus, for each performed test, physical quantities evolve in time. Before a test run, the HPV is at a pressure and temperature necessary to obtain the desired total pressure p_T and total temperature T_T in the plenum. The LPV and and test section are evacuated down to a pressure close to the saturation pressure at the temperature of the LPV. When the operator starts the test, the computer in charge for the test rig control sends a signal for the opening of valve V3 (the ball valve isolating the HPV from the plenum, see Figure 5.2) and triggers schlieren images acquisition. After the complete opening of V3, the main control valve (MCV) opens, letting the high pressure and high temperature fluid contained in the HPV to flow through the plenum and the test section. After the opening transient of the MCV, the maximum pressure and most non-ideal conditions (minimum total compressibility factor $Z_T(p_T, T_T)$) are reached in the plenum.

For current tests, the MCV is left 100% opened, thus no pressure regulation is performed. This is done to explore a wide thermodynamic region from highly non-ideal to almost ideal conditions. Indeed, without operating on the MCV, at test start the total pressure reached in the plenum is the closest to the HPV one. Operating the MCV would result in a constant pressure for a lapse of time and in a longer test time, but in a lower maximum test pressure, for the same one in the HPV. Being the thermodynamic transformation carried out by the MCV at constant enthalpy, a throttling means going further from the saturation curve, thus towards ideal conditions, with respect to the case with totally open MCV and for the same pressure and temperature in the HPV. Cocluding, if the main control valve is left fully open, total pressure (and static pressure along the nozzle as well) constantly decrease, as a result of HPV emptying.

At the same time the LPV is filled, thus increasing its pressure. Due to the pressure ratio β between the plenum and nozzle outlet (whose pressure is similar to the LPV one), at test start (and for the majority of test time) the nozzle operates in under expanded conditions. The pressure ratio β decreases over time, due to the transfer of fluid from HPV to LPV. Thus the flow becomes adapted, under expanded and eventually shockwaves enter in the nozzle diverging portion, until the flow becomes fully subsonic. The presence of shockwaves is detected both through an almost sudden increase in pressure signals along the nozzle axis and through schlieren imaging. In this case the flow is no longer isentropic, therefore only states without shocks entering the nozzle are considered in this analysis.

Total temperature T_T does not necessarily feature a monotone trend. Indeed, it is influenced both by stratification in the HPV and the presence of pipes which can be heated to a temperature slightly different from the incoming fluid.

Due to the quasi-steady state nature of the flow at each instant of time, properties along the nozzle axis are obtained.

The nozzle characteristic time is more than two orders of magnitude lower than the HPV emptying process one, thus the flow can be considered in a quasi-steady state for each time instant. Therefore, it is possible to switch from a representation of total and static pressure over time (Figure 6.1 - top) to profiles along the nozzle axis extracted at different time instants (Figure 6.1 - center). Each of these profiles corresponds to a different total compressibility factor Z_T (therefore degree of non-ideality), as is depicted in Figure 6.1 - bottom. From this chart is clear how the blowdown nature of the facility permits the exploration of a wide thermodynamic region within one single test run with limited effort, having compressibility factor ranging from strong non-ideal states to almost ideal ones. Test evolution is similar for each run and will not be discussed in detail for each test.

Measurements obtained along the nozzle axis are used to compute meaningful quantities. In particular, total to static pressure ratios p/p_T and Mach number will be discussed.

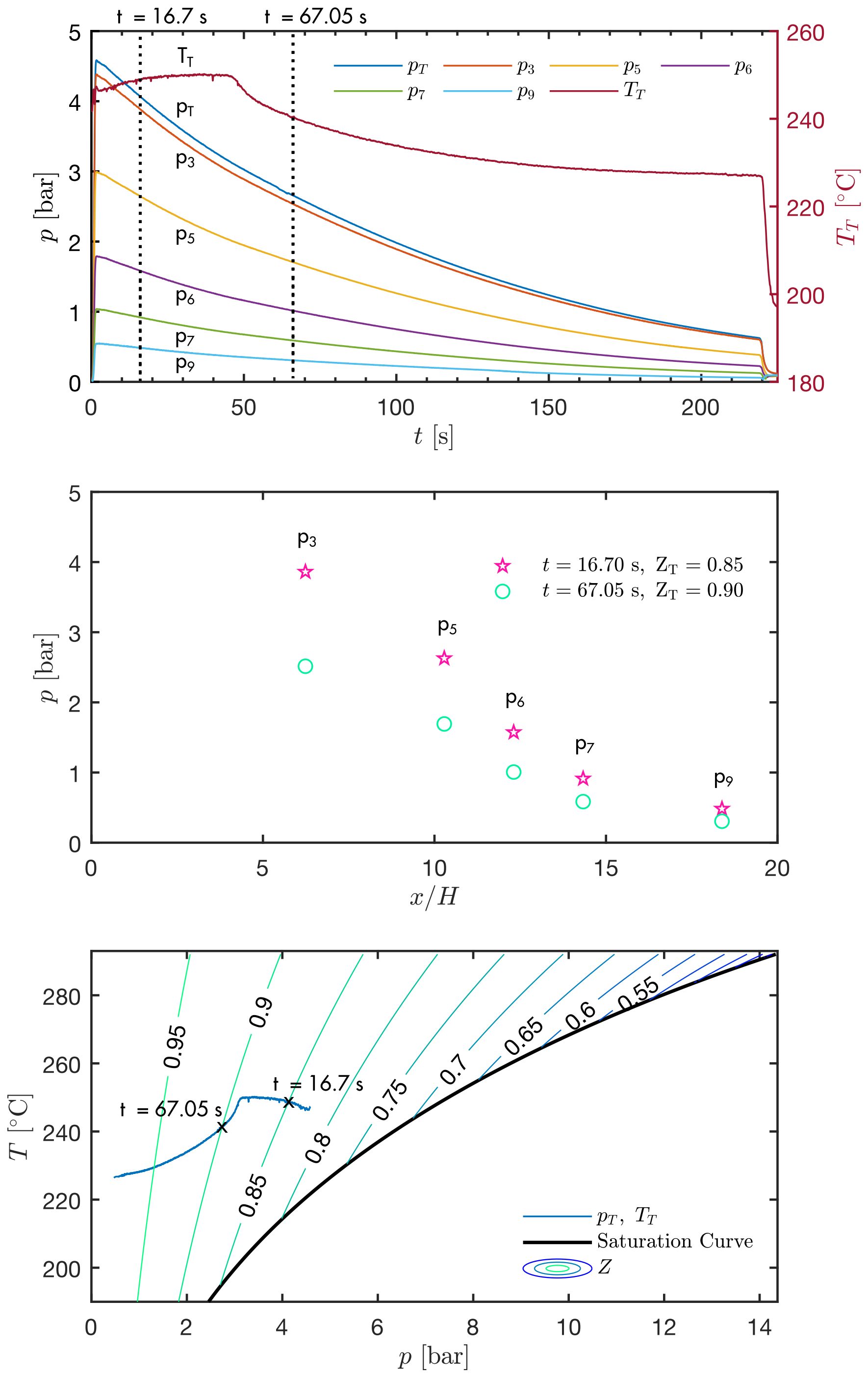

Figure 6.1: Extraction of experimental measurements along the nozzle axis for a quasi-steady state expansion. Top: total and static pressure $p_T - p$ and total temperature T_T measurements over time during a test run. Pressure p_3 to p_9 correspond to different pressure taps along the nozzle axis (see Figure 6.2). Center: by selecting data at different time instants, pressure profiles along the nozzle axis are obtained. x/H is the non dimensional axial coordinate, where H is the throat semi-height. Bottom: time evolution of nozzle total conditions in the pressure p – temperature T plane. The expansions selected at different time instants correspond to different degrees of non-ideality, respresented in terms of total compressibility factor $Z_T(p_T, T_T)$.

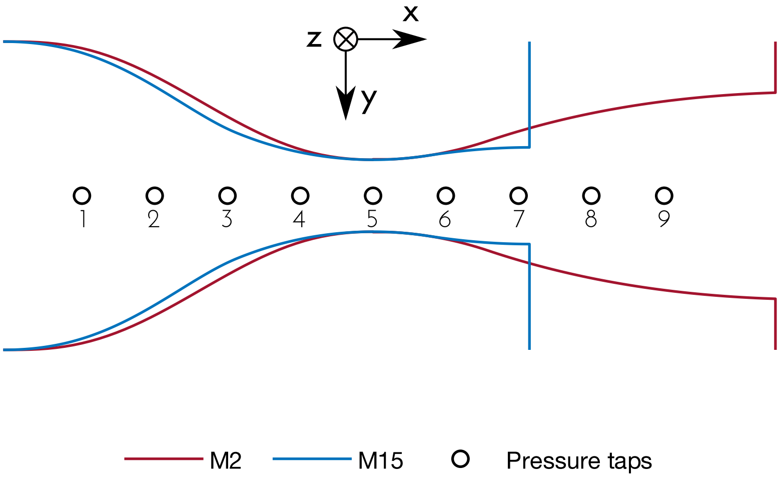

Figure 6.2: Tested nozzles. M2 is designed to achieve an exit Mach number $M = 2.0$, while M15 is designed for $M = 1.5$. Circles indicate the position of pressure taps along the nozzle axis.

6.2 EMPLOYED NOZZLES

Two nozzles were designed to achieve Mach number $M = 2$ *and* $M = 1.5$.

Several tests were carried out exploring various thermodynamic regions, employing two different nozzles, labeled M2 and M15. Their geometry was designed to achieve a uniform Mach number at nozzle outlet of $M = 2$ and $M = 1.5$ respectively, with siloxane MDM and for a predefined total thermodynamic condition.

The diverging portion of the nozzle was designed using the method of characteristics implemented with state-of-the art thermodynamic models able to capture the non-ideal behavior of the flow (Guardone, Spinelli, and Dossena [45]). A first portion of the diverging section is a circular arc, that provides an expansion to the desired outlet pressure value. Downstream, the flow is than treated to obtain a uniform profile at the outlet in the so-called turning region, designed imposing mass conservation. A 5^{th} order polynomial was used for the profile of the converging part. The two portions of nozzle profiles are connected by imposing the same first and second derivative at the nozzle throat.

Due to the batch nature of the TROVA each nozzle works most of the time in off-design conditions, meaning that the flow along the nozzle axis and the achieved exit Mach number may differ from the design case and that the flow may be not uniform at the outlet.

6.2.1 *Nozzle M2*

Nozzle M2 was designed for a uniform Mach number $M = 2$ at nozzle outlet, with siloxane MDM at total conditions $p_T = 4\,\mathrm{bar}$ and $T_T = 253\,°\mathrm{C}$. The throat semi-height is $H = 8.4\,\mathrm{mm}$ and features a non-dimensional radius of curvature of the wall profile of $r_t/H = 10$. A backward facing step is machined at the geometrical throat, with an

Table 6.1: Characteristics of nozzles designed for MDM tests. The nozzle name, design fluid, outlet Mach number, total conditions $p_T - T_T$, the nondimensional throat curvature r_t/H, the throat semiheight H and the recessed step height h, if present, are reported.

Nozzle id	Fluid	M_{des}	p_T [bar]	T_T [°C]	r_t/H	H [mm]	h [mm]
M2	MDM	2.0	4	253	10	8.4	0.1
M15	MDM	1.5	10	277	10	8.4	-

height h of 0.1 mm, corresponding to 1.2% of the throat semi-height H. It was originally machined to fix the position of the throat. Indeed, with a smooth profile, the presence of the boundary layer can slightly move the throat from its geometrical position. Key design parameters of nozzle M2 are reported in Table 6.1, while a sketch is reported in Figure 6.2. The $x - y - z$ coordinate system shown in figure is adopted and will be used throughout the thesis.

6.2.2 *Nozzle M15*

Nozzle M15 was designed to deliver a flow at uniform Mach number $M = 1.5$ at its outlet. Design total temperature and pressure are $p_T = 10\,\text{bar}$ and $T_T = 277\,°\text{C}$. The throat semi-height and nondimensional radius of curvature are the same of nozzle M2 ($H = 8.4\,\text{mm}$ and $r_t/H = 10$). This nozzle does not feature any step at the geometrical throat. However, the surface roughness is increased to $Ra \approx 0.6\,\mu\text{m}$ to promote the formation of the weak waves necessary for Mach number measurement by means of schlieren imaging. A sketch of the M15 nozzle, compared to the M2 one is reported in Figure 6.2. Having the same throat semi-height H and the same relative throat curvature r_t/H but a lower design discharge Mach, nozzle M15 is shorter than M2, thus permitting the visualization of the discharge region also.

6.3 TEST CONDITIONS

The main purpose of the experimental campaign being presented here is to highlight the behavior of a vapor flow in the non-ideal regime. Siloxane MDM is the working fluid chosen for this series of experiments, due to its wide use in high temperature ORCs. Moreover, it features a sufficiently wide thermodynamic region where it exhibits a strong non-ideal behavior.

Table 6.2 reports the total conditions of the tests selected for discussion. Including both M2 and M15 tests, a total of 19 runs was carried out, of which 9 gave satisfactory results and are reported

Table 6.2: Total conditions in the most non-ideal state and in the most ideal one of tests carried out with siloxane MDM and nozzles M2 and M15. Only 9 satisfactory tests out of 19 performed are reported.

Test id	Nozzle	Min. Z_T condition p_T [bar]	T_T [°C]	Z_T [-]	Max. Z_T condition p_T [bar]	T_T [°C]	Z_T [-]
MDM04	M2	4.59	247	0.828	0.796	228	0.970
MDM06	M2	4.636	242	0.817	0.090	228	0.997
MDM08	M2	4.425	233	0.811	0.150	229	0.995
MDM10	M2	9.020	269	0.652	0.797	265	0.977
MDM11	M15	9.199	268	0.634	0.837	264	0.976
MDM13	M15	4.586	239	0.814	0.522	230	0.981
MDM14	M15	8.765	272	0.682	0.197	264	0.994
MDM16	M15	10.027	271	0.592	0.155	262	0.996
MDM17	M15	9.878	272	0.611	0.506	264	0.986

here. For each nozzle, a set of tests at moderate non-ideal conditions (test minimum total compressibility factor $Z_T \approx 0.81 \div 0.83$) and at strong non-ideal conditions (test minimum total compressibility factor $Z_T \approx 0.59 \div 0.68$) were carried out. Particular attention was paid to the maximum temperature of the test, which is below 275 °C for thermal stability reasons (see Chapter 4).

During an experimental run a large thermodynamic region is explored until almost ideal gas conditions, with $Z_T \approx 1$. Achieving the same exact state during a test run is not straightforward. Indeed, test conditions are set in the HPV and not in the plenum, where total conditions $p_T - T_T$ are measured. Depending on the mass of fluid loaded in the HPV (which is loaded with a certain tolerance, see Chapter 5), on the stratification inside the vessel and on the transient process occurring at test start, a slightly different set of total conditions is obtained during a test (Spinelli [76] and Spinelli et al. [77]). Unfortunately, unlike ideal gases, the flow depends on total conditions occurring at each time instant. Thus a perfect test repeatability is not easy to be achieved. However, extended portions of test runs share compatible total conditions, with $p_T - T_T$ points lying within uncertainty bars. For these intervals of data, repeatability and consistency of experimental data were evaluated and proved to be satisfactory.

Table 6.3: MDM nozzle expansions.

Test id	Expansion id	Nozzle	p_T [bar]	T_T [°C]	Z_T [-]
MDM10	M2.MDM.1a	M2	9.024	269	0.650
MDM10	M2.MDM.2a	M2	6.270	276	0.800
MDM10	M2.MDM.3a	M2	0.797	265	0.976
MDM04	M2.MDM.1b	M2	4.578	247	0.823
MDM04	M2.MDM.2b	M2	2.636	240	0.900
MDM04	M2.MDM.3b	M2	0.797	228	0.969
MDM11	M15.MDM.1a	M15	9.199	268	0.633
MDM11	M15.MDM.2a	M15	6.240	275	0.800
MDM11	M15.MDM.3a	M15	0.837	264	0.975
MDM13	M15.MDM.1b	M15	4.586	239	0.811
MDM13	M15.MDM.2b	M15	2.691	243	0.900
MDM13	M15.MDM.3b	M15	0.522	230	0.980
MDM11	M15.MDM.1a*	M15	9.044	269	0.652

6.4 EXPERIMENTAL RESULTS

6.4.1 *Explored region*

Two representative tests at moderate and strong non-ideal conditions were selected for both nozzle M2 and M15. They are MDM10 and MDM04 for nozzle M2 and MDM11 and MDM13 for nozzle M15. Three representative quasi-steady expansions were extracted from each test for discussion. They are selected based on different levels of non-ideality, represented by the total compressibility factor Z_T, spanning from the most non-ideal state of the test run to the most ideal one, passing through an intermediate level. Table 6.3 reports the expansions selected for discussion, along with their total conditions. The chosen nomenclature for expansions is [nozzle name].[fluid].[progressive id], where the letter in the id identifies different tests. Expansion labeled as M15.MDM.1a* occurred at the most non-ideal condition encountered in nozzle M15 tests where acceptable quality schlieren images were available for Mach number measurement and will be discussed in Section 6.4.3.

A temperature T - specific entropy s and a temperature T - pressure p diagram showing the selected expansions are reported in Figure 6.3 and Figure 6.4 for M2 and M15 nozzle respectively. Each expansion can be regarded to be isentropic at the axis, if no shockwaves are entering the diverging portion of the nozzle. Indeed, dissipation phenomena can be considered confined in the boundary layer at Reynolds number characteristic of such flows. The first point of each expansion (labeled A), at the highest temperature and pressure, represents the total conditions $p_T - T_T$, which are measured in the plenum. The ending point (labeled B), at lower pressure and temperature, represents the thermodynamic state corresponding to the static pressure p measured at the last available pressure tap, obtained through an isentropic expansion from the total state. Expansions extracted from test MDM04 (thus M2.MDM.1b-2b-3b), result to be lying almost on the same isentrope. This is not something imposed, but it is due to the total temperature variation, which resulted to be higher in this test with respect to others.

6.4.2 *Pressure measurements*

The measured pressure profile is here analyzed for expansions at different total conditions to highlight the effect of non-ideality on flow quantities. Figure 6.5 - top and Figure 6.6 - top show the static-to-total pressure ratio p/p_T distribution along the nozzle axis for expansions M2.MDM.1a-2a-3a and M2.MDM.1b-2b-3b. As a reference, pressure ratios p/p_T relative to a test performed with Nitrogen on the same nozzle are also plotted. As it can be seen, going from M2.MDM.1a to M2.MDM.3a and from M2.MDM.1b to M2.MDM.3b the pressure ratio decreases. This is clearly a non-ideal effect: indeed, for ideal gases, the static-to-total pressure ratio does not depend on total conditions.

The percentage variation between the three expansions M2.MDM.1a to M2.MDM.3a and between M2.MDM.1b to M2.MDM.3b is represented in Figure 6.5 - bottom and Figure 6.6 - bottom respectively, to highlight differences in p/p_T occurring between the most non-ideal expansion and the most ideal one of each test. Deviations are evaluated in terms of

$$d_{r\%}\left(\frac{p}{p_T}\right) = \frac{\left(\frac{p}{p_T}\right)_{Z_{T,min}} - \left(\frac{p}{p_T}\right)_{Z_{T,max}}}{\left(\frac{p}{p_T}\right)_{Z_{T,max}}} \cdot 100, \tag{6.1}$$

where here the expansions at maximum and minimum total compressibility factor Z_T are M2.MDM.3a-b and M2.MDM.1a-b respectively. The 95% confidence index uncertainty bar was computed, using the Taylor series method, as

$$u_{d_{r\%}}\left(\frac{p}{p_T}\right) = \frac{100}{\left(\frac{p}{p_T}\right)_{Z_{T,max}}} \cdot \\ \cdot \sqrt{\left(u\left(\frac{p}{p_T}\right)_{Z_{T,min}}\right)^2 + \left(\frac{\left(\frac{p}{p_T}\right)_{Z_{T,min}}}{\left(\frac{p}{p_T}\right)_{Z_{T,max}}}\right)^2 \cdot \left(u\left(\frac{p}{p_T}\right)_{Z_{T,max}}\right)^2}, \tag{6.2}$$

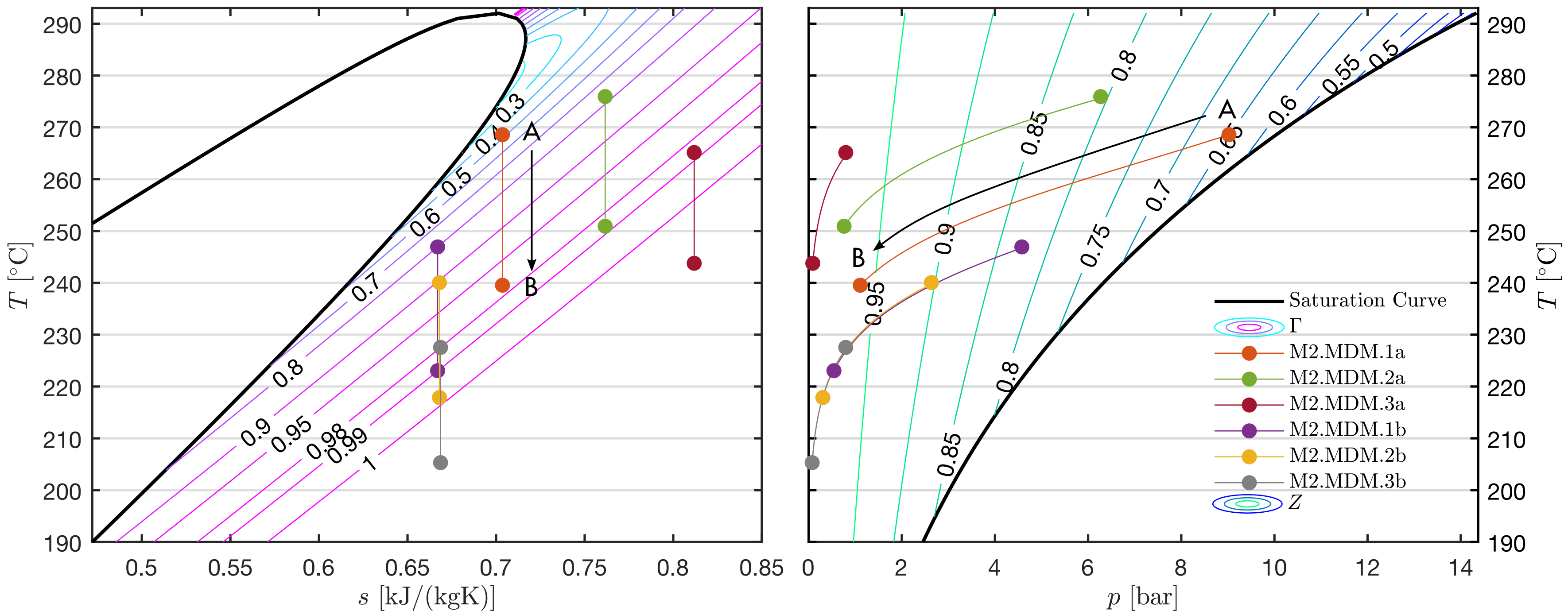

Figure 6.3: Explored thermodynamic region during tests MDM10 and MDM04 with nozzle M2. The chart reports the expansions selected for discussion (see Table 6.3) in a temperature T - specific entropy s diagram (left) and a temperature T - pressure p diagram (right). Contours of fundamental derivative of gasdynamics Γ (left) and of compressibility factor Z (right) are reported along with the liquid-vapor saturation curve.

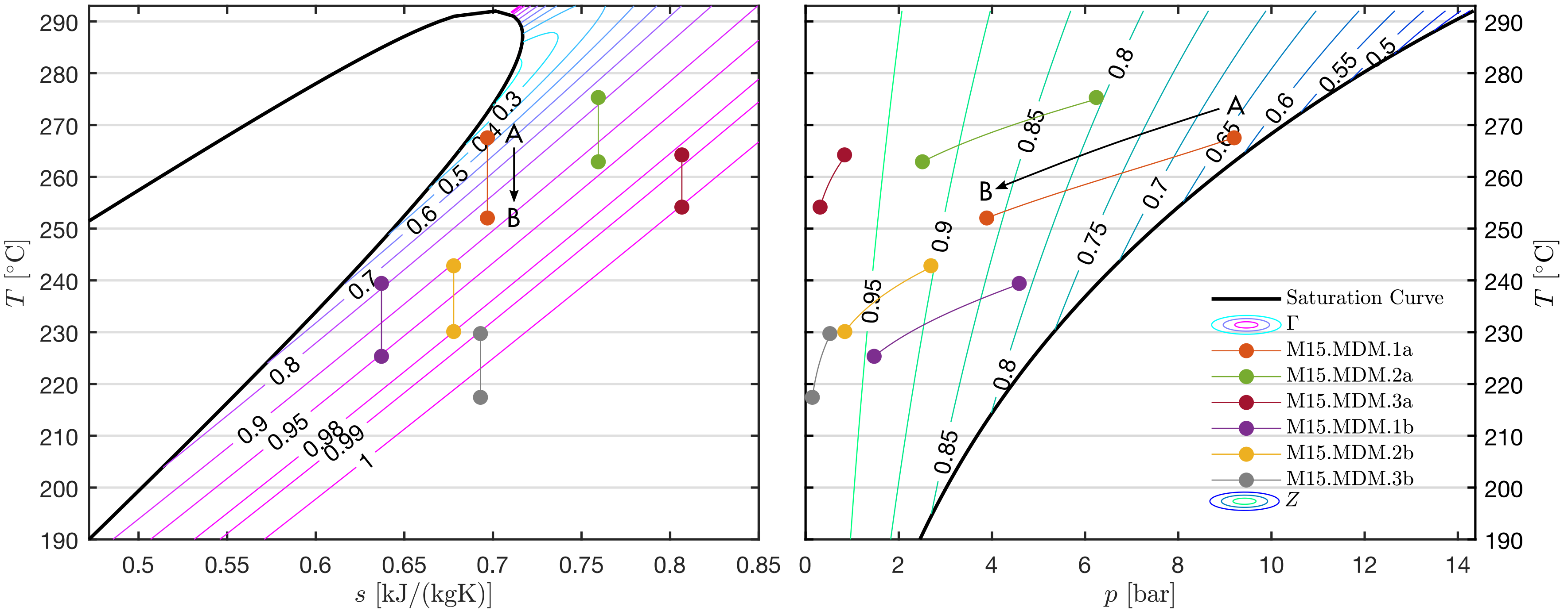

Figure 6.4: Explored thermodynamic region during tests MDM11 and MDM13 with nozzle M15. The chart reports the expansions selected for discussion (see Table 6.3) in a temperature T - specific entropy s diagram (left) and a temperature T - pressure p diagram (right). Contours of fundamental derivative of gasdynamics Γ (left) and of compressibility factor Z (right) are reported along with the liquid-vapor saturation curve.

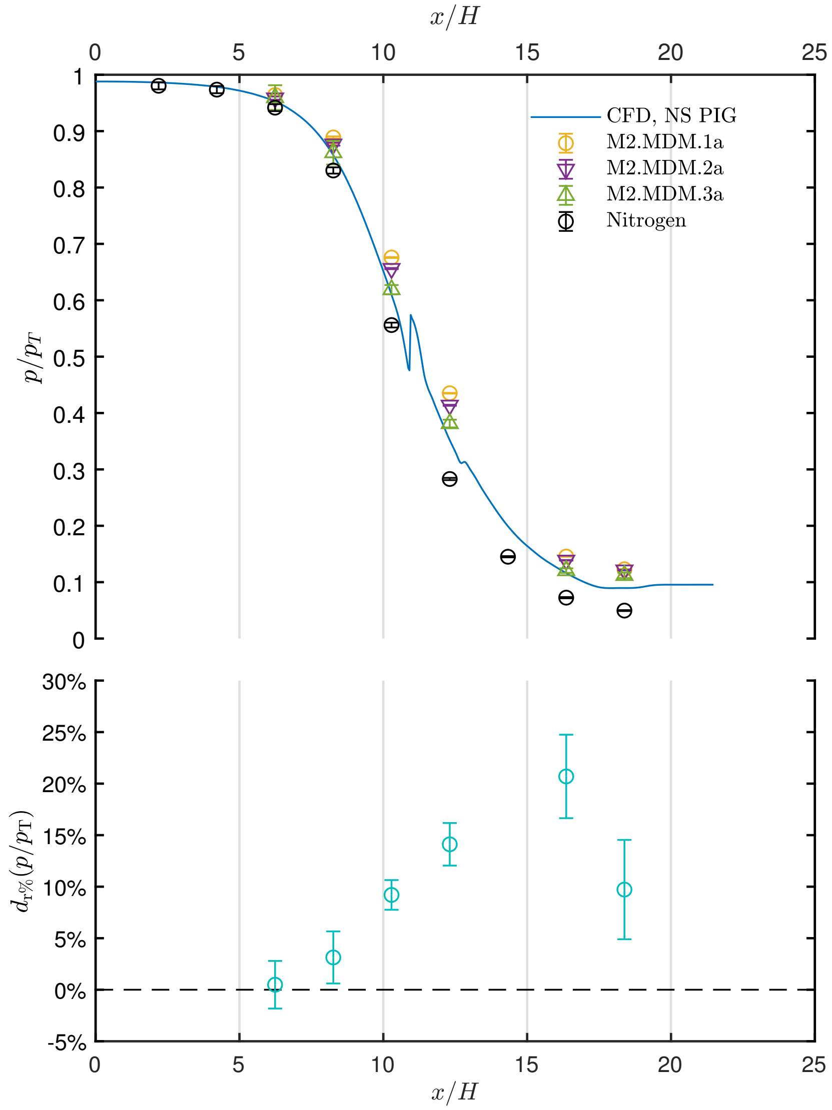

Figure 6.5: Top: Static-to-total pressure ratio p/p_T for expansions M2.MDM.1a-2a-3a (see Table 6.3) and for a test performed with nitrogen on the same nozzle along the nozzle axis. The result on the nozzle axis of a viscous CFD calculation with MDM modeled as polytropic ideal gas (PIG) is plotted. Bottom: relative percentage difference $d_{r\%}(p/p_T)$ between test M2.MDM.1a (minimum Z_T) and M2.MDM.3a (maximum Z_T). All reported uncertainty bars are 95% confidence level.

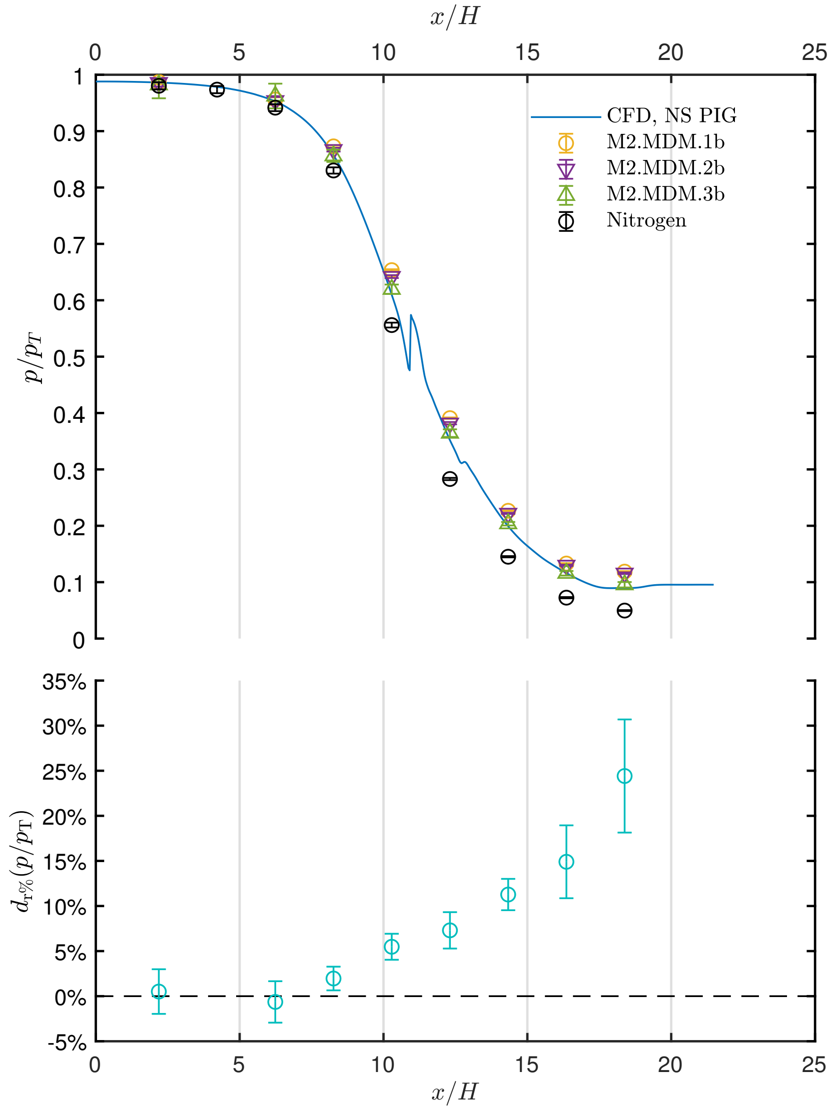

Figure 6.6: Top: Static-to-total pressure ratio p/p_T for expansions M2.MDM.1b-2b-3b (see Table 6.3) and for a test performed with nitrogen on the same nozzle along the nozzle axis. The result on the nozzle axis of a viscous CFD calculation with MDM modeled as polytropic ideal gas (PIG) is plotted. Bottom: relative percentage difference $d_{r\%}(p/p_T)$ between test M2.MDM.1b (minimum Z_T) and M2.MDM.3b (maximum Z_T). All reported uncertainty bars are 95% confidence level.

where

$$u\left(\frac{p}{p_T}\right) = \left(\frac{p}{p_T}\right) \cdot \sqrt{\frac{u_p^2}{p^2} + \frac{u_{p_T}^2}{p_T^2}}. \tag{6.3}$$

The percentage difference $d_{r\%}\left(\frac{p}{p_T}\right)$ increases along the nozzle axis, meaning that going from subsonic to supersonic, the deviation between p/p_T at minimum and maximum Z_T increases. This trend is not to be considered related to measurement uncertainty: indeed, the percentage difference combined expanded uncertainty does not comprise the 0% line, except for the first two active pressure taps in the converging portion. Two different effects take place here. In the converging portion of the nozzle, pressure transducers with the highest full scales, thus highest uncertainty, are employed, being the pressure similar to the plenum one. Further, in that region of the nozzle, pressure ratios are close to one and compressibility effects are limited. For these reasons, it is difficult to resolve deviations of p/p_T and the percentage difference uncertainty interval crosses zero. Uncertainties increase towards the nozzle outlet, where pressure is very low and the relative pressure transducer uncertainty increases. However, compressiblity effects increase along the diverging portion of the nozzle, thus deviations of p/p_T become appreciable.

Pressure ratios change as an effect of non-ideality.

The result of a viscous 2D CFD simulation extracted on the nozzle axis with MDM modeled as polytropic ideal gas (PIG) is reported as reference. The calculation was carried out with the open source SU2 code (Vitale et al. [91]) and the specific heats ratio was set to a mean value of $\gamma_{MDM} = 1.018$, obtained with the state-of-the-art Helmholtz energy equation of MDM by Thol et al. [83] for the thermodynamic region explored. The CFD pressure ratio profile features two bumps, one near the geometrical throat and the second downstream. These are due to the presence of the recessed step, which triggers a series of expansion fan/shockwave/expansion fan patterns and their reflections. Experimental p/p_T profiles at maximum Z_T (M2.MDM.3a and M2.MDM.3b) are in good accordance with CFD results.

The difference between nitrogen and M2.MDM.3a, which features $Z_T \approx 0.98$, is to be attributed to the different fluid molecular complexity rather than non-ideal effects. The considered expansions are both well represented by the ideal gas law and for increasing molecular complexity, the specific heats ratio $\gamma = c_p/c_v$ decreases ($\gamma_{N2} = 1.4$ and $\gamma_{MDM} = 1.018$). Thus, for the same geometry pressure ratios of MDM are higher than those of nitrogen.

Figure 6.7 and Figure 6.8 report the same kind of data for tests performed with the nozzle M15, except for Nitrogen experimental measurements. The CFD profile does not feature the same bump reported for nozzle M2, being M15 without recessed step. The same discussion holds also here and trends observed for M2 tests are confirmed.

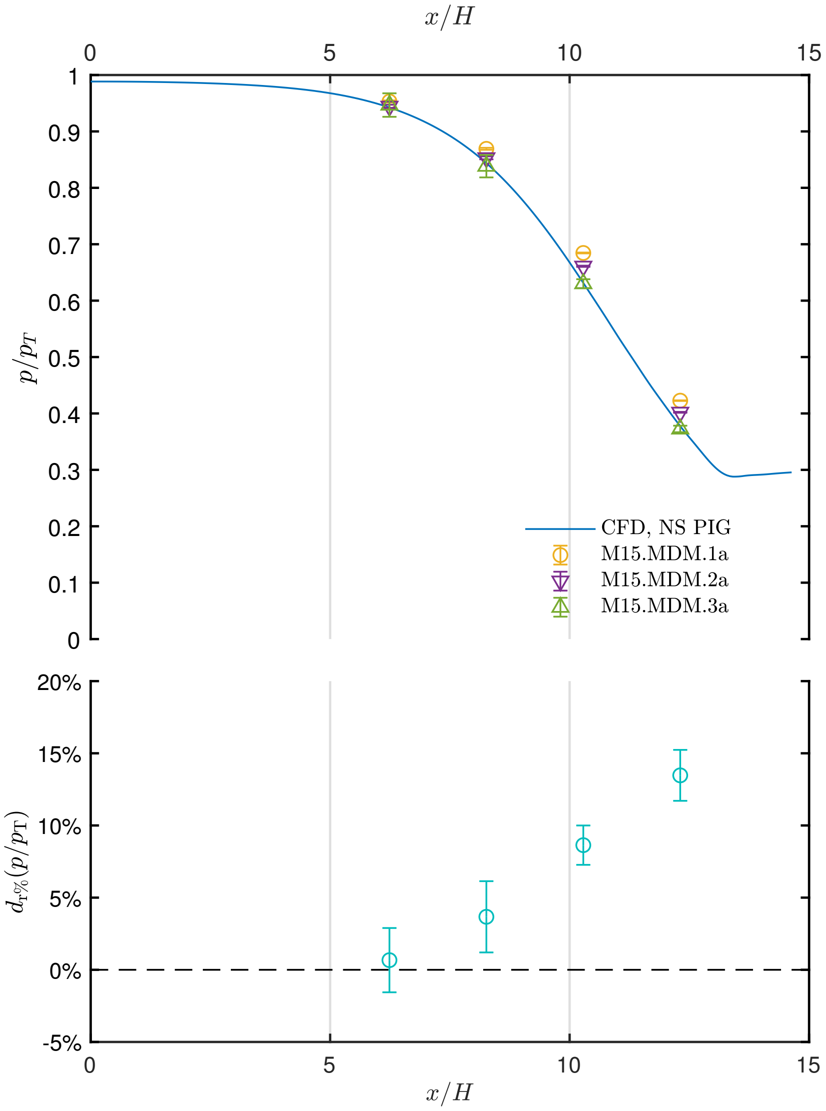

Figure 6.7: Top: Static-to-total pressure ratio p/p_T for expansions M15.MDM.1a-2a-3a (see Table 6.3). The result on the nozzle axis of a viscous CFD calculation with MDM modeled as polytropic ideal gas (PIG) is plotted. Bottom: relative percentage difference $d_{r\%}(p/p_T)$ between test M15.MDM.1a (minimum Z_T) and M15.MDM.3a (maximum Z_T). All reported uncertainty bars are 95% confidence level.

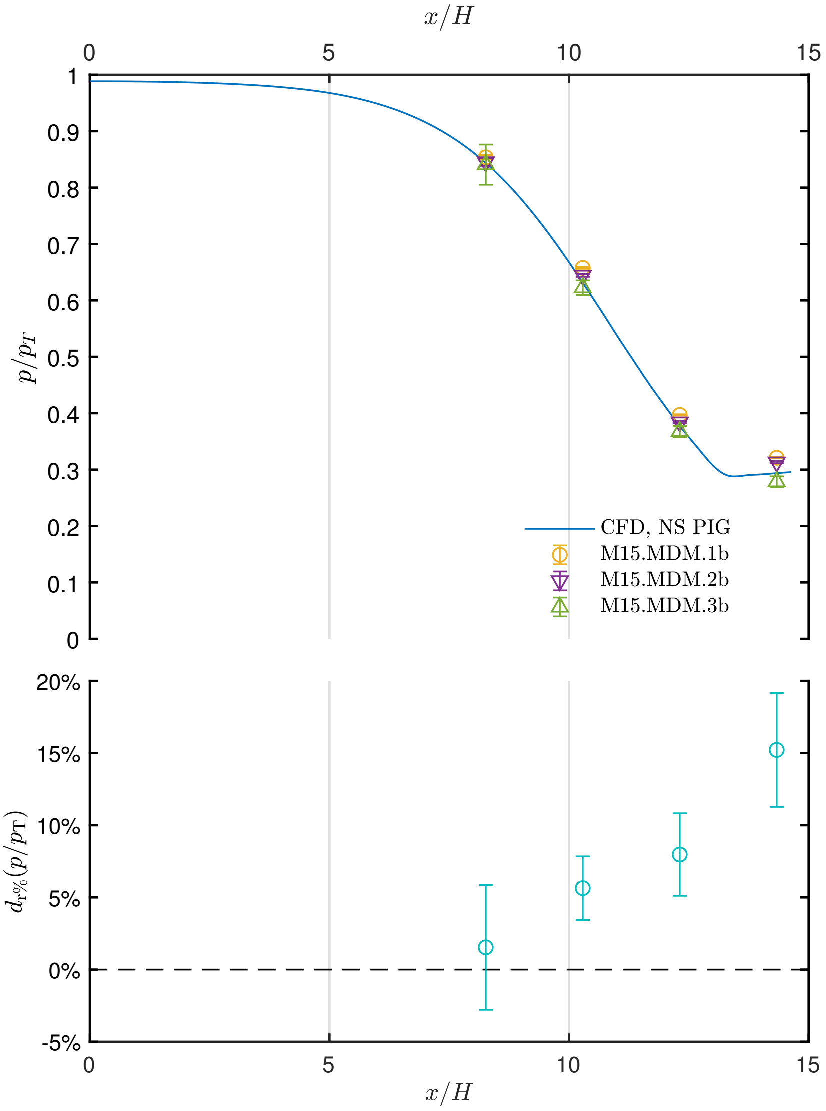

Figure 6.8: Top: Static-to-total pressure ratio p/p_T for expansions M15.MDM.1b-2b-3b (see Table 6.3). The result on the nozzle axis of a viscous CFD calculation with MDM modeled as polytropic ideal gas (PIG) is plotted. Bottom: relative percentage difference $d_{r\%}(p/p_T)$ between test M15.MDM.1b (minimum Z_T) and M15.MDM.3b (maximum Z_T). All reported uncertainty bars are 95% confidence level.

Numerical simulations were carried out for the minimum and maximum Z_T condition of both tests with M2 and M15 nozzles. A comparison between experimental pressure ratios p/p_T of expansions M2.MDM.1a (minimum Z_T) and M2.MDM.3a (maximum Z_T) is reported in Figure 6.9. The same is done for M2.MDM.1b (minimum Z_T) and M2.MDM.3b (maximum Z_T) in Figure 6.10, for M15.MDM.1a (minimum Z_T) and M15.MDM.3a (maximum Z_T) in Figure 6.11 and for M15.MDM.1b (minimum Z_T) and M15.MDM.3b (maximum Z_T) in Figure 6.12.

For tests with nozzle M2 (Figure 6.9 and Figure 6.10) two different sets of simulations are reported: one featuring the recessed step and the other with a smooth geometry at the throat, with the purpose of assessing the accuracy of a simplified simulation. Indeed, due to the presence of the step, a system of shocks and expansion fans develops, requiring grid adaption for a sufficient mesh resolution in correspondence of the aforementioned flow patterns. This increases the number of elements of the grid and slows the calculation of the solution. Thus, the detailed geometry was simulated with the iPRSV by Stelt, Nannan, and Colonna [80] thermodynamic model which has a slightly lower accuracy but is much faster than the Helmholtz energy equation by Thol et al. [83] implemented in RefProp (Lemmon, McLinden, and Huber [54]). Indeed, the iPRSV model is coded within SU2, while RefProp (RP) needs to be called through the FluidProp interface (Colonna and Stelt [22]), which further increases the calculation time. The Helmholtz energy model was used for the simulations carried out on the smooth geometry.

The simulation domain is restricted to the converging-diverging nozzle only and the $k-\omega$ SST was employed for turbulence modeling. The inlet boundary condition (inlet of the converging portion) corresponds to the total temperature T_T and total pressure p_T measured in the plenum for the expansion being simulated. The outlet boundary condition is set at the diverging portion outlet as a static pressure sufficiently lower than the design one. Indeed, the outlet pressure is necessary in the first part of the calculation to guide the solution toward a supersonic flow and is discarded once $M > 1$ is achieved at the nozzle exit. Solutions on various meshes with different grid refinement were carried out to evaluate grid independence.

The iPRSV simulations (Figure 6.9 and Figure 6.10) show a bump near the throat, due to the fan shock structure originating at the recessed step (Zocca et al. [97]). A second, smaller, bump is visible at $x/H \approx 12.5$, where the fan/shock structure crosses again the nozzle axis, after being reflected by the contoured wall. If compared to the RP simulation, the considered perturbation results to be local with an influence that can be considered negligible in the region where the shock-fan structure or reflections do not cross the nozzle axis, as stated by Zocca et al. [97].

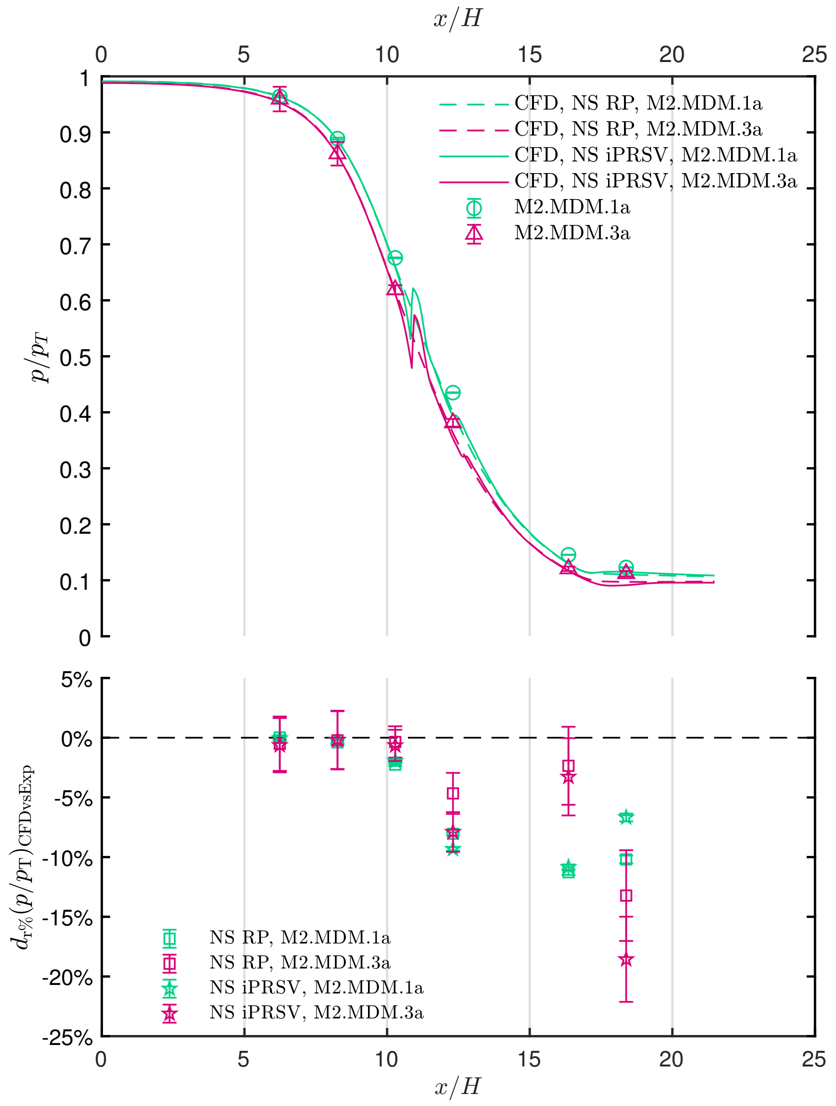

Figure 6.9: Comparison between static-to-total pressure ratio p/p_T along the nozzle axis obtained from experiments and from CFD, for expansions M2.MDM.1a (minimum Z_T, teal) and M2.MDM.3a (maximum Z_T, fuchsia). Data are extracted on the nozzle axis of a numerical simulation of the nozzle with recessed step using the iPRSV model (solid lines) and of a simulation of the nozzle with smooth geometry using the Helmholtz energy model implemented in RefProp, RP (dashed lines). The bottom graph reports the percentage difference $d_{r\%}\left(\frac{p}{p_T}\right)_{CFDvsExp}$ between p/p_T obtained from experiments and from CFD.

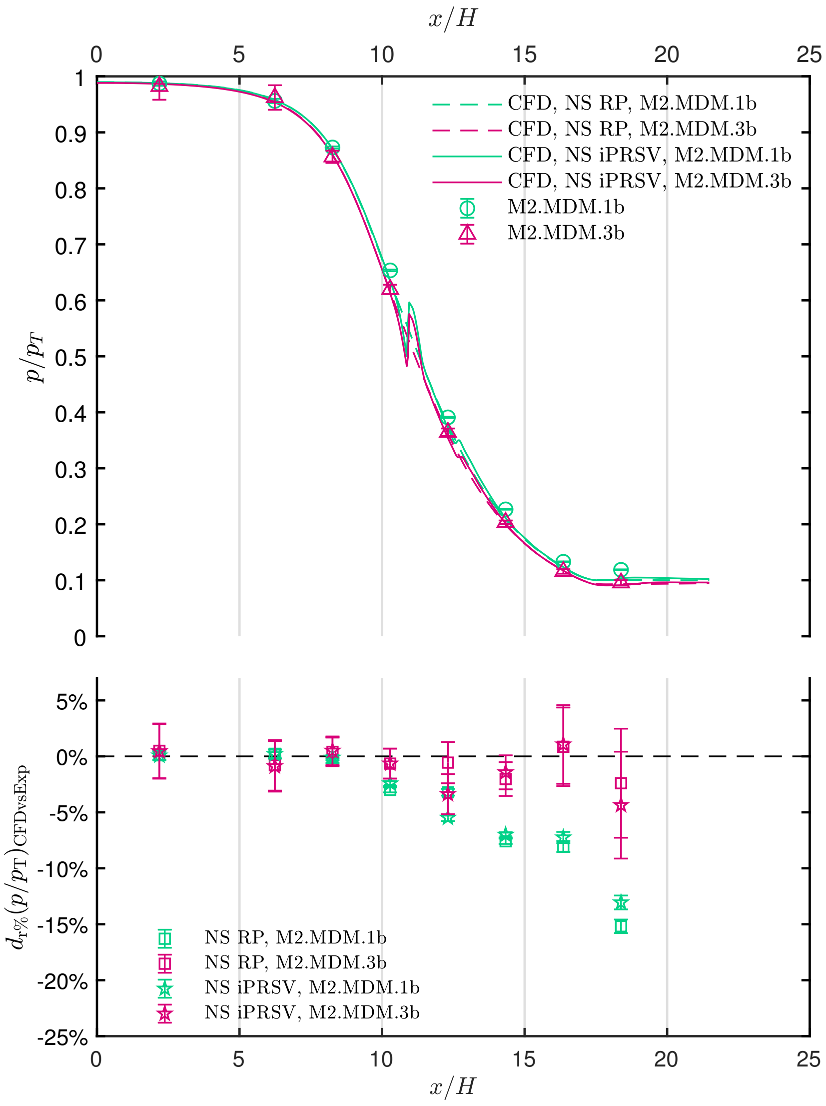

Figure 6.10: Comparison between static-to-total pressure ratio p/p_T along the nozzle axis obtained from experiments and from CFD, for expansions M2.MDM.1b (minimum Z_T, teal) and M2.MDM.3b (maximum Z_T, fuchsia). Data are extracted on the nozzle axis of a numerical simulation of the nozzle with recessed step using the iPRSV model (solid lines) and of a simulation of the nozzle with smooth geometry using the Helmholtz energy model implemented in RefProp, RP (dashed lines). The bottom graph reports the percentage difference $d_{r\%}\left(\frac{p}{p_T}\right)_{\mathrm{CFDvsExp}}$ between p/p_T obtained from experiments and from CFD.

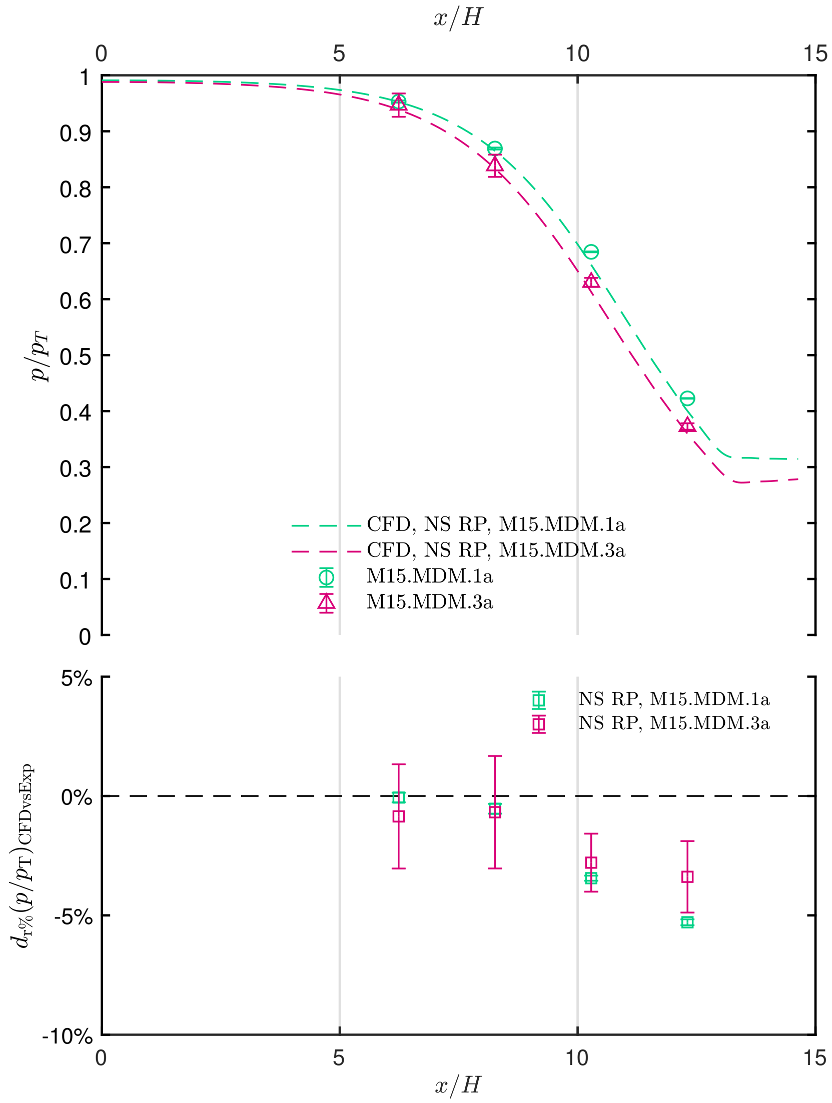

Figure 6.11: Comparison between static-to-total pressure ratio p/p_T along the nozzle axis obtained from experiments and from CFD, for expansions M15.MDM.1a (minimum Z_T, teal) and M15.MDM.3a (maximum Z_T, fuchsia). Data are extracted on the nozzle axis of a numerical simulation using the Helmholtz energy model implemented in RefProp, RP (dashed lines). The bottom graph reports the percentage difference $d_{r\%}\left(\frac{p}{p_T}\right)_{CFDvsExp}$ between p/p_T obtained from experiments and from CFD.

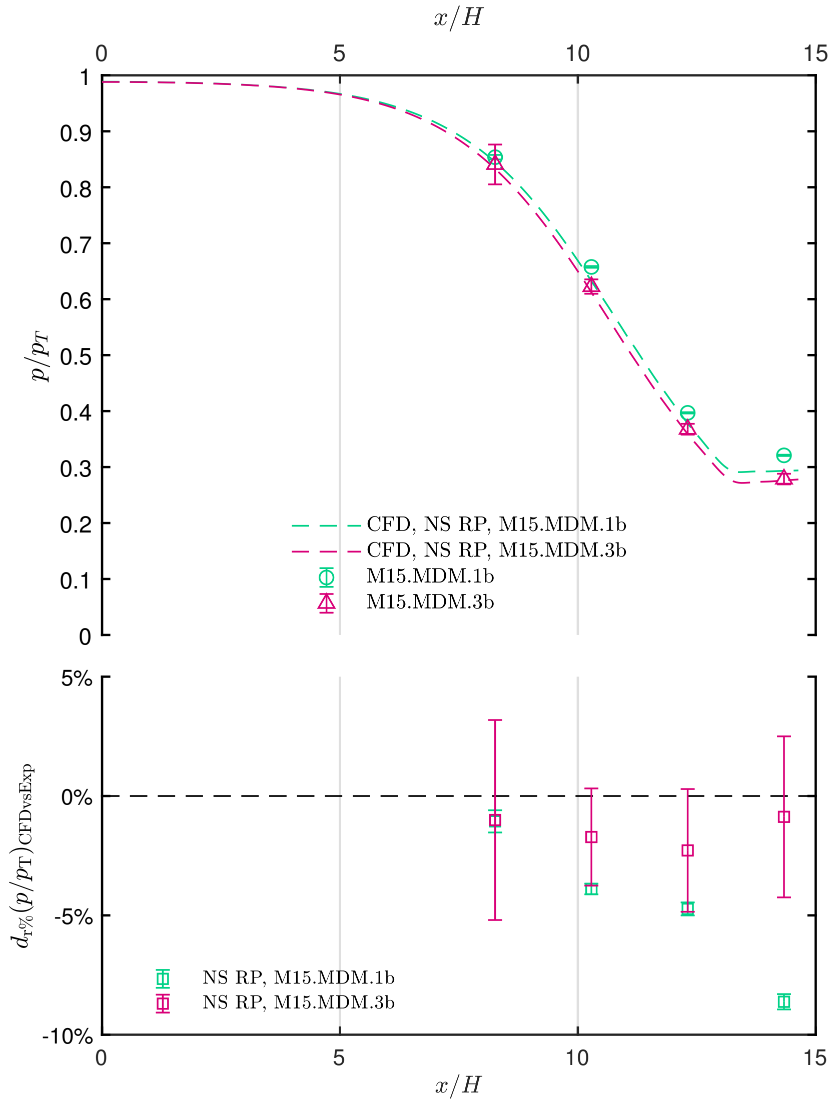

Figure 6.12: Comparison between static-to-total pressure ratio p/p_T along the nozzle axis obtained from experiments and from CFD, for expansions M15.MDM.1b (minimum Z_T, teal) and M15.MDM.3b (maximum Z_T, fuchsia). Data are extracted on the nozzle axis of a numerical simulation using the Helmholtz energy model implemented in RefProp, RP (dashed lines). The bottom graph reports the percentage difference $d_{r\%}\left(\frac{p}{p_T}\right)_{CFDvsExp}$ between p/p_T obtained from experiments and from CFD.

The accordance between CFD and experimental data is evaluated in terms of the percentage deviation of the static-to-total pressure ratio p/p_T, defined as

$$d_{r\%}\left(\frac{p}{p_T}\right)_{CFDvsExp} = \frac{\left(\frac{p}{p_T}\right)_{CFD} - \left(\frac{p}{p_T}\right)_{Exp}}{\left(\frac{p}{p_T}\right)_{Exp}} \cdot 100. \tag{6.4}$$

The 95% confidence level uncertainty bar was calculated assuming no uncertainty coming from the CFD solution. Thus, employing the Taylor series method,

$$\begin{aligned} u_{d_{r\%}}\left(\frac{p}{p_T}\right)_{CFDvsExp} &= \frac{100}{\left(\frac{p}{p_T}\right)_{Exp}} \cdot \\ &\cdot \sqrt{\left(\frac{\left(\frac{p}{p_T}\right)_{CFD}}{\left(\frac{p}{p_T}\right)_{Exp}}\right)^2 \cdot \left(u\left(\frac{p}{p_T}\right)_{Exp}\right)^2}, \end{aligned} \tag{6.5}$$

where $u\left(\frac{p}{p_T}\right)_{Exp}$ corresponds to $u\left(\frac{p}{p_T}\right)$ of Equation 6.3.

The accordance between CFD and experiments is very good in the converging portion until the geometrical throat, which is located at $x/H = 10.29$, where compressibility effects are limited. In the supersonic region the trend is generally of increasing $d_{r\%}\left(\frac{p}{p_T}\right)_{CFDvsExp}$. In particular, the discrepancy between data at lower compressibility factor Z_T (teal) is greater than at high Z_T, except for the last pressure tap at $x/H = 18.38$ in Figure 6.9. Thus, discrepancies between CFD and experiments are very small for the expansions in the almost ideal gas region (high Z_T), except for the last pressure tap in one case. At non-ideal conditions, the accordance is less verified.

Non-negligible deviation between CFD and experimental data is found at the most non-ideal states.

Deviations in pressure ratios between experiments and CFD in a supersonic nozzle flow of R1233zd(E) [1] were observed in a recent study by Robertson et al. [71] that was published almost a couple of years after the results being presented in this chapter. Both Peng-Robinson and Helmholtz energy equations of state were compared, yielding deviations between $9.12 \div 23.36\%$ and $6.63 \div 20.65\%$ respectively at the last pressure tap of the nozzle, which are of the same order of magnitude of those found in the tests presented here.

6.4.3 *Mach number*

Regarding Mach number measurements, only a brief overview of the results is given here. The interested reader can find further details in Cammi [15]. Only tests on nozzle M15 are discussed, indeed, the presence of the recessed step in nozzle M2 disturbs the application of

---

[1] Trans-1-chloro-3,3,3-trifluoropropene - $C_3ClF_3H_2$

the line detection algorithm summarized in Section 5.4.3.2. Further, the superficial roughness of the contoured profiles of M2 is not high enough to trigger Mach waves of sufficient intensity to be effectively detected by the schlieren system and recognized by the algorithm.

On the other side, with nozzle M15 some measurement issue prevent the possibility of obtaining the Mach number at each analyzed condition. Indeed, at expansions characterized by the most non-ideal conditions, the high density of the flow makes the schlieren image almost completely black with very low contrast, due to the measuring range issues cited in Section 5.4.3.1. However, even at the almost ideal gas state Mach waves are of difficult detection, due to the low refractive index gradient associated with each line at such low pressures. For these reasons, expansion M15.MDM.1a* (see Table 6.3 for thermodynamic conditions) is analyzed here as the most non-ideal case where good schlieren images for line detection were present, extracted from test MDM11. Further, the most non-ideal expansion extracted from test MDM13 is analyzed. Finally, expansions M15.MDM.1a* and M15.MDM.2b (the most ideal one where Mach lines were detectable) is made.

Figure 6.13b reports the profile of measured Mach number along the nozzle axis (diverging part) for the expansion M15.MDM.1a*. The schlieren image of the diverging portion of the nozzle along with the corresponding Mach lines is reported in Figure 6.13a.

The line detection algorithm provides the uncertainty of the line angle, called u_α, from which the Mach number uncertainty is

$$u_M = u_\alpha M \sqrt{M^2 - 1}, \tag{6.6}$$

by applying the Taylor series method and using Equation 5.6. The increase of Mach number uncertainty visible in the chart is thus strictly related to the angle α - Mach M relation, which leads to uncertainty rapidly increasing for increasing M.

In Figure 6.13b, the Mach number computed from the total pressure p_T, total temperature T_T and static pressure p is also reported. The calculation was made by resorting to the isentropic expansion assumption and using the Helmholtz energy model for MDM by Thol et al. [83] implemented in RefProp. Finally, the Mach number profile extracted on the nozzle axis of a CFD simulation carried out with the same thermodynamic model is plotted.

A comparison between these three datasets is made by considering the Mach percentage difference, calculated as

$$d_{r\%,M} = \frac{M_i - M_{CFD}}{M_{CFD}} \cdot 100, \tag{6.7}$$

where $i \in [Measured, Calculated]$. The 95% confidence level uncertainty was computed as

$$u_{d_{r\%,M}} = \frac{100}{M_{CFD}} \cdot u_{M_i}, \tag{6.8}$$

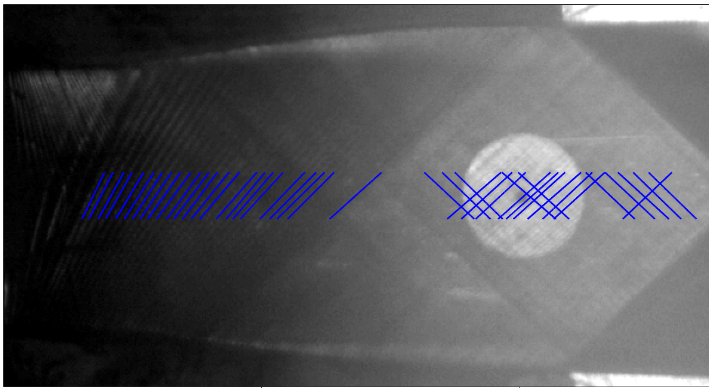

(a) Schlieren image of the diverging portion of the M15 nozzle. Detected Mach lines are superimposed.

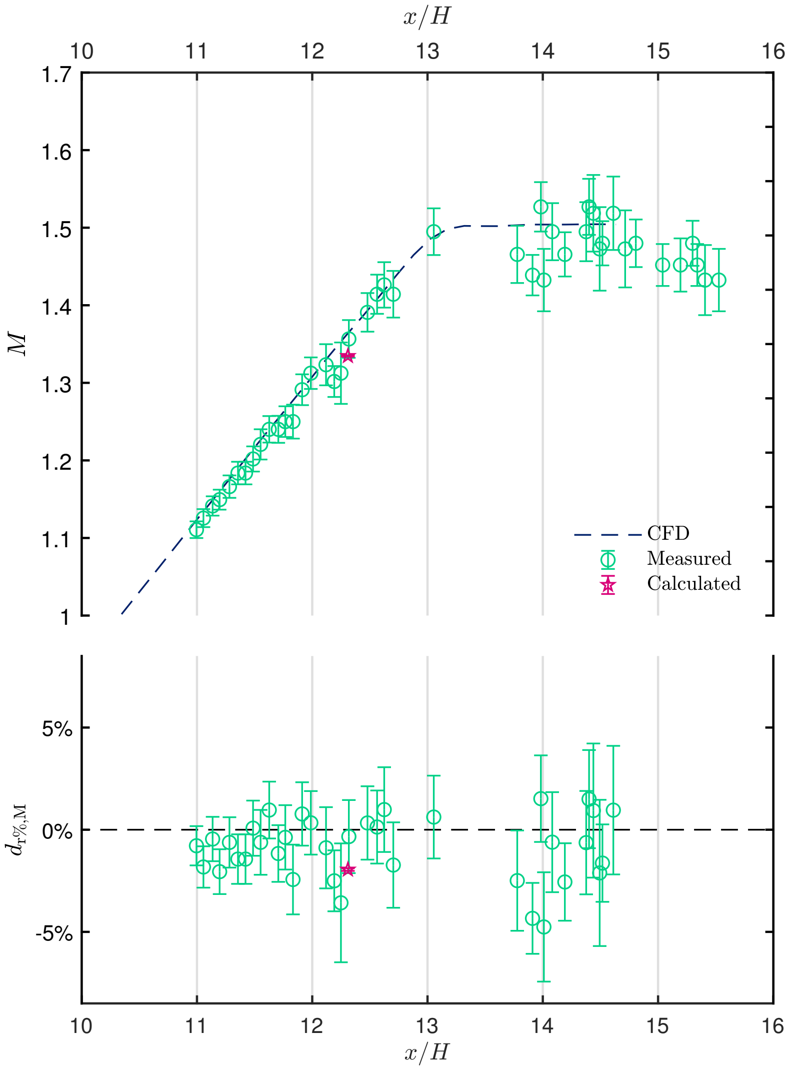

(b) Top: comparison between measured Mach number, the one obtained at the axis from a 2D viscous CFD calculation and the one calculated from total pressure p_T and temperature T_T and static pressure p, asuming isentropic expansion. Bottom: percentage difference $d_{r\%,M}$ of Mach number obtained from measurements, from $T_T - p_T - p$ and CFD. The latter is taken as reference.

Figure 6.13: Mach lines detection for expansion M15.MDM.1a*.

where no uncertainty was considered for the CFD value. u_{M_i} was computed from Equation 6.6 if $i = Measured$, while it was obtained from a Monte Carlo simulation with p_T, T_T and p uncertainties as inputs, if $i = Calculated$.

The same kind of data are reported in Figure 6.14 for expansion M15.MDM.1b. The schlieren image of Figure 6.14a features a higher contrast with respect to Figure 6.13a, due to the lower average density of the flow. Mach lines are clearly visible, as well as expansion fans occurring at nozzle outlet. However, the schlieren knife orientation was such to yield bright expansions and dark compressions. The outlet fan is accompanied by a high density gradient, thus this region is affected by the measuring range issues depicted in Section 5.4.3.1. The accordance between CFD, measured data and computed Mach number is very good, being the deviation $d_{r\%,M}$ below 5%.

A last comparison is made in Figure 6.15 between Mach numbers measured in expansions M15.MDM.2b ($Z_T = 0.9$) and M15.MDM.1a* ($Z_T = 0.65$), the two extreme cases with maximum Z_T and minimum Z_T where good schlieren images were obtainable. Uncertainty bars are overlapping, in particular for $M > 1.4$, but it is clearly visible that the expansion corresponding to the low Z_T condition is related to lower Mach numbers with respect the one at $Z_T \rightarrow 1$, if the same axial coordinate is considered. This is consistent with the one-dimensional theory of nozzle flows and with the increase of static-to-total pressure ratios with non-ideality.

6.5 CONCLUSIONS

In the present chapter, some key results for the understanding of the behavior of non-ideal gas-dynamics were presented.

The fluid employed for this experimental campaign was siloxane MDM. Two nozzles were used, one designed for an outlet Mach number $M = 2$ and the other for $M = 1.5$. Total temperature, total pressure, static pressure and Mach number along the nozzle axis were measured during various tests and different quasi-steady expansions spanning from strong non-ideal conditions to almost ideal ones were extracted.

Experimental data were analyzed and compared to CFD simulations. In terms of static-to-total pressure ratios, the accordance is generally satisfying for expansions at almost ideal conditions, while for non-ideal cases the deviation is higher. Concerning the Mach number, measurements and CFD simulations are in agreement. In general, all data prove the dependence of pressure ratios p/p_T and Mach number M from total conditions p_T and T_T.

Experimental data presented so far are the first ever of this kind and provide very important insights on the behavior of non-ideal compressible-fluid flows, which was widely studied from a theoretical

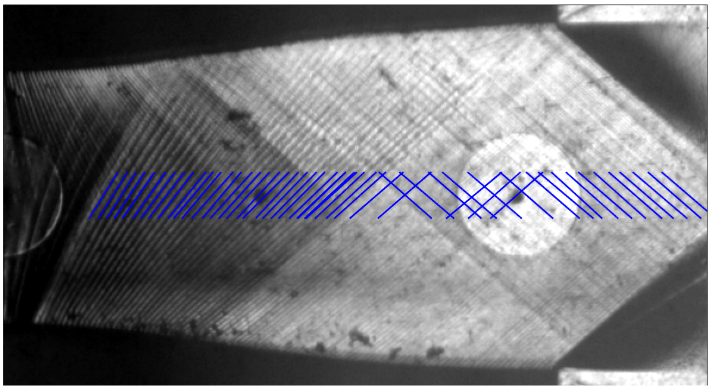

(a) Schlieren image of the diverging portion of the M15 nozzle. Detected Mach lines are superimposed.

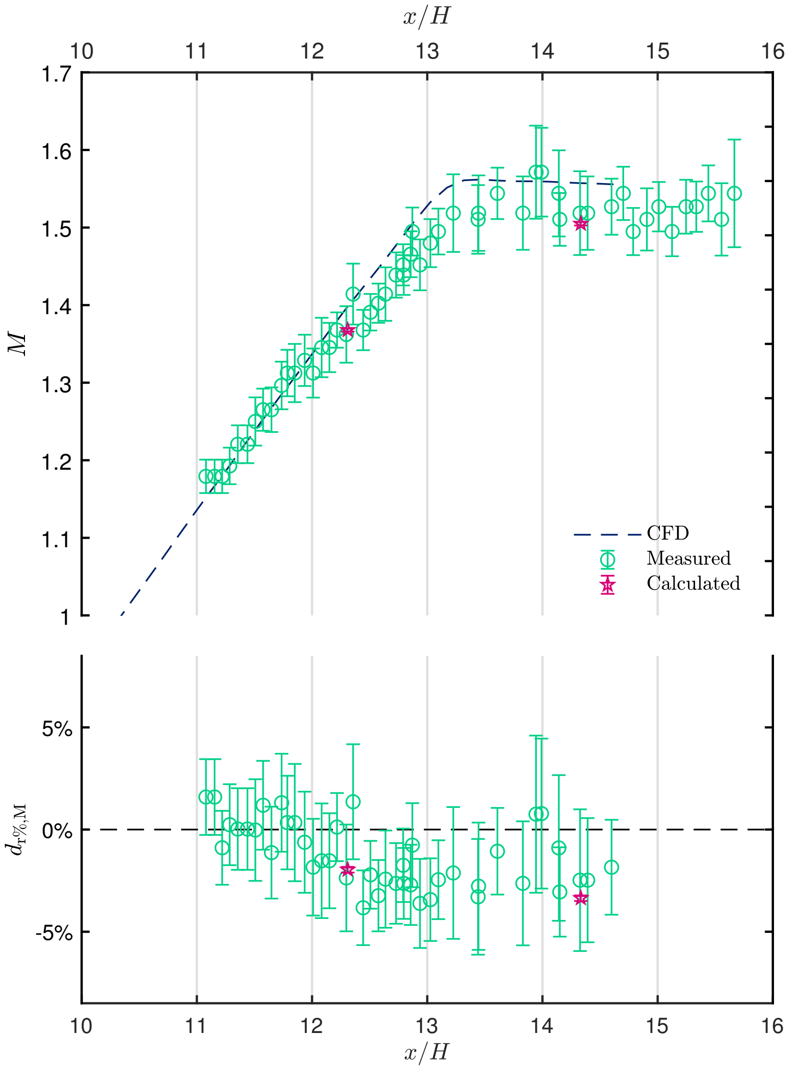

(b) Top: comparison between measured Mach number, the one obtained on the axis of a 2D viscous CFD calculation and the one calculated from total pressure p_T and temperature T_T and static pressure p, asuming isentropic expansion. Bottom: percentage difference $d_{r\%,M}$ of Mach number obtained from measurements, from $T_T - p_T - p$ and CFD. The latter is taken as reference.

Figure 6.14: Mach lines detection for expansion M15.MDM.1b.

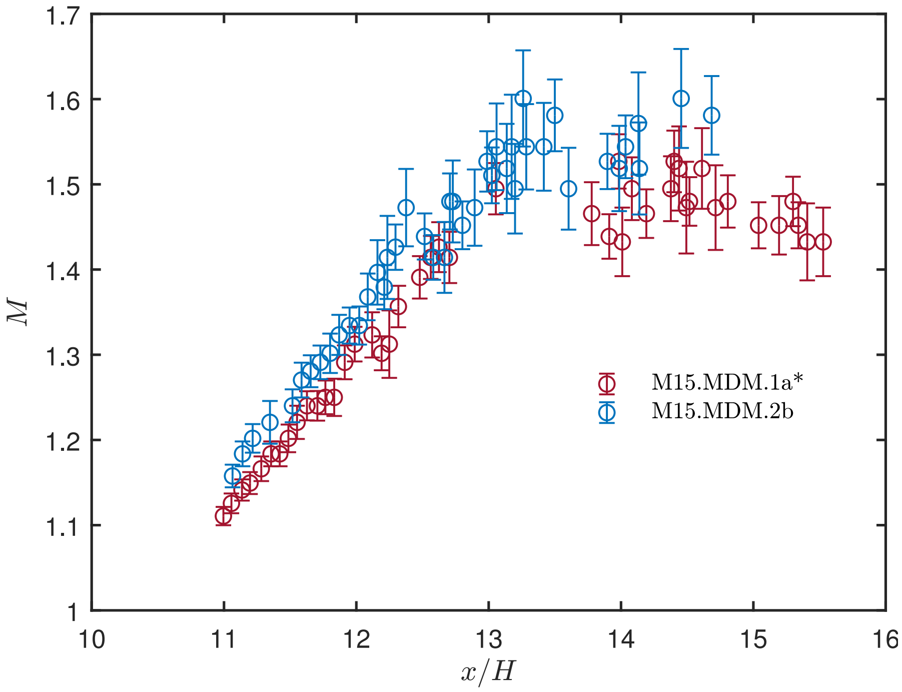

Figure 6.15: Mach number comparison between tests M15.MDM.2b ($Z_T = 0.90$) and M15.MDM.1a* ($Z_T = 0.65$).

and numerical point of view, but lacked of experimental observations. However, these data, though relevant, are incomplete: the independent velocity measurement is needed for a complete characterization of the flow.

7

COMPLETE CHARACTERIZATION OF NON-IDEAL COMPRESSIBLE-FLUID FLOWS

7.1 INTRODUCTION

Chapter 6 dealt with the characterization of a supersonic nozzle flow of siloxane MDM in the so-called dense gas region by means of pressure and temperature measurements and by schlieren imaging. However, despite the abundance of information contained in these data, to fully characterize the flow, a direct velocity measurement is also needed. Indeed, the system of equations describing the fluid motion, constituted by the continuity equation, the momentum balance equations, the conservation of energy equation and the equations of state of the fluid can be written as a function of temperature, pressure and velocity only (see Section 1.1.1). The direct velocity measurement permits to avoid the use of a thermodynamic model and the assumption of isentropic flow for the determination of the velocity vector.

The use of directional pressure probes for velocity measurement is not feasible, since they require a fluid dependent calibration, that is not currently available for the fluid tested in this work. Optical techniques such as Laser Doppler velocimetry (LDV) and particle image velocimetry do not require specific calibration and can provide a space and time resolved velocity measurement with negligible perturbation of the flow. The implementation of such techniques, however, is not straightforward: the flow must be seeded by tracer particles that should not contaminate the fluid and should have a velocity as close as possible to the flow one. Due to the relatively high pressure, temperature and velocity of the flow, the choice and the injection of the suitable tracer particle is not trivial.

No experimental results of direct velocity measurements in non-ideal supersonic flows of organic fluids are available in open literature by the time this work was written. The objective of this chapter is to report and discuss the first ever direct velocity measurements and full punctual characterization of a non-ideal compressible fluid flow. Section 7.2 reports a brief introduction about the LDV technique working principle and the challenges related to the choice of the suitable seeding particle. The choice of experimental conditions and the design of required nozzles is reported in Section 7.3. The analysis of chosen seeding particle dynamics is discussed in Section 7.4. The seeding system design and operation is described in Section 7.5, while the adopted LDV system setup is shown in Section 7.6. The effect of liquid injection in the flow is described in Section 7.7. In Section 7.8, a detailed discussion about the processing of obtained velocity signals is reported. The results of the experimental campaign are shown and discussed in Section 7.9. Conclusions are drawn in Section 7.10.

7.2 LASER DOPPLER VELOCIMETRY

7.2.1 *Measurement principle*

The laser Doppler velocimetry (LDV) is an optical technique for velocity measurement that is non-intrusive and is able to reach a high temporal and spatial resolution. LDV does not require calibration and provides a direct measurement: velocity V is calculated from the definition

$$V = \frac{\Delta s}{\Delta t} \tag{7.1}$$

by measuring the time Δt needed for a particle to pass through a known distance Δs. Thus, the velocity of a particle entrained in the flow is actually measured and this coincides with the flow velocity *only* if the object of the measurement has a relative velocity (the so called *slip velocity*) with respect to the surrounding fluid that equals zero. These seeding particles may be already present in the flow (e. g. condensation droplets in a saturated vapor) or may be injected on purpose.

The most common approach in laser Doppler velocimetry is the dual beam configuration, which is also the one implemented in the TROVA. Since LDV is a consolidated measurement technique, only a brief discussion about its functioning is given here. A more complete discussion on this topic can be found in the books by Tropea, Yarin, and Foss [86] and Albrecht et al. [5].

In LDV, two laser beams are focused in one point, the so called measurement volume, where the measurement is carried out. If tracer particles are very small, the fringe model could be used as an explanation of the functioning principle. This is a model where the wavefronts of two coherent beams of frequency f_b and wavelength λ_b (the lasers used in LDV) interfere at the measurement volume, forming fringes spaced by a distance

$$\Delta x = \frac{\lambda_b}{2 \sin \frac{\Theta}{2}}, \tag{7.2}$$

where Θ is the crossing beam angle (Figure 7.1). These fringes originate from the constructive and destructive interference of the wave fronts. A tracer that passes through the measurement volume scatters light with amplitude modulated by the presence of these fringes. This light is detected by the receiver and converted in an electrical signal.

,

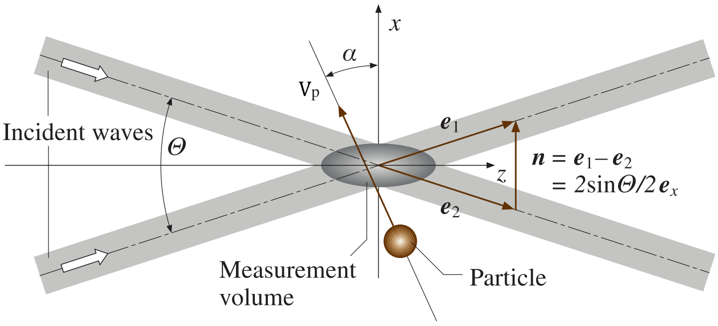

Figure 7.1: Dual beam LDV configuration [86].

The wave scattered by the particle has a carrier frequency that is the same of the incident beam one and an amplitude modulated with a frequency f_d called Doppler frequency, which takes the form

$$f_d = \frac{2\sin(\Theta/2)}{\lambda_b}\left|\vec{V}_p\right|\cos\alpha = \underbrace{\frac{2\sin(\Theta/2)}{\lambda_b}}_{1/\Delta x} V_{p\perp}, \tag{7.3}$$

where $V_{p\perp}$ is the particle velocity perpendicular to the beam bisector (along x in Figure 7.1). From the measurement of f_d and the fringes spacing value, the velocity perpendicular to the fringes can be calculated. If the particle is not small with respect to the wavelength, this model no longer holds. A detailed discussion can be found in the book by Albrecht et al. [5].

The size of the measurement volume impacts directly on the spacial resolution. Assuming an ellipsoidal shape, the semi axis a_0, b_0 and c_0 can be obtained as a function of the focal length of the LDV optics F, the beam expansion ratio E, the beam diameter before expansion d_w, the laser wavelength λ and the angle between laser beams Θ:

$$a_0 = \frac{2F\lambda}{\pi E d_w \cos\Theta/2}, \tag{7.4a}$$

$$b_0 = \frac{2F\lambda}{\pi E d_w}, \tag{7.4b}$$

$$c_0 = \frac{2F\lambda}{\pi E d_w \sin\Theta/2}, \tag{7.4c}$$

$$V_m = \frac{4}{3}\pi a_0 b_0 c_0. \tag{7.4d}$$

The expansion ratio is the characteristic parameter of the beam expander, which increases both beam diameter and distance by a factor equal to E. It is used to reduce the measurement volume dimension, thus increasing spacial resolution and signal quality.

7.2.2 *Particle properties*

To properly measure flow velocity, seeding particle must satisfy both dynamic and optical properties, that are treated in Section 7.2.2.1 and Section 7.2.2.3.

In general, the material of the seeding particle:

- should not be hazardous or toxic;
- should not be corrosive;
- should contaminate in a small amount the facility or its optical interfaces;
- should not be miscible with the working fluid.

7.2.2.1 *Dynamic properties*

The seeding particle should follow the flow streamlines, thus it must exhibit a low inertia to react as quickly as possible to the acceleration imposed by the flow field. By considering all forces acting on a particle entrained in a flow, its motion may be described by the Basset–Boussinesq–Oseen (BBO) equation (Albrecht et al. [5]), valid under the hypothesis of:

1. homogenous velocity profile over the particle;
2. no lift force;
3. spherical particles;
4. negligible particle-particle interaction;
5. $Re_p = \frac{\rho_f d_p |\vec{V}_f - \vec{V}_p|}{\mu} = 0$.

The BBO equation is:

$$\underbrace{\frac{\pi}{6} d_p^3 \rho_p \frac{d\vec{V}_p}{dt}}_{\text{acceleration force}} =$$

$$= \underbrace{-3\pi\mu d_p \left(\vec{V}_p - \vec{V}_f - \frac{1}{24} d_p^2 \nabla^2 \vec{V}_f\right)}_{\text{Stokes drag}} +$$

$$+ \underbrace{\frac{\pi}{6} d_p^3 \rho_f \frac{D\vec{V}_f}{Dt}}_{\nabla P \text{ term}} +$$

$$\underbrace{- \frac{\pi}{12} d_p^3 \rho_f \frac{d}{dt} \left(\vec{V}_p - \vec{V}_f - \frac{1}{40} d_p^2 \nabla^2 \vec{V}_f\right)}_{\text{virtual mass term}} +$$

$$\underbrace{- \frac{3}{2} d_p^2 \sqrt{\pi \rho_f \mu} \int_{t_0}^{t} \frac{d}{dt'} \left(\vec{V}_p - \vec{V}_f - \frac{1}{24} d_p^2 \nabla^2 \vec{V}_f\right) \frac{1}{\sqrt{t - t'}} dt'}_{\text{Basset history term}} + \vec{F},$$

(7.5)

where

d_p is the particle diameter;

$\vec{V}_f$ is the velocity vector of the fluid;

$\vec{V}_p$ is the particle velocity vector;

ρ_f is the fluid density;

ρ_p is the particle density;

μ is the dynamic viscosity of fluid;

t_0 is the start time;

$\vec{F}$ are the external forces acting on the particle, such as the body force (gravity minus buoyancy) $\vec{F}_{G-B} = \frac{\pi}{6} d_p^3 \left(\rho_p - \rho_f\right) \vec{g}$;

$d_p^2 \nabla^2 \vec{V}_f$ are the Faxen terms and are usually negligible, with respect to the other terms [61];

$\frac{d}{dt}$ is the time derivative on the particle trajectory;

$\frac{D}{Dt}$ is the time derivative on the trajectory of fluid elements surrounding the particle.

The assumption of spherical particles is well verified for small particles. The hypothesis of absence of interaction between particles leads to a limit on the concentration of particles. A separation of about 1000 diameters is required.

The global force acting on the particle is the sum of five terms:

STOKES DRAG is due to viscous forces; it applies for low particle Reynolds number, calculated with respect to the slip velocity $\vec{V}_p - \vec{V}_f$: $Re_p = \frac{\rho_f |\vec{V}_p - \vec{V}_f| d_p}{\mu} < 1$. So this law applies for small particles and small slip velocity. However, the Stokes drag is conservative and the actual Drag is higher (see Melling [62]);

∇P TERM this term accounts for the pressure gradients generated by the fluid acceleration, in the vicinity of the particle;

VIRTUAL MASS TERM is the force associated with the virtual mass; this mass equals half of the fluid mass displaced by the sphere;

BASSET HISTORY TERM expresses the drag forces due to the unsteadiness of the flow;

BODY FORCES expresses the body forces acting on the particle, such as gravity or centrifugal forces in swirling flows.

There are solution for this equation in different cases. Some examples of these solutions are reviewed by Albrecht et al. [5] and Melling [62] and are not reported here for brevity.

For small particles, the first part of the Stokes drag term dominates and by neglecting the basset history term, the virtual mass term and the body forces and assuming $\frac{DV_f}{Dt} \approx \frac{dV_p}{dt}$ the following expression for the difference between particle and flow velocity is obtained:

$$V_p - V_f = \frac{d_p^2 (\rho_f - \rho_p)}{18\mu} \frac{dV_p}{dt}. \tag{7.6}$$

Neutrally buoyant particles lead to a correct tracking.

If $\frac{(\rho_p - \rho_f)}{\rho_f} = 0$, the slip velocity tends to zero too, thus particles that have a density similar to the fluid one are desired. The diameter d_p plays a significant role also: the smaller the diameter the smaller the velocity difference.

In liquid flows the density requirement is easily satisfied by using polystirol, polystyrene or other polymers (see Albrecht et al. [5]), while in gas flows typically $\rho_p/\rho_f = O(10^3)$. In such situations the reduction of particle size is mandatory.

7.2.2.2 *Motion equation for finite* Re *number*

The BBO equation (Equation 7.5) is valid under the assumption $Re_p = 0$. The particle Reynolds number Re_p and the flow Reynolds number Re can be defined as

$$Re_p = 2\frac{\rho_f r_p \left|\vec{V}_f - \vec{V}_p\right|}{\mu} \tag{7.7a}$$

$$Re = \frac{\rho_f V_f L}{\mu}. \tag{7.7b}$$

where r_p is the particle radius and L is a characteristic length. Since a velocity measurement has to be performed, $\left|\vec{V}_f - \vec{V}_p\right| / \left|\vec{V}_f\right| \ll 1$ is required. This implies $Re_p \ll (2r_p/L)\,Re$. Usually, r_p/L is small: $r_p/L \sim 10^{-3}$ for liquid flows and $r_p/L \sim 10^{-4}$ for gas flows. So the particle Reynolds number Re_p should satisfy $Re_p \ll 10^{-3} - 10^{-4} Re$. If the flow is laminar, and an accurate tracking is required, the particle Reynolds number Re_p results lower than one. On the other side, in a turbulent flow, Re_p results greater than one. This leads to the conclusion that the BBO (Equation 7.5), as previously seen, is not appropriate for turbulent flows and another equation is required.

A specific equation for particle Reynolds number greater than one is required, if the flow is turbulent.

The simplest approach to account for finite Re_p is to multiply the quasi-steady Stokes drag term by a $\phi = C_D/C_{D,Stokes}$ coefficient, where C_D is the actual drag coefficient and $C_{D,Stokes}$ is the Stokes drag coefficient. Clift and Gauvin [18] report various correlations for ϕ as a function of Re_p.

7.2.2.3 *Optical properties*

LDV is based on the detection of the light scattered by a tracer particle. A particle that scatters as much light as possible is desirable. Scattering differs from reflection, since the incoming radiation is deviated in all directions. Energy is, of course, conserved. The isotropy of scattering depends on the ratio of particle diameter to the wavelength of incoming radiation. Two modes of scattering are possible: the Rayleigh scattering is isotropic and it occurs when the diameter of the particle d_p is much smaller than the wavelength λ of the incoming radiation ($\frac{\pi d_p}{\lambda} \ll 1$); the Mie scattering is anisotropic and is verified for $\frac{\pi d_p}{\lambda} \approx 1$. Typically, particle diameter is of the order of $d_p \approx 1\,\mu m$ for gas and vapor flows, while $d_p \approx 10\,\mu m$ for liquid flows, thus LDV falls in the category of Mie scattering.

The scattering cross section, namely the ratio of the total scattered power to the laser intensity, differs of several orders of magnitude between molecules and particles. This difference permits the detection of particles with respect to the surrounding fluid by the receiving optics of the LDV system (see Melling [62]). Indeed, the scattering cross section is a function of the particle diameter, of the incident radiation wavelength and of the particle refractive index (n) relative to the refractive index of the surrounding fluid. In cases where $d_p > \lambda$, the scattering cross section is proportional to the particle surface area $\left(d_p^2\right)$ and increasing the particle diameter increases the scattered light. When $d_p < \lambda$ becomes proportional to d_p^4 and for decreasing size the scattering scross section (and so the scattered power) decreases rapidly.

Increasing the particle size improves the signal quality.

Due to the anisotropy of the Mie scattering, the scattering cross section is function of the angle with respect to the incoming radiation. Most of the light is scattered in forward direction, but a non negligible portion is scattered backwards. LDV generally works in a near-forward or near-backward scattering mode.

The particle size is a compromise between dynamic and signal quality requirements.

Increasing the particle size for a better signal is in contrast with dynamic requirements. A trade-off is needed, to accurately track the flow and obtain a higher signal quality.

7.3 EXPERIMENTS AND NOZZLE DESIGN

To achieve the goal of the first direct velocity measurement in a vapor flow of a molecularly complex fluid in the non-ideal regime, a test campaign with different nozzles and thermodynamic conditions was planned. Both a converging and a converging-diverging nozzle were tested. The basic idea was to first assess the feasibility of direct velocity measurements in the TROVA, by means of LDV, in a subsonic flow, thus at relatively moderate velocity, in a region of low or no velocity gradient. Subsequently, a supersonic flow was characterized, both in regions of high and almost zero velocity gradient. Therefore, two

Table 7.1: Characteristics of nozzles designed for direct velocity measurement tests. The nozzle name, design working fluid, total design conditions $p_T - T_T$, the non-dimensional throat curvature r_t/H, the throat semi-height H are reported. For the converging nozzle CM07, the design Mach number M_{des} refers to the constant area portion, while for the converging-diverging nozzle M16, it refers to the outlet section.

Nozzle id	Fluid	M_{des}	p_T [bar]	T_T [°C]	r_t/H	H [mm]
CM07	MM	0.7	5	210	sharp	17.1
M16	MM	1.6	21.4	254	5	8

different nozzles were employed, whose characteristics are reported in Table 7.1.

The first, called CM07, is a converging nozzle, where the flow is expanded and accelerated up to sonic conditions, achieved at the nozzle outlet, that corresponds to the geometrical throat. The nozzle profile is sketched in Figure 7.2. It features a large portion at constant area. This region is designed to obtain Mach number $M \approx 0.7$ with low velocity gradient. Indeed, in that region the flow is slightly expanding only due to the growth of the wall boundary layer.

The first converging portion profile is obtained through a 5^{th} order polynomial, while the second one is composed by a straight segment connected to the constant area region through a cubic spline. The design of both converging portions is made so to avoid possible separation bubbles or excessive gradients.

The outflow section is with sharp edge, so to fix the geometrical throat. The outlet semi-height is $H = 17.1\,\mathrm{mm}$, while the constant area semi-height is $Y_c = 19\,\mathrm{mm}$, thus resulting in the area ratio $H/Y_c = A_t/A_c = 0.9$ needed to achieve Mach number $M = 0.7$, where A_t is the throat area and A_c the area of the zero gradient region. The design total conditions are $p_T = 5\,\mathrm{bar}$ and $T_T = 210\,°\mathrm{C}$ with siloxane MM. Of course, since the nozzle sections were designed using the one-dimensional theory, the real Mach number in the zero gradient region can differ slightly from the design one. Further, considering the wide range of total conditions explored within a test run, the nozzle is almost always working off-design.

A subsonic and two supersonic cases will be analysed, thus a converging and a converging-diverging nozzle were designed.

The second employed nozzle is of the converging-diverging type. It is called M16 and is used to perform measurements in the supersonic regime in both a region of almost zero velocity gradient and a region of high velocity gradient. Figure 7.2 shows a sketch of the nozzle profile, while Table 7.1 reports the design data.

The method described in Section 6.2 was used for the design of this nozzle as well. M16 is designed for a uniform outlet Mach number $M = 1.6$ at $p_T = 21.4\,\mathrm{bar}$ and $T_T = 254\,°\mathrm{C}$ with siloxane MM. The throat semi-height is $H = 8\,\mathrm{mm}$, while the non-dimensional curvature

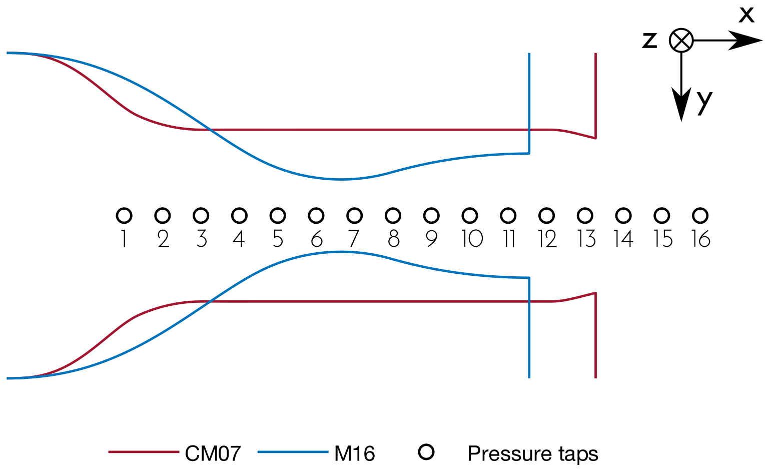

Figure 7.2: Tested nozzles. CM07 features a large constant area region, designed to achieve a Mach number $M = 0.7$. M16 is designed to achieve a mach number $M = 1.6$. Circles indicate the position of pressure taps along the nozzle axis.

is $r_t/H = 5$. In this case also, the nozzle normally operates off-design, thus the flow at outlet is not perfectly uniform and the delivered Mach number is different from $M = 1.6$ and typically higher.

Tests span from strongly non-ideal conditions to almost ideal ones and a single velocity measurement point along the nozzle axis is taken for each run. Indeed, due to the unsteady operation of the facility, it is not possible to traverse the whole nozzle axis during a test: at different instants of time, total conditions vary and, due to flow non-ideality, so is for measured pressure ratios and velocity. Thus, measurements in one position along the axis are taken for varying non-ideality of the flow.

The condition at lowest total compressibility factor encountered in these tests features $Z_T \approx 0.75$ at $p_T \approx 8.5\,\mathrm{bar}$ and $T_T \approx 208\,°\mathrm{C}$. For tests at $M \approx 0.7$ and almost zero velocity gradient, the measurement point is located in the second half of the constant area region, at the axial coordinate corresponding to tap 10 and at half depth of the channel. In supersonic tests, the measurement point is placed just downstream the throat (at tap 8), in the expansion region of the nozzle, for the high gradient case, while it is placed near nozzle outlet (at tap 11), in the turning region, for the near-zero gradient case.

7.4 PARTICLE SELECTION

Flow seeding at conditions occurring in the TROVA is challenging. Indeed, flow features high temperature, high pressure, high velocity and possibility of condensation. This is combined with the need of avoiding fluid contamination. Liquid particles are not suitable: droplets can evaporate due to temperature, can change in dimension due to

Table 7.2: Properties of the particles considered for seeding in the TROVA. The elected one is TiO_2.

		TiO_2	SiO_2	Al_2O_3
Density	$[kg/m^3]$	$3900 - 4200$	2200	3960
Melting point	[°C]	1830	1700	2015
Diameter	[nm]	$150 - 250$	$100 - 150$	430
Refractive index		$2.6 - 2.9$	1.54	1.79

pressure gradients, or can contaminate the working fluid by mixing. Thus, solid particles are to be used.

Metallic oxides show high melting point, thus making them a common choice for high temperature applications, such as combustion. Among others, titanium dioxide (TiO_2), silicon dioxide (SiO_2) and aluminum oxide (Al_2O_3) were selected as candidates for the TROVA flow seeding. Table 7.2 reports their properties: all candidate particles feature very high melting point and sub-micrometric diameter. Titanium dioxide and aluminum oxide feature high density, while silicon dioxide is half as dense. Concerning the refractive index, TiO_2 is by far the better option.

The tracing ability of the considered particles can be assessed by solving the BBO Equation 7.5. As previously discussed, it describes the motion of a spherical particle whose Reynolds number Re_p is zero. The approach discussed in Section 7.2.2.2 was used to evaluate the slip factor $s = (V_f - V_p)/V_f$ of each particle along the nozzle axis. Equation 7.5 is simplified neglecting all terms but the Stokes drag one, which is modified with a ϕ coefficient to account for $Re_p \neq 0$:

$$\frac{\pi}{6} d_p^3 \rho_p \frac{dV_p}{dt} = -3\pi\mu d_p (V_p - V_f)\,\phi. \tag{7.8}$$

The value of ϕ is selected based on the particle Reynolds number. Clift, Grace, and Weber [19] report correlations for ϕ divided in ten intervals of Re_p. For $Re_p < 260$ they are

$$\phi = \begin{cases} 1 + \frac{3}{16} Re_p & \text{if } Re_p \leqslant 0.01 \\ 1 + 0.1315 Re_p^{0.82 - 0.05w} & \text{if } 0.01 < Re_p \leqslant 20 \\ 1 + 0.1935 Re_p^{0.6305} & \text{if } 20 < Re_p \leqslant 260 \end{cases}, \tag{7.9}$$

where $w = \log Re_p$.

A solution of the flow in nozzle M16 was computed using he one-dimensional theory for total conditions $p_T = 8.1$ bar and $T_T = 205$ °C, which are representative of a typical supersonic non-ideal flow in the test section of the TROVA. Equation 7.8 was numerically solved imposing $V_p = 0$ m/s (i.e. $s = 1$) as boundary condition at nozzle inlet,

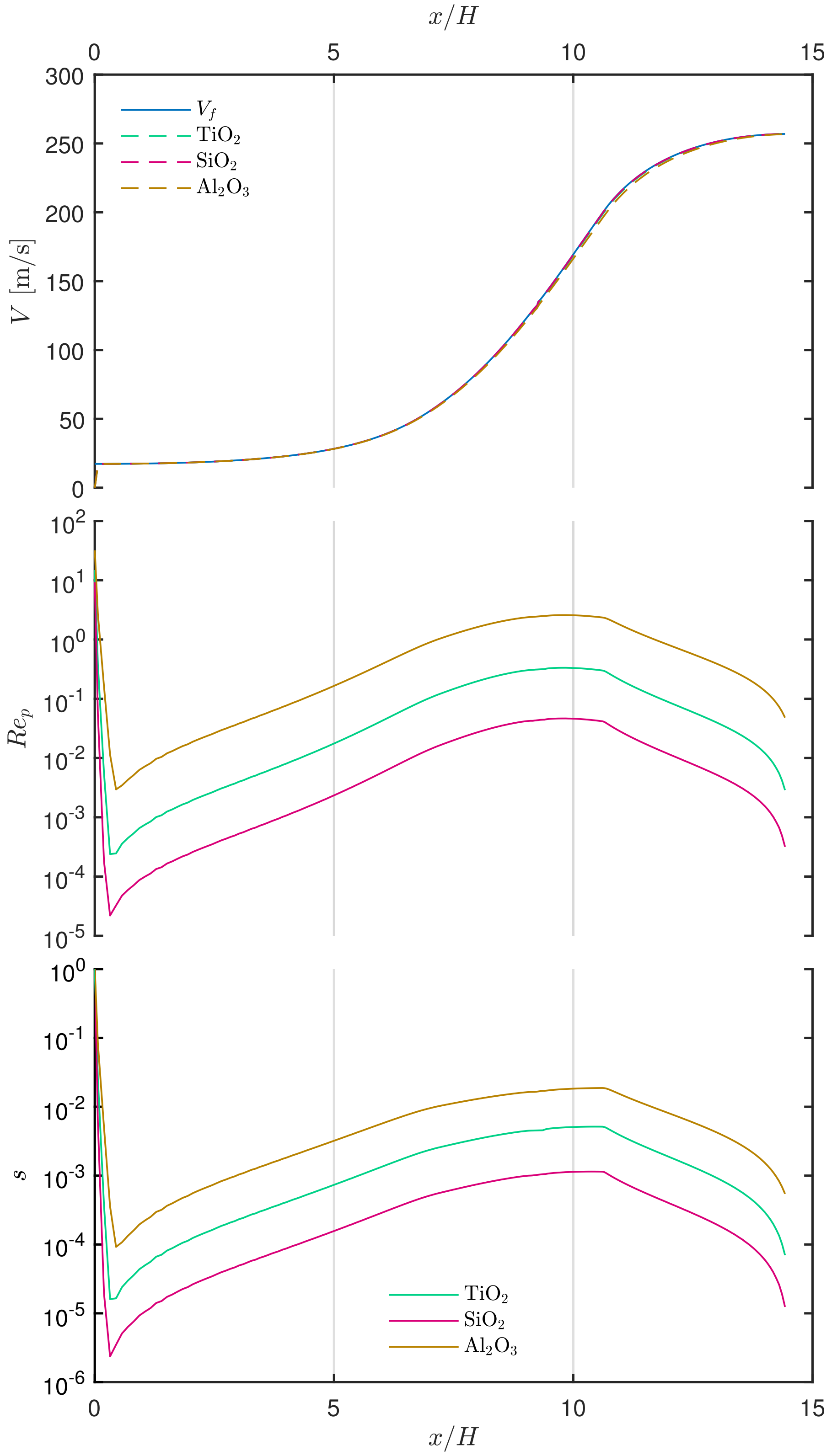

Figure 7.3: Particle tracking along the nozzle axis. Considered particles are TiO_2, SiO_2 and Al_2O_3 (see Table 7.2). Top: fluid velocity V_f is compared to particle velocity V_p. Total conditions of the flow are $p - T = 8.1\,\text{bar}$ and $T_T = 205\,°C$. Center: particle Reynolds number Re_p along the nozzle axis. Bottom: slip factor along the nozzle axis.

to consider the worst case. The result is plotted in Figure 7.3: the top graph reports fluid and particle velocity profiles along the nozzle axis, while the central graph reports the particle Reynolds number and the bottom one displays the slip factor s. Velocity profiles are almost indistinguishable. Re_p is maximum at nozzle inlet, since the particle is injected with zero velocity, and reaches a local maximum at the end of the region of maximum velocity gradient. Re_p is always below 100, thus Equation 7.9 apply. The slip factor is 1 at nozzle inlet, as imposed by the boundary condition, and rapidly decreases below 10^{-4}, which means that particles adapt very quickly to the fluid velocity. Slip factor then increases by more than two orders of magnitude in the region of maximum velocity gradient and then decreases.

200 nm diameter titanium dioxide was selected as tracer particle.

As it was predictable, silicon dioxide shows the lowest slip factor profile, due to its low diameter and density. The worst is aluminum dioxide, while titanium dioxide lies in between. Almost an order of magnitude of slip factor separates the considered particles. However, SiO_2 features also the lowest refractive index (roughly half than the TiO_2 one). This fact, together with the very low particle diameter poses some doubts on the detectability of SiO_2, considering also that the test section is confined by a quartz window and the quality of the signal may be lowered by the presence of unwanted reflections. Values of maximum slip factor $s \lesssim 0.5\%$ are considered satisfying, thus titanium dioxide is chosen, considering its high refractive index and particle diameter that shows a good trade-off between dynamic and optical properties.

7.5 TROVA SEEDING SYSTEM

7.5.1 *Design*

The design flow conditions of the seeding system of the TROVA are $p_T = 25\,\mathrm{bar}$ and temperature $T_T = 300\,°\mathrm{C}$. With such conditions, many common seeding devices are not suitable. Thus a completely customized system was designed by the author of this thesis in a previous work (see Gallarini [41]).

A suspension of tracer particles in MM is used to seed the flow.

To avoid working fluid properties alteration, no auxiliary materials other than the organic fluid itself can be used. Thus, the fundamental principle of the seeding system employs a liquid suspension of solid tracer particles in the working fluid, which is injected through an atomizer at high pressure and temperature in the plenum ahead of the test section. The liquid portion of the suspension evaporates, thus permitting the solid particle to be entrained in the flow. Figure 7.4 shows schematic of the functioning principle.

A further design constraint is the flow rate of seeding particles required to obtain a concentration lower than $\bar{N}_p < 0.1$ particles in the measurement volume (Albrecht et al. [5]). Indeed, this value permits

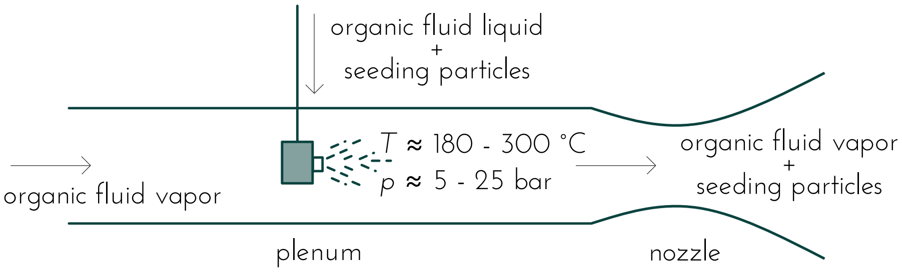

Figure 7.4: Schematic of the principle adopted for seeding the flow. A liquid suspension of tracer particles in the organic fluid is atomized in the organic vapor flow at high temperature and high pressure. The liquid fraction evaporates, leaving solid particles entrained in the vapor flow.

to avoid multiple particle signals, to preserve high signal quality and data rate.

The use of a syringe pump coupled with a ultrasonic atomizer was considered and was finally discarded, due to its very high cost and uncertainties in the operation of the atomizer; indeed, a high pressure and force syringe pump is needed to inject the required volume of suspension at the pressure of the plenum; further, the functioning of the ultrasonic atomizer was under question, due to the nature of the fluid and the presence of solid particles.

The final choice was a system based on a tank, filled with the liquid suspension to be atomized, pressurized with nitrogen, to achieve the pressure required for injection in the plenum. Figure 7.5 reports a schematic of the final design of the system. It features five parts, represented with different colors.

The core is the aforementioned tank, which is designed to withstand a pressure of 50 bar at ambient temperature, its normal working one. It is filled with the solid particles suspension and it is stirred using a propeller stirrer. Indeed, over long periods particles sediment, thus varying the concentration of the suspension that is injected.

The tank is pressurized, using nitrogen, through the pressurizing line (ocher in Figure 7.5). Pressure is set though two stages of pressure reduction and is monitored through the transducer PS3. Valve VS6 is used to empty the gas portion of the tank, thus to reduce its pressure. The liquid level in the tank is monitored (fuchsia lines in Figure 7.5) through a visual level indicator (at low pressure) and with a differential pressure transducer (at high pressure).

A line (depicted in red in Figure 7.5) connects the tank with the TROVA, where a pipe enters the plenum and terminates with an atomizing nozzle, which is located at the axis, pointing towards the test section. The atomizer is fundamental for a good seeding of the flow. Indeed, it is responsible for the distribution of a sufficient amount of seeding on the axis of the nozzle. The first adopted atomizer was hollow cone type with 60° aperture but due to the spray geometry

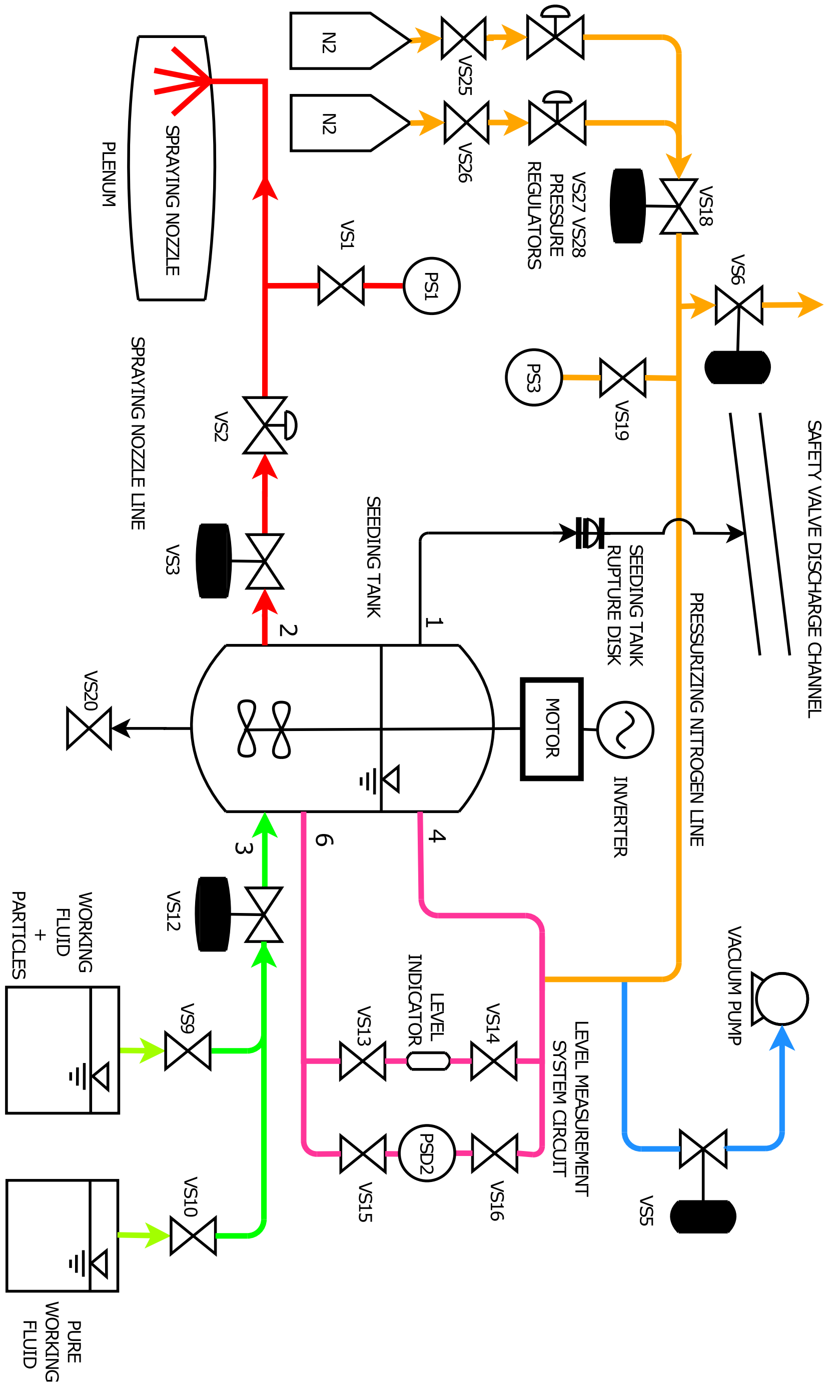

Figure 7.5: Schematic of the seeding system employed in the TROVA.

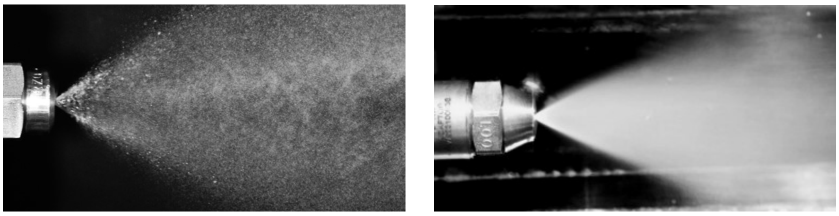

(a) Hollow cone nozzle.

(b) Full cone nozzle.

Figure 7.6: Picture of the spray generated by the hollow cone nozzle with siloxane MDM (the first one tested) and the full cone nozzle with siloxane MM, adopted to improve the seeding of the flow and the data rate of measurements.

Table 7.3: Main features of the adopted full cone atomizer.

Manufacturer	Delavan Spray Technologies
Model	WDB 1.0
Material	416 stainless steel
Strainer	74 µm
Orifice diameter	0.28 mm
Maximum pressure	36 bar

(hollow cone and wide spray angle) it yielded very low data rate. For the measurements carried out in this work, a full cone atomizer was adopted, featuring an aperture angle of 30°. Figure 7.6 shows a comparison between the two nozzles. A picture of a spray of siloxane MDM obtained using the hollow cone nozzle is reported in Figure 7.6a, while Figure 7.6b reports the spray generated with siloxane MM by the new full cone atomizer. The difference in cone angle, cone fullness, and drops dimension is clearly visible. The new atomizer (whose main features are reported in Table 7.3) permits to achieve an injection which is more concentrated on the axis, thus diminishing the portion of particles which is trapped by pipe walls.

The vacuum line (blue in Figure 7.5) connects the tank to the TROVA vacuum pump, which is used to evacuate the tank for its loading, sucking the liquid suspension or pure working fluid from the reservoirs connected to the green line.

7.5.2 *Mixing system functioning assessment*

The mixing system features a shaft with two propellers, one near the bottom of the tank and one at middle-height. An electrical motor provides the required rotational motion, whose speed can be regulated through an inverter. A high pressure rotating lip seal is applied to avoid nitrogen leakages between the mixer shaft and the closing flange at a maximum pressure of 50 bar.

The performance of the mixing system was visually assessed, by building a transparent model of the tank, made of poly(methyl methacrylate). The cylindrical shell was approximated by eight planar windows arranged to form an octagonal prism. The bottom was made of the same material of windows and was machined to approximate the hemispherically shaped bottom of the real tank. The top was equipped with a flange for coupling with the propeller mixer.

The transparent model was filled with the suspension and left about 24 h for solid particles sedimentation. The start-up of the mixer was filmed with a high speed camera. Frames of the initial transient are reported in Figure 7.7. The mixer features two propellers: one is in the field of view of the pictures, while the second one is placed in the hemispherical bottom, near the surface, and it is not visible. Initially, solid particles are settled on the bottom of the model and the suspension is transparent (Figure 7.7a). At $t = 0.38$ s (Figure 7.7b), the propeller mixer turns on. The small white cloud around the rotor is composed by particles that settled on the propeller surface and that are moved due to its rotary motion. At $t = 1.31$ s (Figure 7.7c) particles start to be suspended by the circular motion inducted by the mixer. The process continues until an almost uniform suspension is observed (Figure 7.7f). The mixer was judged suitable.

7.5.3 *Seeding system operation*

First, the suspension needs to be prepared. The seeding particles are poured in a jug containing liquid MM in the right proportion required to attain the needed concentration of particles in the measurement volume.

The volumetric flow rate of vapor (main flow) in the measurement point determines the mean flow rate of particles required to be injected. Various combinations of atomized flow rate and particle concentration in the suspension can be used to obtain the required seeding flow rate. However, it is not possible to control the atomized flow rate throughout an entire test. The pressure difference between the seeding tank and the plenum, which sets the flow rate based on the atomizer characteristic curve, changes at each instant of time. Indeed, while the tank pressure is kept at a constant value by the nitrogen system, pressure in the plenum decreases five to ten times during a run. Thus a mean suspension concentration value must be adopted. Further, a part of the seeding particles is unavoidably lost due to possible sticking on jug, seeding system pipes, tank, and plenum surfaces. Thus a theoretical required particle loading is calculated and it is then tuned, together with seeding tank pressure, based on the empirical observation of data rate and quality of signals. The amount of tracer used in

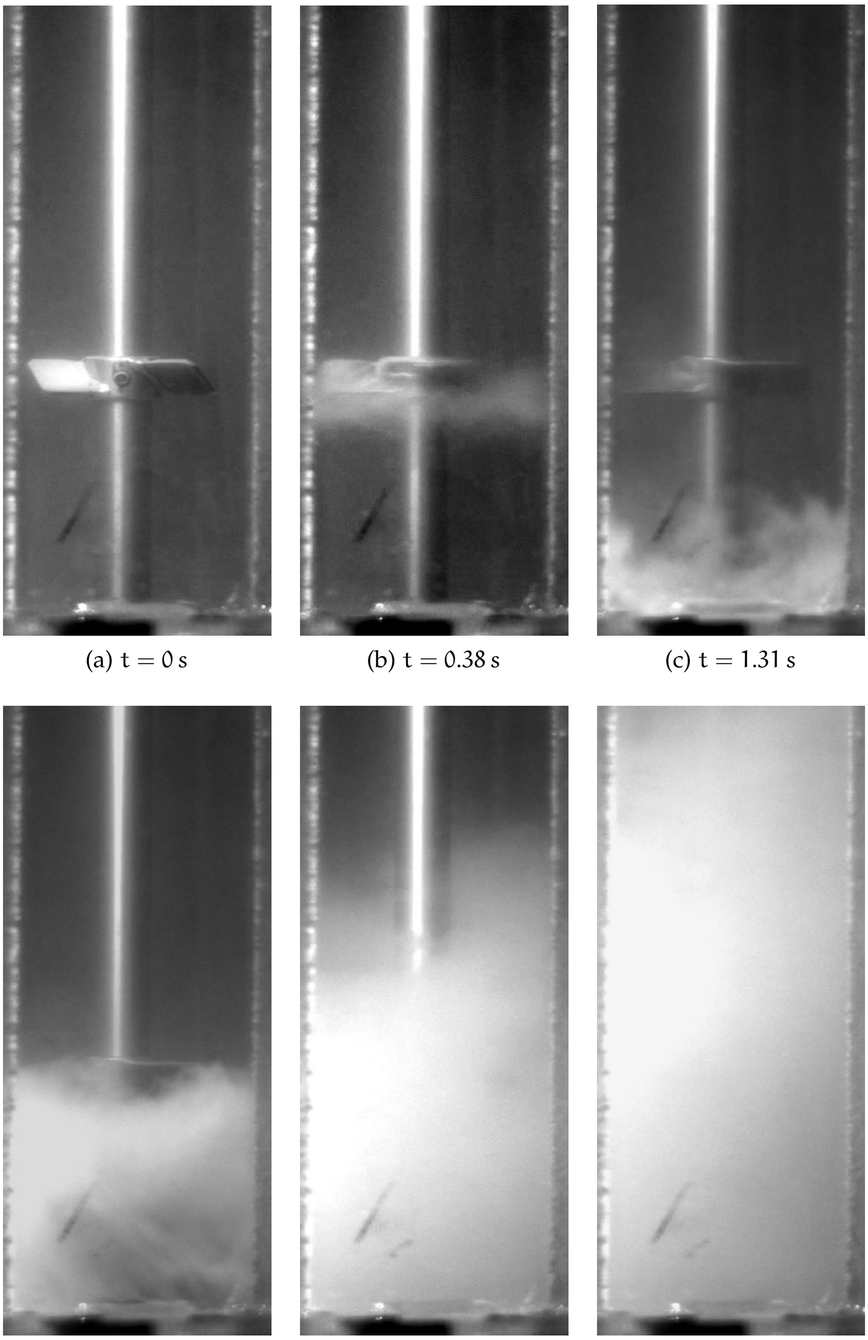

(a) $t = 0\,s$ (b) $t = 0.38\,s$ (c) $t = 1.31\,s$

(d) $t = 1.63\,s$ (e) $t = 2.78\,s$ (f) $t = 5.84\,s$

Figure 7.7: Pictures of the starting transient of the mixing system. The white powder is composed by tracer particles that are mixed by the propeller, to obtain a uniform suspension.

tests presented in this thesis is of the order of $1 \times 10^{-6}\,\mathrm{kg_{TiO_2}/kg_{MM}}$, which means a number of particles of the order of 10^{12} per liter of liquid suspension.

Then, the seeding system needs to be filled with the suspension. The tank is evacuated using the vacuum pump and opening valves VS12 and VS9 the liquid is sucked into the tank. During this operation, the level is continuously monitored through the visual indicator. When the required amount of suspension is loaded, the mixer is turned on to avoid sedimentation. When the test run is approaching, the tank is filled with nitrogen to reach the desired pressure level. Before starting all procedures of online zero and sensor signal check of the TROVA, the mixer is shut-down, to avoid any electromagnetic disturbance.

When the test starts, a triggering signal is sent by the controller computer to the LDV processor, which starts the acquisition. The user can choose the time of valve VS3 opening, which determines the start of injection of the suspension in the plenum. The operator can choose to interrupt and re-start the atomization at any time. When the operator stops the test, valve VS3 closes, interrupting the injection. At this point, the tank pressure can be reduced to ambient one by opening valve V6, which discharges the excess nitrogen. If a following test is scheduled, the mixer can be used to maintain the suspension, otherwise the tank can be emptied through the drainage valve VS20.

7.6 LDV SYSTEM AND EXPERIMENTAL SETUP

A two components LDV system is employed.

Table 7.4 reports the fundamental data of the LDV set-up employed for measurements at CREA Laboratory. It is a two components system, where the emitting sources are two optically pumped semiconductor lasers that provide a monochromatic beam of $1\,\mathrm{mm}$ diameter at a wavelength of $\lambda = 489.5\,\mathrm{nm}$ and $\lambda = 513.9\,\mathrm{nm}$, which correspond to blue and green color respectively. The system is a revamping of an older one, of which the optical component were maintained, while the emitter source and the burst spectrum analyzer were updated. The available optical components were designed to work with a Argon Ion laser, which features multiple emission bands, thus required the beam to be splitted to obtain the monochromatic beams at the required wavelengths. The transmitter box needs a unique multichromatic beam, thus the two monochromatic beams coming from the present solid state lasers are mixed in advance.

Figure 7.8 shows a schematic of the components of the employed LDV system. Once a unique laser beam is obtained, it enters the LDV optics, where it is treated to obtain four separate beams. First, two identical beams are obtained, of which one is shifted of a frequency f_s by the Bragg cell. Each color is then separated in the color splitter, obtaining four different beams, two for each color of which one is frequency shifted. The four beams are sent through a fiber to a

Table 7.4: Data of the adopted LDV system.

Laser		
Manufacturer	Coherent	Coherent
Model	Genesis MX488-1000 SLM	Genesis MX514-1000 SLM
Max. power	1100 mW	1100 mW
Wavelength λ	489.5 nm	513.9 nm
Beam diameter d_w	1 mm	1 mm
LDV optics		
Manufacturer		Dantec dynamics
Transmission	$\lambda = 514.5$ nm	0.7
efficiency	$\lambda = 488$ nm	0.6
Bragg frequency shift f_s		40 MHz
Beam expansion E		1.874
Beam distance		38.19 mm
Lens focal length F		310 mm
Burst spectrum analyzer		
Manufacturer		Dantec
Model		F 800
Max. frequency		200 MHz
Max. bandwidth		160 MHz
Min. bandwidth		80 kHz
Min. transit time		< 42 ns

Table 7.5: Dimensional data of the measurement volume, based on data of the adopted LDV system (Table 7.4).

Wavelength λ	489.5 nm	513.9 nm
$2a_0$	0.104 mm	0.109 mm
$2b_0$	0.103 mm	0.108 mm
$2c_0$	0.899 mm	0.944 mm
V_m	0.005 mm^3	0.006 mm^3
Δx	2.13 µm	2.24 µm

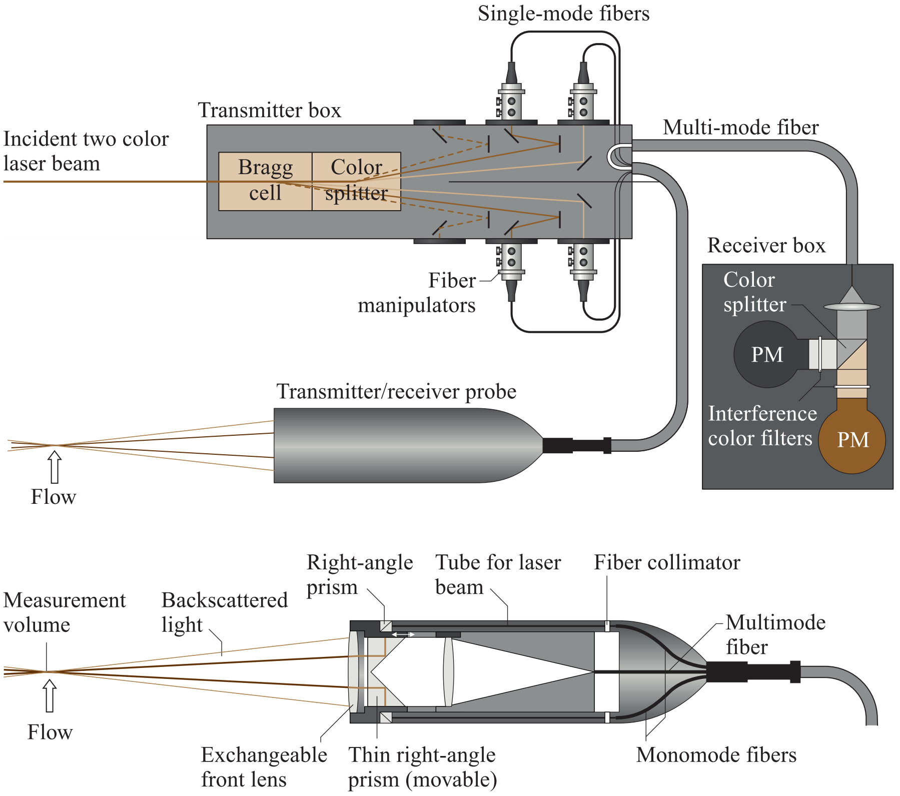

Figure 7.8: Schematic of the employed two colors LDV system [86].

transmitter probe, which focuses the four beams in the measurement point, generating two coincident measurement volumes of different colors, rotated of 90°, to measure two normal velocity components. Being one of the beams of each color frequency shifted, the fringe pattern that originates is moving, thus permitting to distinguish between positive and negative velocity. A particle with zero velocity results in a received frequency f_s, while if the particle is moving accordingly with the fringes the received frequency is lower than f_s and vice-versa. The light scattered by particles is collected and focused on a photodetector (a photomultiplier) which converts the light in a voltage modulated signal. The receiver optics is placed in the same casing of the transmitter probe, thus implementing a back-scattering mode system.

Ahead of the focusing length, a beam expander with ratio $E = 1.874$ increases both beam diameter and distance, thus leading to a decreased measurement volume size. The adopted focusing lens feature a focal length $F = 310\,\mathrm{mm}$. With the data reported in Table 7.4, the measurement volume size results of $\approx 0.1\,\mathrm{mm}$ in x and y coordinates (coincident with the nozzle axis and height, see the coordinate system of Figure 7.2), while $\approx 0.9\,\mathrm{mm}$ in the third direction z (the nozzle depth), see Table 7.5.

The burst spectrum analyzer is a Dantec F 800, which features a maximum input frequency of 200 MHz. The maximum measurable velocity with the considered system parameters is well above 300 m/s, with such a high maximum frequency. Synchronization with external sources is assured by external trigger inputs.

Figure 7.9 shows an overview of the experimental setup. The plenum, with the instrumentation for total conditions measurement and for seeding injection, is the insulated pipe coming from the right of Figure 7.9a. The test section is the body positioned almost at the center of the picture, which discharges in the 90° bend on the left, which brings the vapor to the LPV. On the left-lower side, the LDV probe is mounted pointing towards the glass window of the test section. In the background, in the top-middle of the image, the seeding system is visible. Figure 7.9b shows a detail of the test section and of the LDV probe. Through the quartz window, a converging nozzle is visible: the flow is from right to left. During heating-up, the test section is closed by an insulation pillow which is removed only a few seconds before the test run. The seeding tank is shown in Figure 7.9c, where the mixer motor is visible on top.

7.7 EFFECT OF LIQUID FLUID INJECTION

For a correct functioning of the measurement system, the liquid droplets injected in the plenum must evaporate before reaching the test section. In the seeding tank, the suspension is at ambient temperature, thus the energy required for evaporation must be provided by the main flow. With a simple energy balance, the influence of the spray on the mean flow can be assessed. Figure 7.4 can be used as a reference schematic for the involved fluxes: the organic fluid vapor (A) at pressure and temperature p_T and T_T is mixed with the suspension (B), which is coming from the tank at ambient temperature $T_B = 20\,°C$ and at a pressure which depends on the flow rate to be injected. The resulting flow of $A + B$ is labeled C. The declared maximum allowable pressure in the nozzle of $p = 35\,\mathrm{bar}$ is taken as tank pressure, to consider the worst case of maximum injected flow rate. The organic vapor flow rate is taken from CFD simulations of the employed nozzles.

Typical conditions of the test carried out in this work are reported in Table 7.6, together with results of the energy balance. The ratio of the power necessary to bring the superheated vapor of the main flow to saturated conditions $\dot{Q}_{des}$ to the power required to reach saturated vapor conditions from the spray liquid state $\dot{Q}_{sat}$ is an indication of the energy available for complete evaporation of the spray. $\dot{Q}_{des}/\dot{Q}_{sat}$ ranges between $\approx 150 \div 215$ and $\approx 50 \div 91$ for tests with the CM07 nozzle and M16 respectively. The throat area of the converging nozzle is more than double with respect to the converging-diverging one, thus resulting in an almost double flow rate, which determines the higher $\dot{Q}_{des}/\dot{Q}_{sat}$. The effect of spray on total temperature is small, less than 0.4%. In actual operation, the situation is even more favorable,

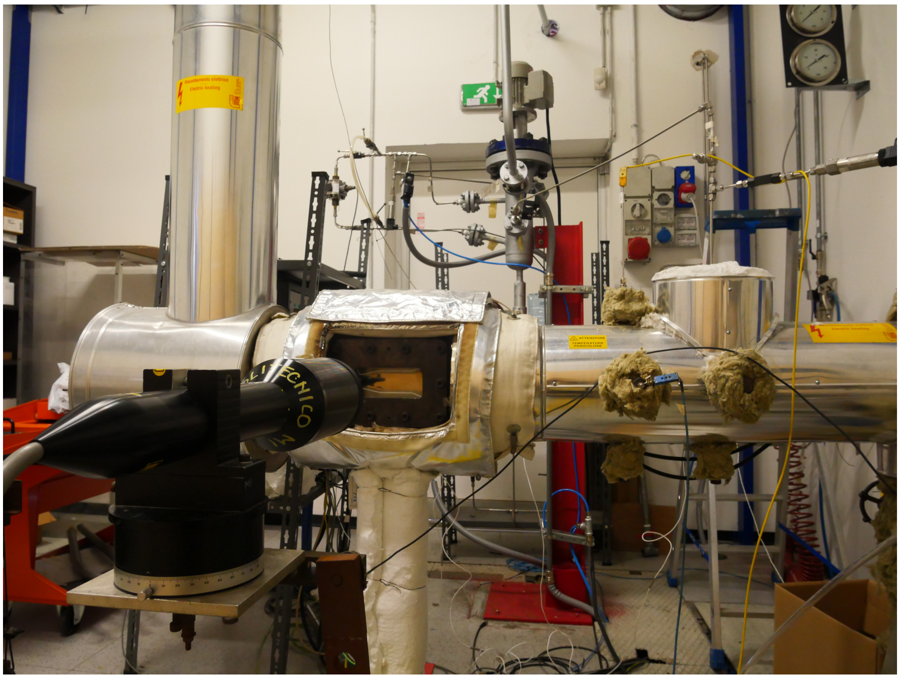

(a) The set-up of the test room. On the left, the LDV probe is positioned in front of the test section, in which, through the optical quartz window, the converging nozzle is visible. The test section is fed through the plenum (the pipe on the right) and discharges the vapor in the low pressure vessel through the up-going pipe on the left. In the background, the vessel and piping pertaining to the seeding system are visible.

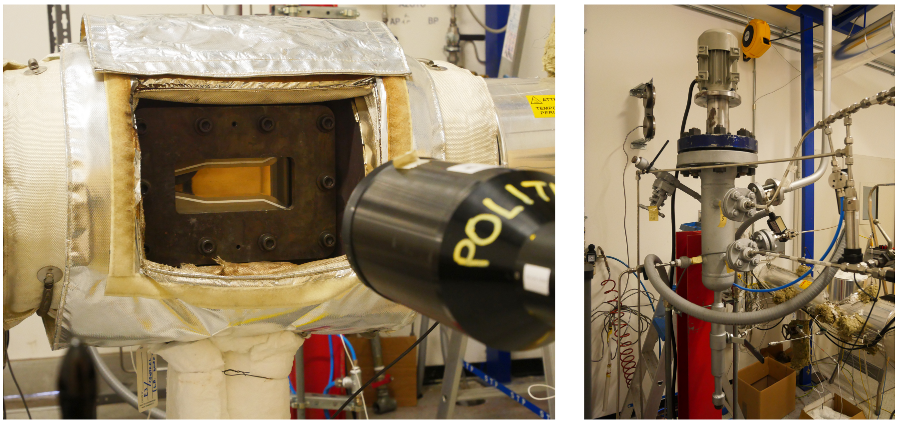

(b) Test section. The optical window that permits to carry out LDV measurements is mounted and the converging nozzle is visible.

(c) The seeding tank, with the mixer motor on top.

Figure 7.9: Test set-up.

Table 7.6: Plenum energy balance. A: organic fluid vapor flow. B: injected liquid suspension flow. C: flow obtained by mixing A and B. Conditions representative of those encountered at the start, at the end and at an intermediate time instant of the test are considered.

Nozzle	CM07			M16		
Test time	Start	Middle	End	Start	Middle	End
T_A [°C]	215	212	203	206	204	197
p_A [bar]	7.5	5.6	1.9	8.3	4	1.3
$\dot{m}_A$ [kg/s]	1.9	1.4	0.5	1	0.5	0.2
T_B [°C]	20	20	20	20	20	20
p_B [bar]	35	35	35	35	35	35
$\dot{m}_B$ [1×10^{-3} kg/s]	1.1	1.1	1.2	1.1	1.1	1.2
T_C [°C]	214.9	211.8	202.3	205.7	203.4	195.0
$\dot{Q}_{des}/\dot{Q}_{sat}$	204	215	150	50	91	59

since the liquid suspension is not injected at ambient temperature, because it heats-up thanks to conduction from the plenum pipe, which is electrically heated.

From a thermodynamic point of view obtained values of $\dot{Q}_{des}/\dot{Q}_{sat}$ confirm that there is enough energy for the complete evaporation of the spray, with negligible influence on total conditions. A detailed analysis from the heat transfer point of view cannot be carried out, since the droplet dimension is not known.

A set of preliminary tests was carried out to experimentally assess the influence of the spray on flow parameters, and no appreciable deviations were found on static-to-total pressure ratios between tests carried out with and without spraying the suspension.

7.8 PROCESSING OF VELOCITY SIGNALS

Tests were carried out acquiring pressure, temperature and velocity signals, which were synchronized through a signal coming from the TROVA control computer. The LDV data set features six variables: x and y velocity components ($\tilde{V}_x$ and $\tilde{V}_y$), particle arrival times ($\tilde{t}_x$ and $\tilde{t}_y$) and transit times ($\tilde{tt}_x$ and $\tilde{tt}_y$), where $\tilde{a}$ is the generic column of the data set consisting of elements a_i. Each row i corresponds to a different particle detected by the system, thus variables are randomly sampled in time. The data rate can range from hundreds to thousands of Hz and this amount of data is elaborated statistically to obtain a mean velocity value and a variance.

Due to the unsteadiness of the TROVA, total conditions of the nozzle change continuously in time, implying a time dependent velocity.

Thus, the statistical analysis is carried out with time discretization of 1 s on intervals of the same width. This provides an interval containing a sufficient number of signals for the statistical analysis, while keeping the mean velocity variation due to unsteadiness within the interval below $\lesssim 0.5\%$. To further reduce the error introduced by the unsteadiness, a $[t-0.5\,\mathrm{s}; t+0.5\,\mathrm{s}]$ centered time interval is adopted: indeed, if the signal can be approximated as a linear function, values in the interval $[0; t+0.5\,\mathrm{s}]$ balance exactly those in $[t-0.5\,\mathrm{s}; 0]$, thus leading to exactly zero error on the mean. The real velocity signal can be approximately considered linear in the time interval, thus the resulting error is almost zero.

The particle-rate is correlated to the volume flow rate through the measurement volume and, thus, to the velocity component being measured. The sample rate increases for increasing velocity, thus a simple arithmetic mean would be positively biased with respect to the real mean value. The correct estimator for the mean velocity is a weighted average. Many alternatives for the weights to be adopted were proposed in literature, each with advantages and disadvantages. Transit time is inversely proportional to the velocity magnitude and it is the recommended choice in systems where this information is available (see Albrecht et al. [5]). For this reason, the average of velocity observations $V_{x,i}$ with transit time $tt_{x,i}$ in the $k-th$ time interval was computed as a transit time weighted average:

$$V_{x,k} = \frac{\sum_{i \in k} tt_{x,i} \cdot V_{x,i}}{\sum_{i \in k} tt_{x,i}}, \tag{7.10}$$

where the equation for the y component can be obtained by replacing the x subscript with y.

Concerning accuracy, there is not a universal agreement upon a relation for the standard error of the weighted average. Some relations, each with some drawbacks, were proposed in literature and Gatz and Smith [42] reported an assessment of their accuracy, using the bootstrap method as a benchmark. This method is a computer based technique which permits to compute the accuracy of statistical estimates, without making parametric assumptions on the distribution underlying the data (see the book by Efron and Tibshirani [34] for details). It is particularly useful in this case, where the distribution function of LDV samples is not known and a weighted average is being used. To avoid possible drawbacks of available relations for the standard error of the weighted mean and due to the very low computer power required to analyze the LDV data set, the bootstrap method was directly implemented.

The bootstrap method is used to statistically analyze obtained LDV data.

Given that $\tilde{a}^k$ is the generic variable composed by elements $a_i : i \in k$, where k identifies the considered time interval, the fundamental principle is very simple:

1. B independent bootstrap samples $\tilde{a}^*_1, \tilde{a}^*_2, \ldots \tilde{a}^*_B$, are selected, each one constituted by n values obtained by sampling with

replacement from the rows of $\tilde{a}^k$, where n is the length of $\tilde{a}^k$. This means that the generic bootstrap sample $\tilde{a}_b^*$ is composed by the same elements of the original sample $\tilde{a}^k$, some appearing one time, others two times, other zero and so on. The variable $\tilde{a}^k$ can either be a vector or a series of column vectors, of which rows are sampled. The latter case applies here, where the sampling is carried out on $\tilde{a}^k = \left[\tilde{t}_x; \tilde{V}_x; \tilde{t}t_x\right]$, thus randomly selecting rows composed of triplets of arrival time, velocity and transit time. Of course, the same applies also if the bootstrap technique is carried out on the y velocity component. The number of independent bootstrap samples is taken as $B = 10^4$;

2. for each bootstrap sample $\tilde{a}_b^*$, the bootstrap replication of the weighted average is computed, thus obtaining $V_{x,b}^*$, where $b = 1, 2, \ldots, B$;

3. the bounds of the 95% confidence level interval of the x-velocity weighted average are computed as the 2.5% and 97.5% percentiles of the distribution of the B bootstrap replications $V_{x,b}^*$.

The obtained interval is taken as the contribution of the dispersion of data to the 95% confidence level uncertainty of the LDV measurement. This method was applied to both the x and y velocity component separately, to obtain the profile of average velocity and its dispersion as a function of test time.

Other uncertainty sources may arise from mean velocity gradients normal to the direction of the component being measured. The velocity of a particle obtained by the laser Doppler system depends on the trajectory of the particle within the measurement volume (thus it depends on the velocity gradient, if present). However, the maximum spacial resolution is the measurement volume itself, thus the mean value computed from measured velocities is representative of an integral of the real mean velocity over the measurement volume. If a non-linear gradient is present, this integral is biased with respect to the real mean velocity at the center of the measurement volume. Indeed, it can be demonstrated (Albrecht et al. [5]) that the integral of the mean x velocity over the measurement volume can be approximated as

$$\bar{V}_{x,MV} = \bar{V}_x\left(y_c\right) + \underbrace{\frac{b_d^2}{8}\frac{d^2\bar{V}_x\left(y\right)}{dy^2}\bigg|_{y=y_c}}_{\text{velocity error}}, \tag{7.11}$$

where $\bar{V}_{x,MV}$ is the integral over the measurement volume of mean velocity $\bar{V}_x\left(y\right)$, y_c is the y coordinate of the center of the measurement volume and b_d is the ellipsoid semi-axis in the y direction. Thus the difference between the mean measured velocity and the real mean velocity is proportional to the squared of the ellipsoid semi-axis multiplied by the mean velocity second derivative in the y direction. This effect may be present both due to gradients in the y and z directions. In the latter case, the velocity error can be evaluated by substituting z to y. In the experiments presented in this work the error contribution was evaluated from velocity profiles from CFD calculations and resulted of the order of 1×10^{-4} m/s in the worst case, thus it was considered negligible.

During a test, density undergoes a significant variation, thus the refractive index in the measurement point changes as a result of the Gladstone-Dale equation (Equation 5.2). The angle between beams Θ changes accordingly, thus causing a slight movement of the measurement volume in the direction of positive z, towards the rear plate. This displacement was estimated for all performed tests, obtaining a maximum value of $106\,\mu\mathrm{m}$, that is considered negligible, due to the 2D nature of the flow.

The last considered source of error is the effect of a gradient of refractive index of the vapor. Indeed, due to a density gradient, laser beams can be deflected, as happens in the schlieren technique (Equation 5.4), leading to both a displacing and rotation of the measurement volume. In the laser Doppler velocimetry case, beams enter the perturbed region with a non-negligible angle in the plane of laser beams with respect to the density gradient, thus a relation different from Equation 5.4 should be considered.

Given that x, y, z are the directions of the nozzle axis, height and depth respectively, the equations governing the propagation of a light beam across the perturbed region are (Merzkirch [63]):

$$\frac{d^2x}{dz^2} = \left[1 + \left(\frac{dx}{dz}\right)^2 + \left(\frac{dy}{dz}\right)^2\right] \cdot \left[\frac{1}{n}\frac{\partial n}{\partial x} - \frac{dx}{dz}\frac{1}{n}\frac{\partial n}{\partial z}\right], \tag{7.12a}$$

$$\frac{d^2y}{dz^2} = \left[1 + \left(\frac{dx}{dz}\right)^2 + \left(\frac{dy}{dz}\right)^2\right] \cdot \left[\frac{1}{n}\frac{\partial n}{\partial y} - \frac{dy}{dz}\frac{1}{n}\frac{\partial n}{\partial z}\right]. \tag{7.12b}$$

Considering a beam in the $x - z$ plane and a density gradient in the x direction, $dy/dz = 0$, $dn/dy = 0$ and $dn/dz = 0$. Further, deviations induced by density gradients are commonly small, thus $dx/dz \ll 1$. Under these hypothesis, above equations reduce to

$$\frac{d^2x}{dz^2} = \frac{1}{n}\frac{\partial n}{\partial x}, \tag{7.13a}$$

$$\frac{d^2y}{dz^2} = 0. \tag{7.13b}$$

The second one leads to the solution $y = constant$, while the first one provides, after integration between points 1 and 2, equations for the trajectory

$$x_2 = \frac{L^2}{2}\frac{1}{n}\frac{\partial n}{\partial x} + L\tan\Theta_1 + x_1, \tag{7.14}$$

and the angle of the beam

$$\tan\Theta_2 = L\frac{1}{n}\frac{\partial n}{\partial x} + \tan\Theta_1. \tag{7.15}$$

In the case of the TROVA test section, point 1 is where the beam enters the fluid flow and point 2 is the nozzle axis, thus L is the nozzle semi-depth. If no refractive index gradient was present, the position of the laser beam at $z = L$ would have been $(x_2)_{\partial n/\partial x = 0} = L\tan\Theta_1 + x_1$, thus the displacement of the beam is

$$x_2 - (x_2)_{\partial n/\partial x=0} = \frac{L^2}{2}\frac{1}{n}\frac{\partial n}{\partial x}. \tag{7.16}$$

Beam angular deflection $\epsilon = \Theta_2 - \Theta_1$ can be obtained from Equation 7.15 after some trigonometric manipulation.

The value of n to be used in previous calculations can be obtained from Equation 5.2, if the Gladstone-Dale coefficient for MM is known. The so-called Lorentz-Lorenz relation reads

$$\underbrace{\frac{(n^2-1)\,M_m}{(n^2+2)\,\rho}}_{\text{Molar refraction}} = \underbrace{\frac{N_A\,\alpha}{3}}_{\text{Molar polarization}}, \tag{7.17}$$

where

n is the refractive index;

M_m is the molar mass;

ρ is the material density;

N_A is the Avogadro number;

α is the mean molecular polarizability.

Under the hypothesis that the molecular polarizability α is a weak function of temperature and pressure, the refractive index of MM can be obtained from

$$n = \sqrt{\frac{M_m + 2R_M\rho}{M_m - R_M\rho}}, \tag{7.18}$$

where R_M is the molar refraction. This equation, for low densities, is well approximated by a straight line. A Gladston-Dale constant $k_{MM} = 4.5 \times 10^{-4}\ m^3/kg$ was found by applying least squares method to values obtained from Equation 7.18 with a refractive index of liquid MM $n_{MM,liq} = 1.3772$ (Wohlfarth [96]). An alternative procedure, which yielded approximately the same result, is to compute the molar refraction R_M applying the principle of additivity of bond and group refractions (Noll [65]), which are tabulated for various chemical bonds (Sauer [72] and Warrick [93]).

The sources of error arising from refractive index gradients were evaluated for the case of maximum gradient using data from CFD simulations (see Section 7.9.3), yielding a maximum angular deviation $|\epsilon| = 0.18°$ and beam displacement $x_2 - (x_2)_{\partial n/\partial x=0} = 14\,\mu m$. The error arising from the angular deviation of the velocity component being measured (the apparent velocity) with respect to the x axis is negligible, being $\cos\epsilon \cdot 100 = 99.9995$. The displacement of the beam leads to an error which depends on the velocity gradient at the measurement point and was estimated to be $0.07\,m/s$ with respect to a mean velocity of $\approx 180\,m/s$. Further $x_2 - (x_2)_{\partial n/\partial x=0}$ is to be compared to the diameter of pressure taps, which is $300\,\mu m$, thus the displacement is lower than the resolution of pressure measurements. For the aforementioned reasons, the contribution of density gradient on measurement uncertainty was neglected.

The scatter of velocity samples is the only significant contribution to velocity uncertainty.

Summarizing, the only considered contribution to velocity measurement uncertainty is the one originating from the scatter of velocity samples.

7.9 COMPLETE FLOW CHARACTERIZATION: DIRECT VELOCITY MEASUREMENT RESULTS

In this section, results of the complete characterization of non-ideal compressible fluid flows by means of pressure, temperature and direct velocity measurements are reported and thoroughly discussed. The flow is characterized in a single measurement point on the nozzle axis. Three different cases are analyzed:

- a subsonic flow at $M \approx 0.7$, with near-zero velocity gradient (Section 7.9.1);
- a supersonic flow at $M \approx 1.7$, in a region of near-zero velocity gradient (Section 7.9.2);
- a supersonic flow at $M \approx 1.4$, in a region of high velocity gradient (Section 7.9.3).

7.9.1 *Subsonic non-accelerating flow*

7.9.1.1 *Test conditions and consistency*

Three tests were chosen for consistency and repeatability assessment. The thermodynamic conditions of the tests are reported in Table 7.7 in terms of most non-ideal condition, corresponding to minimum total compressibility factor Z_T, and most ideal one, corresponding to maximum Z_T. From now on, the notation [Nozzle name].[Test id] is used to refer to a test, while keeping clear the type of nozzle.

Total conditions were chosen to meet the desired minimum value of total compressibility factor, which was set at $Z_T \lessapprox 0.8$. Based on

Table 7.7: Thermodynamic conditions of tests carried out on the nozzle CM07 with siloxane MM. Total pressure p_T, total temperature T_T, and total compressibility factor $Z_T(T_T, p_T)$ are reported for the most non-ideal condition and for the most ideal one.

		Min. Z_T condition			Max. Z_T condition		
Test id	Nozzle	p_T [bar]	T_T [°C]	Z_T [-]	p_T [bar]	T_T [°C]	Z_T [-]
MM78	CM07	7.385	218	0.807	0.823	202	0.979
MM79	CM07	6.914	217	0.820	0.714	204	0.982
MM81	CM07	7.517	215	0.799	0.976	200	0.975

the thermodynamics of the fluid, an interval of total pressure and temperature needed to achieve the desired value of compressibility factor is identified. The specific value of pressure is then chosen to have a maximum pressure at the measurement point as close as possible to the full scale of the available pressure transducers, to reduce measurement uncertainty, while temperature is increased with respect to the saturation value to obtain a sufficiently superheated vapor to avoid condensation during the run. A further constraint is, of course, the thermal stability of the working fluid. The moderate level of non-ideality permits to have maximum temperatures always below 220 °C, which are totally safe from the thermal stability point of view (Chapter 4).

The explored thermodynamic region is quite large and goes from slightly superheated non-ideal flows with $Z_T \approx 0.8$ to almost ideal gas flows with $Z_T \approx 0.98$. As for tests discussed in Chapter 6, the MCV was maintained fully open for the whole test. The employed nozzle is CM07, the converging one.

After a series of preliminary tests, the pressure gradient in the nozzle axis direction $\partial p/\partial x$ in the region between pressure taps p_9 and p_{11} resulted to be the lowest, thus the location of pressure tap number 10 was chosen as measurement point.

The LDV measurement volume was placed with the direction of the two measured velocity components aligned with the nozzle x and y axis. The measurement volume was positioned at the center of the channel, in both y and z directions. No velocity component is measured along z. The green laser is used to measure the x velocity component, while the blue is used for the y one.

Figure 7.10 shows the measured quantities during the three selected tests. Starting from the bottom graph, total conditions explored during the test are superimposed to contours of total compressibility factor Z_T and plotted along with the saturation curve of MM. This graph permits to appreciate the extent of the explored thermodynamic region and is the reference basis for the central and top graph. The central graph

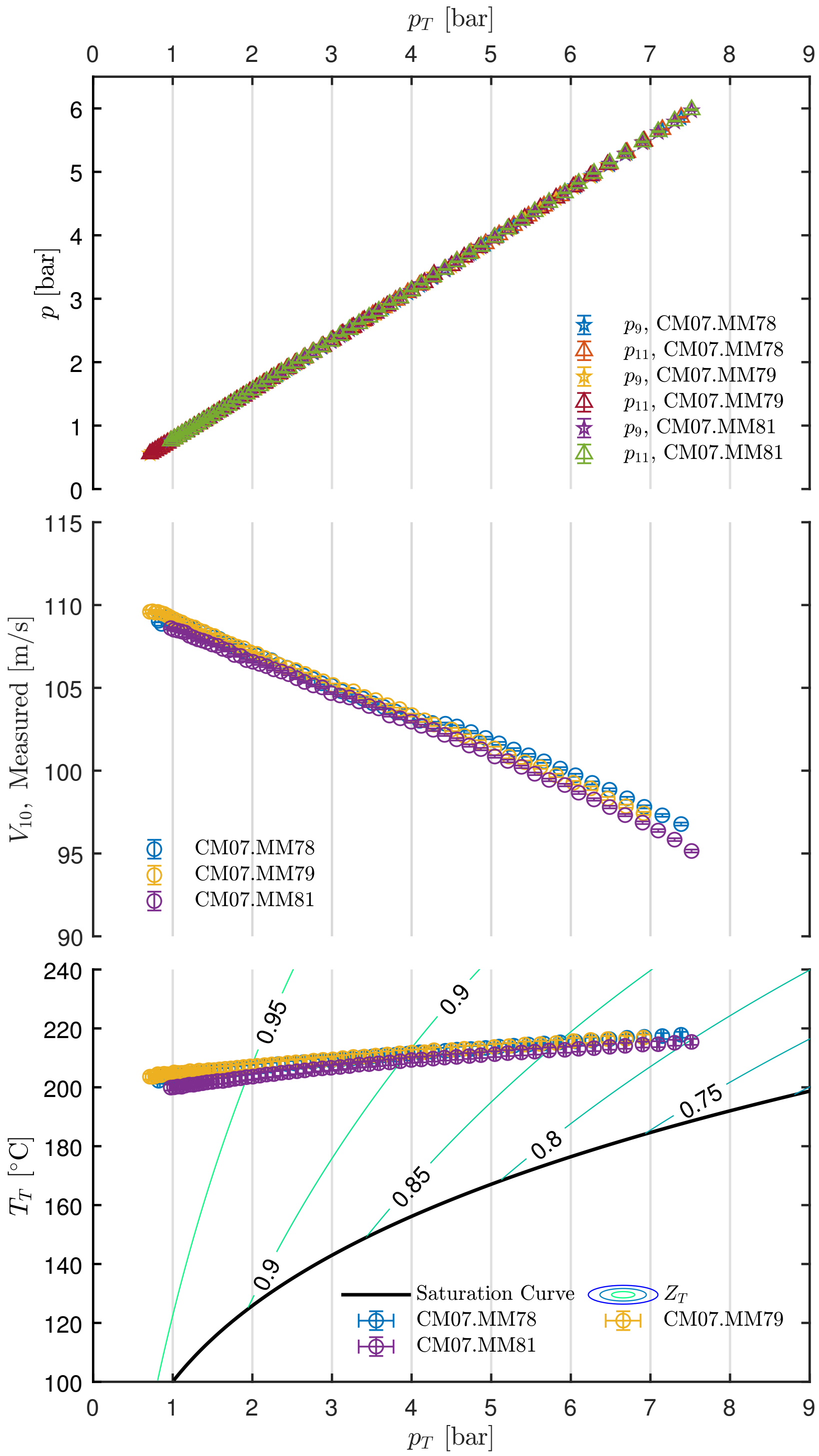

Figure 7.10: Repeatability of tests CM07.MM78-79-81 (see Table 7.7 for thermodynamic conditions). Top: static pressure at the nozzle axis measured at tap 9 and 11 (p_9 and p_{11}) as a function of total pressure p_T. Center: velocity measured at the nozzle axis in correspondance of tap 10, V_{10} as a function of p_T. Bottom: total temperature T_T as a function of total pressure p_T, along with the saturation curve of MM and superimposed to contours of total compressibility factor Z_T. All uncertainty bars correspond to 95% confidence level.

shows the directly measured velocity at tap 10, as a function of total pressure p_T. Each point in the velocity graph corresponds to a point in the total conditions graph, where the relation with total pressure, total temperature and total compressibility factor can be seen. The top graph shows the measured static pressure p at tap 9 and 11 (p_9 and p_{11}), the two taps where pressure was measured, in the uniform region. The repeatability and consistency of measurements is considered very good, even if uncertainty bars of each test run do not always overlap. Indeed, due to the operation of the TROVA (Section 5.3.3) the repeatability of test total conditions is not straightforward, due to uncertainties related to the mass loaded, to the stratification of the HPV, and to the unsteady dynamics of the plant.

7.9.1.2 *Results*

Test CM07.MM81 is now taken as representative of the campaign and is discussed in detail. Aiming at better understanding the analyzed thermodynamic region and the transformation occurring in the nozzle, Figure 7.11 is reported. The left graph shows a temperature T - specific entropy s diagram where the saturation curve and fundamental derivative of gasdynamics Γ iso-lines are plotted along with the expansions that were carried out during the test. Only a representative selection of those analyzed during the entire test is plotted for clarity. Indeed, during a test several hundreds of quasi steady states are acquired, depending on the actual duration of the useful portion of the test. On the right of Figure 7.11 a pressure p - temperature T plot shows the same expansions of the previous chart along with the MM saturation curve and compressibility factor Z contours. Expansions start from the total state, labeled A, and end in the static state corresponding to the condition at the measurement point (tap 10), following the direction of the arrow. As in the case of tests discussed in Chapter 6, the expansion can be regarded as isentropic at the nozzle axis, being viscous effects confined in the boundary layer, which is thin compared to the nozzle semi-height.

The bootstrap method, recalled in Section 7.8, was applied to compute the x and y velocity components at tap 10 ($V_{10,x}$ and $V_{10,y}$) as a function of test time, which corresponds to different p_T and T_T. Figure 7.12 reports the resulting velocity components as a function of total conditions: total pressure p_T is reported on the first horizontal axis, while the corresponding total temperature T_T is reported on the second lower horizontal axis. The y-velocity component is approximately zero, while $V_{10,x}$ is of the order of $100\,\mathrm{m/s}$, thus proving the correct alignment and positioning of the probe. Given the difference of two orders of magnitude between the x and y component, from now on the velocity magnitude is always taken equal to the x velocity component. Indeed, even with a conservatively high value of $V_y = 5\,\mathrm{m/s}$,

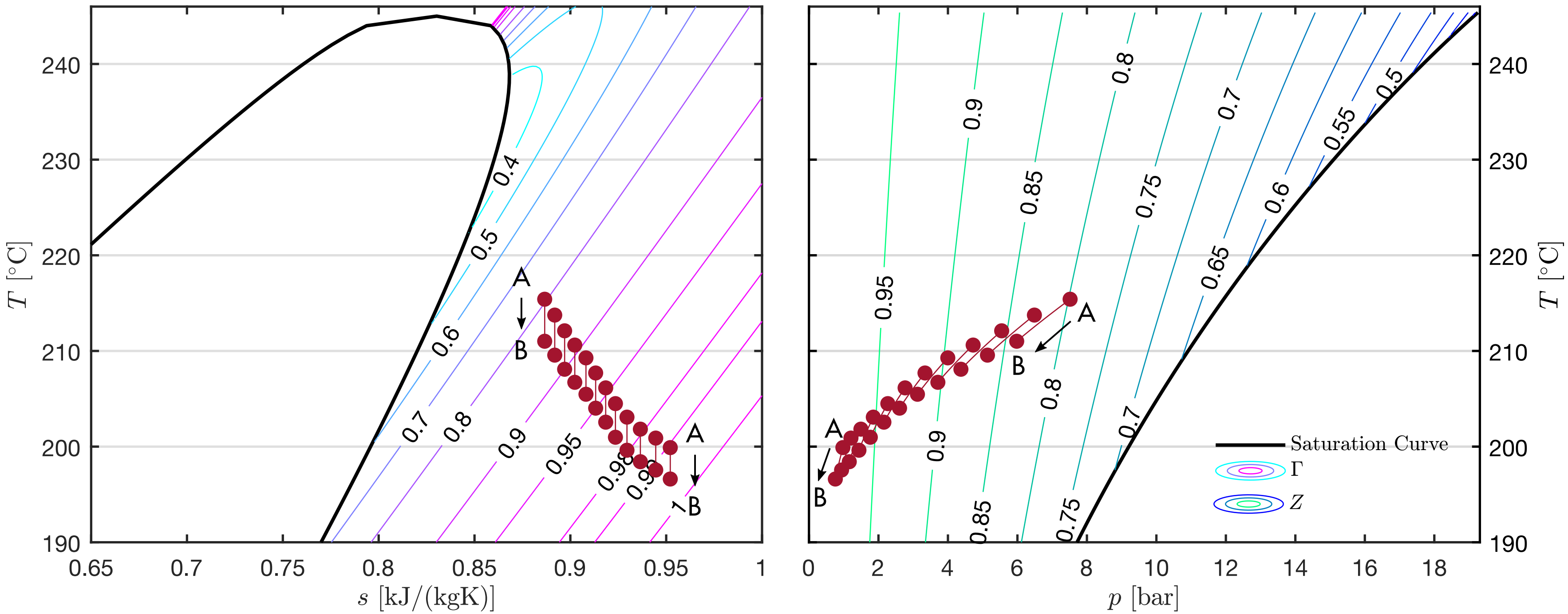

Figure 7.11: Explored thermodynamic region during tests CM07.MM81. The chart reports the expansions carried out during the test and selected for discussion in a temperature T - specific entropy s diagram (left) and a temperature T - pressure p diagram (right). Contours of fundamental derivative of gasdynamics Γ (left) and of compressibility factor Z (right) are reported along with the liquid-vapor saturation curve. Expansions proceed from the total state (A) to the static state corresponding to the measurement point (B).

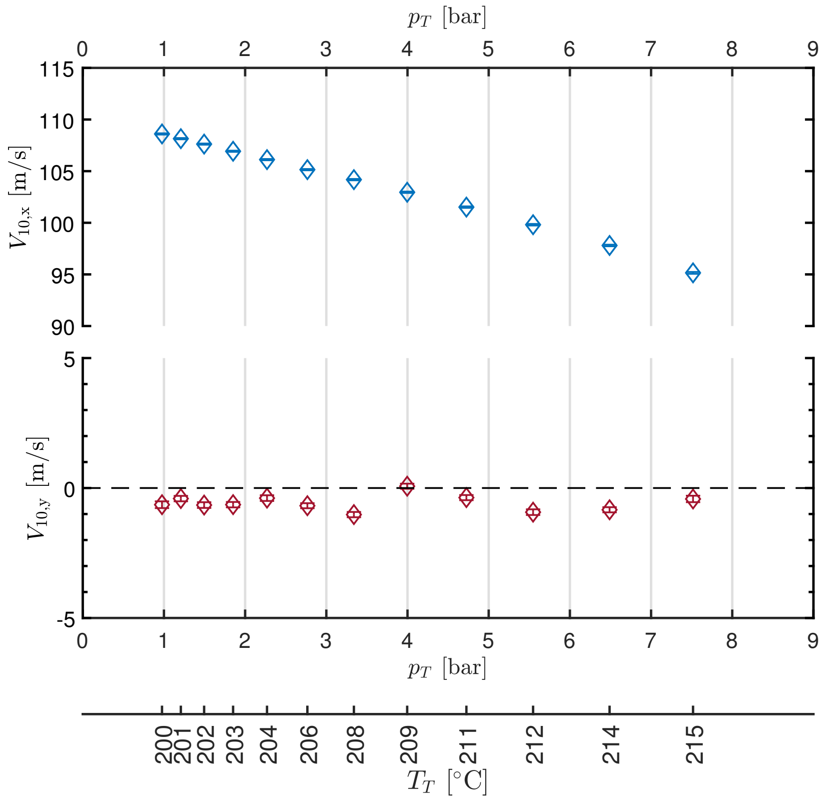

Figure 7.12: Measured x and y velocity components at tap 10 as a function of total pressure p_T and total temperature T_T for the test CM07.MM81.

the difference between the velocity magnitude V and the x component V_x would be approximately 0.1%.

Results of test CM07.MM81 are now discussed. Static-to-total pressure ratio and velocity as a function of total conditions are analyzed. Experimental quantities are compared to those extracted at the measurement point from a 2D viscous CFD calculation carried out with Ansys Fluent. The flow symmetry with respect to the nozzle x axis is exploited; the computational domain is composed by the converging nozzle with a sudden enlargement after the geometrical throat. The mesh is hybrid: triangular in the nozzle core and in the downstream enlargement, and quadrilateral with proper refinement near the wall, for a correct solution of the boundary layer. Differently from the the case of the supersonic nozzle discussed in Chapter 6 where only the converging-diverging portion was modeled, in the case of a converging nozzle the region where the flow is discharged must also be modeled. Indeed, in this case, at the nozzle outlet (geometrical throat) the flow is still slightly subsonic, thus the downstream enlargement is needed to reach $M = 1$ and defining a sonic line, as happens in the real condition occurring in the TROVA. A grid independence study was carried out, and the finest mesh consisting of 191 560 elements was used for all presented calculations. The employed turbulence model is $k - \omega$ SST, the thermodynamic model is the Helmholtz energy EOS for MM by Thol et al. [82] implemented in RefProp, and the solver is density based. Applied boundary conditions are "pressure inlet", where total pressure and total temperature measured in the plenum are specified at the inlet, and "pressure outlet", where the downstream static pressure is imposed at the enlargement outlet. The solution is initialized with a uniform zero velocity flow at pressure and temperature equal to inlet total conditions. The Full Multi Grid (FMG) initialization is then used to speed up convergence. The solution is computed as steady for each of the considered thermodynamic conditions. Indeed, as already mentioned, the characteristic time of the nozzle is much smaller than the one of the evolution in time of total conditions, thus at each instant of time the flow in the nozzle can be considered as quasi-steady.

For a comparison with LDV, the flow velocity can be computed also from total conditions and the measured static pressure, by resorting to the isentropic expansion hypothesis. Enthalpy and entropy of the total state are computed from p_T and T_T using the Helmholtz energy model for MM. Entropy is conserved along the expansion, thus the enthalpy in correspondence of the pressure tap can be computed as a function of entropy of the total state and measured pressure. From a simple steady energy balance the flow velocity can then be computed. The following equations summarize the procedure:

$$h_T = h\left(p_T, T_T\right) \tag{7.19a}$$

$$s = s\left(p_T, T_T\right) \tag{7.19b}$$

$$h = h(p, s) \tag{7.19c}$$

$$V = \sqrt{2\left(h_T - h\right)}. \tag{7.19d}$$

Figure 7.13 shows the experimental results of test CM07.MM81. The chart structure is similar to the one already discussed for repeatability. The bottom graph reports the total conditions p_T and T_T along with the MM saturation curve and total compressibility factor Z_T contours. The central graph shows the measured velocity (purple) along with those calculated from total conditions and the measured static pressure under the isentropic hypothesis. As previously mentioned, pressure was measured at tap 9 and 10, thus two velocity values are reported. The velocity extracted at the measurement point from the CFD calculation is also plotted. The top graph reports the measured and extracted from CFD static-to-total pressure ratio. The right axis reports the compressibility factor at the measurement point, computed from total conditions and the measured static pressure.

The pressure ratio at the two selected taps is almost the same, thus confirming the non accelerating behavior of the flow in this region. As expansions starting from more ideal states (increasing Z_T) are considered, decreasing p/p_T are observed, accordingly with the result of Chapter 6 and the 1D theory.

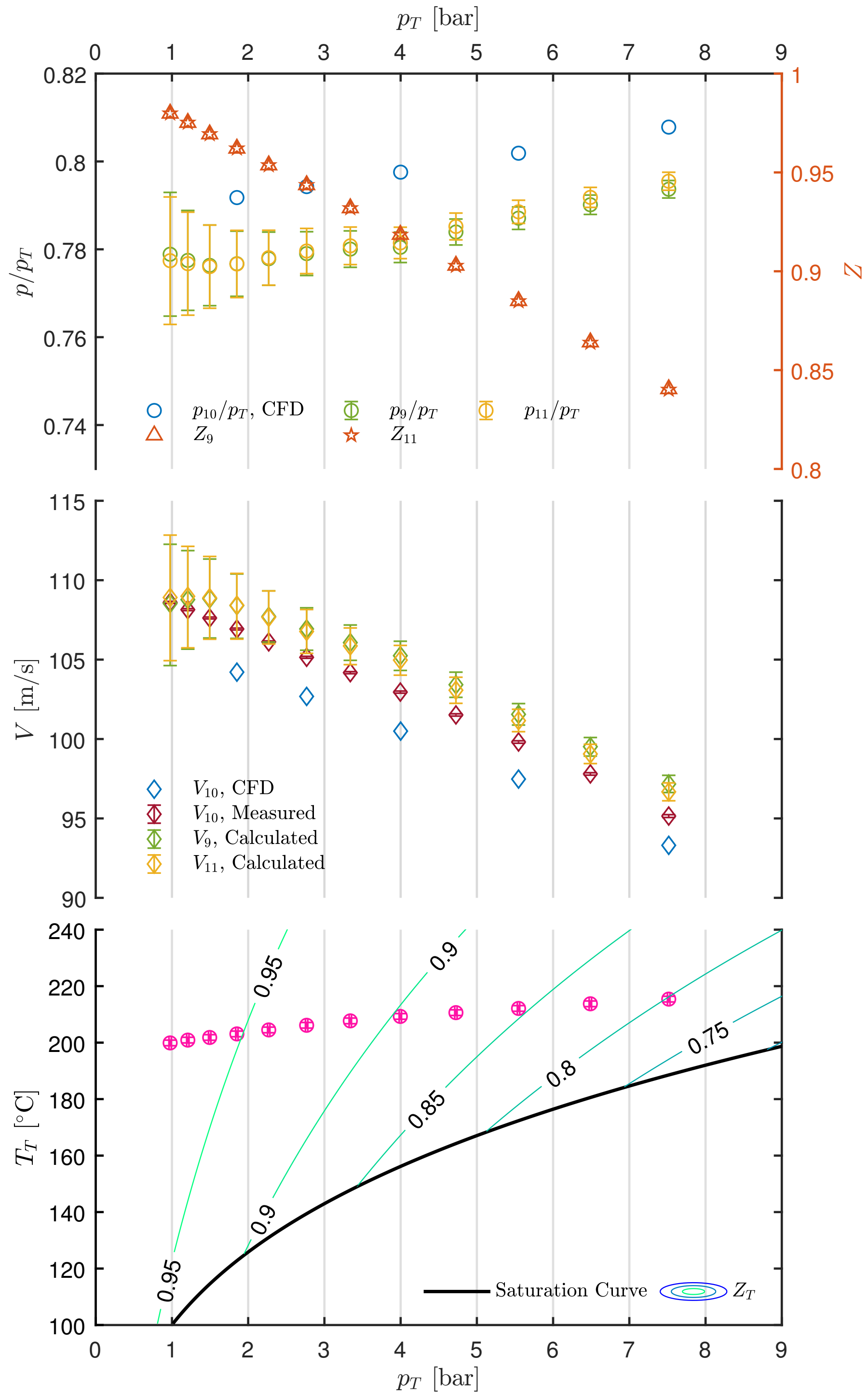

Figure 7.13: Results of test CM07.MM81. Top left axis: static pressure at the nozzle axis measured at tap 9 and 11 (p_9 and p_{11}) as a function of total pressure p_T. Top right axis: compressibility factor at the measurement point. Center: velocity measured at the nozzle axis in correspondence of tap 10 (V_{10}) as a function of p_T along with velocity calculated from p_T, T_T and p. Velocity extracted at the measurement point from CFD is also plotted. Bottom: total temperature T_T as a function of total pressure p_T, along with the saturation curve of MM and superimposed to contours of total compressibility factor Z_T. All uncertainty bars correspond to 95% confidence level.

Velocity increases as dilute conditions are approached. In the ideal-gas case, for a given position along the nozzle axis, the Mach number, total-to-static temperature and pressure ratio are fixed. Thus, velocity can change only if a variation of temperature occurs. Indeed, the speed of sound depends on temperature only ($c^2 = \gamma RT$). In the considered case, total and static temperature at tap 10 slightly reduce as ideal gas states are approached. This, in the case of an ideal gas, would lead to a limited *decrease* of velocity, due to $V = M \cdot c$. From another point of view, enthalpy is function of temperature only, thus velocity is proportional to the difference $(T_T - T)^{1/2} = [T_T(1 - T/T_T)]^{1/2}$, thus to total temperature, since T/T_T is fixed from the cross sectional area ratio. An increase of velocity would be related to increasing T_T, contrarily to what is observed here. For this reason the increase of velocity observed in test CM07.MM81 is to be ascribed to non-ideal effects.

At non-ideal gas states, the speed of sound is lower than its ideal counterpart due to the effect of repulsive and attractive forces. The former have a positive contribution that, however, is more than compensated by the negative one due to attractive forces, thus leading to a speed of sound lower than ideal gas (Colonna and Guardone [21]). Moving from dense gas states to ideal gas ones, the negative effect of attractive molecular forces and the positive one originating from repulsive ones tends to zero, thus increasing the values of speed of sound. Mach number also increases, as it was observed in Section 6.4.3, thus leading to an increasing velocity due to $V = M \cdot c$.

Pressure ratio and velocity trends are well captured. The accordance between measurements and computed values is evaluated through percentage differences defined as

$$d_{r\%}\left(\frac{p}{p_T}\right) = \frac{\left(\frac{p}{p_T}\right)_{CFD} - \left(\frac{p}{p_T}\right)_{Exp}}{\left(\frac{p}{p_T}\right)_{Exp}} \cdot 100, \tag{7.20}$$

and

$$d_{V,r\%} = \frac{V_{Calc} - V_{Exp}}{V_{Exp}} \cdot 100, \tag{7.21}$$

where V_{Exp} refers to the measured velocity, while V_{Calc} refers to the velocity computed from $p - p_T - T_T$ or the one extracted from CFD. The related uncertainty is obtained as

$$u_{d_{r\%}}\left(\frac{p}{p_T}\right) = \frac{100}{\left(\frac{p}{p_T}\right)_{Exp}} \cdot \cdot \sqrt{\left(\frac{\left(\frac{p}{p_T}\right)_{CFD}}{\left(\frac{p}{p_T}\right)_{Exp}}\right)^2 \cdot \left(u\left(\frac{p}{p_T}\right)_{Exp}\right)^2}, \tag{7.22}$$

and

$$u_{d_{V,r\%}} = \frac{100}{V_{Exp}} \cdot \cdot \sqrt{\left(u\left(V_{Calc}\right)\right)^2 + \left(\frac{V_{Calc}}{V_{Exp}}\right)^2 \cdot \left(u\left(V_{Exp}\right)\right)^2}. \tag{7.23}$$

No uncertainty is considered for values extracted from CFD. $u\left(V_{Exp}\right)$ corresponds the one computed from the bootstrap technique applied to LDV data. In the case of velocity computed from $p - p_T - T_T$, the uncertainty was computed with the Monte Carlo method, using the measurement uncertainties as input.

Figure 7.14a shows $d_{r\%}\left(p/p_T\right)$ as a function of total conditions p_T and T_T. The agreement is very good, as the percentage deviation is approximately below 2.2% for each considered condition. $d_{V,r\%}$ is reported in Figure 7.14b and shows a very good agreement between LDV measurements and both CFD and values computed from pressure and temperature. The deviation is approximately below 2% in this case also. The good accordance between LDV and computed values from $p - p_T - T_T$ proves the consistency between LDV and both pressure and temperature measurements.

As a reference, the relative percentage uncertainty of the quantities reported in Figure 7.13 is plotted in the graph of Figure 7.15. The relative uncertainty of pressure ratios (and consequently of computed velocities) increases as total pressure decreases, due to the decrease of measured value and the consequent increase of relative uncertainty of pressure measurements.

Very good accordance between measurements and computed values.

Summarizing, the accordance between measurements and computed values is very good, with deviations below 2%. Measured trends of both p/p_T and V prove the non-ideal behavior of the flow.

7.9.2 *Supersonic non-accelerating flow*

7.9.2.1 *Test conditions and consistency*

After the feasibility of laser Doppler velocimetry in a subsonic non-accelerating flow was proved, the following step is the characterization of a supersonic non-accelerating flow, thus entailing a higher velocity, with respect to the case of Section 7.9.1. Therefore, the nozzle employed in this campaign is M16. Two different tests are presented here for the assessment of consistency and repeatability, whose thermodynamic conditions are reported in Table 7.8. The two extreme cases of minimum and maximum total compressibility factor are reported, showing that expansions featuring $0.75 \lesssim Z_T \lesssim 0.96$ were observed. The maximum temperature is $< 210\,°\mathrm{C}$, which is far below the interval where thermal stability problems may arise. The MCV was 100% open far all the test, thus total pressure is resulting from the emptying of the HPV.

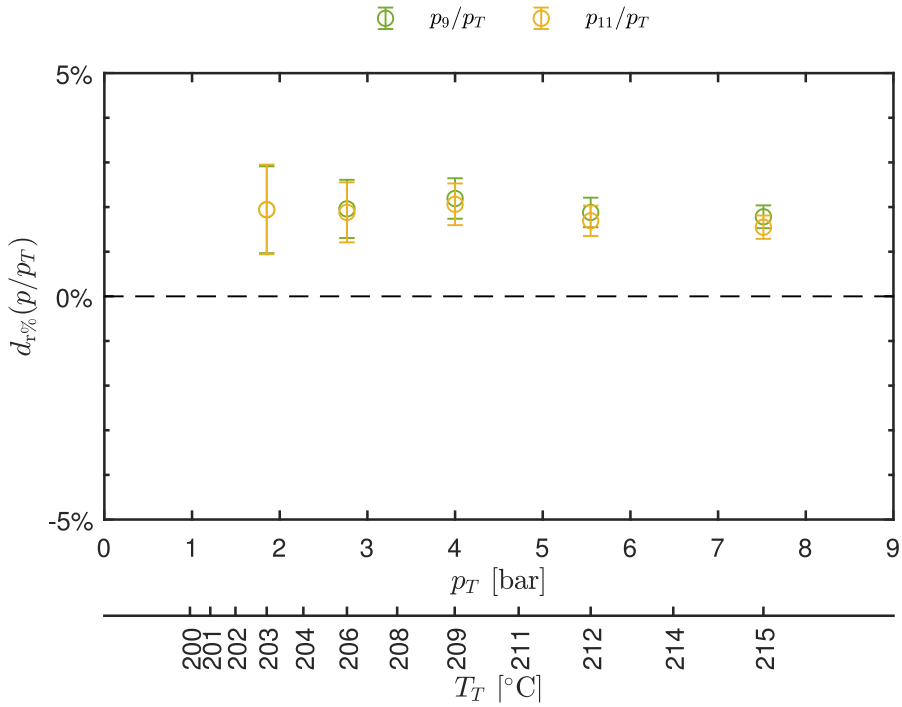

(a) Percentage difference of total-to-static pressure ratio $d_{r\%}\left(\frac{p}{p_T}\right)$.

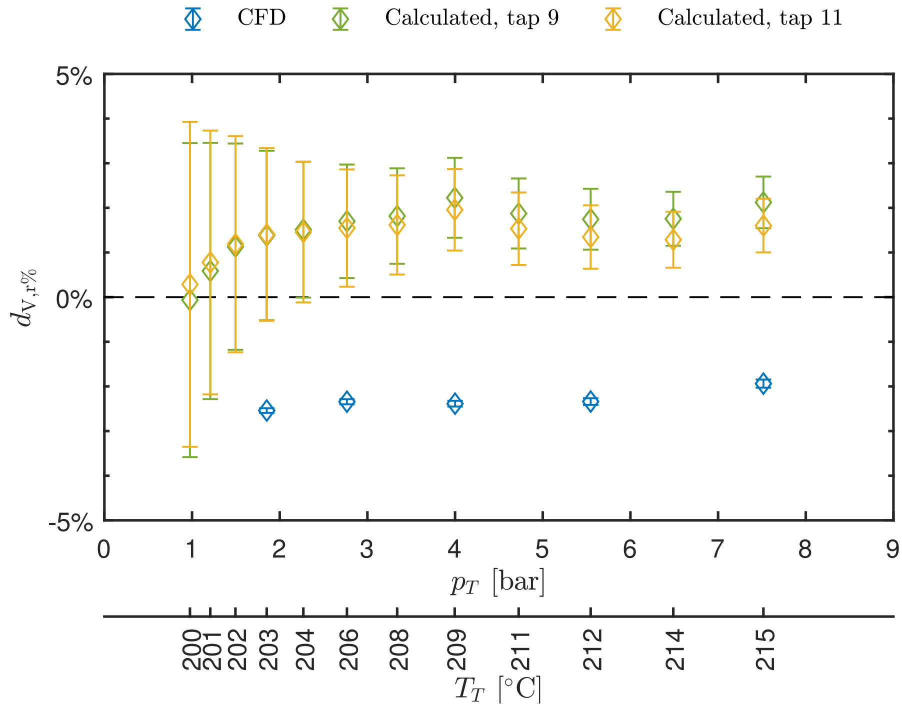

(b) Percentage difference of velocity $d_{V,r\%}$.

Figure 7.14: Percentage differences between measured and computed values as a function of total conditions p_T and T_T for test CM07.MM81.

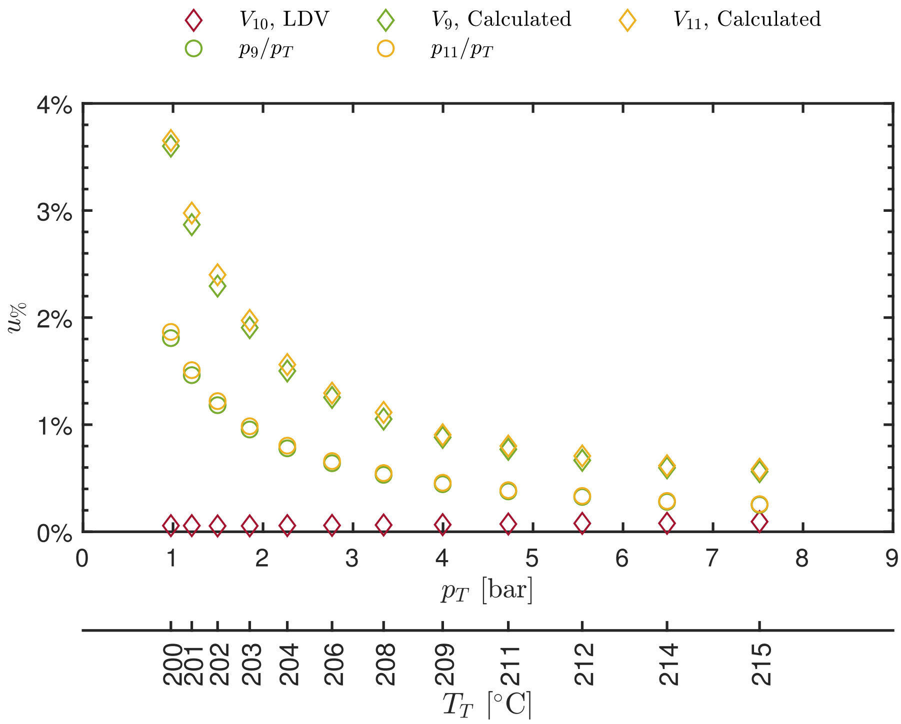

Figure 7.15: Relative percentage uncertainties of observed quantities of test CM07.MM81.

Table 7.8: Thermodynamic conditions of tests carried out on the nozzle M16 in correspondence of tap 11 with siloxane MM. Total pressure p_T, total temperature T_T, and total compressibility factor $Z_T(T_T, p_T)$ are reported for the most non-ideal condition and for the most ideal one.

		Min. Z_T condition			Max. Z_T condition		
Test id	Nozzle	p_T [bar]	T_T [°C]	Z_T [-]	p_T [bar]	T_T [°C]	Z_T [-]
MM93	M16	8.277	206	0.749	1.330	197	0.964
MM94	M16	8.400	207	0.749	1.528	197	0.959

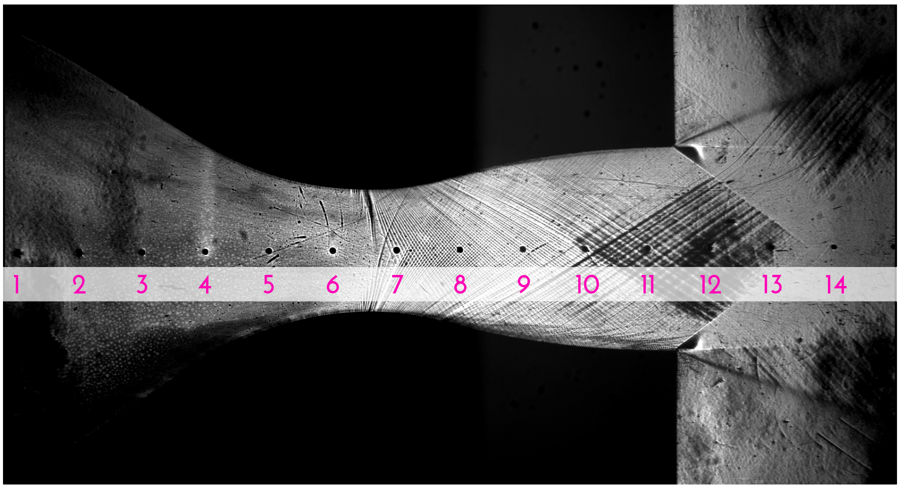

Figure 7.16: Schlieren image of the flow in the M16 nozzle. The numbered black dots are the pressure taps.

The nozzle, after the geometrical throat, features a first part responsible for the expansion and acceleration of the flow to the desired state, and a second part designed to turn the current to obtain a uniform flow at the outlet (at design point). In this region, gradients along the nozzle axis are approximately zero. At off-design conditions, instead, the cross-sectional area profile does not allow to attain a perfectly uniform flow. Indeed, the profile of flow quantities at the discharge section along the y coordinate features a uniform region near the nozzle axis, with gradients as profiled walls are approached. Thus an almost zero gradient region is still present, but with different dimension and position. To give an idea Figure 7.16 shows a schlieren image taken from a test performed with nozzle M16, where the position of pressure taps is highlighted. The flow goes from left to right. Between taps 10 to 14, an almost uniform region, as shown by nearly parallel Mach lines, is present. The chosen measurement point is in correspondence of tap 11, which is the last tap upstream of the nozzle outlet in the almost uniform region.

The configuration of the LDV system is the same as for subsonic tests. Pressure is measured at the same position where velocity measurements are taken (tap 11).

Figure 7.17 shows a comparison between measured quantities during tests M16.MM93-94. The static pressure p is reported in the top chart, while the central one shows measured velocity. From the bottom graph total conditions p_T and T_T are obtainable. Measurements and tests conditions are consistent.

7.9.2.2 *Results*

The test M16.MM94 is chosen as representative of this condition and is now discussed. The explored thermodynamic region is shown in

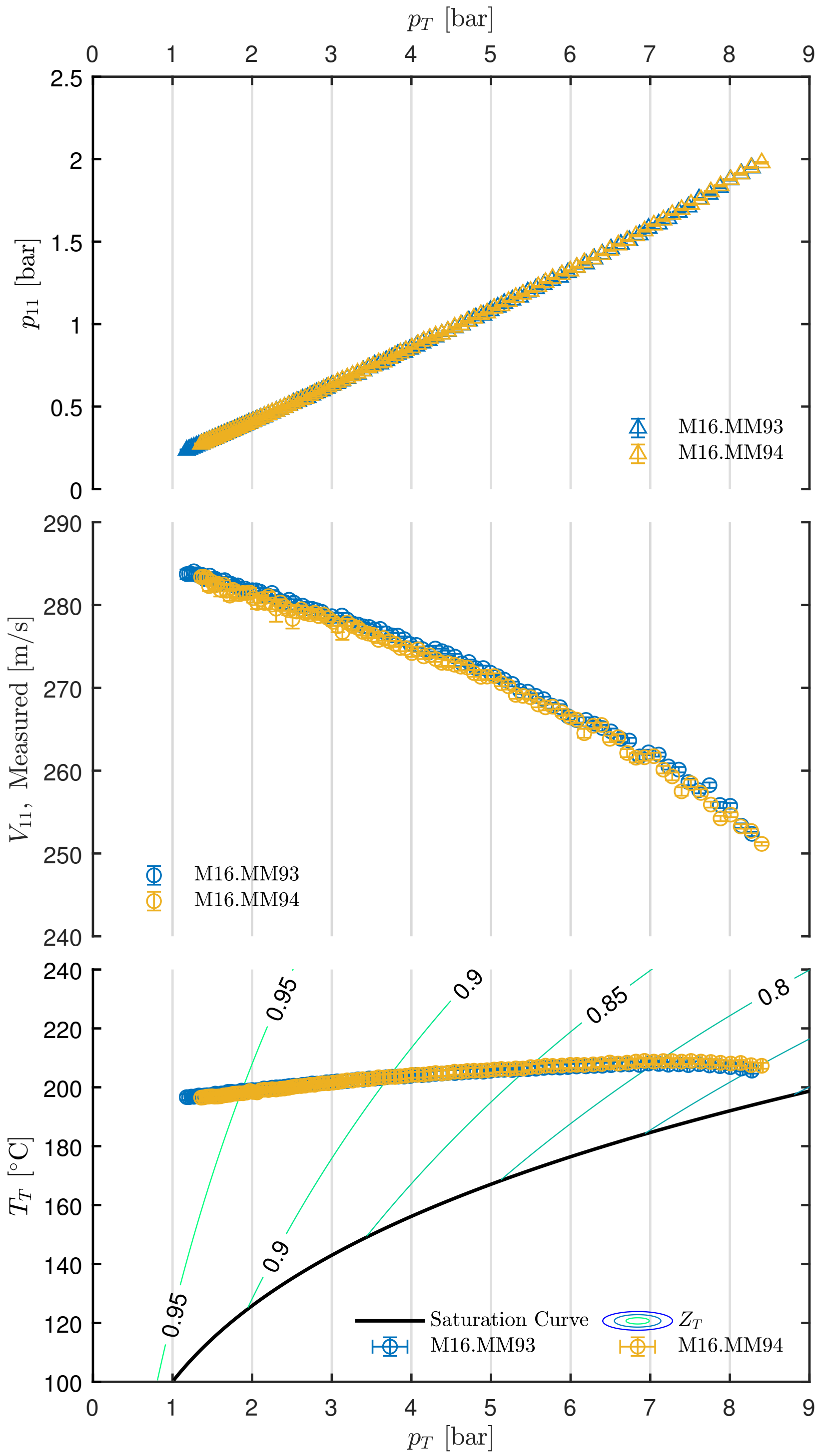

Figure 7.17: Repeatability of tests M16.MM93-94 (see Table 7.8 for thermodynamic conditions). Top: static pressure at the nozzle axis measured at tap 11 (p_{11}) as a function of total pressure p_T. Center: velocity measured at the nozzle axis in correspondance of tap 11, V_{11} as a function of p_T. Bottom: total temperature T_T as a function of total pressure p_T, along with the saturation curve of MM and superimposed to contours of total compressibility factor Z_T. All uncertainty bars correspond to 95% confidence level.

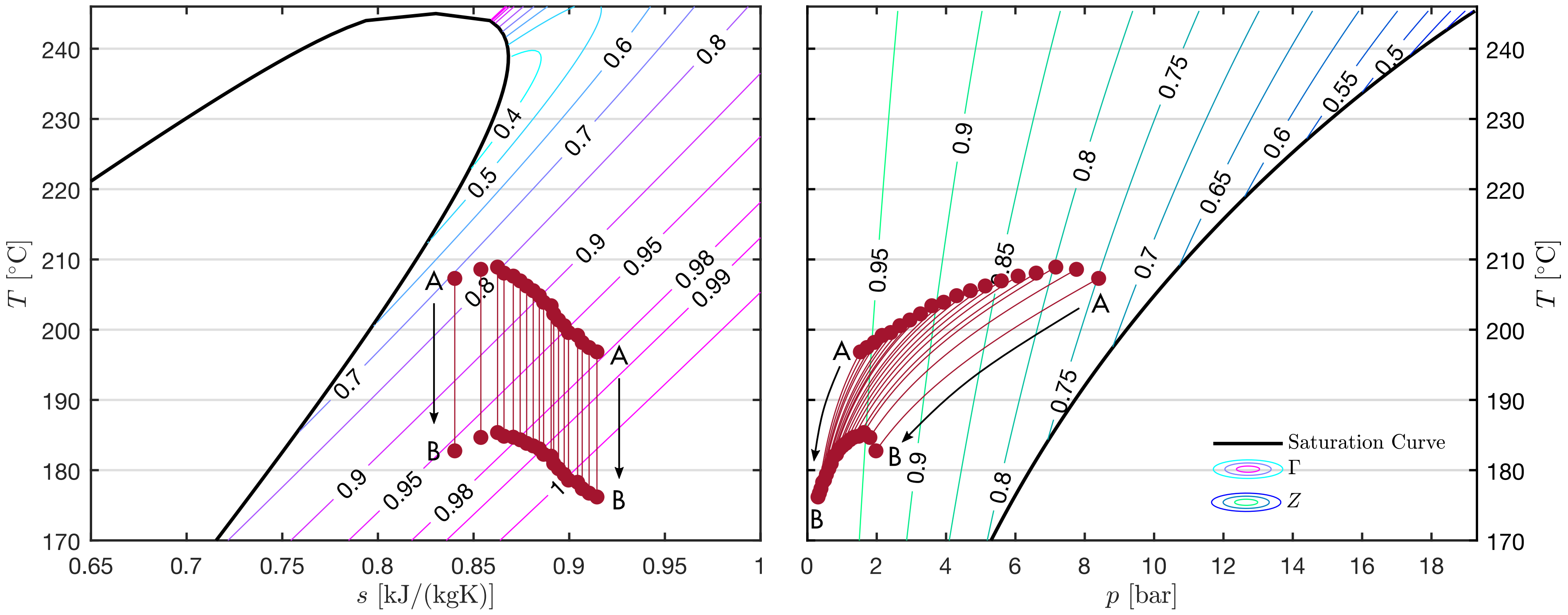

Figure 7.18: Explored thermodynamic region during tests M15.MM94. The chart reports the expansions carried out during the test and selected for discussion in a temperature T - specific entropy s diagram (left) and a temperature T - pressure p diagram (right). Contours of fundamental derivative of gasdynamics Γ (left) and of compressibility factor Z (right) are reported along with the liquid-vapor saturation curve. Expansions proceed from the total state (A) to the static state corresponding to the measurement point (B).

Figure 7.18, where the expansions selected for discussion are reported on a temperature T - specific entropy s diagram, along with Γ iso-lines, and on a pressure p - temperature T diagram, superimposed to Z contours. Each expansion starts from total state (labeled A) and ends at static state B, corresponding to the measurement point. As already discussed, the transformation can be considered isentropic. Due to the retrograde shape of the Andrews curve of MM, as the the expansion proceeds along the nozzle, the fluid becomes more and more superheated, thus the local compressibility factor at the measurement point is $\gtrsim 0.95$.

Figure 7.19 shows the experimental results of test M15.MM94. The bottom chart reports the total temperature T_T and pressure p_T for each selected expansion. The top graph reports experimental static-to-total pressure ratios, along with those obtained at the measurement point from a 2D CFD calculation. The domain was restricted to the converging diverging nozzle while the mesh is quadrilateral and structured. Appropriate refinement near the wall is present, to properly solve the boundary layer. Three meshes of different element size were considered and the finest one consisting of 37 152 cells was employed for all calculations, after a grid independence analysis. The calculation was carried out with Ansys Fluent and the $k-\omega$ SST model was adopted for turbulence modeling. The thermodynamic model is the Helmholtz energy one implemented in RefProp for MM (Thol et al. [82]) and the solver is density based. The "pressure inlet" boundary condition is specified, where total pressure and total temperature measured in the plenum are set. At outlet, static pressure is imposed through the "pressure outlet" boundary condition. This latter value is used to make the solution go supersonic from the initial state and is then discarded as Mach number at the outlet becomes $M_{out} > 1$. Thus, the outlet static pressure is set to a value slightly lower than the one needed to achieve a supersonic flow in the whole nozzle. As for the CM07 case, the solution is initialized at zero velocity and at inlet pressure and temperature. Also in this case, the Full Multi Grid (FMG) initialization is used to speed up convergence.

The decreasing trend of p/p_T for decreasing total pressure of the top chart of Figure 7.19 is in accordance with the increase in total compressibility factor Z_T, that can be appreciated from the contours of the bottom chart. The central graph reports the measured velocity at tap 11, compared to the one obtained from the CFD simulation and the one computed from total conditions and static pressure, by resorting to the insentropic transformation hypothesis. Velocity increases as ideal states are approached, as discussed in the case of the subsonic nozzle test.

The comparison in terms of percentage difference of static-to-total pressure ratios between CFD and experiments (Equation 7.20 and Equation 7.22) reported in Figure 7.20a shows a non-negligible devia-

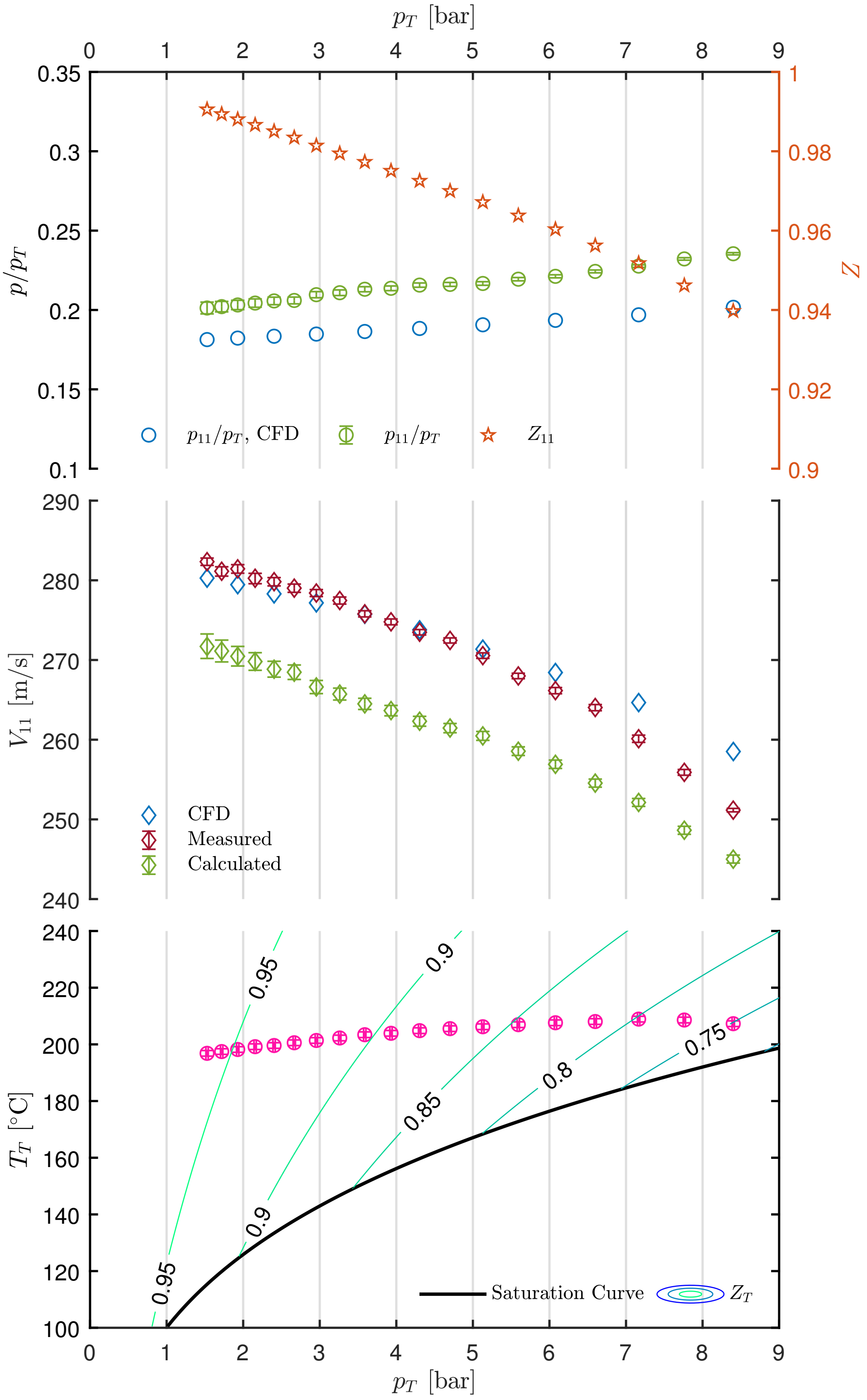

Figure 7.19: Results of test M15.MM94. Top left axis: static pressure at the nozzle axis measured at tap 11 (p_{11}) as a function of total pressure p_T. Top right axis: compressibility factor at the measurement point. Center: velocity measured at the nozzle axis in correspondance of tap 11 (V_{11}) as a function of p_T along with velocity calculated from p_T, T_T and p. Velocity extracted at the measurement point from CFD is also plotted. Bottom: total temperature T_T as a function of total pressure p_T, along with the saturation curve of MM and superimposed to contours of total compressibility factor Z_T. All uncertainty bars correspond to 95% confidence level.

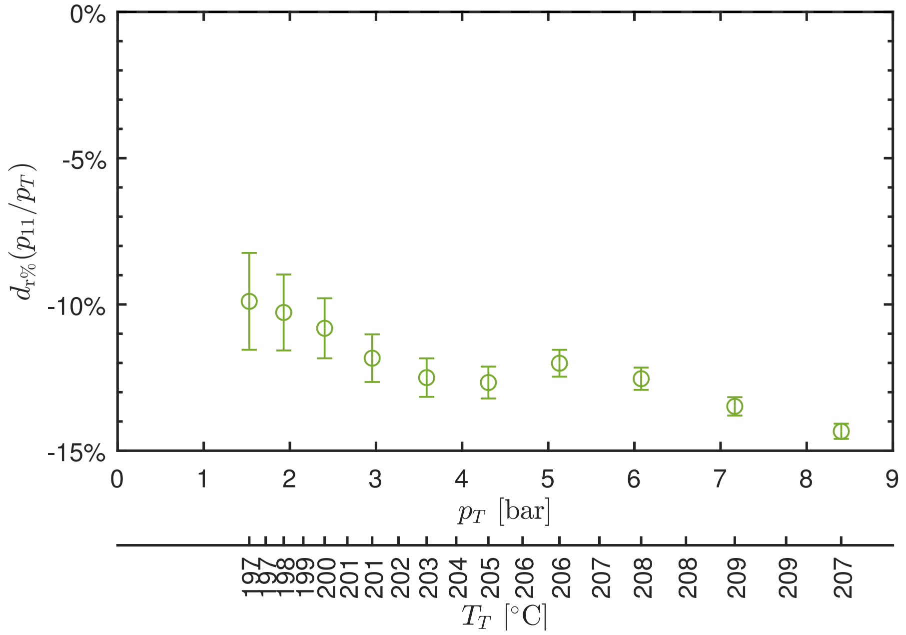

(a) Percentage difference of total-to-static pressure ratio $d_{r\%}\left(\frac{p}{p_T}\right)$.

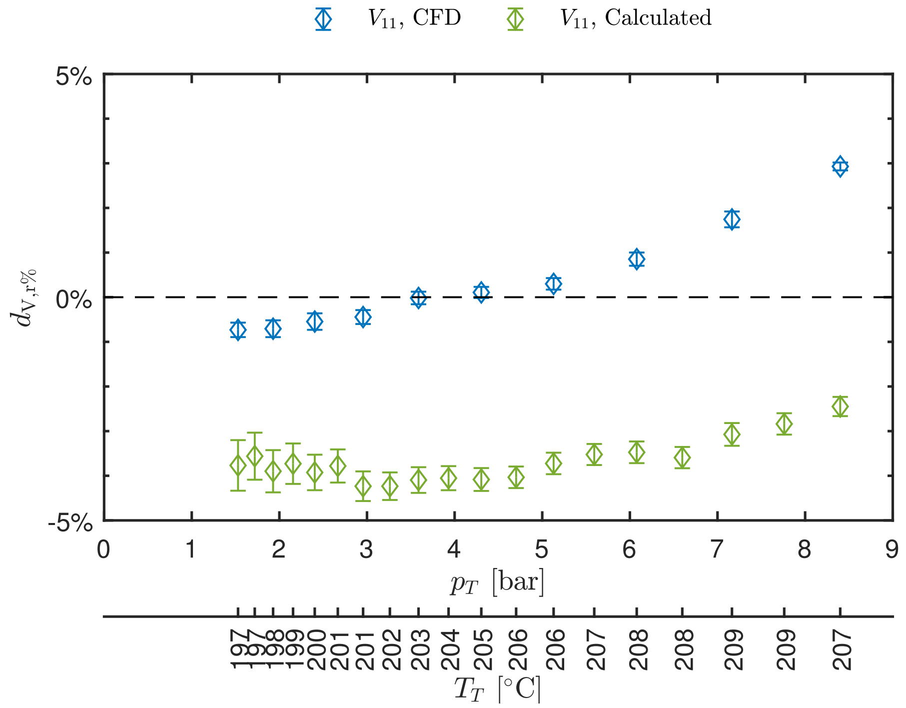

(b) Percentage difference of velocity $d_{V,r\%}$.

Figure 7.20: Percentage differences between measured and computed values as a function of total conditions p_T and T_T for test M15.MM94.

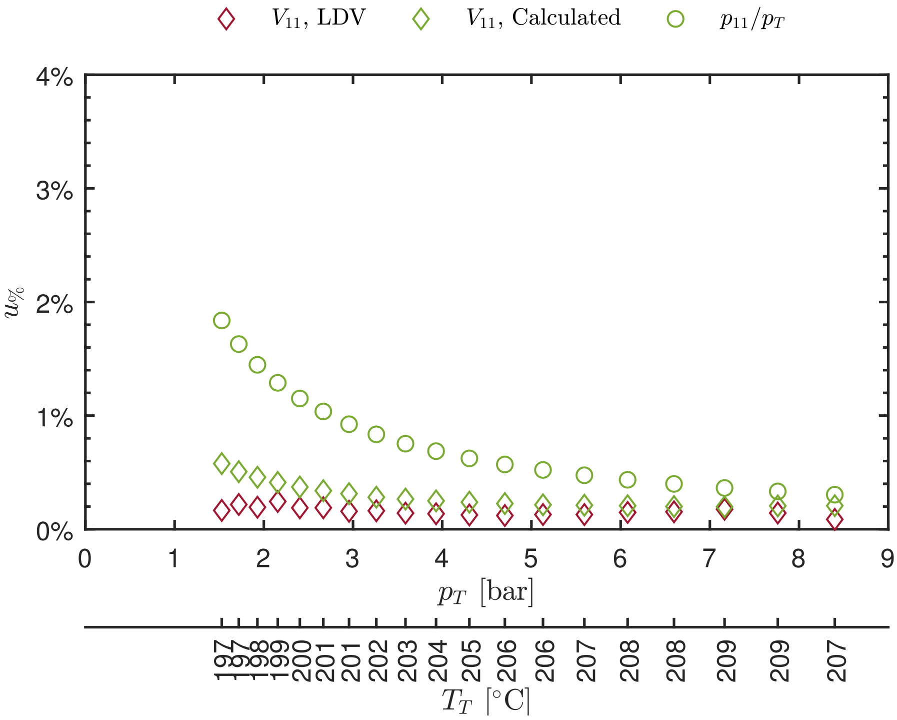

Figure 7.21: Relative percentage uncertainties of observed quantities of test M15.MM94.

tion, that is as high as 14.3% in the most non-deal state and decreases to ≈ 9.9% at the highest Z_T. These values are of the same order of the deviations already observed in tests carried out with MDM and nozzle M2 (Section 6.4.2). As already mentioned in Chapter 6, similar results were observed by Robertson et al. [71]: deviations of p/p_T at the last pressure tap between CFD and experiments were found to be $9.12 \div 23.36\%$ and $6.63 \div 20.65\%$ for Peng-Robinson and Helmholtz energy model respectively, for a supersonic flow ($M \approx 2$) of R1233zd(E).

Measured and computed velocities were compared by means of percentage deviations with respect to those measured by LDV (Equation 7.21 and Equation 7.23). Regarding CFD data, the deviation is maximum (≈ 2.9%) at the expansion corresponding to minimum Z_T, while reduces to less than 1% at maximum Z_T passing through the zero line. Velocity computed from pressure and temperature measurements deviates from a minimum of ≈ 2.4% to a maximum of ≈ 4.2%. In general, the accordance is very good between CFD and LDV, while it is worse but still satisfactory between LDV and velocity calculated from $T_T - p_T - p$. It is worth to point out that deviations between CFD and experimental pressure ratios of $\approx 10 \div 15\%$ lead to a discrepancy of only $\approx 4 \div 5.5\%$ between CFD and computed velocity.

The accordance in terms of pressure ratios is not fully satisfactory, while it is good in terms of velocity.

To conclude, the relative uncertainties of the measurements discussed in this section are given in Figure 7.21. Regarding LDV, $u_{\%}$ is always below 0.25%, while the p/p_T one lies in a range $0.3\% \div 1.8\%$.

Table 7.9: Thermodynamic conditions of tests carried out on the nozzle M16 with siloxane MM, for the measurement of velocity at tap 8, a region of high velocity gradient at approximately Mach number $M = 1.4$. Total pressure p_T, total temperature T_T, and total compressibility factor $Z_T(T_T, p_T)$ are reported for the most non-ideal condition and for the most ideal one.

Test id	Nozzle	Min. Z_T condition p_T [bar]	T_T [°C]	Z_T [-]	Max. Z_T condition p_T [bar]	T_T [°C]	Z_T [-]
MM101	M16	8.047	210	0.769	1.318	200	0.966
MM102	M16	8.321	208	0.752	1.488	199	0.960
MM103	M16	8.134	204	0.750	1.372	197	0.963

The increase of percentage uncertainty when going towards ideal states is related to the low corresponding total and static pressure. Obviously, the same trend holds for computed velocity also, with a maximum value of $\approx 0.6\%$.

7.9.3 *Supersonic accelerating flow*

7.9.3.1 *Test conditions and consistency*

The aim of these tests is to characterize the flow and assess the feasibility of laser Doppler velocimetry in a supersonic accelerating flow. Thus the tested nozzle is M16. Three tests are here reported for a consistency and repeatability analysis. Table 7.9 reports the thermodynamic conditions at minimum and maximum Z_T during the test. The total compressibility factor goes from a minimum of $Z_T \approx 0.75$ to a maximum of $Z_T \approx 0.97$. From the thermal stability point of view, in this case also, the temperature needed to reach test conditions is safe. For all tests no pressure regulation was applied through the MCV.

The LDV measurement volume is placed in correspondence of tap 8, the second one downstream the geometrical throat, in the expansion region of the nozzle. Density and velocity gradients are non-negligible in that region. Figure 7.16 reports a schlieren image of the flow in the M16 nozzle, where the measurement position can be seen.

The configuration of the LDV system is the same as for the already discussed tests. Pressure is measured at the same position of the LDV probe (tap 8).

Figure 7.22 reports a comparison between measured quantities during tests M16.MM101-102-103. The top chart reports the static pressure p while the central graph the measured velocity V_8 and the bottom graph the total temperature T_T, all as a function of total pressure p_T. The accordance and repeatability of tests is good, if the

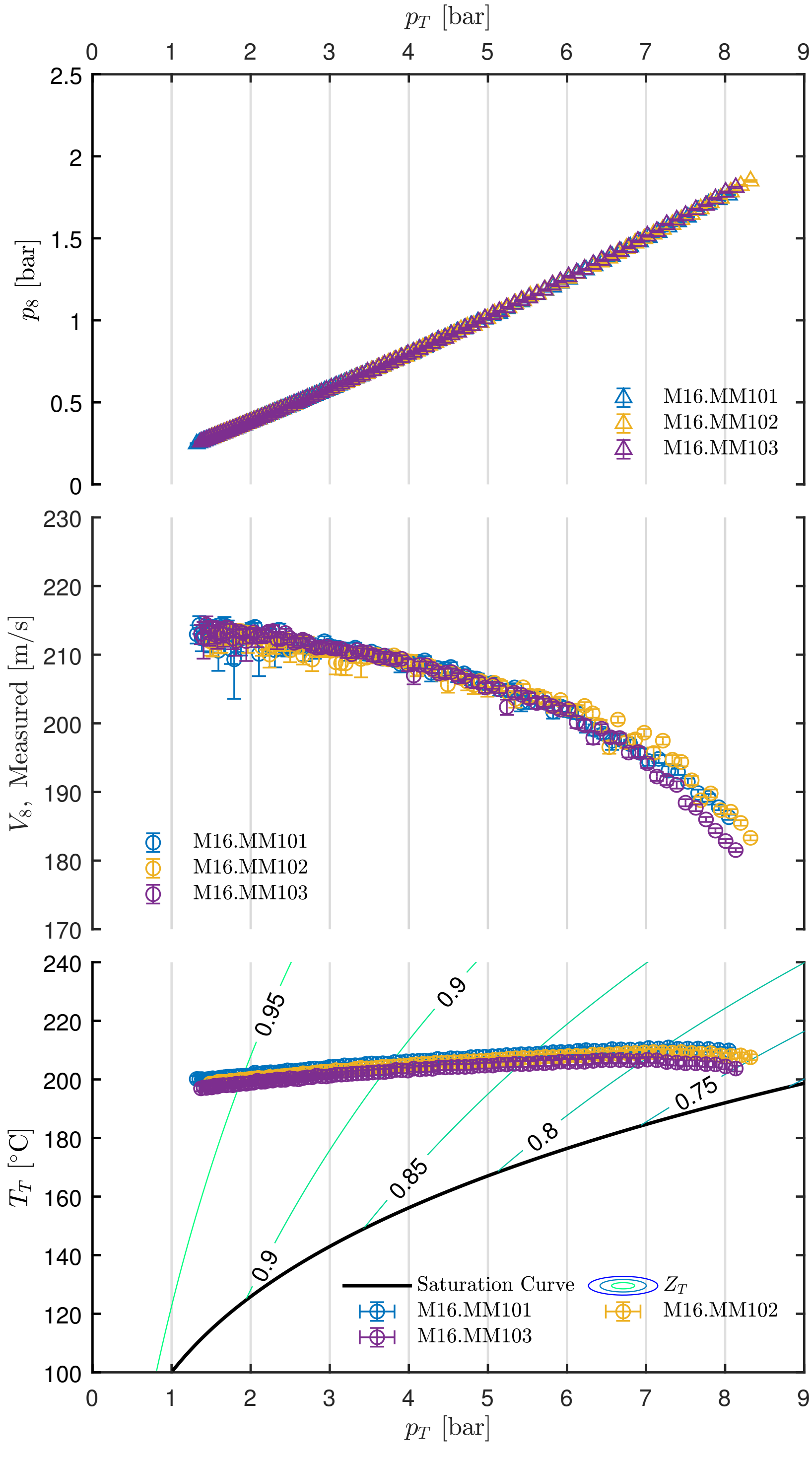

Figure 7.22: Repeatability of tests M16.MM101-102-103 (see Table 7.9 for thermodynamic conditions). Top: static pressure at the nozzle axis measured at tap 8 (p_8) as a function of total pressure p_T. Center: Velocity measured at the nozzle axis in correspondance of tap 8, V_8 as a function of p_T. Bottom: total temperature T_T as a function of total pressure p_T, along with the saturation curve of MM and superimposed to contours of total compressibility factor Z_T. All uncertainty bars correspond to 95% confidence level.

functioning principle of the employed wind tunnel is considered, as in the case of the already discussed CM07 and M16 tests.

7.9.3.2 *Results*

The test M16.MM101 is chosen for detailed results discussion. Figure 7.23 reports the expansions selected from the considered test, both in a temperature T - specific entropy s diagram (left, with contours of Γ) and a temperature T - pressure p diagram (right, with contours of Z). The expansion starts at total state A and reaches the condition at tap 8 labeled as B, following the direction of the arrow. Due to the flow expansion, at the measurement point the compressibility factor is $Z \gtrsim 0.95$, even if the expansion starts at non-negligible non-ideal conditions. The Γ at total conditions is $\Gamma \lesssim 1$.

Experimental results of test M16.MM101 are reported in Figure 7.24, with the same format as those of the already discussed tests. The bottom chart reports the total conditions of the expansions selected for discussion. The top chart compares the measured pressure ratios with those obtained at the measurement point from a 2D CFD calculation, carried out with the same setup already discussed in Section 7.9.2. The increase of pressure ratio for increasing non-ideality (increasing Z_T and thus p_T) is well captured by both measurements and CFD and is in accordance with the 1D theory and all previously discussed results.

The central graph shows the measured velocity V_8 along with the velocity extracted from the CFD simulation and the one computed from total conditions and static pressure, as explained in Section 7.9.1.2. The trend of the three sets of data is similar, but while the accordance between CFD and calculated velocity is optimal, measured ones show a slight deviation at high levels of non-ideality. Looking at bursts signals during the test, at test start, thus at high pressure, the distribution of measured velocities has a slightly wider tail towards low velocities with respect to following time instants. The numerosity of such bursts is small but sufficient to slightly bias the mean value. This tail could be ascribed to the presence, at test start, of impurities or agglomerated particles sedimented in between tests in the plenum or in the pipe connecting the seeding system to the atomizer. These particles could be dragged by the current during the initial part of the test. Further, at such high pressure and low Z_T conditions, the degree of superheating is the lowest of the whole test, thus the non-complete evaporation of the spray may occur. However, this was considered not probable, due to the results of the energy balance of Section 7.7 and since along the nozzle expansion the degree of superheating increases. However, to clarify this aspect further tests are currently planned. The increasing velocity for increasing Z_T is, in this case also, an indication of non-ideality of the flow, resulting from the increase of both Mach number and speed of sound resulting from the increase of Γ.

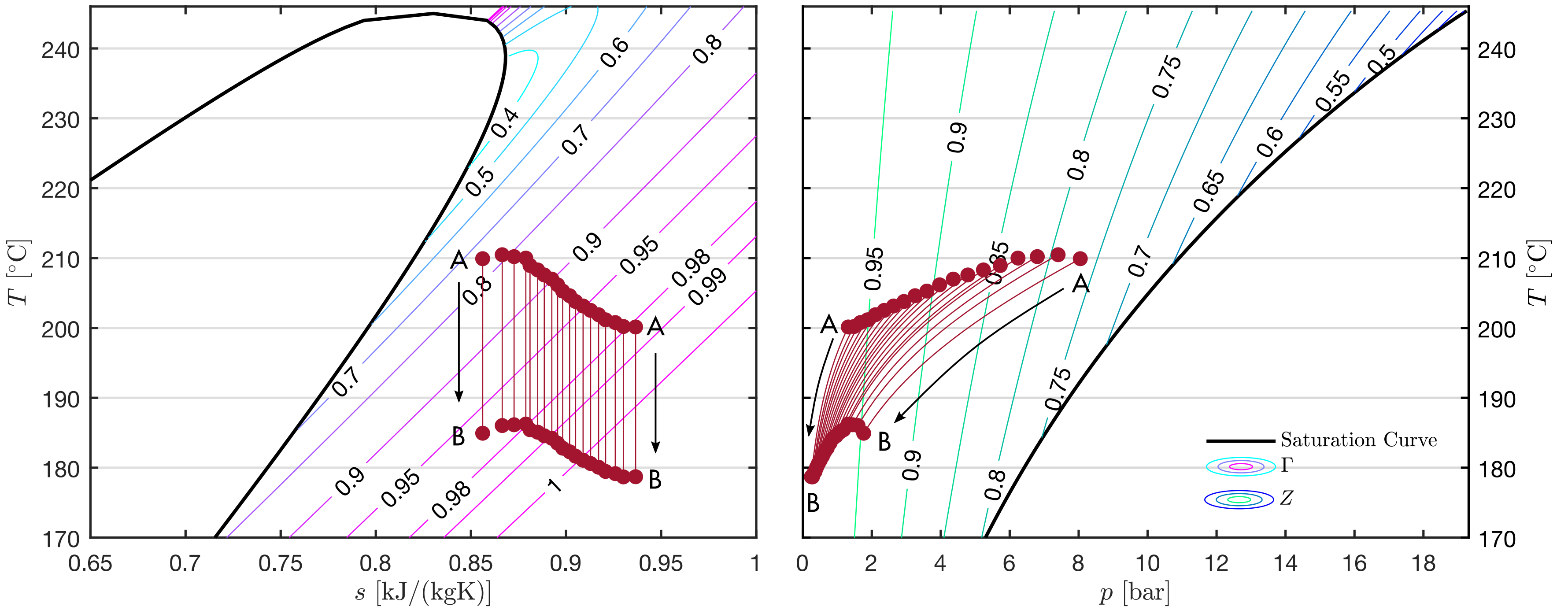

Figure 7.23: Explored thermodynamic region during tests M15.MM101. The chart reports the expansions carried out during the test and selected for discussion in a temperature T - specific entropy s diagram (left) and a temperature T - pressure p diagram (right). Contours of fundamental derivative of gasdynamics Γ (left) and of compressibility factor Z (right) are reported along with the liquid-vapor saturation curve. Expansions proceed from the total state (A) to the static state corresponding to the measurement point (B).

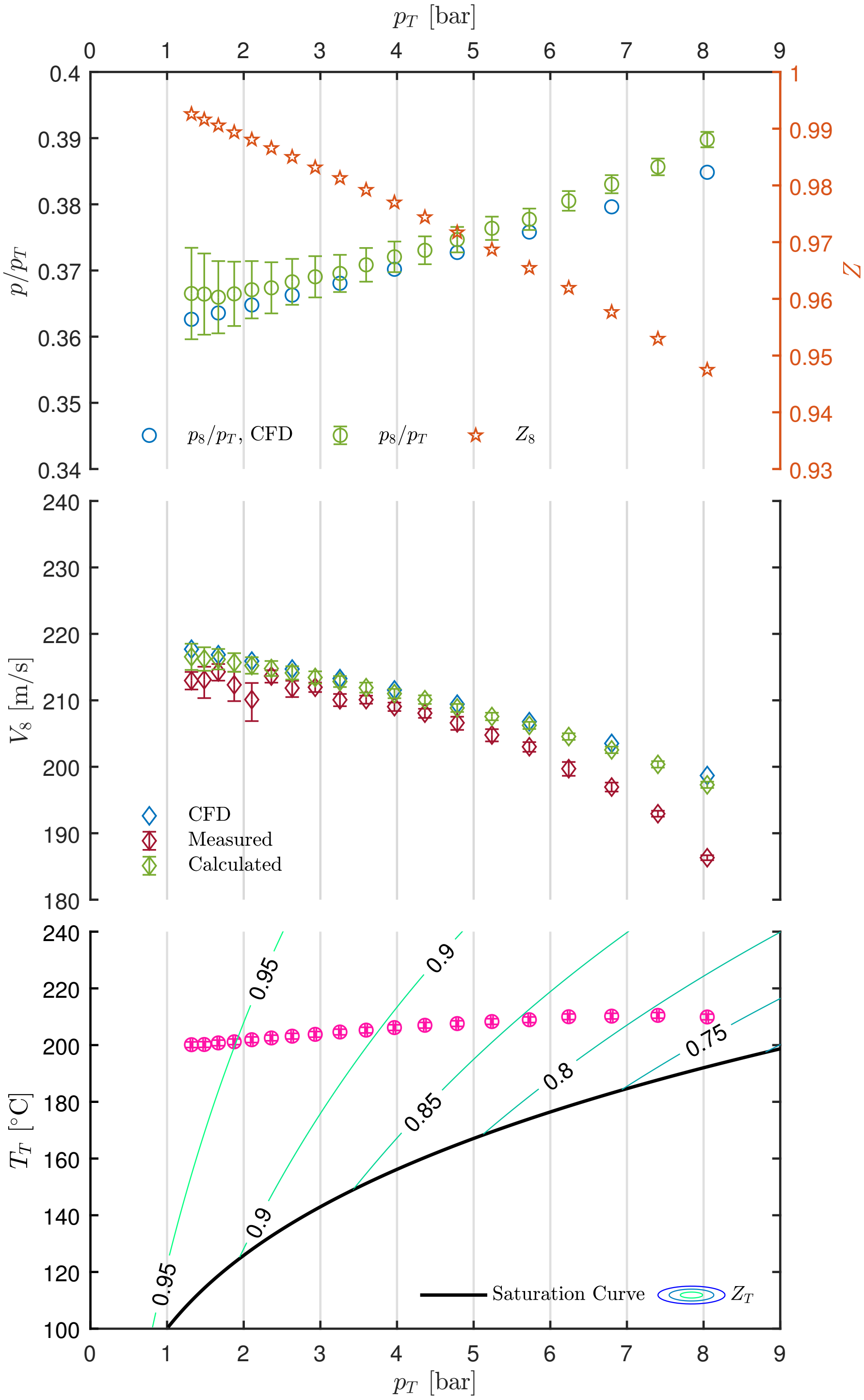

Figure 7.24: Results of test M15.MM101. Top left axis: static pressure at the nozzle axis measured at tap 8 (p_8) as a function of total pressure p_T. Top right axis: compressibility factor at the measurement point. Center: velocity measured at the nozzle axis in correspondence of tap 8 (V_8) as a function of p_T along with velocity calculated from p_T, T_T and p. Velocity extracted at the measurement point from CFD is also plotted. Bottom: total temperature T_T as a function of total pressure p_T, along with the saturation curve of MM and superimposed to contours of total compressibility factor Z_T. All uncertainty bars correspond to 95% confidence level.

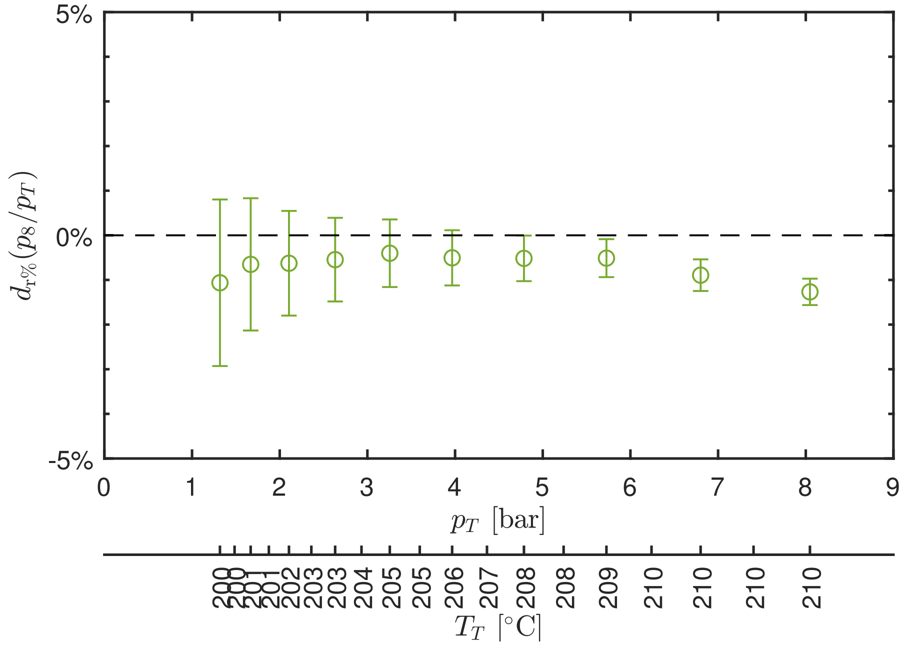

(a) Percentage difference of total-to-static pressure ratio $d_{r\%}\left(\frac{p}{p_T}\right)$.

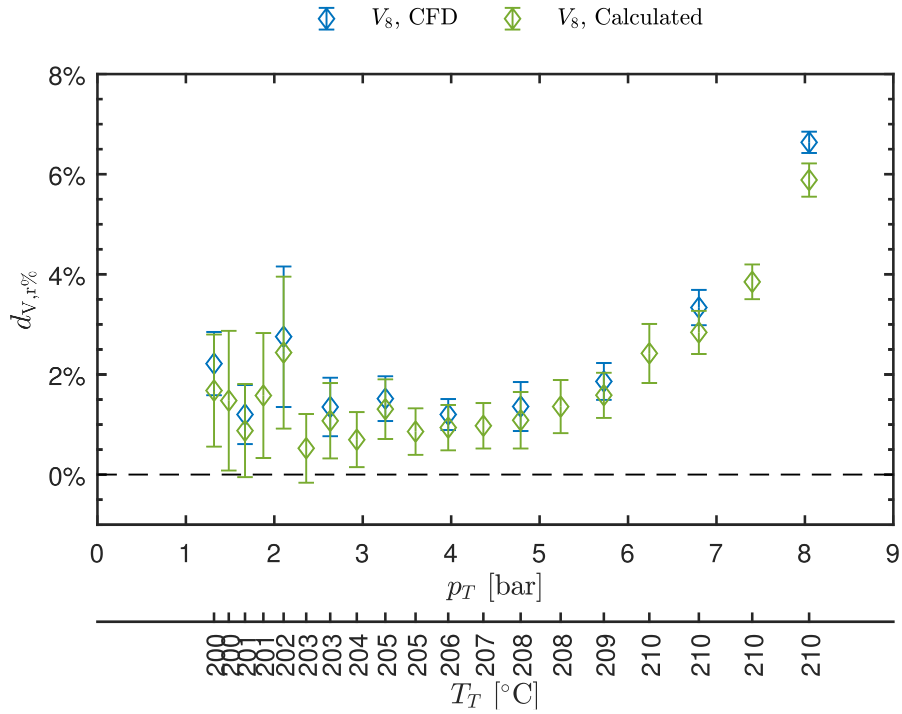

(b) Percentage difference of velocity $d_{V,r\%}$.

Figure 7.25: Percentage differences between measured and computed values as a function of total conditions p_T and T_T for test M15.MM101.

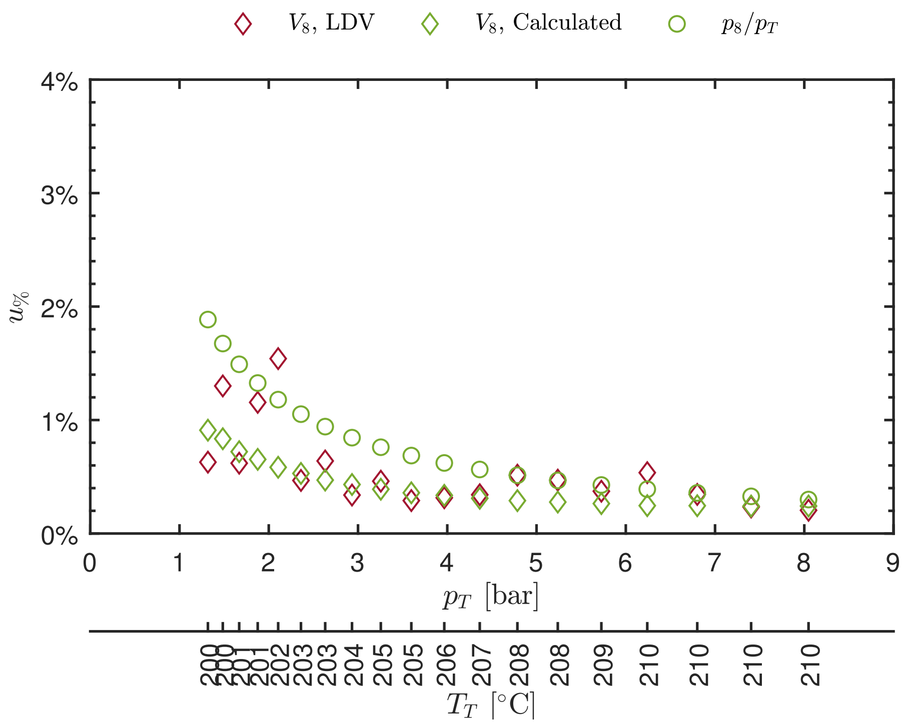

Figure 7.26: Relative percentage uncertainties of observed quantities of test M15.MM101.

For a better evaluation of the deviations, Figure 7.25a and Figure 7.25b report the percentage difference of pressure ratios and velocities respectively, as a function of total conditions. Equations Equation 7.20, Equation 7.21, Equation 7.22, Equation 7.23 were used. The accordance among CFD and measurements is very good, in the case of pressure ratios, with discrepancies lower than 1.5%. Regarding velocity, the discrepancy between CFD and computed velocity is very low. LDV instead features a discrepancy with both CFD and the computed velocity most of the times below 4%, with the exception of the point at the highest pressure with reaches about 6.6%.

Relative percentage uncertainties are reported in Figure 7.26. LDV values increase with respect to other tests, meaning that the dispersion of observed data is greater.

The feasibility of LDV in a supersonic accelerating flow is confirmed by the low deviations between computed and measured data.

Concluding, the accordance between measurements and calculations is globally considered satisfactory. The behavior at conditions where the maximum discrepancy between velocities is observed needs to be further investigated.

7.10 CONCLUSIONS

In this chapter, the first ever complete characterization of a point in a non-ideal compressible fluid flow was reported. To reach this objective, beside temperature and pressure measurement, the first ever direct velocity measurement in such flows was carried out. The hostile environment represented by the flow to be characterized led to the design of a specifically conceived seeding system, based on the atomization of a suspension of solid particles in the working fluid. The particle suitable for seeding the flow is solid, thus titanium dioxide was selected. Two different nozzles were tested from non-ideal to almost ideal thermodynamic conditions and results were analyzed in terms of pressure ratio and velocity as a function of total conditions. Their trends and the dependency on total conditions were verified and proved the non-ideality of analyzed flows.

Experimental results were compared to CFD simulations and values computed using the isentropic expansion hypothesis. Discrepancy below 2.2% and 1.3% for pressure ratios was found in the subsonic non-accelerating case and the supersonic accelerating one respectively. In tests with the CM07 nozzle, the observed pressure deviation with respect to CFD is substantially independent on thermodynamic conditions, while in the supersonic accelerating flow case a slight better agreement was observed going from non-ideal states to ideal ones. Regarding the supersonic non-accelerating case, a rather unsatisfactory maximum deviation of 14.3% was obtained in the most non-ideal case, which decreased to $\approx 10\%$ towards ideal conditions.

Regarding velocities, the observed deviations are always below 4%, except in the most non-ideal expansion in the supersonic accelerating flow test, where the maximum deviation is 6.6%. In the subsonic case, observed velocity discrepancies are almost independent on total conditions ($\approx 2\%$). However, in the other two cases the discrepancy between measured velocity and CFD decreases from the non-ideal region to the ideal one. In the supersonic accelerating case, velocities obtained from CFD and pressure and temperature measurements agree and show a similar trend, both going from $\approx 6.5\%$ deviation at minimum Z_T to $< 3\%$ deviation at maximum Z_T with respect to the measured velocity. In the non-accelerating case, the discrepancy between them goes from a maximum of 5.4% to a minimum of 3%, with CFD resulting in a better agreement with measured velocity.

In tests where a dependency of deviations on non-ideality is present, the maximum absolute value of deviation occurs *always* at the most non-ideal state and reduces towards ideal conditions. The feasibility of LDV measurements in non-ideal compressible-fluid flows is proved.

8

CONCLUSIONS AND OUTLOOK

The complete characterization of a non-ideal compressible-fluid flow was performed in three peculiar conditions. A nozzle was selected as the simplest geometry of relevance for the study of fundamentals of the fluid-dynamics of such flows and for its representativeness of industrial applications, such as organic Rankine cycle turbines. The first experimental observations of non-ideal flows provided pressure and temperature measurements, complemented with schlieren visualizations, from which the Mach number was measured (Chapter 6). For a complete characterization of the flow, the independent measurement of velocity was necessary. To accomplish this goal, the LDV technique was chosen and a specifically designed seeding system was implemented (Chapter 7). The adopted apparatus was conceived for seeding high temperature, high pressure and potentially condensible flows, where the fluid *must not* be contaminated, and it is suitable to every application where at least some of these requirements are present.

Working fluids selected for the experimental campaigns were siloxane MM and MDM. Due to the need of heating the fluid at high temperature to reach the thermodynamic region where non-ideal behavior is present, it was necessary to test the thermal stability of the aforementioned working fluids. First, a method based of the deviation of the VLE curve of the fluid was employed, but it yielded contradictory results, due to the low volatility of the tested fluid (Chapter 3). Thus, an improved method was employed, based on chemical analysis of both vapor and liquid phases of the sample subjected to thermal stress (Chapter 4). MM proved to be more stable than MDM. Due to the current interest in the use of mixtures in ORCs, an equimolar mixture of MM and MDM was also tested, showing a behavior that appears to be different from the simple superimposition of pure fluid ones.

Based on the results provided by the thermal stability analysis, the full punctual characterization of a flow of a molecularly complex fluid operating at non-ideal conditions was carried out by means of laser Doppler velocimetry. Three different conditions were observed yielding maximum deviations below 6.6%, that reduce to $\approx 0 \div 4\%$ in most cases, between measured velocity and the one obtained from CFD or computed from pressure and temperature measurements. Generally, discrepancies reduce going from low Z_T to almost ideal gas states. Regarding pressure ratios, the deviation between measurements and CFD is below 2.2% and 1.3% for the subsonic non-accelerating and supersonic accelerating flows respectively. Regarding the supersonic non-accelerating flow the discrepancy is between $\approx 10\%$ and 14.3%, showing that high Mach number non-ideal flows require further study.

These are the very first direct measurements ever exploiting the LDV technique in a high velocity non-ideal flow and show the feasibility of laser Doppler velocimetry in this framework.

Current and future activities will be devoted at obtaining a complete characterization of the the flow with pressure, temperature and velocity measurements along the whole nozzle axis, employing the know how gained during the present research. Further, a research project is currently underway, aimed at providing a reliable procedure for the calibration of directional pressure probes for non-ideal flows, that will be carried out in the TROVA. The LDV system presented in this thesis will be used to provide reference values of velocity. Beside experimental activities, an extensive effort is being made for the numerical simulation of directional probes, which could become, if reliable and validated, a tool for performing their numerical calibration. These activities are building blocks that pose the basis for future tests on linear cascades.

Concerning the thermal stability topic, activities will not conclude with this research. A detailed analysis of the influence of pressure and stress time will give a broader understanding of the phenomena occurring when siloxanes are exposed at high temperatures. Further, other compositions of mixtures will be tested to better understand the role of each of the components. A closed loop test bench implementing a micro-ORC is currently being designed, to assess the influence of cyclic stress as the one experienced by the fluid in real plants. The activities reported up to now are devoted to the understanding of the thermal stability as a property of the fluid itself. However, in real plants the fluid interacts with other substances possibly present. The compatibility with contaminants such as lubricants will be tested with dedicated static tests.

BIBLIOGRAPHY

[1] *ASHRAE Standard 97-2007 (RA 2017) – Sealed Glass Tube Method to Test the Chemical Stability of Materials for Use within Refrigerant Systems (ANSI Approved)*. 2017. URL: https://www.techstreet.com/ashrae/standards/ashrae-97-2007-ra-2017?product_id=1982751.

[2] *ASTM D2879-10, Standard Test Method for Vapor Pressure-Temperature Relationship and Initial Decomposition Temperature of Liquids by Isoteniscope*. West Conshohocken, PA, 2015. DOI: 10.1520/D6743-11R15. URL: http://www.astm.org/cgi-bin/resolver.cgi?D6743-11(2015).

[3] *ASTM D6743 - 11(2015), Standard Test Method for Thermal Stability of Organic Heat Transfer Fluids*. West Conshohocken, PA, 2010. DOI: 10.1520/D2879-10. URL: http://www.astm.org/cgi-bin/resolver.cgi?D2879-10.

[4] Rima Abbas, Andre Schedemann, Christian Ihmels, Sabine Enders, and Jürgen Gmehling. "Measurement of Thermophysical Pure Component Properties for a Few Siloxanes Used as Working Fluids for Organic Rankine Cycles." In: *Industrial & Engineering Chemistry Research* 50.16 (2011), pp. 9748–9757. DOI: 10.1021/ie200256f. eprint: https://doi.org/10.1021/ie200256f. URL: https://doi.org/10.1021/ie200256f.

[5] H.E. Albrecht, M. Borys, N. Damaschke, and C. Tropea. *Laser Doppler and Phase Doppler Measurements Techniques*. 1st. New York: Springer-Verlag Berlin Heidelberg, 2003.

[6] Wendy C. Andersen and Thomas J. Bruno. "Rapid Screening of Fluids for Chemical Stability in Organic Rankine Cycle Applications." In: *Industrial & Engineering Chemistry Research* 44.15 (2005), pp. 5560–5566. DOI: 10.1021/ie050351s. eprint: https://doi.org/10.1021/ie050351s. URL: https://doi.org/10.1021/ie050351s.

[7] G. Angelino and C. Invernizzi. "Cyclic Methylsiloxanes as Working Fluids for Space Power Cycles." In: *J. Sol. Energy Eng.* 115.3 (1993). URL: http://dx.doi.org/10.1115/1.2930039.

[8] Gianfranco Angelino and Piero Colonna. "Multicomponent Working Fluids For Organic Rankine Cycles (ORCs)." In: *Energy* 23.6 (1998), pp. 449–463. URL: http://dx.doi.org/10.1016/S0360-5442(98)00009-7.

[9] Gianfranco Angelino and Costante Invernizzi. “Experimental investigation on the thermal stability of some new zero ODP refrigerants.” In: *International Journal of Refrigeration* 26.1 (2003), pp. 51 –58. ISSN: 0140-7007. URL: https://doi.org/10.1016/S0140-7007(02)00023-3.

[10] C Antonini, G Persico, and A L Rowe. “Prediction of the dynamic response of complex transmission line systems for unsteady pressure measurements.” In: *Measurement Science and Technology* 19.12 (2008), p. 125401. DOI: 10.1088/0957-0233/19/12/125401. URL: https://doi.org/10.1088%2F0957-0233%2F19%2F12%2F125401.

[11] O. Badr, S.D. Probert, and P.W. O’Callaghan. “Selecting a working fluid for a Rankine-cycle engine.” In: *Appl. Energy* 21.1 (1985), pp. 1–42. URL: http://dx.doi.org/10.1016/0306-2619(85)90072-8.

[12] E.S. Blake, W.C. Hammann, James W. Edwards, T.E. Reichard, and M. R. Ort. “Thermal Stability as a Function of Chemical Structure.” In: *J. Chem. Eng. Data* 6.1 (1961), pp. 87–98. URL: http://dx.doi.org/10.1021/je60009a020.

[13] Ludovico Calderazzi and Piero Colonna di Paliano. “Thermal stability of R-134a, R-141b, R-13I1, R-7146, R-125 associated with stainless steel as a containing material.” In: *Int. J. Refrig* 20.6 (1997), pp. 381 –389. URL: http://dx.doi.org/10.1016/S0140-7007(97)00043-1.

[14] G Camino, S.M Lomakin, and M Lazzari. “Polydimethylsiloxane thermal degradation Part 1. Kinetic aspects.” In: *Polymer* 42.6 (2001), pp. 2395 –2402. ISSN: 0032-3861. DOI: https://doi.org/10.1016/S0032-3861(00)00652-2. URL: http://www.sciencedirect.com/science/article/pii/S0032386100006522.

[15] G. Cammi. “Measurements techniques for non-ideal compressible fluid flows: applications to organic fluids.” PhD thesis. Politecnico di Milano, 2019.

[16] G. Cammi, C.C. Conti, A. Spinelli, and A. Guardone. “Experimental characterization of nozzle flow expansions of siloxane MM for ORC turbines applications.” In: *Energy* (Under review, 2020).

[17] Soo-Yong Cho, Chong-Hyun Cho, and Sang-Kyu Choi. “Experiment and cycle analysis on a partially admitted axial-type turbine used in the organic Rankine cycle.” In: *Energy* 90 (2015), pp. 643 –651. ISSN: 0360-5442. DOI: https://doi.org/10.1016/j.energy.2015.07.092. URL: http://www.sciencedirect.com/science/article/pii/S0360544215009871.

[18] R. Clift and W.H. Gauvin. "Motion of Entrained Particles in Gas Streams." In: *The Canadian Journal of Chemical Engineering* 49 (Aug. 1971), pp. 439–448.

[19] R. Clift, J.R. Grace, and M.E. Weber. *Bubbles, drops, and particles*. Academic Press, 1978.

[20] H. W. Coleman and W. G. Steele. *Experimentation, Validation, and Uncertainty Analysis for Engineers*. 3rd ed. Wiley, 2009.

[21] P. Colonna and A Guardone. "Molecular interpretation of non-classical gas dynamics of dense vapors under van der Waals model." In: *Phis. of Fluids* 18 (2006), pp. 056101,1–14.

[22] P. Colonna and T. P. van der Stelt. *FluidProp: a program for the estimation of thermo physical properties of fluids*. Software, http://www.FluidProp.com. Energy Technology Section, Delft University of Technology, The Netherlands, 2004. URL: www.FluidProp.com.

[23] P. Colonna, N.R. Nannan, A. Guardone, and E.W. Lemmon. "Multiparameter equations of state for selected siloxanes." In: *Fluid Phase Equilib.* 244.2 (2006), pp. 193 –211. URL: http://dx.doi.org/10.1016/j.fluid.2006.04.015.

[24] P. Colonna, A. Guardone, N. R. Nannan, and C. Zamfirescu. "Design of the Dense Gas Flexible Asymmetric Shock Tube." In: *Journal of Fluids Engineering* 130.3 (Mar. 2008). 034501. ISSN: 0098-2202. DOI: 10.1115/1.2844585. eprint: https://asmedigitalcollection.asme.org/fluidsengineering/article-pdf/130/3/034501/5658486/034501_1.pdf. URL: https://doi.org/10.1115/1.2844585.

[25] P. Colonna, J. Harinck, S. Rebay, and A. Guardone. "Real-Gas Effects in Organic Rankine Cycle Turbine Nozzles." In: *J. Prop. Power* 24 (2008), pp. 282–294.

[26] Piero Colonna, Emiliano Casati, Carsten Trapp, Tiemo Mathijssen, Jaakko Larjola, Teemu Turunen-Saaresti, and Antti Uusitalo. "Organic Rankine cycle power systems: from the concept to current technology, applications, and an outlook to the future." In: *Journal of Engineering for Gas Turbines and Power* 137.10 (2015), p. 100801.

[27] C. C. Conti, A. Spinelli, G. Cammi, M. Zocca, F. Cozzi, and A. Guardone. "Schlieren Visualizations of Non-Ideal Compressible Fluid Flows." In: *13th International Conference on Heat Transfer, Fluid Mechanics and Thermodynamics (HEFAT 2017)*. 2017.

[28] H. M. Curran. "Organic Working Fluids in Rankine Engines." In: *Journal of Energy* 5.4 (1981), pp. 218–223. DOI: 10.2514/3.62532. eprint: https://doi.org/10.2514/3.62532. URL: https://doi.org/10.2514/3.62532.

[29] Xiaoye Dai, Lin Shi, and Weizhong Qian. "Review of the Working Fluid Thermal Stability for Organic Rankine Cycles." In: *Journal of Thermal Science* 28.4 (2019), pp. 597–607. ISSN: 1993-033X. DOI: `10.1007/s11630-019-1119-3`. URL: `https://doi.org/10.1007/s11630-019-1119-3`.

[30] Xiaoye Dai, Lin Shi, and Weizhong Qian. "Thermal stability of hexamethyldisiloxane (MM) as a working fluid for organic Rankine cycle." In: *International Journal of Energy Research* 43.2 (2019), pp. 896–904. DOI: `10.1002/er.4323`. eprint: `https://onlinelibrary.wiley.com/doi/pdf/10.1002/er.4323`. URL: `https://onlinelibrary.wiley.com/doi/abs/10.1002/er.4323`.

[31] Norman R. Draper and Harry Smith. *Applied Regression Analysis*. John Wiley & Sons, 2014. DOI: `10.1002/9781118625590`.

[32] Francisco J. Durá Galiana, Andrew P.S. Wheeler, and Jonathan Ong. "A Study of Trailing-Edge Losses in Organic Rankine Cycle Turbines." In: *Journal of Turbomachinery* 138.12 (June 2016). 121003. ISSN: 0889-504X. DOI: `10.1115/1.4033473`. eprint: `https://asmedigitalcollection.asme.org/turbomachinery/article-pdf/138/12/121003/6305003/turbo\_138\_12\_121003.pdf`. URL: `https://doi.org/10.1115/1.4033473`.

[33] Petar R. Dvornic. *Thermal Properties of Polysiloxanes*. Dordrecht: Springer Netherlands, 2000, pp. 185–212. ISBN: 978-94-011-3939-7. URL: `http://dx.doi.org/10.1007/978-94-011-3939-7_7`.

[34] B. Efron and R.J. Tibshirani. *An Introduction to the Bootstrap*. Chapman and Hall, 1994. ISBN: 9780412042317.

[35] Tobias G. Erhart, Jürgen Gölz, Ursula Eicker, and Martijn Van den Broek. "Working Fluid Stability in Large-Scale Organic Rankine Cycle-Units Using Siloxanes—Long-Term Experiences and Fluid Recycling." In: *Energies* 9.6 (2016). ISSN: 1996-1073. DOI: `10.3390/en9060422`. URL: `https://www.mdpi.com/1996-1073/9/6/422`.

[36] M. A. Fabuss, A. S. Borsanyi, B. M. Fabuss, and J. O. Smith. "Thermal Stability Studies of Pure Hydrocarbons in a High Pressure Isoteniscope." In: *J. Chem. Eng. Data* 8.1 (1963), pp. 64–69. URL: `http://dx.doi.org/10.1021/je60016a018`.

[37] Stephen Fergason, Alberto Guardone, and Brian Argrow. "Construction and Validation of a Dense Gas Shock Tube." In: *Journal of Thermophysics and Heat Transfer* 17.3 (2003), pp. 326–333. DOI: `10.2514/2.6789`. eprint: `https://doi.org/10.2514/2.6789`. URL: `https://doi.org/10.2514/2.6789`.

[38] K. R. Fisch and F. D. Verderame. "Automatic Recording Apparatus for Thermal Stability Determinations." In: *J. Chem. Eng. Data* 6.1 (1961), pp. 131–134. URL: http://dx.doi.org/10.1021/je60009a027.

[39] Ora L. Flaningam. "Vapor pressures of poly(dimethylsiloxane) oligomers." In: *Journal of Chemical & Engineering Data* 31.3 (1986), pp. 266–272. DOI: 10.1021/je00045a002. eprint: https://doi.org/10.1021/je00045a002. URL: https://doi.org/10.1021/je00045a002.

[40] Wayne A. Fuller. *Measurement Error Models*. John Wiley & Sons, Inc., 1987. DOI: 10.1002/9780470316665.

[41] S. Gallarini. "Design and commissioning of a laser Doppler velocimetry seeding system for non-ideal fluid flows." MA thesis. Politecnico di Milano, 2016.

[42] Donald F. Gatz and Luther Smith. "The standard error of a weighted mean concentration—I. Bootstrapping vs other methods." In: *Atmospheric Environment* 29.11 (1995), pp. 1185 –1193. ISSN: 1352-2310. DOI: https://doi.org/10.1016/1352-2310(94)00210-C. URL: http://www.sciencedirect.com/science/article/pii/135223109400210C.

[43] Daniel M. Ginosar, Lucia M. Petkovic, and Donna Post Guillen. "Thermal Stability of Cyclopentane as an Organic Rankine Cycle Working Fluid." In: *Energy & Fuels* 25.9 (2011), pp. 4138–4144. URL: http://dx.doi.org/10.1021/ef200639r.

[44] John Hall Gladstone and T. P. Dale. "XIV. Researches on the refraction, dispersion, and sensitiveness of liquids." In: *Philosophical Transactions of the Royal Society of London* 153 (1863), pp. 317–343. DOI: 10.1098/rstl.1863.0014. eprint: https://royalsocietypublishing.org/doi/pdf/10.1098/rstl.1863.0014. URL: https://royalsocietypublishing.org/doi/abs/10.1098/rstl.1863.0014.

[45] A. Guardone, A. Spinelli, and V. Dossena. "Influence of Molecular Complexity on Nozzle Design for an Organic Vapor Wind Tunnel." In: *Journal of Engineering for Gas Turbines and Power* 135 (Apr. 2013).

[46] A.J. Head, M. Novara, M. Gallo, F. Schrijer, and P. Colonna. "Feasibility of particle image velocimetry for low-speed unconventional vapor flows." In: *Experimental Thermal and Fluid Science* 102 (2019), pp. 589 –594. ISSN: 0894-1777. DOI: https://doi.org/10.1016/j.expthermflusci.2018.10.028. URL: http://www.sciencedirect.com/science/article/pii/S0894177718305181.

[47] *Preliminary Design of the ORCHID: A Facility for Studying Non-Ideal Compressible Fluid Dynamics and Testing ORC Expanders.* Vol. Volume 3: Coal, Biomass and Alternative Fuels; Cycle Innovations; Electric Power; Industrial and Cogeneration; Organic Rankine Cycle Power Systems. Turbo Expo: Power for Land, Sea, and Air. V003T25A001. June 2016. DOI: `10.1115/GT2016-56103`. eprint: `https://asmedigitalcollection.asme.org/GT/proceedings-pdf/GT2016/49743/V003T25A001/2429898/v003t25a001-gt2016-56103.pdf`. URL: `https://doi.org/10.1115/GT2016-56103`.

[48] Peter C. Hung, George W. Irwin, Robert C. Kee, and Seán McLoone. "Difference equation approach to two-thermocouple sensor characterization in constant velocity flow environments." In: 2005.

[49] C. M. Invernizzi. "Valutazione della stabilità termica di fluidi di lavoro per cicli rankine: apparato sperimentale e risultati di calibrazione." In: *La Termotecnica* XLIV.4 (1990). in Italian, pp. 69–76.

[50] I. B. Johns, E. A. McElhill, and J. O. Smith. "Thermal Stability of Organic Compounds." In: *I&EC Product Research and Development* 1.1 (1962), pp. 2–6. URL: `http://dx.doi.org/10.1021/i360001a001`.

[51] I. B. Johns, E. A. McElhill, and J. O. Smith. "Thermal Stability of Some Organic Compounds." In: *J. Chem. Eng. Data* 7.2 (1962), pp. 277–281. URL: `http://dx.doi.org/10.1021/je60013a036`.

[52] Luuc Keulen, Elisabeth Mansfield, Ian H. Bell, Andrea Spinelli, and Alberto Guardone. "Bubble-Point Measurements and Modeling of Binary Mixtures of Linear Siloxanes." In: *Journal of Chemical & Engineering Data* 63.9 (2018), pp. 3315–3330. DOI: `10.1021/acs.jced.8b00200`. eprint: `https://doi.org/10.1021/acs.jced.8b00200`. URL: `https://doi.org/10.1021/acs.jced.8b00200`.

[53] L.S. Langston. "Secondary Flows in Axial Turbines—A Review." In: *Annals of the New York Academy of Sciences* 934.1 (2001), pp. 11–26. DOI: `10.1111/j.1749-6632.2001.tb05839.x`. eprint: `https://nyaspubs.onlinelibrary.wiley.com/doi/pdf/10.1111/j.1749-6632.2001.tb05839.x`. URL: `https://nyaspubs.onlinelibrary.wiley.com/doi/abs/10.1111/j.1749-6632.2001.tb05839.x`.

[54] E. W. Lemmon, M. O. McLinden, and M. L. Huber. *NIST Reference Fluid Thermodynamic and Transport Properties REFPROP, Version 7.0, Users Guide*. Physical, Chemical Properties Division, National Institute of Standards, and Technology. Boulder, Colorado 80305, 2002.

[55] E. W. Lemmon, I. H. Bell, M. L. Huber, and M. O. McLinden. *NIST Standard Reference Database 23: Reference Fluid Thermodynamic and Transport Properties-REFPROP, Version 9.4.4.10*. 2017.

[56] D. Bruggemann M. Preißinger. "Thermal stability of hexamethyldisiloxane (MM) for high temperature applications." In: *3rd International Seminar on ORC Power Systems* (2015).

[57] E. Macchi and M. Astolfi. *Organic Rankine Cycle (ORC) Power Systems. Technologies and applications*. New York: Woodhead Publishing Series in Energy: Number 107, Elsevier, 2017.

[58] John Mandel. "Fitting Straight Lines When Both Variables are Subject to Error." In: *Journal of Quality Technology* 16.1 (1984), pp. 1–14. DOI: `10.1080/00224065.1984.11978881`. eprint: `https://doi.org/10.1080/00224065.1984.11978881`. URL: `https://doi.org/10.1080/00224065.1984.11978881`.

[59] W. F. Manders and J. M. Bellama. "Multiphoton infrared laser-induced degradation of polydimethylsiloxane and hexamethyldisiloxane." In: *Journal of Polymer Science: Polymer Chemistry Edition* 23.2 (1985), pp. 351–357. DOI: `10.1002/pol.1985.170230211`. eprint: `https://onlinelibrary.wiley.com/doi/pdf/10.1002/pol.1985.170230211`. URL: `https://onlinelibrary.wiley.com/doi/abs/10.1002/pol.1985.170230211`.

[60] T. Mathijssen, M. Gallo, E. Casati, N.R. Nannan, C. Zamfirescu, A. Guardone, and P. Colonna. "The flexible asymmetric shock tube (FAST): a Ludwieg tube facility for wave propagation measurements in high-temperature vapours of organic fluids." In: *Experiments in fluids* 56.195 (2015). DOI: `https://doi.org/10.1007/s00348-015-2060-1`.

[61] R. Mei. "Velocity Fidelity of Flow Tracer Particles." In: *Experiments in fluids* 22 (1996), pp. 1–13.

[62] A. Melling. "Tracer Particles and Seeding for Particle Image Velocimetry." In: *Measurement Science and Technology* 8 (1997), pp. 1406–1416.

[63] W. Merzkirch. *Flow Visualization*. Academic Press, 1987. ISBN: 978-0-12-491351-6.

[64] Douglas C. Montgomery, George C. Runger, and Norma F. Hubele. *Engineering Statistics*. 5th ed. Wiley, 2010.

[65] W. Noll. *Chemistry and Technology of Silicones*. Academic Press, 1968. ISBN: 9780323141406.

[66] Marco Pasetti. "Stabilità termica di fluidi di lavoro per cicli ORC, Metodo di misura e risultati sperimentali." PhD thesis. Università degli studi di Brescia, 2013.

[67] Marco Pasetti, Costante M. Invernizzi, and Paolo Iora. "Thermal stability of working fluids for organic Rankine cycles: An improved survey method and experimental results for cyclopentane, isopentane and n-butane." In: *Appl. Therm. Eng.* 73.1 (2014), pp. 764 –774. URL: http://dx.doi.org/10.1016/j.applthermaleng.2014.08.017.

[68] Bruce E. Poling, John M. Prausnitz, and John P. O'Connell. *The properties of gases and liquids*. 5th ed. New York: McGraw-Hill, 2000. ISBN: 0070116822 9780070116825.

[69] F. Reinker, E.Y. Kenig, and S. aus der Wiesche. "Closed Loop Organic Vapor Wind Tunnel CLOWT: Commissioning and Operational Experience." In: *Proceedings of the 5th International Seminar on ORC Power Systems*. 2019.

[70] Felix Reinker, Eugeny Y. Kenig, Max Passmann, and Stefan aus der Wiesche. "Closed Loop Organic Wind Tunnel (CLOWT): Design, Components and Control System." In: *Energy Procedia* 129 (2017). 4th International Seminar on ORC Power SystemsSeptember 13-15th 2017POLITECNICO DI MILANOBOVISA CAMPUSMILANO, ITALY, pp. 200 –207. ISSN: 1876-6102. DOI: https://doi.org/10.1016/j.egypro.2017.09.158. URL: http://www.sciencedirect.com/science/article/pii/S1876610217340274.

[71] *Development and Commissioning of a Blowdown Facility for Dense Gas Vapours*. Vol. Volume 3: Coal, Biomass, Hydrogen, and Alternative Fuels; Cycle Innovations; Electric Power; Industrial and Cogeneration; Organic Rankine Cycle Power Systems. Turbo Expo: Power for Land, Sea, and Air. V003T28A002. June 2019. DOI: 10.1115/GT2019-91609. eprint: https://asmedigitalcollection.asme.org/GT/proceedings-pdf/GT2019/58608/V003T28A002/6439123/v003t28a002-gt2019-91609.pdf. URL: https://doi.org/10.1115/GT2019-91609.

[72] Robert O. Sauer. "Group and Bond Refractions in Organosilicon Liquids." In: *Journal of the American Chemical Society* 68.6 (1946), pp. 954–962. DOI: 10.1021/ja01210a013. eprint: https://doi.org/10.1021/ja01210a013. URL: https://doi.org/10.1021/ja01210a013.

[73] C. H. Sieverding. "Recent Progress in the Understanding of Basic Aspects of Secondary Flows in Turbine Blade Passages." In: *Journal of Engineering for Gas Turbines and Power* 107.2 (Apr. 1985), pp. 248–257. ISSN: 0742-4795. DOI: 10.1115/1.3239704. eprint: https://asmedigitalcollection.asme.org/gasturbinespower/article-pdf/107/2/248/5702799/248_1.pdf. URL: https://doi.org/10.1115/1.3239704.

[74] R. Span and W. Wagner. “Equations of State for Technical Applications. I. Simultaneously Optimized Functional Forms for Nonpolar and Polar Fluids.” In: *International Journal of Thermophysics* 24.1 (2003), pp. 1–39.

[75] R. Span and W. Wagner. “Equations of State for Technical Applications. II. Results for Nonpolar Fluids.” In: *International Journal of Thermophysics* 24.1 (2003), pp. 41–109.

[76] A. Spinelli. “Design and Construction of a Test Rig for Organic Vapours.” PhD thesis. Politecnico di Milano, Dec. 2010.

[77] A. Spinelli, M. Pini, V. Dossena, P. Gaetani, and F. Casella. “Design, Simulation, and Construction of a Test Rig for Organic Vapors.” In: *Journal of Engineering for Gas Turbines and Power* 135 (Apr. 2013).

[78] A. Spinelli, G. Cammi, S. Gallarini, M. Zocca, F. Cozzi, P. Gaetani, V. Dossena, and A. Guardone. “Experimental evidence of non-ideal compressible effects in expanding flow of a high molecular complexity vapor.” In: *Experiments in fluids* 59.126 (2018). DOI: `https://doi.org/10.1007/s00348-018-2578-0`.

[79] Andrea Spinelli, Giorgia Cammi, Camilla Cecilia Conti, Simone Gallarini, Marta Zocca, Fabio Cozzi, Paolo Gaetani, Vincenzo Dossena, and Alberto Guardone. “Experimental observation and thermodynamic modeling of non-ideal expanding flows of siloxane MDM vapor for ORC applications.” In: *Energy* 168 (2019), pp. 285 –294. ISSN: 0360-5442. DOI: `https://doi.org/10.1016/j.energy.2018.11.071`. URL: `http://www.sciencedirect.com/science/article/pii/S0360544218322837`.

[80] T.P. van der Stelt, N.R. Nannan, and P. Colonna. “The iPRSV equation of state.” In: *Fluid Phase Equilibria* 330 (2012), pp. 24 –35. ISSN: 0378-3812. DOI: `https://doi.org/10.1016/j.fluid.2012.06.007`. URL: `http://www.sciencedirect.com/science/article/pii/S0378381212002506`.

[81] Daniel R. Stull. “Vapor Pressure of Pure Substances. Organic and Inorganic Compounds.” In: *Industrial & Engineering Chemistry* 39.4 (1947), pp. 517–540. DOI: `10.1021/ie50448a022`. eprint: `https://doi.org/10.1021/ie50448a022`. URL: `https://doi.org/10.1021/ie50448a022`.

[82] M. Thol, F.H. Dubberke, G. Rutkai, T. Windmann, A. Köster, R. Span, and J. Vrabec. “Fundamental equation of state correlation for hexamethyldisiloxane based on experimental and molecular simulation data.” In: *Fluid Phase Equilibria* 418 (2016). Special Issue covering the Nineteenth Symposium on Thermophysical Properties, pp. 133 –151. ISSN: 0378-3812. DOI: `https://doi.org/10.1016/j.fluid.2015.09.047`. URL: `http://www.sciencedirect.com/science/article/pii/S0378381215301527`.

[83] Monika Thol, Frithjof H. Dubberke, Elmar Baumhögger, Jadran Vrabec, and Roland Span. "Speed of Sound Measurements and Fundamental Equations of State for Octamethyltrisiloxane and Decamethyltetrasiloxane." In: *Journal of Chemical & Engineering Data* 62.9 (2017), pp. 2633–2648. DOI: `10.1021/acs.jced.7b00092`. eprint: `https://doi.org/10.1021/acs.jced.7b00092`. URL: `https://doi.org/10.1021/acs.jced.7b00092`.

[84] P. A. Thompson. "A fundamental derivative in gas dynamics." In: *Phys. Fluids* 14 (1971), pp. 1843–1849.

[85] P. A. Thompson and K. C. Lambrakis. "Negative shock waves." In: *J. Fluid Mech.* 60 (1973), pp. 187–208.

[86] C. Tropea, A. L. Yarin, and J. F. Foss. *Springer Handbook of Experimental Fluid Mechanics*. Springer-Verlag Berlin Heidelberg, 2007.

[87] Teemu Turunen-Saaresti, Antti Uusitalo, and Juha Honkatukia. "Design and testing of high temperature micro-ORC test stand using Siloxane as working fluid." In: *Journal of Physics: Conference Series* 821 (2017), p. 012024. DOI: `10.1088/1742-6596/821/1/012024`. URL: `https://doi.org/10.1088%2F1742-6596%2F821%2F1%2F012024`.

[88] *The University of Queensland Refrigerant and Supercritical CO2 Test Loop*. Vol. Volume 3: Coal, Biomass and Alternative Fuels; Cycle Innovations; Electric Power; Industrial and Cogeneration; Organic Rankine Cycle Power Systems. Turbo Expo: Power for Land, Sea, and Air. V003T25A013. June 2016. DOI: `10.1115/GT2016-58110`. eprint: `https://asmedigitalcollection.asme.org/GT/proceedings-pdf/GT2016/49743/V003T25A013/2430086/v003t25a013-gt2016-58110.pdf`. URL: `https://doi.org/10.1115/GT2016-58110`.

[89] Antti Uusitalo, Juha Honkatukia, and Teemu Turunen-Saaresti. "Evaluation of a small-scale waste heat recovery organic Rankine cycle." In: *Applied Energy* 192 (2017), pp. 146 –158. ISSN: 0306-2619. DOI: `https://doi.org/10.1016/j.apenergy.2017.01.088`. URL: `http://www.sciencedirect.com/science/article/pii/S0306261917300995`.

[90] V. Valori, G.E. Elsinga, M. Rohde, J. Westerweel, and T.H.J.J. van der Hagen. "Particle image velocimetry measurements of a thermally convective supercritical fluid." In: *Experiments in Fluids* 60.143 (2019). DOI: `https://doi.org/10.1007/s00348-019-2789-z`.

[91] Salvatore Vitale, Tim Adrian Albring, Matteo Pini, Nicolas Ralph Gauger, and Piero Colonna. "Fully turbulent discrete adjoint solver for non-ideal compressible flow applications." In: *Journal of the Global Power and Propulsion Society* 1 (2017), pp. 252–270.

DOI: 10.22261/JGPPS.Z1FVOI. URL: http://dx.doi.org/10.22261/JGPPS.Z1FVOI.

[92] H. P. Wang, S. J. Olson, R. J. Goldstein, and E. R. G. Eckert. "Flow Visualization in a Linear Turbine Cascade of High Performance Turbine Blades." In: *Journal of Turbomachinery* 119.1 (Jan. 1997), pp. 1–8. ISSN: 0889-504X. DOI: 10.1115/1.2841006. eprint: https://asmedigitalcollection.asme.org/turbomachinery/article-pdf/119/1/1/5840436/1_1.pdf. URL: https://doi.org/10.1115/1.2841006.

[93] E. L. Warrick. "The Application of Bond Refractions to Organosilicon Chemistry." In: *Journal of the American Chemical Society* 68.12 (1946), pp. 2455–2459. DOI: 10.1021/ja01216a004. eprint: https://doi.org/10.1021/ja01216a004. URL: https://doi.org/10.1021/ja01216a004.

[94] T. Weith, F. Heberle, M. Preißinger, and D. Brüggemann. "Performance of Siloxane Mixtures in a High-Temperature Organic Rankine Cycle Considering the Heat Transfer Characteristics during Evaporation." In: *Energies* (2014). DOI: https://doi.org/10.3390/en7095548.

[95] *Design of a Closed-Loop Optical-Access Supersonic Test Facility for Organic Vapours*. Vol. Volume 3: Coal, Biomass, and Alternative Fuels; Cycle Innovations; Electric Power; Industrial and Cogeneration; Organic Rankine Cycle Power Systems. Turbo Expo: Power for Land, Sea, and Air. V003T28A002. June 2018. DOI: 10.1115/GT2018-75301. eprint: https://asmedigitalcollection.asme.org/GT/proceedings-pdf/GT2018/51043/V003T28A002/2789412/v003t28a002-gt2018-75301.pdf. URL: https://doi.org/10.1115/GT2018-75301.

[96] Christian Wohlfarth. *Refractive index of hexamethyldisiloxane: Datasheet from Condensed Matter · Volume 50: "Optical Constants" in SpringerMaterials (https://doi.org/10.1007/978-3-662-49236-9_20)*. Ed. by M. D. Lechner. Copyright 2017 Springer-Verlag Berlin Heidelberg. DOI: 10.1007/978-3-662-49236-9_20. URL: https://materials.springer.com/lb/docs/sm_lbs_978-3-662-49236-9_20.

[97] M. Zocca, A. Spinelli, F. Cozzi, and A. Guardone. "Influence of a recessed step at the throat section of a supersonic nozzle." In: *The Aeronautical Journal* 122.1251 (2018). DOI: 10.1017/aer.2018.5.

[98] M. Zocca, A. Guardone, G. Cammi, F. Cozzi, and A. Spinelli. "Experimental observation of oblique shock waves in steady non-ideal flows." In: *Experiments in fluids* 60.101 (2019). DOI: https://doi.org/10.1007/s00348-019-2746-x.